Photoelectrochemical Studies of Sensitized Solar Cells: Sensitization of TiO_2 with Ruthenium Complexes and Cadmium Seleno-Sulfides

Ali Sepehri Fard

A DISSERTATION SUBMITTED TO
THE FACULTY OF GRADUATE STUDIES
IN PARTIAL FULFILLMENT OF THE REQUIREMENTS
FOR THE DEGREE OF
DOCTOR OF PHILOSOPHY

GRADUATE PROGRAM IN CHEMISTRY
YORK UNIVERSITY
TORONTO, ONTARIO

April 2013

Abstract

Photoelectrochemistry (PEC) of dye- and semiconductor sensitized solar cells is studied. In the first part, the structural effect of terpyridine (tpy) and dipirazinilpyridine (dpp) sensitizing dyes on the performance of solar cells is investigated. Mesoporous thin films of TiO_2 on conductive glass are sensitized with carboxylic or ester functionalized tpy and dpp ruthenium dyes. The solar conversion behavior of all dyes is investigated based on the results obtained from PEC, incident photon to current efficiency (IPCE), electrochemistry and also optical techniques such as FTIR, UV-Vis and fluorescence. PEC efficiencies of up to 1.56% are achieved by tpy dye named **H2** when used in a cell with a plain I^-/I_3^- electrolyte. The effect of the additives in the electrolyte on the behaviour of the dyes is also studied and it is shown that due to the change of the location of the conduction band (CB) of TiO_2 in the presence of these additives, the electron injection efficiencies of the dyes changes and directly translates in to lower efficiency values.

In an independent but related study on dye-sensitized solar cells (DSSC), a new class of siliconized triaryalmine compounds are used as hole transport material (HTM) to replace the conventional I^-/I_3^- electrolyte. These compounds increase the gained photovoltage (V_{oc}) of the device up to 1 V which is an exceptional development in the field of DSSCs based on HTMs. Open-circuit photovoltage decay studies are employed to address the issues with respect to large recombination with these compounds in a solar cells.

In the last part of my research, the effect of the preparation techniques of cadmium seleno-sulfides (CdSeS) on the performance of semiconductor-sensitized solar cells (SSSCs) is studied. TiO_2 films are sensitized with different compositions of $CdSe_xS_{1-x}$ where x stands for the

molar ratio of Se in the structure of the sensitizer. The sensitization is performed by chemical bath deposition in NH_3 and sodium trinitriloacetate (NTA) solution and the effect of the performance of the resulting cell is related to the structure of the sensitizer deposited through each chemical bath. PEC and optical techniques are used to fulfill this purpose.

Acknowledgment

I would like to thank my supervisor *Prof. SYLVIE MORIN* for all her support, encouragement and help during all steps of my journey in research and life at York University. All previous and current members of Morin's lab, specially Dr. Siguan Chen, Dr. Ashur Aushana, Dr. Mohammad Khanfar, Dr. Erwin Lin, Dr. Susan Zheng, Shohreh Zehedi Jasbi, Moriam Ore and Maryam Hariri made my time beautiful, productive and meaningful.

I would like to thank Prof. *PIERRE G. POTVIN* for his entire supportive role in my research, collaboration and constructive attitude which made this work possible. Dr. Arta Stublla from Potvin's lab is greatly acknowledged for being a great collaborator.

I would like to thank Prof. *GINO LAVOIE* for his positive support in my supervisory committee and adding value to my work with his piece of mind whenever possible.

All members of chemistry department at York University, specially Ms. Mary Mamais and Magy Baket are acknowledged for their constant help throughout my life at York University.

I would have never been able to pursue my research life without my family's support. I want to thank my parents, my brother and sister and my aunts, Feri, Giti and Lili, for their love, care and paving my way ahead towards my goals. The beauty my fiancé, Shokoofeh Shahangian added to my life kept my heart warm and my feet strong, to love life and to embrace all its challenges and flourish.

State of Collaboration

The studies presented in this thesis on chapters 4 and 5 were only possible through collaboration with Prof. P. G. Potvin's lab, department of chemistry at York university and Prof. B. P. Bender, department of chemical engineering and applied chemistry at university of Toronto, respectively.

We received all organometallic ruthenium complexes studied in chapter 4 of the thesis from Prof. Potvin's lab where his PhD student Dr. Arta Stublla synthesized and fully characterized these compounds. Excited-state lifetime measurements are performed in Prof. Qing-Bin Lu and by Ting Luo at department of Physics, University of Waterloo, Ontario.

The hole-transport materials studied in chapter 5 are all synthesized in Prof. Bender's lab by his PhD student Mr. Brett A. Kamino and were fully characterized before we received them. DFT calculation for these compounds is performed by Mr. Brett A. Kamino as well. Preparation of the hole-transport redox mediator, Cell fabrication and photoelectrochemical experiments are performed by me.

Scanning Electron Microscopy experiments are performed by the assistance of Karen Rethoret at York University where I collected the required images and interpreted the results. Sal Boccia at University of Toronto collected EDX spectra of our samples and calculated the atomic ratios with the aid of the EDX software and reported the results and charged us for the incurred cost.

Table of Contents

List of Tables

List of Figures

List of Abbreviations

1. **BET** : Brunauer-Emmett-Teller
2. **CB:** Conduction Band
3. **CBD**: Chemical Bath Deposition
4. **CBH:** Chemical Bath
5. **DSSC** : Dye-Sensitized Solar Cell
6. **EDX:** Energy Dispersive X-ray Analysis
7. **Eq.:** Equation
8. ***ff***: Fill Factor
9. **FTIR:** Fourier Transform Infrared Spectroscopy
10. **FTO:** Fluorine-doped Tin Oxide
11. **FWHM:** Full Width at Half-Maximum
12. **HOMO:** Highest Occupied Molecular Orbital
13. **HTM:** Hole-Transport Material
14. **IPCE:** Incident Photon-to-Current Conversion Efficiency
15. **LHE:** Light-Harvesting Efficiency
16. **LUMO:** Lowest Unoccupied Molecular Orbital
17. **MLCT:** Metal-to-Ligand Charge Transfer
18. **NBGS:** Narrow Band Gap Semiconductor
19. **NHE:** Normal Hydrogen Electrode
20. **NTA:** Nitrilo *tri*-Sodium Acetate
21. **OCVD:** Open-Circuit Photovoltage Decay
22. **OPA:** Optical Parametric Amplifier
23. **PEC:** Photoelectrochemistry
24. **PMT:** Photomultiplier Tube
25. **PXRD:** Powder X-ray diffraction
26. **QD:** Quantum Dot
27. **QDSSC:** Quantum-Dot Sensitized Solar Cell
28. **SCE:** Saturated Calomel Electrode

29. **SEM:** Scanning Electron Microscopy
30. **SHE:** Standard Hydrogen Electrode
31. **SSSC:** Semiconductor-Sensitized Solar Cell
32. **SSC:** Sensitized Solar Cell
33. **TBP:** Tertiary Butyl Pyridine (*tert*-But-Pyr)
34. **TOC:** Transparent Conductive Oxide
35. **UV-Vis:** Ultraviolet-visible spectroscopy
36. **WBGS:** Wide Band Gap Semiconductor
37. **XPS:** X-ray photoelectron spectroscopy

Chapter 1: Introduction to Solar Energy and Sunlight Conversion

1.1 Energy of the Sun, Source of Life on Earth

The existence of life on our planet is owed to the energy of sunlight captured by different means that creatures on earth have developed over time. Without solar energy, the evolution of various complicated life forms as they are known today is unattainable.

Fossil fuels, also originating from the solar energy stored in the chemical bonds of molecules, are the dominant source of energy for human activities on our planet. Different types of life on earth, humans, animals, plants etc. are completely dependent on the sun energy stored in chemical bonds. The discovery of fire enabled human beings to use energy for other forms of activities. Over millennia, mankind manipulated and discovered different techniques to harness the energy from the Sun. Most of these techniques were the least efficient methods of energy production and consumption. Today, in almost all developed and many of the developing countries, complicated techniques such as hydroelectric power generation are well established. However many of these techniques are yet environmentally costly and lack sustainability and renewability. These methods convert the energy of the sun to more useful forms and a massive portion of the energy consumed nowadays is generated by these techniques.

Such technologies stem in the industrial revolution era when humans started an endless chase of more efficient methods to produce energy. This evolved to be even more important once it became obvious that the economic success of a country was directly linked to its energy production, consumption and maintenance.

Direct conversion of sunlight into useful forms of energy reduces the number of intermediates and steps to generate energy and hence reduces the loss of energy upon conversion. Ever since the photovoltaic effect was discovered in 1839 and the photoconversion concept was introduced as one of the methods for energy generation, human beings used all their means to increase the efficiency of this technique (Becquerel, 1872). There is a strong desire to produce a highly efficient solar cell that is capable of energy conversion under any weather and illumination conditions. There is a marked increase in effort in recent years toward this goal as the cost of energy and pollution associated with the other energy production methods have jeopardised many aspects of human life and also our planet. In simple words with human energy consumption increasing, fossil fuels are being depleted.

With great confidence, one can say that the number of articles and papers that are directly and indirectly related to the solar cell research is plentiful. A limited search for the term "solar cell" in Google Scholar for the years 1994 to 2013 shows more than 790,000 hits and when limited to the term "dye-sensitized solar cells" shows more than 13,900 hits. Despite all efforts to date, research on solar cells has not been able to

introduce a device that is efficient and cost-effective, i.e. suitable for widespread use and capable of replacing almost all other energy production techniques. Over time, photovoltaics have evolved and some of these techniques are briefly described below.

The basic principles of the traditional solar cells are briefly discussed in this chapter and a short history is given. The next chapter will solely focus on the new generation photoelectrochemical solar cells, which are the main subject of this research.

1.2 Advent of Photovoltaics; Brief History and Technical Aspects of Different Generations of Solar Cells

1.2.1 Classical Systems; Discovery of Photovoltaic Phenomena and Properties of Photovoltaic Materials (1899-1939)

The photovoltaic effect, conversion of light to electricity, was discovered in 1839 by the French physicist Alexandre Edmond Becquerel. He found that in some metals, the conductance rises with illumination (Becquerel, 1839; 1872). Willoughby Smith discovered the photovoltaic effect in selenium in 1873 (Smith, 1873). In 1876, with his student R. E. Day, William G. Adams discovered that illuminating a junction between selenium and platinum also yielded a photovoltaic effect (Adam Day, 1877). The term "photovoltaic" was used to show that upon illumination, a voltage is generated across a material or across a junction between two materials, which creates a potential drift for the flow of electrons. Figure 1.1 shows a simple picture of a traditional photovoltaic device based on a p-n junction.

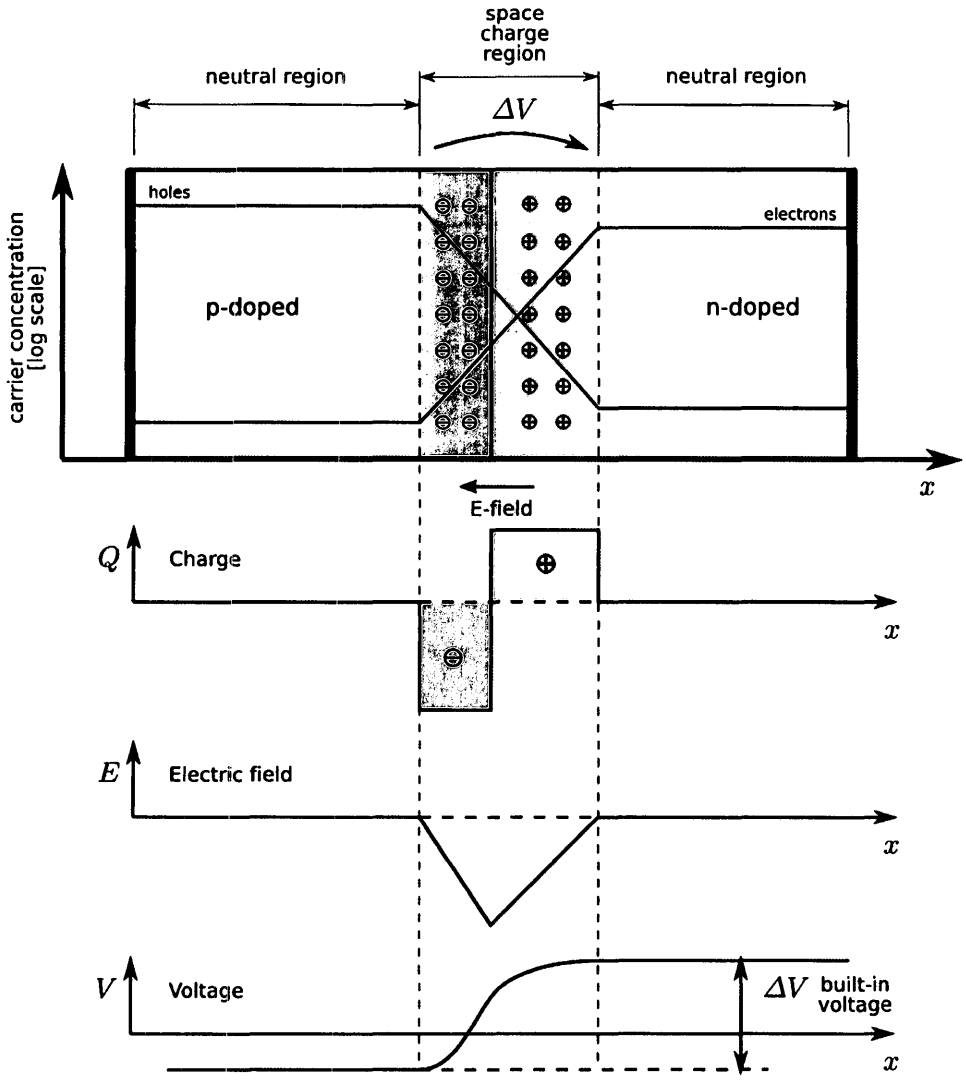

Figure 1.1 An illustration of the photovoltaic effect and the principle of the charge depletion region in a doped semiconductor used in a photovoltaic device. Axis "x" shows the geometrical dimension along the p-doped and n-doped junction and axis "y" serves to show carrier concentration, charge abundance (Q), electric field (E) and voltage (V) along the junction when the junction is illuminated with a wavelength that fulfills the excitation of the charges. (printed with permission from NREL)

In a semiconductor that has more density of one of the charge carriers (i.e. negative or positive charges) upon illumination, the charge carriers become excited and

their population in higher energy levels of the semiconductor increases. This creates a region in the semiconductor named depletion layer (region) where electrons (negative charges) and holes (positive charges) are dissociated. If the charges can be dissociated faster than their recombination rate (the rate at which the charges join each other again after losing their excitation energy), then a current can flow across the device and the external circuit connected to the two ends of the junctions (the region between the hole-rich and electron-rich domains of the semiconductor). Such a mechanism is very sensitive to the presence of impurities in the structure of the semiconductor used in the cells. The impurities introduce energy levels in the lattice of the semiconductor, which in turn, act as centers for recombination of the electrons and holes and reduce the photocurrent that is generated by the cell. This has made the production of such cells very expensive as high purity materials are required to gain enough efficiency from such cells.

The photovoltaic phenomenon has been the basis of any traditional photovoltaic device created from 1877 until now, for more than 130 years. Albert Einstein was the author of the most comprehensive theoretical work about the photoelectric effect in 1904 (Einstein, 1905) and was awarded a Nobel Prize in 1921 for his theoretical explanation. In 1916, Robert Millikan experimentally proved Einstein's theory where they both showed how the electrons in a semiconductor get excited upon illumination and how they leave positive charges behind after excitation wherever a potential drift is available.

A Polish scientist named Czochralski discovered a method for monocrystalline silicon production in 1918 (Czochralski, 1918). Using his method, the first silicon monocrystalline solar cell was fabricated in 1946 (Ohl, 1946). They were later introduced to the market.

The need for energy production for space shuttles and satellites initiated an intense and productive research in solar cells where the first germanium solar cell was made in 1951. Up to the year 1989, research and commercialization of photovoltaics advanced together and improved both efficiency and cost of solar cells (Luque, 2003).

Figure 1.2 shows the improving history of all important solar cell achievements in a short glimpse. It shows that earlier in 1970 the best performing cells had 20% efficiency, which increases to over 40% efficiency by 2013. It is however noticeable that these cells are not yet cost-effective enough for commercialization purposes (Luque, 2003).

Figure 1.2 A historical review of different solar cells efficiencies (Kazmerski, 2000). (printed with permission from NREL)

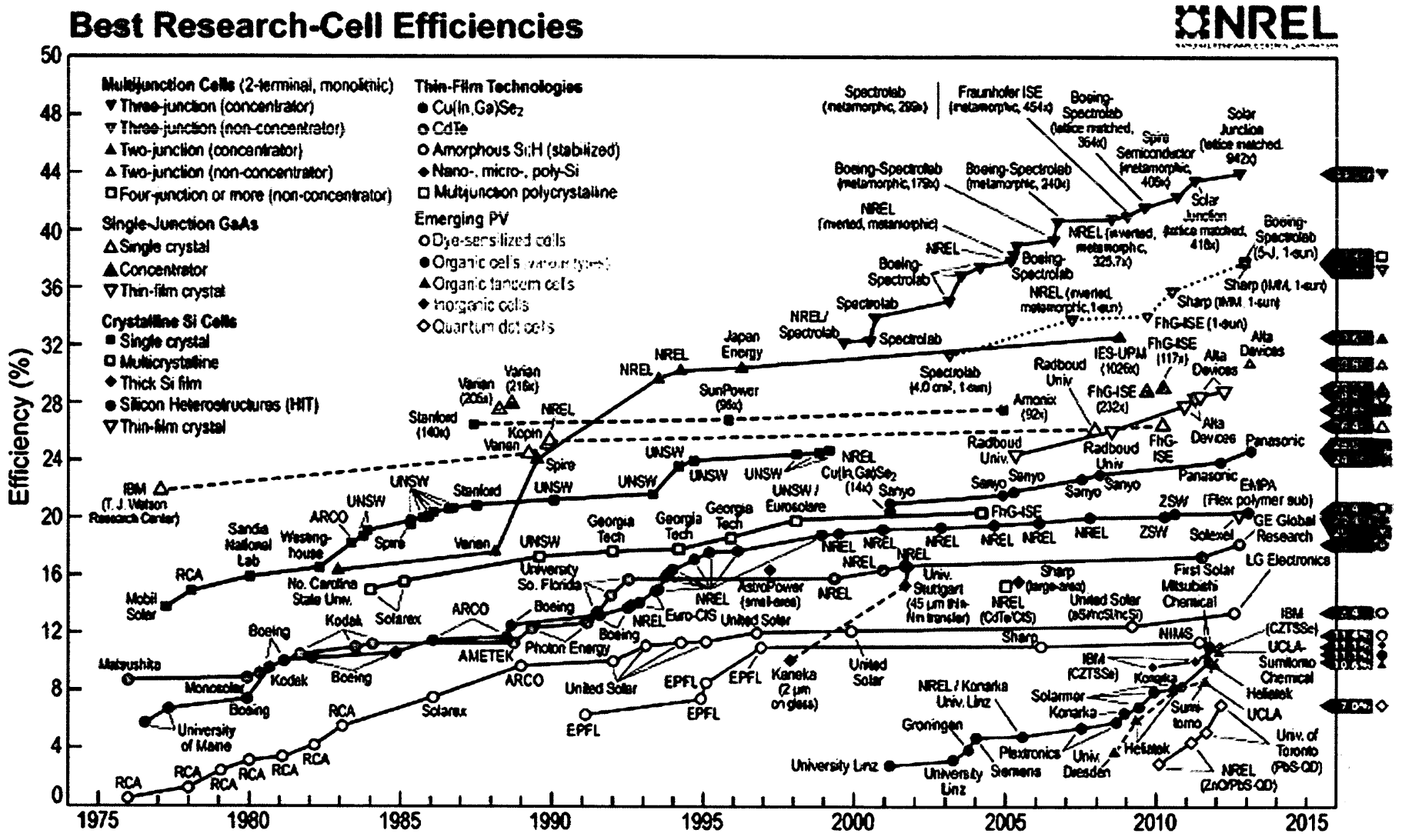

In the 1970s, large photovoltaic companies such as Solar Power Corporation and Solarex were established and this led towards the installation of massive solar systems around the globe in 1980s.

In the following paragraphs some of the most dominant solar cell technologies are described.

1.3 Different Types of Solar Cells for Sunlight Harvesting

1.3.1. Solar Cells Based on Silicon Structures

Solar cells based on monocrystalline silicon wafers reached conversion efficiencies close to 25%, and it has been demonstrated that a wafer thinned down to about 50 μm still allows one to obtain a cell efficiency of 21.5% (Wang[c], 1996). Figure 1.3 demonstrates the function of a silicon solar cell.

Regardless of the structure of the silicon used in fabricating the silicon cells, the basics remain the same as what was described before. The silicon layer acts as the photon absorber and the excited electrons are depleted from the p-n junction of the cell.

There are different morphologies and structures of silicon cells studied and also commercialized. The most significant ones are monocrystalline silicon, silicon wafers, and amorphous silicon.

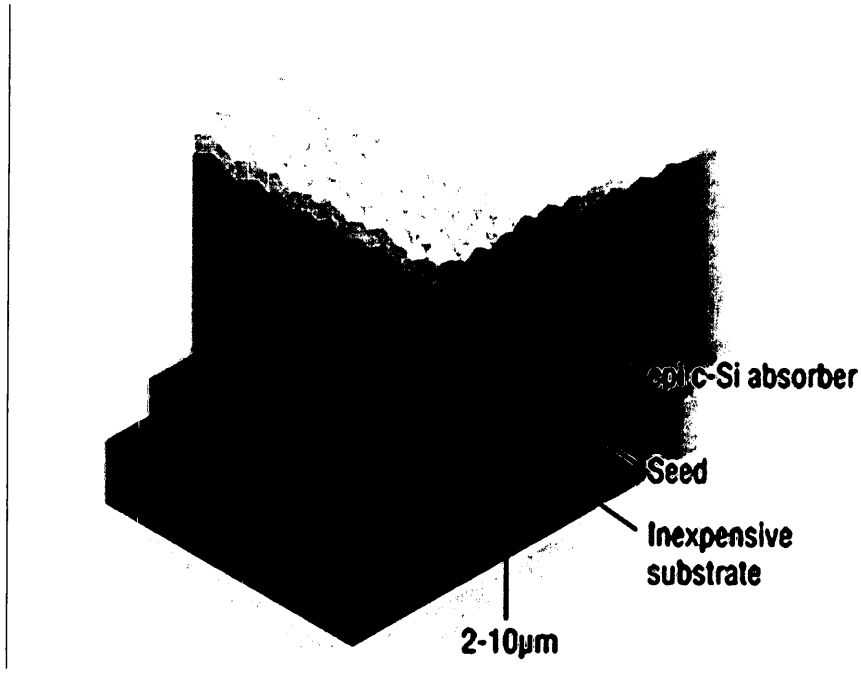

Figure 1.3 Schematic diagram of the film crystal silicon solar cell. A high-quality crystal silicon absorber is grown epitaxially on a seed layer applied to an inexpensive foreign substrate (e.g., display glass or rolled metal foil). (Printed with permission from NREL)

Amorphous solids, like common glass, are materials in which the atoms are not arranged in any particular order. They do not form crystalline structures at all, and they contain large numbers of structural and bonding defects. The efficiency for amorphous silicon cells, on the order of 10%, is slightly lower, but is largely compensated by lower production costs. Producing such cells needs less energy. It was not until 1974 that researchers began to realize that amorphous silicon could be used in photovoltaic devices by properly controlling the conditions under which it was deposited and by carefully modifying its composition (Shah, 2006). Today, amorphous silicon is commonly

used for solar-powered consumer devices that have low power requirements (e.g., wrist watches and calculators).

Amorphous silicon absorbs solar radiation 40 times more efficiently than does single-crystal silicon, so a film only about 1 micron thick can absorb 90% of the usable solar energy. This is one of the most important factors affecting its low cost potential. Other principal economic advantages are that amorphous silicon can be produced at a lower temperature and can be deposited on low-cost substrates. These characteristics make amorphous silicon the leading thin-film photovoltaic material (Markvart, 2003).

1.3.2. Multijunction Cells

Most common photovoltaic devices use a single junction, or interface, to create an electric field within a semiconductor such as a photovoltaic cell. In a single-junction photovoltaic cell, only photons whose energy is equal to or greater than the band gap of the cell material can free an electron for an electric circuit. In other words, the photovoltaic response of single-junction cells is limited to the portion of the sun's spectrum whose energy is above the band gap of the absorbing material, and photons with less energy are not used. One way to resolve this limitation is to use two or more different cells, with more than one band gap and more than one junction, to generate a voltage. These are referred to as multijunction cells (also called cascade or tandem cells). Multijunction devices can achieve higher total conversion efficiency because they can convert more of the energy spectrum of light to electricity (Figure 1.4).

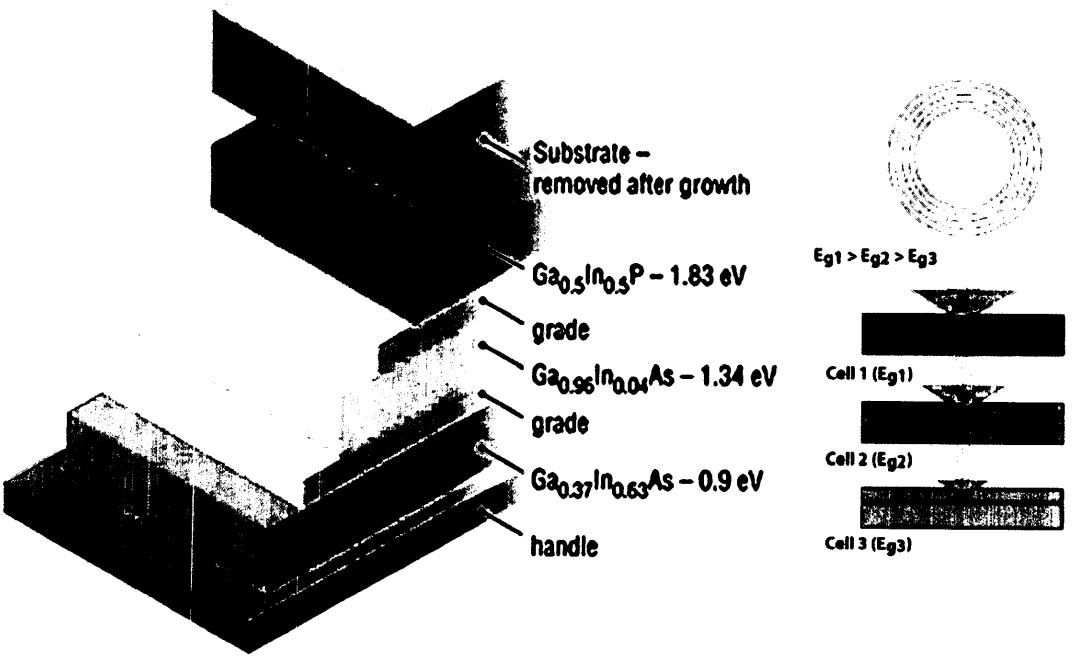

Figure 1.4 Schematic structure of multijunction solar cells. The diagram on the right shows how different layers of such cells are tuned to be able to absorb photos with different wavelengths so that the overall absorption covers the entire visible light. (Printed with permission from NREL)

In a typical multijunction photovoltaic cell, individual single-junction cells with different energy band gaps are stacked on top of one another. Sunlight first shines on the material with the largest band gap, and the highest-energy photons are absorbed. Photons that are not absorbed in the first cell continue on to the second cell, which absorbs the higher-energy portion of the remaining solar radiation while remaining transparent to the lower energy photons (Friedman, 2010).

Although two-junction cells have been built, most research is focusing on three-junction and four-junction devices, using materials such as germanium (Ge) to capture the lowest-energy light in the lowest layer (Friedman, 2010, Markvart, 2003).

The cells described in the following sections benefit from a combination of multijunction and polycrystalline structure which locates them among the most efficient and cost-effective cell introduced so far.

1.3.3. III-V Solar Cells

The photovoltaic technologies based on Group III and V elements from the periodic table (IUPAC groups 13 and 15), show very high conversion efficiencies under either normal sunlight or sunlight that is concentrated (Markvart, 2003). Single-crystal cells of this type are usually made of gallium arsenide (GaAs), which can be alloyed with elements such as indium, phosphorus, and aluminum to create semiconductors that respond to different spectral energies (Luque, 2003). GaAs is especially suitable for use in multijunction and high-efficiency solar cells for several reasons:

1. The GaAs band gap is 1.43 eV, nearly ideal for single-junction solar cells.
2. GaAs has high absorptivity and it requires a cell only a few microns thick to absorb sunlight (crystalline silicon requires a layer 100 microns or more in thickness).
3. Unlike silicon cells, GaAs cells are relatively insensitive to heat (cell temperatures can often be quite high, especially in concentrator applications).

4. Alloys made from GaAs using aluminum, phosphorus, antimony or indium, have characteristics complementary to those of gallium arsenide, allowing great flexibility in cell design.
5. GaAs is very resistant to radiation damage. This, along with its high efficiency, makes GaAs very desirable for space applications.

One of the greatest advantages of gallium arsenide and its alloys as photovoltaic cell materials is the wide range of design options possible (Luque, 2003). A cell with a GaAs base can have several layers of slightly different compositions that allow a cell designer to precisely control the generation and collection of electrons and holes.

Figure 1.4 shows a schematic structure of a III-V cell based on multiple layers of absorbers and different compositions of GaInAs and GaInP.

The greatest barrier to the success of GaAs cells has been the high cost of a single-crystal GaAs substrate. For this reason, GaAs cells are used primarily in concentrator systems, where the typical concentrator cell is about 0.25 cm^2 in area and can produce ample power under high concentrations (Luque, 2003).

1.3.4. Polycrystalline Thin Film

Thin-film photovoltaic cells use layers of semiconductor materials only a few micrometers thick, attached to an inexpensive backing such as glass, flexible plastic, or stainless steel. Semiconductor materials thin films include amorphous silicon (a-Si),

copper indium diselenide (CIS), and cadmium telluride (CdTe). Because the quantity of semiconductor material required for thin films is far smaller than for traditional photovoltaic cells, the cost of thin film manufacturing is far less than for crystalline silicon solar cells.

Single-crystal cells have to be individually interconnected into a module, but thin-film devices can be made as a single unit. Layer upon layer is deposited sequentially on a glass superstrate, from the antireflection coating and conducting oxide, to the semiconductor material and the back electrical contacts.

Unlike most single-crystal cells, the typical thin-film device does not use a metal grid for the top electrical contact. Instead, it uses a thin layer of a transparent conducting oxide (TCO), such as tin oxide. A separate antireflection coating may be used atop of the device, or the transparent conducting oxide may serve this function as well (Luque, 2003).

Figure 1.5 shows the structure of a cell fabricated with different absorbers of polycrystalline CdTe and copper-indium-gallium-selenide (CIGS) as two of the most efficient solar cells introduced as of today (see Table 1.1).

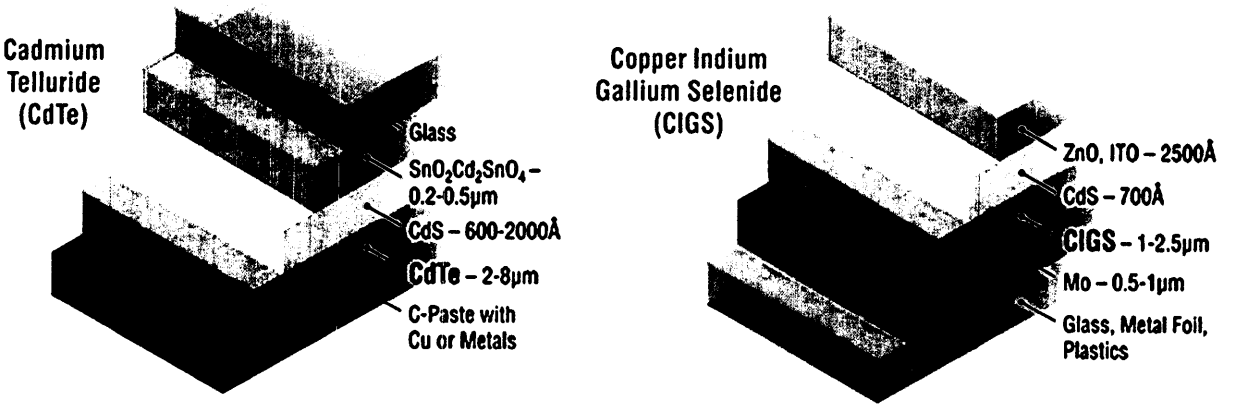

Figure 1.5 (Left). Schematic illustration of a typical CdTe superstrate thin-film PV device. In this design, the layers of the device are deposited onto a glass "superstrate" that allows sunlight to enter. The sunlight passes through the glass and produces electrical current and voltage in the lower layers.

(Right). Schematic illustration of a typical CIGS substrate thin-film PV device. In this design, the layers of the device are deposited onto a glass, metal, or polymer substrate. Sunlight enters through the top layer of the device (the transparent conducting oxide) and produces electrical current and voltage in the lower layers. (Printed with permission from NREL)

1.3.5. New Generation Solar Cells Based on Photoelectrochemistry

In this section, I provide a review on the cells based on photoelectrochemistry and the principle operation and design will follow in the next chapter as these cells are the core of this thesis.

By the advent of the nanostructures and their fast growth in different aspects of science and technology, harvesting sunlight using low-price materials prepared from

nanostructures became the core of many research groups' attention (Kamat, 1993; Roy et.al. 2011; Bimberg, 2008; Gratzel, 1983; Kalyanasundaram and Gratzel, 1993; Van de Krol and Gratzel, 2012; Ramamurthy and Schanze, 2003).

Due to the vast variety of such structures and their applications, only the most significant types of such solar cells will be discussed in this chapter.

At the end of last century, the possibility to use devices based on molecular components for the construction of a robust, large-scale solar electricity production facility seemed impossible. But the influential paper by O'Regan and Gratzel in 1991 excited researchers to take on the challenge (O'Regan, 1991). With the development of dye-sensitized solar cells (DSSCs), conventional solid-state photovoltaic technologies are now challenged by devices functioning at a molecular and nanometer level (Hagfeldt, 1995).

Record efficiencies of up to 12% for small cells and about 9% for minimodules, promising stability data, passing, for example, the critical 1000 hours stability test at 80°C with a durable efficiency of 8-9%, and means of energy-efficient production methods have been accomplished. The prospect of low-cost investments and fabrication are key features. DSSCs perform also relatively better compared with other solar cell technologies under diffuse light conditions and at higher temperatures. DSSCs offer the possibilities to design solar cells with a large flexibility in shape, color, and transparency.

Integration into different products opens up new commercial opportunities (Hagfeldt, 2000).

Over time, the concept of sensitization with dyes turned into sensitization of the semiconductors with anything that was capable of absorbing photons energy and employing it for exciting the electrons. Among those "sensitizers", narrow band-gap semiconductors such as CdS, CdSe, CdTe, $CuInS_2$, Cu_2S, PbS, PbSe, InP, InAs, Ag_2S, Bi_2S_3 and Sb_2S_3 etc received the most attention from different groups (Kumar and Scholes, 2008; Ruhle et al 2010). So the sensitized solar cells (SSCs) research field started to expand in any possible way in the hope of generating electricity at the lowest cost.

Besides the exciting possibilities of using SSCs for solar energy application, the riddles of the device are as thrilling. How does it work? SSCs should not work based on the early photovoltaic textbooks simply not work (Nelson, 2003). The paradigm was to use highly pure semiconductor materials, avoiding defects and interfaces, and to rely on a built-in electrical field to separate the photogenerated electron-hole pairs. SSCs, in contrast, were based on a huge internal interface prepared in a simple laboratory environment without strict demands on the purity of the materials. It was a mystery how the SSCs could work in the absence of a built-in electric field. The initial research developed a relatively simple picture of how DSCs operate and this is reviewed by Katoh et al. (2004) (Kalyanasundaram, 2010; Travino, 2011).

The basic characteristics and conceptual models, reviewed in several recent articles have been reasonably successful to describe various reactions and interactions (Gratzel, 2001; 2005; Ardo and Meyer, 2009; Peter, 2007a, 2007b; Bisquert, 2004; O'Regan and Durrant, 2009; Hetsch et al, 2011; Hodes, 2008; Hagfeldt, 2004, 2010; Kamat, 2008; Archer and Nozik, 2008; Smestad, 2002). With time, however, the chemical complexity of the SSCs device has become more and more evident. The SSC is a good example of a molecular system where the function of the overall device is better than predicted that from the sum of the properties of its components (Hagfeldt et al., 2004; Kamat, 2008).

There are complex interactions between the device components, in particular, at the oxide/sensitizer/electrolyte interface, but the interactions also depend on external variables such as solar irradiation, temperature, and device working conditions. Also inherent in the devices are multi-scaling properties, both in time and in length, which need to be characterized and handled for the optimization of the overall device performance.

SSCs research groups have been established around the world with the biggest activities in Europe, Japan, Korea, China, USA, Canada and Australia. The field is growing at rapid pace such that it would be difficult for one to track all papers being published in a month (Hagfeldt et al., 2004).

The industrial interest in DSSCs is strong with large multinational companies such as BASF, Bosch, and Corus in Europe and Toyota, Sharp, Panasonic, Sony, Fujikura, and Samsung in Asia. Research companies such as Dyesol, Australia, Solaronix, Switzerland, and Peccell, are expanding focusing on selling material components and equipment.

The use of a semiconductor instead of a dye to sensitize the nanoporous oxide film is often perceived to impart some advantages to the cells, mainly higher absorption (typically by a factor of 5 to 7) of the semiconductor coating compared with a single molecular layer of dye; greater stability of the semiconductor compared to organometallic or even pure organic dyes; and tailoring of optical absorption over a wider wavelength range than possible with dyes due both to the inherently wider band-gap range of semiconductors as well as the ability to tailor the band-gap by size quantization (Ruhle et. al 2010; Hodes 2008). More recently, the possibility of exploiting multiple exciton generation to obtain high efficiencies adds another potential advantage that could be exploited in the future (Nozik, 2002; Schaller, 2004). In spite of these potential advantages, the solar efficiency of semiconductor-sensitized solar cells (SSSC) with a liquid junction has only reached 2.8% at present (Ruhle et al., 2010; Niitsoo et al., 2006; Diguna et al., 2007).[1.1a]

We can estimate the absorption of a typical II-VI semiconductor (IUPAC groups 12-14), assuming the realistic scenario of a single layer of 5 nm particles adsorbed onto a 20 nm-particle-size porous oxide film. Assuming full coverage, each oxide particle is

equivalent to 10 nm of absorbing semiconductor. Allowing for the varying thickness of spherical particle coverage and the fact that there will be no coverage of the oxide at points of contact between the oxide particles, we can divide this 10 nm by 2 to give a thickness of 5 nm semiconductor/20 nm oxide. This translates to 250 nm semiconductor for a 1 μm thick oxide film, already a fairly strongly-absorbing film. A 1 μm thick II-VI semiconductor absorbs strongly (more strongly than typical dye cells of 10 μm oxide thickness). Therefore, no more than a few micrometers thick oxide film is needed for good absorption. Of course, this estimation will vary with the absorption coefficient of the semiconductor (some absorb more strongly than II-VIs and others more weakly).

Despite all the complications to understand and fabricate efficient solar cells, the thirst for finding solutions to humankind's energy crisis has never settled. Table 1.1 and other tables published by Green et al. (2013) show how much effort has been in place in order to devise techniques and also improve our knowledge to win the energy race (Green et al., 2013).

Table 1.1 Confirmed terrestrial cell and submodule efficiencies measured under the global AM1.5 spectrum (1000 W m^{-2}) at 25°C (IEC 60904-3: 2008, ASTM G-173-03 global) (all information is obtained from Green (2013); the reference numbers in the table and the footnote belong to the same article).

Classification[a]	Efficiency (η) (%)[b]	Area[c] (cm^2)	V_{oc} (V)	J_{sc} (mA cm^{-2})	ff[d] (%)	Test Center[e] (and date)	Ref.
Silicon							
Si (Crystalline)	25.0±0.5	4.00 (da)	0.706	42.7[f]	82.8	Sandia (3/99)[g]	[18]
Si (multicrystalline)	20.4±0.5	1.002 (ap)	0.664	38.0	80.9	NREL (5/04)[g]	[19]
Si (thin film transfer)	20.1±0.4	242.6 (ap)	0.682	38.14[h]	77.4	NREL (10/12)	[4]
Si (thin film submodule)	10.5±0.3	94.0 (ap)	0.492[i]	29.7[i]	72.1	FhG-ISE (8/07)[g]	[20]
III-IV Cells							
GaAs (thin film)	28.8±0.9	0.9927 (ap)	1.122	29.68[i]	8605	NREL (5/12)	[21]
GaAs (multicrystalline)	18.4±0.5	4.011 (t)	0.994	23.2	79.7	NREL (11/95)[g]	[22]
InP (crystalline)	22.1±0.7	4.02 (t)	0.878	29.5	85.4	NREL (4/90)[g]	[23]

Table 1.1 continued:

Classification[a]	Efficiency (η) (%)[b]	Area[c] (cm^2)	V_{oc} (V)	J_{sc} (mA cm^{-2})	ff[d] (%)	Test Center[e] (and date)	Ref.
Thin Film Chalcogenide							
CIGS (cell)	19.6±0.6[k]	0.996 (ap)	0.713	34.8[l]	79.2	NREL (4/09)	[24]
CIGS (submodule)	17.4±0.5	15.993 (da)	0.681 5[i]	33.84[i]	75.5	FhG-ISE (10/11)	[25]
CdTe (cell)	18.3±0.5	1.005)ap)	0.857	26.95[h]	77.0	NREL (10/12)	[5]
Amorphous/ Nanocrystalline Si							
Si (amorphous)	10.1±0.3[m]	1.036 (ap)	0.886	16.75[f]	67.8	NREL (7/09)	[26]
Si (nanocrystalline)	10.1±0.2[n]	1.199 (ap)	0.539	24.4	76.6	JQA (12/97)	[27]
Photochemical Dye sensitized	11.9±0.4[o]	1.005 (da)	0.744	22.47[h]	71.2	AIST (9/12)	[6]
Dye sensitized (submodule)	9.9±0.4[o]	17.11 (ap)	0.719[i]	19.4[i]	71.4	AIST (8/10)	[28]
Organic							
Organic thin-film	10.7±0.3[o]	1.013 (da)	0.872	17.75[h]	68.9	AIST (10/12)	[10]
Organic (submodule)	6.8±0.2[o]	395.9 (da)	0.798[i]	13.50[i]	62.8	AIST (10/12)	[13]
Multijunstion Devices							
InGaP/GaAs/InGaAs	37.7±1.2	1.047 (ap)	3.014	14.57[h]	86.0	AIST (9/12)	[14]
a-Si/nc-Si/nc-Si (thin film)	13.4±0.4[p]	1.006 (ap)	1.963	9.52[h]	71.9	NREL (7/12)	[15]
a-Si/nc-Si (thin film cell)	12.3±0.3%[q]	0.962 (ap)	1.365	12.93[r]	69.4	AIST (7/11)	[29]
a-Si/nc-Si (thin film submodule)	11.7±0.4[n,s]	14.23 (ap)	5.462	2.99	71.3	AIST (9/04)	[30]

Table 1.1 continued:

V_{oc} is photovoltage at open circuit, J_{sc} is photocurrent density at short circuit and ff is fill factor if the cells

Footnotes of Table 1.1 (the table versions refer to different versions of Prog. Photovolt: Res. Appl.)

[a]CIGS, $CuInGaSe_2$; a-Si, amorphous silicon/hydrogen alloy; nc-Si, nanocrystalline or microcrystalline silicon.
[b]Effic., efficiency.
[c](ap), aperture area; (t), total area; (da), designated illumination area.
[d]FF, fill factor.
[e]FhG-ISE, Fraunhofer Institut für Solare Energiesysteme; JQA, Japan Quality Assurance; AIST, Japanese National Institute of Advanced Industrial Science and Technology.
[f]Spectral response reported in Version 36 of these Tables.
[g]Recalibrated from original measurement.
[h]Spectral response and current–voltage curve reported in the present version of these Tables.
[i]Reported on a 'per cell' basis.
[j]Spectral response and current–voltage curve reported in Version 40 of these Tables.
[k]Not measured at an external laboratory.
[l]Spectral response reported in Version 37 of these Tables.
[m]Light soaked at Oerlikon prior to testing at NREL (1000 h, 1 sun, 50°C).
[n]Measured under IEC 60904–3 Ed. 1: 1989 reference spectrum.
[o]Stability not investigated. References 9, 11 and 12 review the stability of similar devices.
[p]Light soaked under 100 mW cm^{-2} white light at 50°C for over 1000 h.
[q]Stabilised by manufacturer.
[r]Spectral response and current–voltage curve reported in Version 39 of these Tables.
[s]Stabilised by 174 h, 1 sun illumination after 20 h, 5 sun illumination at a sample temperature of 50°C.

1.4 Notes

1.1a A recent paper using CdS on TiO_2 nanotubes in sulfide electrolyte (no elemental sulfur added to the electrolyte) reported a cell efficiency of 4.15%. (a) Sun, W.-T.; Yu, Y.; Pan, H.-Y.; Gao, X.-F.; Chen, Q.; Peng, L.-M J. Am. Chem. Soc. 2008, 130, 1124. However, this is not a true conversion efficiency since the photovoltage was measured relative to the Ag/AgCl reference electrode rather than to the counter electrode in the sulfide electrolyte. The real cell efficiency would be ca. 1%. The efficiency reported by Niitsoo et al. (2006) was also measured with a three electrode setup. The reference electrode in this case was a Pt wire pseudopolysulfide (the electrolyte used) reference. The real efficiency would be decreased slightly by polarization of the counter electrode (assuming a counter electrode of the same size as the photoelectrode). For a good counter electrode in polysulfide see (b) Hodes, G.; Manassen, J.; Cahen, D. J. Electrochem. Soc., 1980, 127, 544, this translates to a drop in real efficiency by ca. 0.1%. This, however, would be compensated by the fact that the cell was measured in illumination equivalent to a bright day (typically 950 W m^{-2}, though not specifically measured, while the illumination intensity was taken to be 1 KW m^{-2}).

Chapter 2: Optoelectronics of Sunlight Harvesting by Photoelectrochemical Cells

In this chapter some of most researched and significant types of photoelectrochemical solar cells are briefly described and then the solar cells which are central to this thesis, i.e. Dye-Sensitized Solar Cells and Semiconductor-Sensitized Solar Cells are described in more depth.

Over time there has been an enormous amount of research carried on different solar cell technologies so describing all these techniques and the science behind them is far from the scope of this thesis. This introduction will start with a description of photoelectrochemical solar cells and its physical and chemical concepts. These concepts will be then used to explore dye- and semiconductor-sensitized solar cells as the main focus of this thesis.

2.1. Photoelectrochemical Cells

Bard and Rajeshwar categorize photoelectrochemical cells into three types (Figure 2.1) (Rajeshwar, 2006). The first type is regenerative in nature and the species that are photooxidized at the n-type semiconductor electrode are simply re-reduced at the counter electrode (Figure 2.1a). Instead of an electrocatalytic electrode where the counter electrode reaction occurs in the dark (this is the situation shown in Figure 2.1a), a p-type semiconductor photocathode may also be deployed in a tandem regenerative

cell (Hodes, 1977a; 1977b). In all these cases, the cells operate in the photovoltaic mode where the input photon energy is converted into electricity.

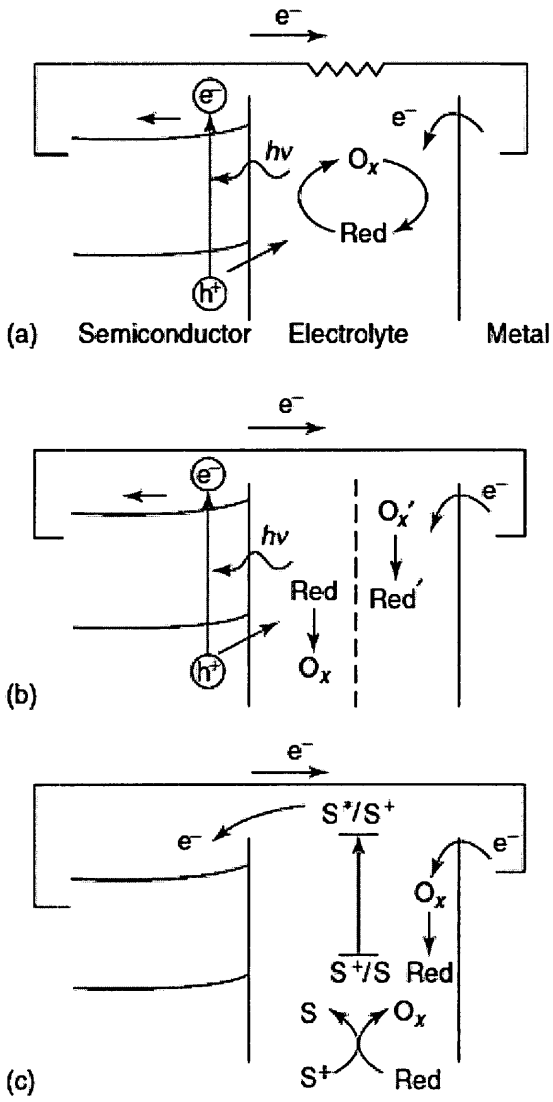

Figure 2.1 Different types of photoelectrochemical devices for solar energy conversion; **a)** Regenerative, **b)** Photoelectrolytic, **c)** Dye-sensitized. (Rajeshwar, 2006). (Printed with permission from Wiley-vch)

Interestingly enough, it is the second type of device, namely the photoelectrolytic cell (Figure 2.1b), that first caught the attention of the scientific and technological community in the 1970s who was searching for alternative energy sources to fossil-derived fuels. In a landmark paper, Fujishima and Honda (1972) demonstrated that sunlight could be used to drive the photoelectrolysis of water using an n-TiO_2 photoanode and Pt counterelectrode. Unfortunately, the requirements for efficient splitting of water are rather stringent.

In the third type of energy conversion device, the initial photoexcitation does not occur in the semiconductor (unlike in the device counterparts in Figures 2.1a and 2.1b) but rather in a visible light-absorbing dye (Figure 2.1c). Subsequent injections of an electron from the photoexcited dye into the semiconductor conduction band results in the flow of a current in the external circuit. Sustained conversion of light energy is facilitated by regeneration of the reduced form of the dye via a reversible redox couple (e.g. iodide/triiodide) (O'Regan, 1991). Therefore, this device, similar to its counterpart in Figure 2.1a, operates in a photovoltaic mode, or perhaps more appropriately said, in a photogalvanic mode.

Other variants of the three types of device operation may be envisioned for semiconductor-liquid junctions.

In contrast to conventional systems, where the semiconductor has both the task of light absorption and charge carrier transport, the two functions are separated in the

new generation photoelectrochemical cells, which are mainly known as dye-sensitized solar cells (DSSCs) and semiconductor-sensitized solar cells (SSSCs) (also, here, referred to as quantum-dot sensitized solar cells, QDSSCs) (Memming, 2001). Both of these types of cells are referred to as sensitized-solar cells (SSCs) in this thesis.

Light is absorbed by a sensitizer that is attached to the surface of a wide band gap semiconductor. Charge separation takes place in the sensitizer via photo-induced electron injection from the sensitizer into the conduction band of the solid. Carriers are transported in the conduction band of the semiconductor to the charge collector. In DSSCs, near-quantitative conversion of incident photons into electric current is achieved over a large spectral range extending over the whole visible region. Overall solar (standard AM1.5) to electric conversion efficiencies over 11% have been reached for DSSCs based on so-called Black Dye (Nazeeruddin, 2001).

2.1.1 Basic Principles

Conventional solar cells convert light into electricity by exploiting the photovoltaic effect that exists at semiconductor junctions. These photovoltaic devices are based on the concept of charge separation at an interface of two materials of different conduction mechanism, normally between solid-state materials, either n- and p-type regions with electron- and hole-majority carriers in a single semiconductor material, heterojunctions between different semiconductors or at a semiconductor-metal junction.

In contrast, the photoelectrochemical cells work on a different principle, whereby the processes of light absorption and charge separation are differentiated. Light absorption is performed by a monolayer of sensitizer (S) (in case of SSSCs there may be multiple layers of the sensitizer) at the semiconductor surface (Figure 2.2). After being excited by a photon of light, the sensitizer (S*) is able to transfer an electron to the semiconductor by a process called injection. Electrons in the semiconductor are collected through their transport in the electrode. This transport occurs mainly by diffusion (Södergren, 1994; Cao, 1996; Schwarzburg, 1999). The original state of the sensitizer is subsequently restored by electron donation from the electrolyte, usually an organic solvent containing a redox system, such as the iodide/triiodide couple in DSSCs or sulfide-based electrolytes in SSSCs. This process is called regeneration. The regeneration of the sensitizer by a redox couple intercepts the recapture of the conduction band electron by the oxidized sensitizer. The redox couple is regenerated in turn by the reduction at the counter electrode, the circuit being completed via electron migration through the external load. The theoretical maximum voltage (ΔV) that such a device could deliver corresponds to the difference between the redox (Nernst) potential of the mediator and the quasi-Fermi level of the electron in the semiconductor (Oskam, 2001).

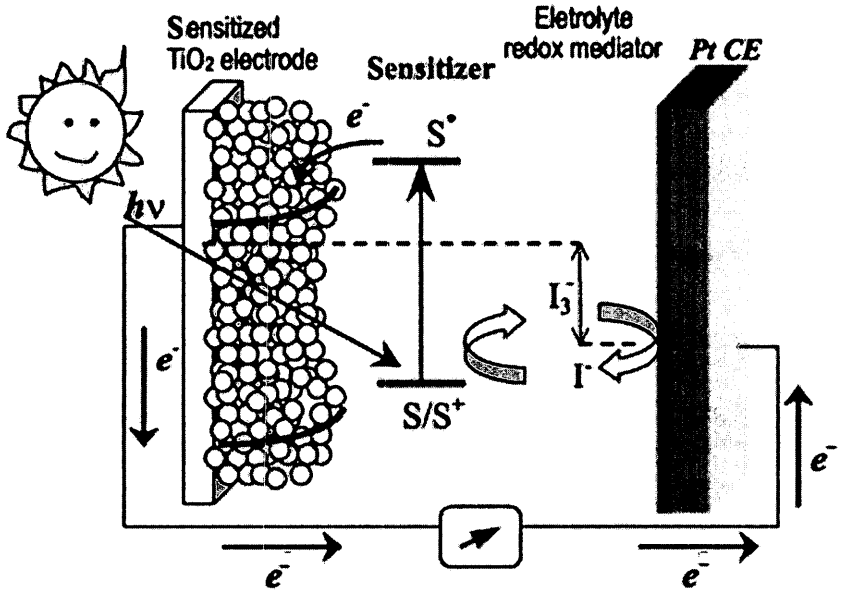

Figure 2.2. Schematic structure and performance steps of a solar cell based on sensitization concept (Gratzel, 2004a). (Printed with permission from ACS).

The absorption of light by a monolayer of sensitizer, specifically if it is a dye molecule, is always weak due to the very small cross-section for light absorption of the sensitizer molecules and species compared to the area they occupy on the surface. A respectable photovoltaic efficiency cannot therefore be obtained by the use of a flat semiconductor surface but rather by use of a porous, nanostructured film of very high surface roughness. When light penetrates the photosensitized, semiconductor sponge, it crosses hundreds of attached sensitizer monolayers (Cahen, 2000). The nanocrystalline structure equally allows a certain spreading of the radiation. The final result is a greater absorption of light and its efficient conversion into electricity. The material of choice is TiO_2 (anatase), although alternative wide band-gap oxides such as ZnO and Nb_2O_5 have

also given promising results (Tennakone, 1999; Sayama, 1998). The mesoporous oxide layer is composed of nanometer-sized particles which have been sintered together to allow electronic conduction to take place.

In spite of the heterogeneous structure of the materials, electron diffusion from the bulk to the supporting conductor takes place nearly without losses. Recombination between the injected electron in the conduction band of the semiconductor and the hole on the oxidized sensitizer is indeed very slow compared to the reduction of the latter by the redox mediator in solution (Hodes, 2008). Moreover, the electron-hole recombination in the semiconductor, which is not favorable for the efficiency of the classical photovoltaic cells, does not exist here, because no hole in the valence band correspond to the electron in the conduction band. The consequence is that even under low irradiance intensities, the efficiency stays the same, contrary to what is observed with classical systems (O'Regan and Gratzel, 1991; Tributsch, 2004).

2.1.1.1 Light Harvesting by Monomolecular Layers

For the absorption of solar rays by a sensitizer attached as a monolayer to the surface of an oxide film, there is a fundamental problem of the limited light-capture cross-section of the dye molecule.

The cross-section σ is related to the molar extinction coefficient ε by the formula:

$$\sigma = \frac{\varepsilon \cdot 1000}{N_A} \qquad \text{Eq. 2.1}$$

where N_A is Avogadro's number. Typical ε values for dyes lie between 10^4 and 5×10^5 M^{-1} cm^{-1} yielding for the light-capture cross-section values between 0.0016 and 0.08 nm^2 (Nazeeruddin, 1993). The area the sensitizer molecule occupies on the surface of the supporting oxide is much larger, e.g., about 1-2 nm^2 (Nazeeruddin, 1993). Hence, at most a few percent of the incident light can be absorbed. A successful strategy to solve the problem of light absorption through such molecular layers is found in the application of high surface area films consisting of nanocrystalline oxide particles with a diameter of 10-20 nm (Barbe, 1997). The mesoporous morphology of the layer plays a crucial role in the harvesting of sunlight. Depending on film thickness, their real surface area can easily be made 100-1000 times larger than the apparent one. This allows for the capture of the incoming photons efficiently despite the fact that the oxide is covered only by a monolayer of dye. When light penetrates the dye-covered oxide "sponge", it crosses hundreds of adsorbed dye monolayers. Thereby, photons whose energy is close to the absorption maximum of the dye, are completely absorbed (O'Regan, 1991). The mesoporous structure thus mimics the light absorption by green leaves. As the chlorophyll-containing thylakoids are stacked, visible light is absorbed completely by traversing many superimposed vesicles containing the dye.

2.1.1.2 Mesoscopic Oxide Semiconductor Films

Mesoporous oxide films are commonly produced via a sol-gel type process involving a hydrothermal step. The favoured material is titanium dioxide, TiO_2. It has many advantages for sensitized photochemistry and photoelectrochemistry as low-cost, widely available, nontoxic materials and as such is even used in health care products (Hagfeldt, 1995). Moreover, it is insensitive to visible light due to its large bandgap of 3.2 eV and begins to absorb only in the near ultraviolet. It can be sensitized by a large variety of dyes, some of them allowing incident photon/electron conversion efficiencies near unity (Hagfeldt, 2004). The nanoporous structure permits the specific surface concentration of the sensitizing dye to be sufficiently high for total absorption of the incident light, a necessity for efficient solar energy conversion, since the area of the monomolecular distribution of adsorbate is 2-3 orders of magnitude higher than the geometric area of the substrate (Gratzel, 2001; 2005). Figure 2.3, which is an scanning electron microscope (SEM) image of TiO_2 thin film, illustrates the morphology of such a nanocrystalline TiO_2 (anatase) layer deposited on a transparent conducting oxide (TCO) glass.

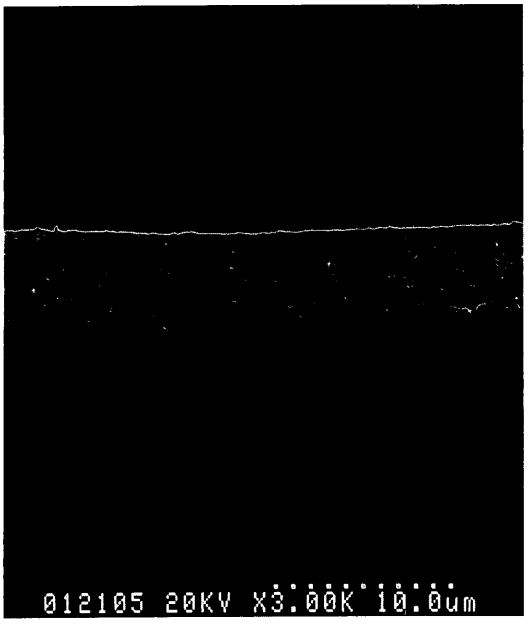

Figure 2.3. SEM image of cross section of a mesoporous TiO_2 films on a conductive glass.

2.1.1.3 Photoinduced Charge Separation at the Dye/Oxide Interface in DSSCs

The use of mesoporous oxide films as a substrate to anchor the dye molecules allows sunlight to be harvested over a broad spectral range in the visible region. The dye acts as an electron transfer sensitizer, where upon excitation by light, it injects electrons into the conduction band of the oxide resulting in separation of positive and negative charges.

For efficient photoconversion of solar energy, the charge injection must occur with quantum yield close to unity. Some rate constants for electron transfer from excited dyes into TiO_2 have been determined by time-resolved laser photolysis experiments (Katoh, 2004; Durant 2004; Benko, 2001). These rates vary over 8 orders of magnitude depending on the type of dye employed. The fastest injection times are

observed for dyes with a suitable anchoring group, such as carboxylate or phosphonate substituent or a catechol moiety, through which the sensitizer is firmly grafted onto the surface of titania. The role of these groups is to provide good overlap between the dye molecule's excited-state orbital and the empty acceptor levels, i.e., the Ti(IV) 3d orbital manifold forming the conduction band of TiO_2 (Nazeeruddin, 1993). The extent of coupling is expressed by the electronic coupling matrix element |V| which is related to the rate constant for charge injection k_i by the equation:

$$k_i = (2\pi/h)|V|^2\rho \qquad \text{Eq. 2.2}$$

Here h is the Planck's constant and ρ is the density of electronic acceptor states in the conduction band of the semiconductor. The equation assumes that electron transfer from the excited dye molecules into semiconductors is activationless and hence exhibits a temperature-independent rate. This has been confirmed experimentally (Burfeindt, 1996). For example, the charge injection from excited perylene dye was found to be temperature-independent from 4 to 300K (Namba, 1965). The explanation for this is that there is a continuum of electric states in the conduction band accessible to the injected electron, which, combined with the different vibrational levels of the other reaction product, i.e. the oxidized dye, yields a multitude of possible reaction pathways. At least one channel is likely to be without any barrier, implying that the driving force of the electron transfer compensates the reorganization energy, i.e., the free energy necessary to rearrange the nuclear coordinates of the dye/solvent system

accompanying electron transfer. The activationless channel is the fastest and hence will be the preferred one for the reaction (Gratzel and Moser, 2001).

The most promising results have so far been obtained with ruthenium complexes where at least one of the ligands was 4,4'-dicarboxy-2,2'-bipyridyl. The carboxylate groups serve to attach the Ru-complex to the surface of the oxide and to establish good electronic coupling between the π^* orbital of the ligand, which is the lowest unoccupied orbital (LUMO) of the complex, and the 3d wave-function manifold of the TiO_2 film. The substitution of the bipyridyl by the carboxylate groups lowers the energy of the LUMO. Since the electronic transition is of MLCT (metal-to-ligand-charge transfer) character, optical excitation transfers the electron to a site from which electron injection into the semiconductor can readily occur. With molecules like these, charge injection occurs in the femtosecond time domain (Gratzel, 2001). In contrast, the recapture of the electrons by the oxidized dye is at least six orders of magnitude slower. The rationale for this behavior is that the back reaction involves a d-orbital localized on the ruthenium metal whose electronic overlap with the TiO_2 conduction band is small. The spatial contraction of the wave-function upon oxidation of the Ru(II) to the Ru(III) state weakens further the electronic coupling (Haque, 2000; 2005). A second very important contribution to the kinetic retardation of the charge recombination arises from the fact that this process is characterized by a large driving force and small reorganization energy, the respective values for $RuL_2(NCS)_2$ being about 1.5 and 0.3 eV, respectively (L can be terpyridine ligand with various structure) (Haque, 2000; 2005). This places the

electron recapture clearly in the inverted Marcus region, reducing its rate by several orders of magnitude. This also provides a rationale for the observation that this interfacial redox process is almost independent of temperature and is surprisingly insensitive to the environment that is in contact with the film (Gerischer, 1968).

Of significance for the inhibition of charge recombination is the existence of a local electric field at the surface of the titanium dioxide film. While no depletion layer is formed within the oxide, due to the small size of the particles and their low doping level, a surface field is established spontaneously by proton transfer from the carboxylic acid or phosphonic acid anchoring groups of the ruthenium complex to the oxide surface, producing a surface dipole layer (Gregg, 2004). If the film is placed in contact with a protic solvent the latter can also act as proton donor. In aprotic media, Li^+ or Mg^{2+} are potential determining ions for TiO_2, and they may be used to charge the surface positively (Dare-Edwards, 1980). The local potential gradient from the negatively charged sensitizer to the positively charged oxide drives the injection in the desired direction. The same field inhibits also the electrons from exiting the solid after injection has taken place (Gregg, 2003; 2004).

Investigations have centered so far largely on *cis*-dithiocyanato-bis(2,2'-bipyridyl-4,4'-dicarboxylate)-ruthenium(II), $RuL_2(SCN)_2$ (known as N3 dye), which displays extraordinary properties as a charge transfer sensitizer (Tsubomura, 1976). The adsorption of this complex onto mesoporous TiO_2 (anatase) from acetonitrile/tert-

butanol solvent mixture follows a Langmuir isotherm. The binding constant and the area occupied by the sensitizer at the surface were determined to be $5x10^4$ M^{-1} and 1.6 nm^2/molecule, respectively. Model studies, using the dcbpy ligand adsorbed onto single-crystal TiO_2 (110) rutile, investigated by means of X-ray photoelectron spectroscopy, X-ray absorption spectroscopy, and quantum chemical calculations, are in favor of the bridging bidentate configuration (Patthey, 1999). The dye is attached via two of its four carboxylate groups, which straddle one row of titanium ions (Finnie, 1998). The anchoring occurs either through chelation or an ester-type bond to the surface titanium ions (Desilvestro, 1985).

2.1.1.4 Charge Carrier percolation and collection

The migration of electrons within the TiO_2 conduction band to the current collector involves charge-carrier percolation over the mesoporic particle network. This important process which leads to nearly quantitative collection of injected electrons has attracted a great deal of attention (Hagfeldt and Gratzel, 2000). The intriguing findings made with these films can be rationalized in terms of a random walk of the electron via traps. The trapping and detrapping times are broadly distributed. Further discussion on this subject will follow under the section of Electron transfer dynamics (section 2.1.1.6).

2.1.1.5 Back-Reaction and Recapture of the Injected Electron by the Electrolyte

It should be noted that apart from recapture of the electrons by the oxidized dye there is an additional loss channel in the nanocrystalline injection cell that involves reduction of the triiodide ions in the electrolyte present within the mesoporous network.

$$I_3^- + 2e_{cb}^- (TiO_2) \longrightarrow 3I^- \quad \text{Eq. 2.3}$$

This reaction can be studied by measuring the dark current of the dye-loaded film under forward bias. The latter should be kept at a minimal level as it determines the voltage of the photovoltaic cell (Gregg, 2003; 2004). The concept of dark current and its correlation is driven from our knowledge of silicon solar cells. However, one must be cautious when using the concept for DSSCs or SSSCs, since the dark recombination pathways in these cells are different from the recombinations under illumination, even if performing such experiment has been informative (Gratzel and Moser, 2001).

2.1.1.6 Electron Transfer Dynamics

As explained before, at the base of the design of the DSSC is a photoanode constituted by a monolayer of a molecular redox dye-sensitizer (S) adsorbed onto a layer of nanocrystalline semiconductor (SC) oxide particles. "S" can also stand for any other sensitizer that is used for sensitization of wide-band gap semiconductors in solar cells. Upon light absorption by the sensitizer (Eq. 2.4), excited states of the

photosensitizer readily inject an electron into the conduction band of the solid (Eq. 2.5). Charge injection has been found for numerous efficient systems to occur in the femtosecond timeframe, thus successfully competing against deactivation of the dye excited state (Eq. 2.6) (Gratzel and Moser, 2001). The electron back-transfer from the conduction band to dye cations (Eq. 2.7) takes place much more slowly, typically in the microsecond-millisecond domain (Desilvestro, 1985; Haque, 1998). In the presence of a redox mediator (M), this interfacial charge recombination competes kinetically with the reaction of the mediator with the oxidized sensitizer (Eq. 2.8). Charge transport by the electrolyte in the pores of the semiconductor film to the counter electrode and that of injected electrons within the nanocrystalline film to the back-contact should be fast enough to compete efficiently with the electron recapture reaction (Eq. 2.9).

$S \mid SC + h\upsilon \longrightarrow S^* \mid SC$	excitation	Eq. 2.4
$S^* \mid SC \longrightarrow S^+ \mid SC + e_{cb}^-(SC)$	injection	Eq. 2.5
$S^* \mid SC \longrightarrow S \mid SC$	relaxation	Eq. 2.6
$S^+ \mid SC + e_{cb}^-(SC) \longrightarrow S \mid SC$	recombination	Eq. 2.7
$S^+ \mid SC + M \longrightarrow S \mid SC + M^+$	regeneration of dye	Eq. 2.8
$M^+ + e_{cb}^-(SC) \longrightarrow M$	electron recapture reaction	Eq. 2.9

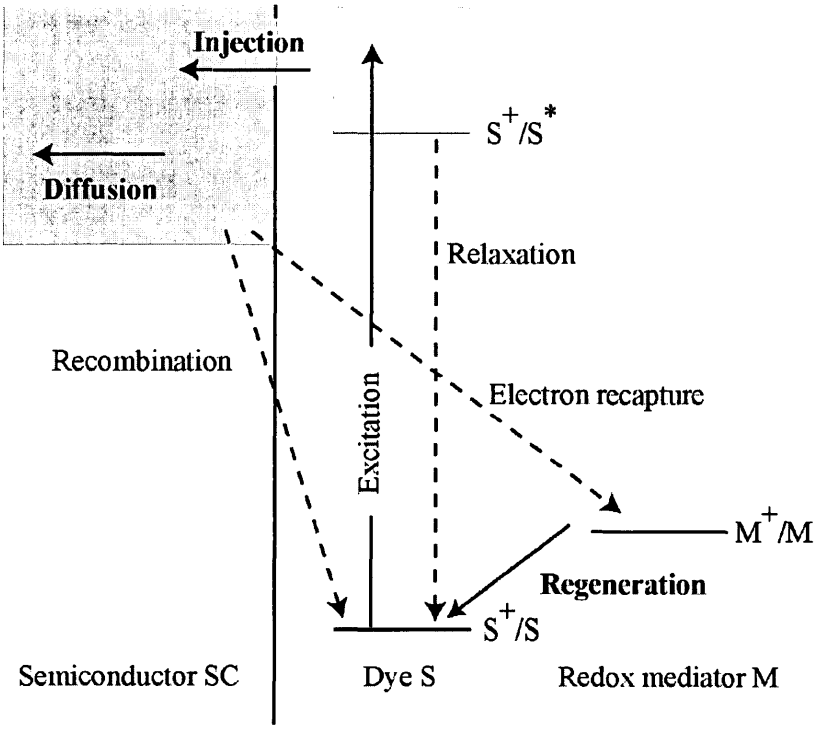

Figure 2.4. Electron transfer processes at a sensitized heterojunction.

These electron transfer processes are illustrated in Figure 2.4. Orders of magnitude for the electron transfer rates in the classical DSSC are summarized in Table 2.1.

Table 2.1. Orders of magnitude for the different electron transfer processes rates taking place in a classical DSSC (Hodes, 2008).

Process	Time-Scale
Excitation	Femtosecond
Injection	Femtosecond
Relaxation	Picosecond
Recombination	Micro to Millisecond
Regeneration of Dye	Nanosecond
Electron Recapture Reaction	Micro to Millisecond

Electron transport is believed to be purely diffusional. It is however possible that the charging of TiO_2 nanoparticles results in a band-edge shift that causes the buildup of an electrical field across the TiO_2 layer because of the electron concentration dependence on position (Schlichthörl, 1997; Vanmaekelbergh, 1999). This electrical field has been shown to serve as an additional driving force for electron transport and can increase the apparent diffusion coefficient by approximately 10% at one sun light intensity (Vanmaekelbergh, 1999; Ferber, 2001). The magnitude of this driving force has been derived for a non-exponential trap distribution (Vanmaekelbergh, 1999). Most of the studies reviewed assume an exponential trap-state distribution. It is shown that at the operating conditions of the Gratzel cell, the contribution of this additional driving force is significant. A similar approach can lead to expressions describing ambipolar (or mutual or chemical) diffusion (Onsager, 1932). A comprehensive description of electron transport must take into account the transport driven by both concentration gradients and electrical fields. It is convenient to express the gradient of the electrochemical potential as a thermodynamic driving force (Vanmaekelbergh, 1999; Onsager, 1932; Gregg, 2003). The electron flux (J_n) is given by expression:

$$J_n = -nm_n \frac{\nabla \bar{\mu}_n}{q} \qquad \text{Eq. 2.10}$$

Where n is the number of electrons, q is the charge of one electron, m_n is the electron mobility, μ_n the electrochemical potential, and ∇ is the spatial gradient operator given by

$\nabla = \partial / \partial x + \partial / \partial y + \partial / \partial z$. The term $\nabla \mu_n/q$ is the driving force F_n for electron transport ($F_n = (\nabla \mu_n/q)-E$), which is the sum of a electronics field (φ) driven term ($E = \nabla \varphi$) and a chemical potential gradient term ($\nabla \mu_n$) inasmuch as the electrochemical potential is the sum of an electrical (φ) and a chemical potential contribution (Vanmaekelbergh, 1999).

The open-circuit photovoltage (V_{oc}) of the Gratzel cell is defined as the difference between the quasi-Fermi level of electrons in TiO_2 in the light (μ_n) and the Fermi level in the dark (μ_{n°) (Huang, 1997; Schiff, 2003):

$$V_{oc} = \mu_n - \mu_{n^\circ} \qquad \text{Eq. 2.11}$$

Because of equilibration of the TiO_2 film with the TCO substrate and the electrolyte phase, the Fermi level in the dark is the same as the Fermi level of the redox electrolyte, which is constant under illumination at open circuit. As discussed above, the photovoltage of the cell is mainly due to a light-induced change of the chemical potential of electrons in the TiO_2 phase and, to a lesser extent, a light-induced change of the electrical potential of the TiO_2 particles resulting in band-edge movement (van de Lagemaat, 2000; Kron, 2003; Pichot, 2000; Schlichthörl, 1997). In the absence of band-edge movement, the photoinjected electron density (n_{cb}) in the conduction band of TiO_2 depends on the dark electron concentration $n_{cb,0}$ and the difference (Eq. 10) between the quasi-Fermi level under light and the Fermi level in the dark (Huang, 1997):

$$n_{cb} = n_{cb,0} \exp[q(\bar{\mu}_n - \bar{\mu}_n^0)/kT] \qquad \text{Eq. 2.12}$$

where μ_n° is chemical potential under standard conditions. A similar expression can be written for the total photoinjected electron density n when electrons reside predominantly in an exponential distribution of traps:

$$n = n_{t,0} \exp[q(\bar{\mu}_n - \bar{\mu}_n^0)/m_c] \qquad \text{Eq. 2.13}$$

where m_c is the characteristic energy of the exponential trap-state distribution and $n_{t,0}$ the trapped electron density in the dark. The latter expression shows that the average trap depth can be determined from measurements of the electron charge in the film versus the open-circuit voltage (Schlichthörl, 1997). Measurements of m_c from the voltage dependence of the photoinjected charge and from the transport kinetics are in reasonable agreement. The values for m_c determined from the voltage measurements are, however, systematically slightly higher than those obtained from transport measurements, which is probably due to the same phenomenon causing the electron diffusion length to depend on the light-intensity (Schlichthörl, 1999; Benkstein, 2003; Kopidakis; 2000; van de Lagemaat, 2001).

2.2. Sensitizers

Since the advent of sensitized solar cells, there has been a very wide variety of sensitizers being used including, but not limited to, organometallic molecules, organic molecules and narrow band-gap semiconductors.

In this introductory discussion, only coordination sensitizers and narrow band-gap semiconductors are covered as these two categories are the subject of this work.

2.2.1 Coordination Compounds as Sensitizers

There has been significant amount of research performed all across the world on different organic and coordination molecules as sensitizers in DSSCs and presenting a thorough review of all this effort is beyond the scope of this work. There are many useful literature publications in the form of books and articles where in-depth information can be found (Kalyanasundaram, 2010; Hagfeldt, 2004, 2010; Robertson, 2006; Polo, 2004; Campbell, 2004; Nazeeruddin, 2004, 2005). For the purpose of this work, I will focus on the ruthenium compounds based on polypyridine ligands.

The main requirements for an efficient dye sensitizer are as follows: (i) large spectral overlap with the solar emission spectrum, with the optimal threshold wavelength for single-junction quantum converters being around 900 nm; (ii) suitable ground- and excited-state redox properties properly tuned with respect to the energy levels of the semiconductor substrate and the electrolyte solution; and (iii) the presence of interlocking groups for grafting the dye on the semiconductor surface as well as to ascertain intimate electronic coupling between its excited-state wave function and the conduction band manifold of the semiconductor.

On a ground-breaking paper, Gratzel introduced the so-called dye N3, the polypyridine-Ru dyes with the structure of $[Ru(tcterpy)(NCS)_3]^-$ (tcterpy = bis-(4,4-

dicarboxylic acid-2,2-bipyridine), which was proven to have the ideal properties as sensitizers (Nazeeruddin, 1993). Since then efforts commenced all around the world in order to improve the performance of such dyes by studying their structure and the strucutres effect on the final fabricated devices. Ruthenium polypyridine complexes have been intensively employed as sensitizers due to their appropriate redox, spectroscopic and excited-state properties (Sugihara, 1998; Yanagida, 2000; 2002; Schwarz, 2000; Hara, 2001a; 2001b; Islam. 2001; Nazeeruddin, 1997).

Polypyridine complexes of d^6 metal ions show intense metal-to-ligand charge transfer (MLCT) bands in the visible region with potential interest for promoting charge injection processes to the conduction band of wide band-gap semiconductors, such as TiO_2, SnO_2 and ZnO. The energies of the MLCT states can be altered systematically by modifying the anchoring ligands as well as by changing the ancillary ligands or their substituent (Kalyanasundaram, 1998).

Ever since N3 was reported as a very efficient energy conversion dye, efforts have been made to either match or improve its performance. One approach that has been attempted by several investigators is the substitution of the NCS^- ancillary ligands. This search for efficient *cis*-[$Ru(dcbH_2)_2LL'$] sensitizers ($dcbH_2$=4,4'-(CO_2H)2-2,2'-bipyridinehas) led to a wide variety of new photosensitizers. Their performance in solar cells is shown in Table 2.2.

Data presented in Table 2.2 point out that the substitution of the ancillary ligands has not, so far, improved the performance of the cells in terms of overall efficiency, η, or IPCE values, even though the new dyes could be successfully employed as semiconductor sensitizers. On the other hand, these new photosensitizers usually provide a wider coverage of the solar spectrum, promoting light harvesting in a lower energy region. The MLCT bands are susceptible to a greater electron donating or withdrawing ability of the ancillary ligand as can be seen in a series of complexes using pteridinediones or diimine thiolates (Islam, 2001; Anandan, 2002). Such transitions are sensitive to changes made in the anchoring group, $dcbH_2$, and the distinct positioning of the carboxylic group can also promote absorption shifts and be conveniently employed to tune the spectroscopic response of the sensitizer (Xie, 2000).

Table 2.2. Photoelectrochemical data obtained with solar cell sensitized by *cis*-[$Ru(dcbH_2)_2LL'$]

Complex	V_{oc}(V) [a]	J_{sc} (mA cm^{-2}) [a]	IPCE (%)[a]	*ff*[a]	η(%)[a]	References
$Ru(dcbH_2)_2(dmp)]Cl_2$	0.289	0.315	33.24	0.55	2.0	Anandan, 2002
$[Ru(dcbH_2)_2(mdmp)]Cl_2$	0.330	0.400	42.21	0.61	3.2	Anandan, 2002
$[Ru(dcbH_2)_2(phdmp)]Cl_2$	0.420	0.604	63.74	0.38	3.8	Anandan, 2002
$[Ru(dcbH_2)_2(blAlo)]Cl_2$	0.320	0.390	41.15	0.45	2.2	Anandan, 2002
$[Ru(dcbH_2)_2(pydmp)]Cl_2$	0.212	0.220	48.36	0.65	2.5	Anandan, 2002
$[Ru(dcbH_2)_2(aphb)]$	0.58	5.5		0.48	1.51	Mosurkal, 2002
poly$[Ru(dcbH_2)_2(aphb)]$	0.34	2.1		0.48	0.33	Mosurkal, 2002
$[Ru(dcbH_2)_2(CNpy)(H_2O)]^{2+}$			~60			Garcia, 2001; 2002
$Ru(dcbH_2)_2(qdt)$	0.595	11.1	45	0.70	3.7	Islam, 2001
$Ru(dcbH_2)_2(ecda)$	0.580	5.4	30	0.65	2.0	Islam, 2001
$Ru(dcbH_2)_2(bdt)$	0.540	2.1	7	0.66	0.7	Islam, 2001
$Ru(dcbH_2)_2(tdt)$	0.504	1.1		0.70	0.4	Islam, 2001
$[Ru(dcbH_2)_2(isq)_2]^{2+}$			~40			Garcia, 1998; 2001
$[Ru(dcbH_2)_2(ppy)(H_2O)]^{2+}$			>50			Garcia, 2001
$[Ru(dcbH_2)_2(ppy)_2]^{2+}$			~40			Garcia, 2001
$[Ru(3,3'\text{-}dcbH_2)_2(NCS)_2]$	0.47	8.0	21			Xie, 2000
$[Ru(5,5'\text{-}dcbH_2)_2(NCS)_2$	0.49	7.8	37			Xie, 2000
$[Ru(dcbH)_2Cl_2]$	0.57	2.6		0.38	2.1	Schwarts, 2000

Table 2.2 continued:

Complex	Voc(V)[a]	Jsc (mA/cm^2)[a]	IPCE (%)[a]	*ff*[a]	η(%)[a]	References
$[Ru(dcbH_2)_2(acac)]Cl$	0.674	13.20	>50	0.68	6.0	Takahashi, 2000
$[Ru(dcbH_2)_2(mpdionate)]Cl$	0.677	8.56		0.67	3.9	Takahashi, 2000
$[Ru(dcbH_2)_2(dphdionate)]Cl$	0.689	8.67		0.68	4.0	Takahashi, 2000
$Ru(dcbH_2)_3Cl_2$	0.52	1.0		0.37	0.7	Schwarts, 2000
$[Ru(dcbH_2)_2(ppt)]$			~60			Lees, 1999
$[Ru(dcbH_2)_2(2\text{-}ppt)]$			~60			Lees, 1999
$[Ru(dcbH_2)_2(bpzt)]$			~65			Lees, 1999
$[Ru(dcbH_2)_2(2\text{-}ppzt)]$			~55			Lees, 1999

[a]V_{oc}: Open-circuit photovoltage; J_{sc}: Short-circuit photocurrent, IPCE: Incident-photon to current efficiency; *ff*: fill factor; η: Efficiency.

All these compounds have broad absorption spectra with intense MLCT bands overlapping the solar spectrum, along with suitable photoelectrochemical properties. The carboxylic groups provide strong adsorption of the dye to the TiO_2 surface and the necessary electronic coupling between the charge transfer excited state of the sensitizer and the wavefunction of the semiconductor conduction band. As a consequence, excitation of these complexes with visible light results in a very fast electron transfer through the carboxylic groups to the semiconductor as described in the literature and previously in this text. The excited states' properties and charge recombination and quenching of these dyes are thoroughly studied in order to give a complete insight on the electronic properties of the molecules and how they interact with semiconductor at

the semiconductor/dye/electrolyte interface (Kiwi, 1982; Kamat, 1997, Li, 1999; Santiago, 2002; Katoh, 2004; Anderson, 2004).

As per the interest of my research, DSSCs with dyes of terpyridine and dipyrazinyl-pyridine ligands, synthesized and characterized in Potvin's research lab at York University, Toronto, are thoroughly studied (Stublla, 2010). The presence of heteroatoms in the structure of the tpy (2-2':6,6'--terpyridine) and dpp (2,6-(dipyrazin-2-yl)-pyridine) ligands (Figure 2.5) is shown to directly affect the properties of polypyridine ruthenium dyes (Balzani, 2001; Fallahpour, 2003; Liegghio, 2001, Stublla, 2010; Juris, 2001). The σ-donor orbitals of these ligands is located on nitrogen atoms and the π-donor and π*-acceptor orbitals on the aromatic rings (Fallahpour, 2003). The presence of any peripheral groups on these tridentate ligand has a direct effect on the charge delocalization and also the position of the molecular orbitals upon complexation. Upon photo-excitation, MLCT from the d orbitals of the metal (d_π) occurs where the excited electrons are excited to the π* orbitals that are mainly located on the electron-withdrawing ligands (Sauvage, 1994; Balzani, 2001).

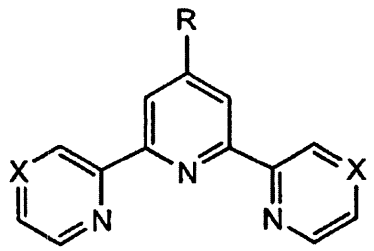

X= N, CH R= COOH or 4-C_6H_4COOH
COOEt or 4-C_6H_4COOEt

Figure 2.5. Structure of tpy (X = CH) and dpp (X = N) ligands used in our Ru dye sensitizers. When R = COOH or COOEt, there is no aromatic spacer between the anchoring group and the central pyridine, and when R = 4-C_6H_4COOH or 4-C_6H_4COOH, there is a phenylene aromatic ring between the two.

The lifetime of the excited state is dictated by the strength of the ligand field and has significant importance in choosing the dyes for DSSC applications. In our work this effect was studied by using tpy and dpp ligands with carboxylic acid or ester functional groups. The presence of these groups is expected not only to impact the molecular energy levels, but also to be influential in the solar cell's performance, the attachment of the dye to the TiO_2 substrate, the light absorption and the interaction between the dye and the redox mediator in the DSSCs.

The dpp complexes are expected to have longer lifetimes of the excited states compared to their tpy analogues as dpp compounds' absorption peaks are located at higher wavelengths and they also have more positive redox potentials (Liegghio, 2001;

Crutchley, 1982; Haga, 1985). The existence of a phenylene ring spacer between the carboxylic acid or ester groups and the aromatic tpy or dpp rings is studied. This will assist us in understanding the charge transfer rates between the π^* orbitals of the ligand and the carboxylic acid and ester groups. These groups are responsible for the anchoring of the sensitizers on the substrate and charge transfer between the sensitizer and the semiconductor substrate. So the combination of the excited-state lifetime and the rate of charge transfer between the sensitizer and the substrate are both crucial in choosing a sensitizer in DSSCs (Gregg, 2004). A thorough discussion will follow in the related chapter (chapter 4).

2.2.2 Narrow Band-Gap Sensitizers (NBGS)

The Sensitization of wide-band gap semiconductors such as ZnO and TiO_2 with narrow-band gap semiconductors has attracted extensive attention due to the promise that it has shown (Remacle, 1998; Soloviev, 2001; Tessler, 2002; Anikeeva, 2009; Shevchenko, 2008; Jdira, 2006; Wuister, 2004; An, 2006; Lifshitz, 1998; Rogach, 1996; 2007; Takagahara, 1992; Kan, 2003; Vogel, 1990; 1994; Zaban, 1998; Hodes, 1987; Gorer, 1994; 1995; Ginger, 1999; Greenham, 1996; Huynh, 2002; Choi, 2009; Leschkies, 2009; Hillhouse, 2009; Loef, 2009; Tachan, 2010; Ruhle, 2008; Weintraub, 2009; Toivola, 2009).

Ruhle et al. (Ruhle, 2010) show a relatively thorough table on not all, but the most significant NBGS used in the sensitization of wide band-gap semiconductor (WBGS).

These materials seem even more interesting when preparation procedures and costs are also considered. Narrow band-gap semiconductors have been investigated for almost a century. Our knowledge of their preparation and control of their optoelectronic and chemical properties is very well established (Rosenheim, 1906a; 1906b). Narrow band-gap semiconductors have generally high absorption coefficients, long-term stability and also the possibility of exploiting multiple exciton generation to achieve higher conversion efficiencies and even surpassing the thermodynamic limits on photoconversion efficiency (Hodes, 2008; Beard, 2009; Wurfel, 2002; Isborn, 2008). By controlling the crystal size of these semiconductors, one can also change their band-gap according to quantum confinement effect (Ruhle, 2010).

There are different techniques for the synthesis and adsorption of narrow band-gap semiconductors (NBGS) such as chemical bath deposition (CBD), Successive Ionic Layer Adsorption and Reaction (SILAR), monodisperse synthesis and attachment through linkers and direct adsorption of mono-disperse quantum dots (QDs). Each of these techniques offer different physical and chemical properties of the NBGS crystals (Ruhle 2010; Niesen, 2002).

The attachment of the NBGS to the wide band-gap semiconductors (WBGS) via a linker (an organic molecule that can attach to the NBGS from one end and to the WBGS from the other end) has some merits as well as some disadvantages. The presence of a linker (or as may be thought of, a spacer) can reduce the electron injection efficiency

between the sensitizer (here the NBGS) and the substrate. This has also been signified in the previous sections with respect to dyes used in DSSCs. Also, the electronic properties of the NBGS can change on the surface and the alteration of the energy states may not be desirable more specifically since the mono-disperse NBGS are synthesized with the hope to control the electronic characteristics of the nano crystals (Niesen, 2002; Kamat, 2008). Linkers, however, assure strong grafting of the NBGS on the surface which increases the durability of such devices (Mora-Sero, 2008; Robel, 2006).

In contrast, chemical bath deposition (CBD) is not capable of controlling the size of the semiconductors and any possible alteration to the deposition conditions will merely result in the same size control that is offered by monodisperse techniques. Despite that, CBD is proven to be the most cost-effective and accessible technique in the lab for deposition of semiconductors and also sensitization of WBGS. Any possible mixture of ternary or quaternary semiconductors can be prepared by CBD (Hodes, 2003; 2007). CBD is also shown to be more effective in sensitizing WBGS for applications is SSSCs (Mora-Sero, 2008). It can offer more coverage so there will be less of the substrate exposed to the electrolyte solution in the solar cell and it does not need a linker in order to connect to the substrate, therefore there is no potential barrier between the sensitizer and the substrate.

Synthesis of ternary alloys of NBGS has been interesting to many researchers (Kainthla, 1982; Mane, 1997; Mane, 2000). With ternary alloys, a wider range of

photoabsorption becomes possible. Ternary alloys also have more energy levels compared to the binary alloys, which can be beneficial when used in solar cells. The presence of more energy states can introduce more charge transfer pathways which in turn may increase the efficiency of electron transfer. It may however, also increase the rate of electron/hole recombination through the interaction with the redox mediator (Hodes, 2008).

The interest of my research is in cadmium selenide and cadmium sulfide (cadmium chalcogenide) as NBGS for the sensitization of TiO_2 for application in SSSCs. Herein I describe the sensitization of TiO_2 mesoporous films with $CdSe_xS_{(1-x)}$ composition where "x" is the molar ratio of selenide precursor added in the chemical bath. By varying the ratio of each chalcogenide through varying the molar ratio of selenide and sulfide precursors added in the chemical bath, different photoconversion activities are expected that can then be correlated to preparation methods and the resulting optoelectronic and photochemical properties of the sensitizers.

Cadmium selenosulfides are the most studies chalcogenides and narrow band-gap semiconductors (Rosenheim, 1906a; Rosenheim, 1906b; Hodes, 2008; Beard, 2009; Wurfel, 2002; Isborn, 2008; Ruhle, 2010). Cadmium sulfide with a bulk band gap of 2.40 eV starts to absorb photons at the onset wavelength of ca. 517 nm, while the onset of bulk cadmium selenide absorption is at ca. 713 nm (Xu, 2000; Kainthla, 1982). As previously mentioned, preparation of a ternary alloys of these two chalcogenides

provides us with the opportunity of harvesting a wider range of photons compared to the binary alloys of the same semiconductors. The deposition of ternary alloys on mesoporous substrates of wide band gap semiconductors (in many cases, TiO_2) leads to a variety of unknown physical and chemical phenomena that will affect the photoconversion characteristics of the solar cell devices. One may encounter a wide range of complications, from particle size of the deposited sensitizer, to the sensitizers' interaction with the electrolyte solution employed in the solar cells (Ruhle 2010). The mechanisms and the CBD synthesis of CdSeS ternaries will be discussed in more details in the following chapters.

When studying the literature for the electron transfer kinetics and dynamics in cells fabricated with NBGS as sensitizers, there is much less data available on charge transfer rates. In addition, one must be aware that, although the rates shown for the DSSCs are for optimized cells, this is not the case for the SSSCs. Thus, we can only use best values, and in many cases, the equivalent values with which to compare with the DSSC are yet unknown or at least not completely reliable. Among the limited information on electron injection rates from a sensitizing semiconductor into an oxide, many rate values given in older studies often refer to upper limits rather than actual times. The rates were measured using either dispersed colloidal systems or dry electrodes, and are often measured under conditions far from those at which a solar cell is measured. Within these limitations, based on the information available in the

literature, I will show some typical values and ideas about the injection timeframes and charge transport in SSSCs.

The fastest quenching rate (electron injection rate from the excited NBGS to TiO_2) reported so far is on the order of a picosecond for Cd_3P_2 and CdS on TiO_2 (Kietzmann, 1991). More recent articles report rates of the order of tens of picoseconds for CdS on TiO_2 and 16 ps for CdSe on TiO_2 (in both articles the measurement is performed in the absence of an electrolyte/hole conductor) (Blackburn, 2003; Shen, 2005).

When a semiconductor is covered with an organic capping layer (either the WBGS substrate or the NBGS sensitizer), we expect longer injection times than for bare semiconductors directly connected to the substrate or sensitizer. The same is expected for NBGS sensitizers that are linked by molecules to the oxide. Thus, in most research, electron injection has been measured to occur over a wide range of rates varying from a few picoseconds to 100 ps for ca. 3 nm CdSe nanocrystals attached to TiO_2 through molecular linkers (Robel, 2006). Also, average electron lifetimes for the same system, strongly depends on the CdSe crystal size. This lifetime varies from <100 ps for 2.4 nm CdSe crystals to 100 ns for 7.5 nm crystals (Robel, 2007). CdSe with smaller sizes, have higher conduction band levels which in turn increases the rate of electron injection due to the larger driving force available. There is a ca. 0.5 eV change in band-gap over this size range, principally due to changes in the conduction band level (Kocha, 2002).

Competing electron-hole recombination times in the semiconductor vary over orders of magnitude. When II-VI semiconductors are passivated (covered with non-electroactive materials) they typically show recombination lifetimes of ca. 10-9 s. For unpassivated semiconductors, the rate could be much faster (Hodes 2008). Even faster recombination times can be found for some other semiconductors, such as Cu_xS, in which recombination in the semiconductor may extensively compete with or even nullify the electron injection into the oxide. Also much slower recombinations can be found, as in PbS, a fairly common sensitizer used in SSSCs, with the recombination time up to microseconds (Hodes, 2008). Recombination may be band-to-band or trap-mediated. In band-to-band recombination, charges are directly transferred from the excited states to the redox mediator. In trap-mediated recombination, the excited charges are first transferred to a trap state on the surface which has lower energy than the excited state. Then this charge is transferred to the redox mediator from the surface trap. This brings us to a major difference in principle (and probably also in practice) between the DSSC and SSSC: the probable existence of surface traps on the sensitizing semiconductor.

Electron transport rates of metal oxide (TiO_2) will probably be essentially the same for the DSSC and SSSC assuming that, in both systems, the same electrolyte solution is applied. However the different surface-adsorbed species may be more important here due to different interfaces between the oxide and electrolyte, because of effects of adsorbed species on the oxide surface states or simply due to different

areas of exposed oxide which will vary for DSSCs and SSSCs. The surface electronic structure of the TiO_2 is shown to be affected by the interaction between the dye and solution species (Schwanitz, 2007; Cameron, 2005). The chelation of the dye to TiO_2 furthermore reduces electron transfer to polyiodide electrolyte (Fitzmaurice, 1993). One of the main differences between DSSCs and SSSCs is that, except for few studies, tri-iodide has never been effectively used for SSSCs simply due to the fact that most NBGSs are not stable in I^-/I_3^- electrolytes. Polysulfide has been the dominant electrolyte for many SSSCs. The rates for hole injection from the semiconductor to the electrolyte will depend on both the semiconductor and the electrolyte and can vary considerably from one system to another. In SSSCs, this is even more complicated once we know that holes are very rapidly trapped in nanocrystals of most semiconductors (often on the picoseconds time scale). Therefore we are often in practice dealing with a trapped hole (Zaban, 1998). In fact, it is widely believed that charge injection from a semiconductor to an electrolyte occurs via such surface traps (see Meissner, 1988 and the references therein). In a study of electron- and hole-transfer rates from semiconductors to solutions, Lewis suggests charge-transfer times ranging from picoseconds to milliseconds (Lewis, 1991). For redox species that are strongly adsorbed to the semiconductor surface such as occurs for metal chalcogenides in polysulfide solution, the hole-transfer rates that can be treated to some extent as an intramolecular charge transfer, are expected to be very fast (Kamat, 1993).

According to these complications pertaining to the sensitization of TiO_2 with NBGS, a different thermodynamic studies and establishment of new physical and mathematical equations deem necessary for better understanding the SSSCs. In fact our previous knowledge of photoelectrochemistry of DSSCs is not completely beneficial in depicting all aspects surrounding the SSSCs functions. Some serious attempts have been published so far which are opening new ways in understanding the SSSCs (Archer, 2008; Tachibana, 2009; Mora-Sero, 2007).

2.3. Redox Mediators

The most dominant electrolyte used in sensitized solar cells based on TiO_2 substrate has been polyiodide and mainly iodide/triiodide electrolyte. The main reason for this choice has been the compatibility of this electrolyte with TiO_2, the slow charge transfer from TiO_2 to I^-/I_3^- and the non-corrosive behaviour on TiO_2 when illuminated (Nazeeruddin, 1993).

Despite this, iodide/triiodide has never been the ultimate favorite redox mediator in sensitized solar cells for a variety of reasons. First, iodide/triiodide needs an organic solvent for preparation and to be compatible with the majority of the sensitizers. Most of these solvents are very volatile, which necessitates sealing the cells for long-term performance and study. It also has an intense color and absorbs visible photons, which limits the illumination of the cells only to back-illumination. Front-illumination has almost never been an option. It has also been shown that iodide/triiodide is mainly

suitable for sensitizer dyes that have thiocyanato (NCS) or other metal-stabilizing ligands as one of the ligands surrounding the metal center (Nazeeruddin, 2001). This will limit the choice of sensitizer to a great extent. In addition, the redox potential of the iodide/triiodide offers a limited open-circuit photovoltage (V_{oc}) which in turn adds more limitation to all other thermodynamic restrictions intrinsic in sunlight conversion.

Considering these limitations there has been plenty of motivation for researchers around the world to investigate any other types of redox mediators. Alternative electrolytes that have received attention include cobalt polypyridine complexes, nickel bis(dicarbollides), nitroxide radicals, 5-mercapto-1-methyl tetrazole, 2-mercapto-5-methyl-1,3,4-thiadiazole (MeMT), and tetramethyl thiourea (Feldt, 2010; Wang[a], 2010; Spokoyny, 2010; Kato, 2010; Wang[b], 2010; Tian, 2010; Liy, 2011). Among all of these materials, only Co-polypyridine complexes could really rival the iodide/triiodide electrolyte with respect to the overall performance and efficiency of the cells because these cobalt complexes have slow charge-transport kinetics on the surface of TiO_2 (Cameron, 2004; Sapp, 2002; Nakade, 2005).

There has also been intense research carried on to develop solid-state sensitized solar cells (Hamann, 2011). This removes the demand for volatile solvents needed for the performance of the redox mediators. The best efficiency reported for solid-state solar cells has been measured by Burschka et al (Burschka, 2011) in Gratzel's group where they used the hole-transport material (HTM), spiro-MeOTAD (2,2'7,7'-tetrakis-

(N,N-di-p-methoxyphenyl-amine)-9,9'-spirobifluorene) with a cobalt-based p-dopant in a cell sensitized with an organic dye to obtain an efficiency of 7.2%.

Applying HTMs, and specially solid HTMs, in solar cells has introduced new parameters related to the performance of the cells. The compatibility of the sensitizer with the HTM with respect to the hydrophobicity and hydrophilicity, pore-filling into the nano-structure of TiO_2 and processability of the HTM are among those important parameters. The main reason spiro-MeOTAD has been a successful HTM is simply due to the two last reasons. It is very easily processed and applied in the cell during the fabrication process. It is also compatible with TiO_2 surfaces and penetrates in the pores of the substrate without much obstruction (Burschka, 2011). Moreover the recombination kinetics of cells with MeOTAD are not favored over charge collection and injection (Burschka, 2011).

It is clear that significant modification to the original DSSC has been employed in order to achieve reasonable efficiencies with organic materials. However none of these materials have yet addressed the need for sustainable, affordable and environment-friendly chemicals in solar cells.

There have been some classes of organic HTMs that have not got the attention of many researchers in photoelectrochemistry fields. These compounds, such as arylamines, have been used in the electronic industry for many years as their production

cost is very low and also they do not require high safety measures in order for one to be able to work with them (Shirota, 2007).

Triarylamines are a well-known class of hole transport materials and have been used in many organic electronic devices such as organic light emitting diodes (OLEDs), photovoltaics, organic field effect transistors (OFETs), and xerographic photoreceptors (OPRs) (Shirota, 2007; Xu[b], 2009; Hendrickx, 1999; Ribierre, 2007; 2008). These compounds benefit from low toxicity, ease of synthesis and good stability. Moreover, their flexible synthesis allows for a wide range of electronic and physical properties to be achieved (Bender, 2001). Several triarylamine derivatives have been previously shown to work as redox couples in DSSCs. The first reported example used *N,N'*-di-*m*-tolyl-*N,N'*-diphenylbenzidine (TPD) as a redox mediator in solution (Gregg, 2001). It was found that when this redox couple was highly doped by using oxidizing agents (10% doping), the resulting cell performed extremely poorly due to rapid charge recombination between the redox mediator and the ruthenium dye. Significantly better performance was achieved by anode passivation. The liquid triarylamine, tris(4-methoxyethoxyphenyl)amine, was shown to work as a neat redox couple in a DSSC achieving an efficiency of 2.4% under AM1.5 illumination (Snaith, 2006).

Triarylamines are cost-effective for preparation and synthesis (Kamino, 2011). They are soluble in non-volatile organic solvents and are easily processable. They usually are not considered as toxic materials and they are stable under ordinary conditions.

Applying them in solar cells can be beneficial in reducing the production costs as they are completely organic materials and also do not need special conditions for processing and handling.

In my work, I will show how we used a class of triaryamines as HTM in our DSSCs. These HTMs were prepared in Prof. Bender's lab at University of Toronto, Department of Chemical Engineering and Applied Science (Figure 2.7) (Kamino, 2011). These compounds were fully characterized and they were chosen as proper prototype candidates for HTMs in our DSSCs based on the electrochemical, chemical and physical properties.

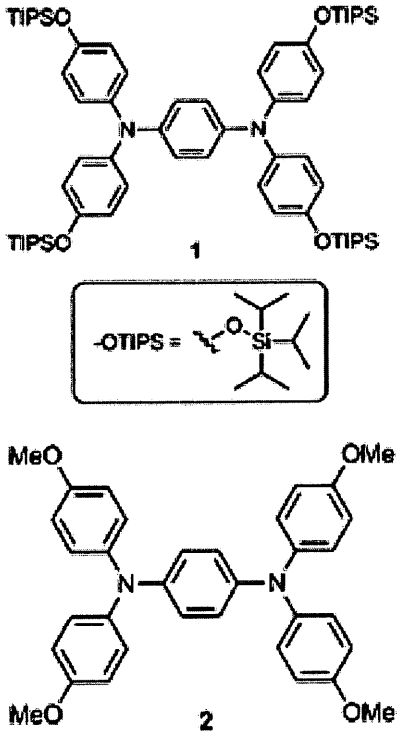

Figure 2.7. Structure of *N*, *N*, *N'*, *N'*-tetra(4-triisopropylsilyl ether)phenyl)1,4-phenylenediamine (compound **1** also abbreviated as 1,4PDATIPS) and *N*, *N*, *N'*, *N'*-tetra(4-methoxy)phenyl)1,4-phenylenediamine (compound **2** also abbreviated as 1,4PDA) used as HTMs in my research.

2.4. Outline of the Thesis

According to what was described above, the main interests of my research have focused on two major subjects:

1- Study of structural effects of sensitizing dyes on the performance of DSSC with respect to the energy levels and opto-electronic properties of the dyes and, in an independent but relevant study, the employment of siliconized triarylamine compounds as HTMs in DSSCs and studying the physical, chemical and structural impact of these HTMs on the performance of the cells.

2- Study of the ternaries of $CdSe_xS_{(1-x)}$ and sensitizer in SSSCs. For this purpose, the effect of the preparation methodology, the mechanisms of deposition and sensitization, the change in photoelectrochemical behavior of the sensitizers due to the change in the preparation technique and the compatibility of the cell components with the sensitizer have been studied. To the best of my knowledge, there has been no record of such thorough study published yet. However there is still significant demand to expand this research even further and add to the knowledge that has been generated so far.

Chapter 3: Experimental Procedures

In this chapter, all of the methodologies for performing the experiments as well as the techniques and procedures for the preparation of the samples, calibration of the devices and measurement protocols are described.

3.1 Materials

Unless otherwise stated, all the chemicals used were from Aldrich with analytical grade purity (unless otherwise mentioned) and used as received. The synthesis of the Ru dyes is reported elsewhere (Stublla, 2010). The dye *cis*-di(isothiocyanato)-bis(4,4'dicarboxy-2,2'-bipyridine)ruthenium(II) (the so-called N3 dye) was used as a reference and was purchased from Solaronix SA Co. Aeroxide TiO_2 P25 nanoparticles, a mixture of 30% rutile and 70% anatase, with Brunauer-Emmett-Teller (BET) surface area of 55 m^2 (Degussa Co.) was used to prepare the anodes. Transparent fluorine-doped SnO_2 conductive glass (Tec 7 FTO, Pilkington Co., 8 Ω cm^{-2}) was used as a substrate for the photo-anode (TiO_2 films) and cathode (Pt) electrodes.

The HTM compounds (*N*, *N*, *N'*, *N'*-tetra(4-triisopropylsilyl ether)phenyl)1,4-phenylenediamine, compound **1** also abbreviated as 1,4PDATIPS and *N*, *N*, *N'*, *N'*-tetra(4-methoxy)phenyl)1,4-phenylenediamine, compound **2** also abbreviated as 1,4PDA)) are prepared in Prof. Bender's lab in University of Toronto, Department of

Chemical Engineering and Applied Science (Figure 2.7) and fully characterized (Kamino, 2011).

3.2 Preparation Procedures

3.2.1 TiO_2 Films and Pt Counter Electrode

The so-called "compact layer" of TiO_2 on fluorine-doped tin oxide (FTO) conducting glass (10 cm × 5 cm) and subsequent nanoporous TiO_2 layer were prepared following a literature procedure (Biancardo, 2006; 2007).

For this purpose, FTO glass was cut in the desired size and washed with soap and water and clean laboratory paper. Then it was rinsed with doubly-distilled water and dried with compressed air.

A solution of Ti-isopropoxide ($Ti(OiPr)_4$), acetylacetone and ethanol (1 : 0.7 : 5.2, volume ratio) was prepared as coating solution. The FTO glass pieces were sonicated in a Aquasonic 50T (VWR) sonication bath for 30 min in a mixture (1:1 v:v) of acetone and isopropanol and were dries in ambient conditions. They were coated with 1.00 mL of the coating solution using spin coating techniques. The dropping step was performed in a 200 seconds period while the spin-coating speed was at 2200 rpm. The as-made films were baked in the oven at 500°C for 20 min. The FTO glass with TiO_2 compact layer was then covered with TiO_2 nanocrystaline layer prepared with the method described here below.

Colloidal suspensions of P25 TiO_2 were prepared as follows: 6.00 g of P25 powder was placed in 12.00 mL of Milli-Q water (Millipore) in a small flask (Sepehrifard, 2008). After homogenization by stirring with a glass rod, acetylacetone (3.00 mL) and Triton X-100 (1.00 mL) were slowly added to the suspension. The suspension was then sonicated for 1h and constantly stirred for another 30 min with a magnetic stirrer. The TiO_2 film was prepared by the doctor-blade method, where one layer of adhesive tape (Scotch, 3M) was used as a spacer to control the thickness of the TiO_2 film. Once dry, the TiO_2 film was baked at 450°C in air for 1 h, and then cooled to room temperature. The thickness of the TiO_2 films was controlled by adjusting the thickness of the adhesive tape spacer and the concentration of the TiO_2 suspension. The thickness values vary based on the requirements of each experiment and are reported on the discussion section. The thickness of the films was measured with scanning electron microscopy (SEM) by taking images from the cross section of the films using a Hitachi S4500 FESEM machine. The thicknesses are mentioned wherever necessary (Sepehrifard, 2008).

The Pt-coated counter-electrode was prepared as described by Sepehrifard et al (2008). The Pt-coated conducting glass was prepared through sputtering. An adhesive layer of Cr was deposited on the glass piece prior to the sputtering of Pt. The thickness of the sputtered Pt layer was ca. 1.5 μm.

3.2.2 Dyes Solutions and TiO_2 Sensitization with Dyes

TiO_2 film sensitization was performed by heating the films to 120°C for 30 min and then dipping them into 0.5 mM dye solutions in acetonitrile. A solution of N3 and Z907 (Figure 3.1) dyes at that concentration was prepared in methanol. Dye Z907 was only used in the experiments with hole transport materials. Two different conditions were used for dye adsorption: a) films were kept in dye solutions for ca. 14 h at either room temperature (denoted RT in the text) or with warming to ca. 50-60°C (denoted WS). Warming was only applied for the ester-functionalized dyes. The films were then rinsed with acetonitrile to remove physisorbed dye molecules. The films were usually used immediately after their preparation. However in case storage of the sensitized films was required, they were kept in dark under an inert atmosphere.

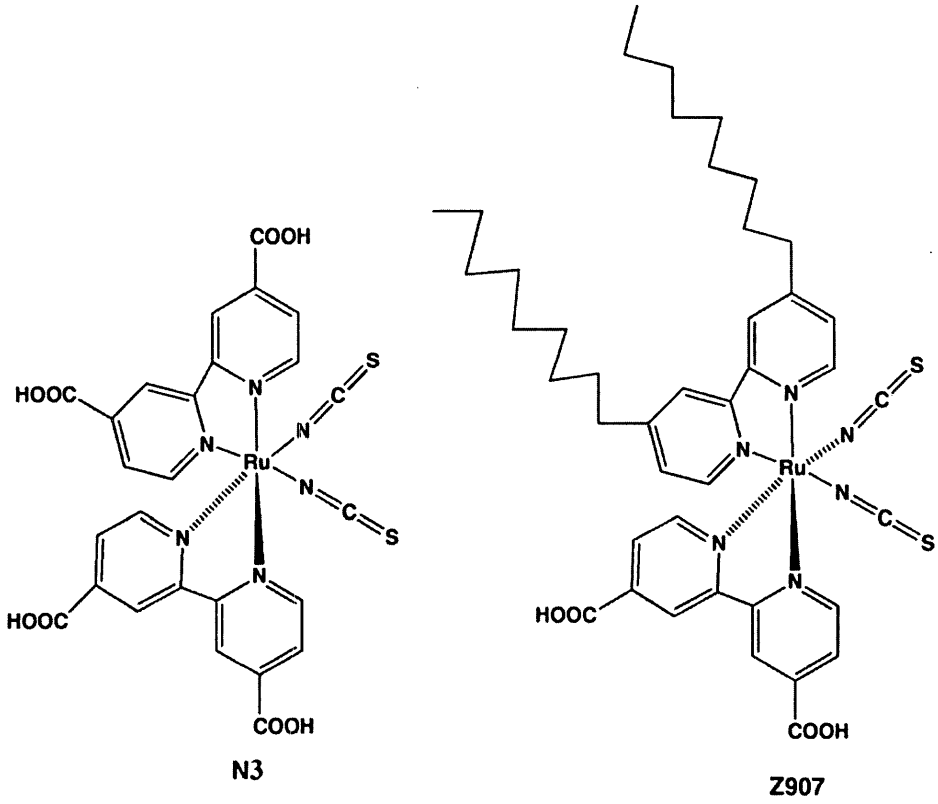

Figure 3.1. Schematic structure of dyes **a)** N3 and **b)** Z907.

3.2.3 $CdSe_xS_{(1-x)}$ Deposition on TiO_2

Cadmium selenosulfide ($CdSe_xS_{(1-x)}$) nanocrystals with different compositions were deposited from two different chemical baths: an ammonia chemical bath (denoted as NH_3 CBH) and an NTA chemical bath (denoted as NTA CBH where NTA is sodium trinitriloacetate).

For each of the baths a solution of sodium selenosulfate (Na_2SeSO_3) with the desired concentration, as specified below, was prepared by refluxing Se powder in sodium sulfite solution at 70°C for 4 hours under ordinary indoor luminescent light.

Thiourea was used as the source of sulfide in both baths. NH_3 was used to control the release of sulfide and selenide from their precursors in NH_3 CBH and also to adjust the pH, based on the procedure found in paper with Kainthla et al, (Kainthla, 1982).

In NTA CBHs, 0.15 M of sodium nitrilotriacetate in all of the baths was used as complexing agent. It must be mentioned that this concentration serves to keep the Cd:NTA molar ratio at 1.88. This ratio is chosen as our standard ratio. However, changing it affects the mechanism of the deposition, which will be discussed further in the relater chapter. The pH of the NTA CBD solutions was adjusted to the values found in Table 3.1 by using a 1.0 M solution of NaOH and adding few drops so that the volume does not change (Gorer, 1994).

Table 3.1 Initial pH of NTA CBHs adjusted once the components are mixed with each other.

Bath Composition	pH of the bath
CdS	10.70
$CdSe_{0.25}S_{0.75}$	10.52
$CdSe_{0.50}S_{0.50}$	10.35
$CdSe_{0.75}S_{0.25}$	10.17
CdSe	10.00

Each of the chemical baths, with different compositions of the proposed CdSeS was prepared according to the concentrations listed in table 3.2. It must be noted that the compositions of the prepared CBs do not necessarily deposit nano crystals with the

same percent composition on the surface, as the rate of release of sulfide and selenide from their precursors is relatively different.

Table 3.2 Composition of baths prepared for different $CdSe_xS_{(1-x)}$ ternaries compositions. The values in parenthesis belong to the NTA CBH.

CB Composition	CdS	$CdSe_{0.25}S_{0.75}$	$CdSe_{0.50}S_{0.50}$	$CdSe_{0.75}S_{0.25}$	CdSe
$Cd(NO_3)_2$ (M)	0.03 (0.080)	0.03 (0.080)	0.03 (0.080)	0.03 (0.080)	0.03 (0.080)
NH_3 (M)	4.79	3.92	3.04	2.17	1.32
Na_2SeSO_3 (M)	0.00 (0.00)	0.01 (0.022)	0.02 (0.045)	0.03(0.067)	0.04 (0.090)
Thiourea (M)	0.04 (0.090)	0.03(0.067)	0.02 (0.045)	0.01 (0.022)	0.00M

*For NTA CBH, T=45°C, Cd:NTA = 1.88, the final concentration of NTA was kept at 0.150 M. The films were kept in the CB for 4 hours.
*For NH3 CBH, T=66°C; the films were kept in the CB for 30min.
*The compositions shown as $CdSe_xS_{1-x}$ refer to the molar ratios (x) of the baths and not what is necessarily deposited on the TiO_2 films.

After the solution mixtures were prepared the TiO_2 films were immersed in the solution for the allocated time and were left in the solution for the time mentioned in Table 3.2. Then the films were taken out of the baths, thoroughly washed with water and dried with argon stream and kept under inert atmosphere and in dark for further experiments. Figure 3.1 shows the photos of the films prepared in both NH_3 and NTA baths.

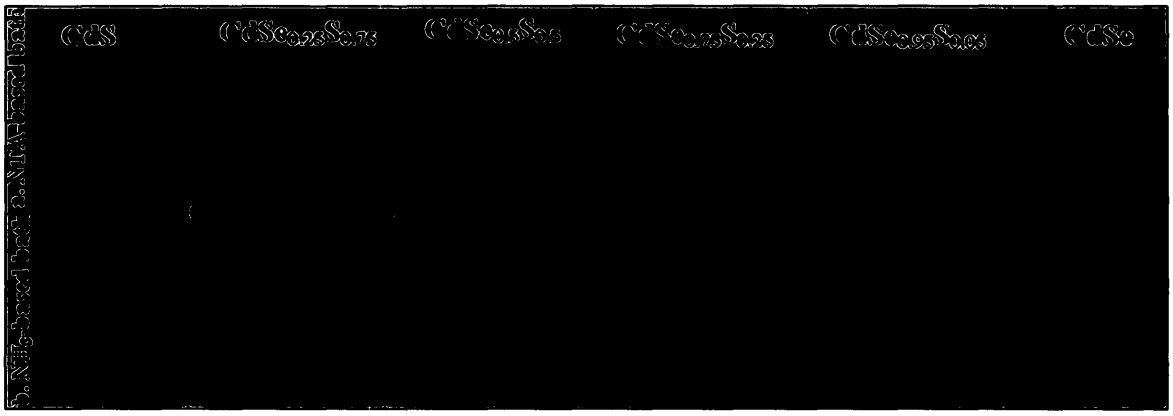

Figure 3.2. Photo of TiO_2 films sensitized with different $CdSe_xS_{(1-x)}$ compositions and prepared in a) NTA CBH and b) NH_3 CBH. The compositions shown as $CdSe_xS_{1-x}$ refer to the molar ratios (x) of the baths and not what is necessarily deposited on the TiO_2 films.

3.2.4 Electrolytes and Hole-Transport Materials Solutions

Two kinds of iodide/triiodide (I^-/I_3^-) electrolyte solutions were used for the characterization of the solar cells: electrolyte **A**, prepared using a mixture of 0.5 M LiI and 0.05 M I_2 in dry acetonitrile, was used for the tpy and dpp dyes while electrolyte **B**, prepared using a mixture of 0.5 M LiI, 0.05 M I_2 and 0.1 M 4-tert-butylpyridine (TBP) in a 7:3 (v/v) mixture of acetonitrile and 3-methyl-2-oxazolidinone (NMO), was utilized for the N3 dye. A rationale for this choice is given in chapter 4.

The hole-transport material (HTM) solutions were prepared by making a solution of the HTM (0.26 M), *tert*-butylpyridine (TBP) (1.6 M), Bis (trifluoromethane) sulfonimide lithium salt (LiTFSI) (2.8×10^{-2} M) in dichloromethane (DCM). The silyl ether HTM (*N*, *N*, *N'*, *N'*-tetra(4-triisopropylsilyl ether)phenyl)1,4-phenylenediamine,

abbreviated as 1,4 PDATIPS) is denoted as electrolyte **1** and the methyl ether derivative is denoted as **2** (also abbreviated as 1,4 PDA) (Fig. 2.7).

For SSSC experiments, polysulfide electrolyte (3 M S, 2 M Na_2S) was prepared by dissolving the required amount of sulfur in sodium sulfide solution. All polysulfide solutions were prepared and used fresh.

3.3 Physical and Photochemical Characterization

3.3.1 UV-Vis, Luminescence and FTIR Spectroscopy

All UV-Vis spectra of solutions were obtained using an Ultraspec 4300 pro (Biochrom) UV-Vis instrument. UV-Vis spectroscopy of the sensitized TiO_2 films was performed by using a Perkin-Elmer (Lambda 1050) instrument equipped with an integrating sphere accessory. The quantities of dyes anchored on TiO_2 with a given geometric electrode area were determined by desorption of the dyes from the TiO_2 surface into alkaline ethanol/water solutions and measurement of the UV-visible absorption of the resulting solutions (pH from 9 to 11) (Murakoshi, 1995). A calibration curve drawn with standard concentration in the basic solution was used to calculate the concentration of the desorbed dyes.

The luminescence spectra of the dye solutions (4 to 7 × 10^{-5} M in acetonitrile) were recorded at 4°C using a Cary Eclipse fluorescence spectrophotometer.

The lifetime measurements were performed at room temperature without any treatment of the solutions and used to determine the band gap energies of the dyes. A femtosecond laser amplifier system (Spitfire, Spectra-Physics) was used as the light source. The laser system produces 100-120 fs-long, 1 mJ laser pulses centered at 800 nm at a repetition rate of 1 kHz. An optical parametric amplifier (OPA) was used to produce the pump pulse at a wavelength of 490nm for photoexcitation. The pump pulse was focused by a lens into a sample cell. The emitted fluorescence in the forward direction was collected by two parabolic mirrors, focused at the entrance of a monochromator, and detected by a photomultiplier tube (PMT). The data was collected using LabVIEW software, Professional version. The sample was held in a 5mm cell with a stirring bar to avoid any photoproduct accumulation. The instrumental response function was estimated with a pure water sample at 490 nm to be a Gaussian function with a full width at half-maximum (FWHM) of 4.5 ns. The fluorescence decay curves of the samples were then fitted by a single-exponential function and the decay lifetimes determined therefrom. All the excited state lifetime measurement experiments were performed at room temperature.

Transmission-mode FTIR (Nexus 870, Thermo Nicolet) was used to monitor dye anchoring. The sensitized TiO_2 films were scratched off the conducting glass into a mortar, then ground with KBr to make the needed pellets under a hydraulic press. A pellet made from an un-sensitized TiO_2 film was used as background. The FTIR spectra of the pure dyes were obtained from separate KBr pellets for comparisons.

3.4 Photoelectrochemical experiments

A sandwich type cell configuration was employed. The sensitized TiO_2 films were used as working electrodes. The Pt-coated FTO electrodes served as cathodes. Teflon tape was used as spacer in order to create a passage for the introduction of the electrolyte solution through capillary action. In case of the experiments with HTMs, the HTM solution was inserted between the electrodes using a micropipette and the cells were sealed properly using the Kapton tapes.

The photoelectrochemical characterizations of the cells were carried out using radiation of AM 1.5 simulated light (PTI) equipped with a 450 W Xe lamp (short-arc lamp, USHIHO), with IR (Edmund Optics) and UV (Andover Corp.) filters. A power meter (13 PEM 001, Melles Griot) was also used to measure the light intensity prior to the experiments. A monochromator (101/102, PTI) and a Volta Lab 80 potentiostat (Radiometer, Copenhagen) were used to measure the Incident Photon-to-Current Efficiency (IPCE) for each dye. The monochromator and the potentiostat were triggered simultaneously so that the wavelength and the corresponding current densities were collected using VoltaMaster 4 software as the interface. The wavelength sweep rate was typically 5 nm s^{-1}. In all of the measurements, the light entered the cell through the anode side where an area of 0.58 cm^2 was illuminated. At least two cells or anode samples were measured for each dye in order to obtain a good representation of the dye performance.

The open-circuit photovoltage decay (OCVD) measurements were performed using the same method introduced by Zaban et al. at an intensity of 100 mW cm^{-2} (Zaban, 2003). For this purpose the cell was illuminated to a steady voltage. The illumination was turned off with a shutter. Typically, the measurement interval was 10 to 50ms. The decay analysis in the following chapters refers only to values measured after the shutter obtained full darkness. The same electrochemical setup and software as was mentioned above was used for OCVD experiments. In all the measurements, the light entered the cell through the anode side where an area of 0.58 cm^2 was illuminated.

The calculations of the PEC experiments are described in figure 3.2 typical i-V curve derived from photoelectrochemical experiments. Solar energy-to-electricity conversion efficiency, η, under white light irradiation (e.g. AM1.5) is obtained by the following equation (Peter, 2007b; Kalyanasundaram, 1998):

$$\eta = \frac{J_{SC} \times V_{OC} \times ff}{I_0} \times 100\% \qquad \text{Eq. 3.1}$$

so:

$$\eta = \frac{J_{MPP} \times V_{MPP}}{I_0} \times 100\% \qquad \text{Eq. 3.2}$$

where J_{sc} (short-circuit current density), V_{oc} (open-circuit photovoltage) and *ff* (fill factor), all of which are derived from the i-V curve of the solar cell (Figure 3.3) and I_0 is

photon flux, which equals to 100 mW cm^{-2} under 1.5 Air Mass, accepted as the standard illumination condition for photoelectrochemical measurements of solar cells.

The fill factor is the ratio of the product of current density (*J*) and photovoltage (*V*) at the maximum power point (MPP) (shown in Figure 3.1 as V_{MPP} and J_{MPP}) of the cell, to J_{sc} and V_{oc} (Eq. 3.3) (Peter, 2007b; Kalyanasundaram, 1998):

$$ff = \frac{J_{MPP} \times V_{MPP}}{J_{SC} \times V_{OC}} \qquad \text{Eq. 3.3}$$

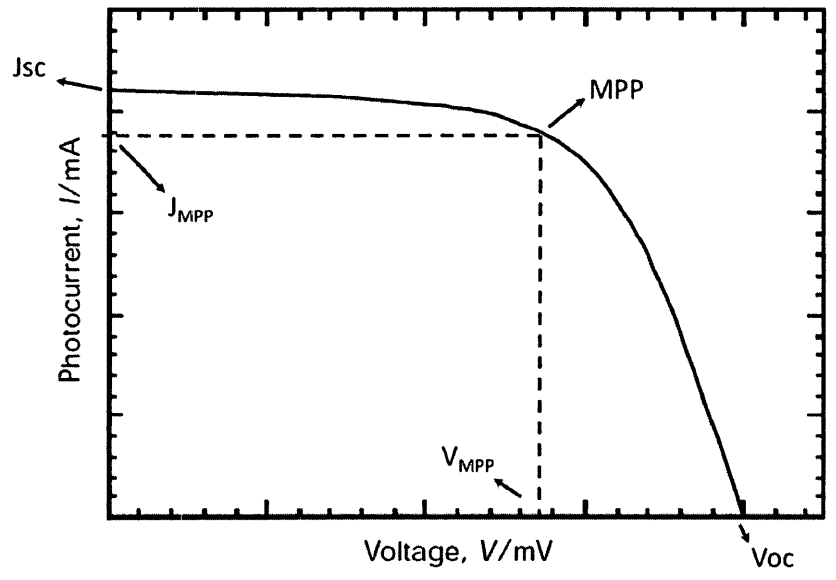

Figure 3.3. Photocurrent vs. photovoltage (i-V) curve of a typical photoelectrochemical cell. MPP stands for maximum power point.

In Figure 3.4 an example of IPCE graph is presented (Gratzel, 2003). In general, IPCE shows how efficient a sensitizer is in converting photons of different wavelengths

to electrons. Dyes with higher IPCE values are more panchromatic in the visible region and so are more useful in DSSC applications.

IPCE is an evaluation of the effective quantum yield of the device and is mostly influenced by the dye molecule, its effectiveness in photon to current conversion (light harvesting efficiency) and charge injection yield. Besides that, IPCE is dependent on charge collection efficiency of the fabricated cell, which is related to the morphology of the semiconductor (Kalyanasundaram, 1998).

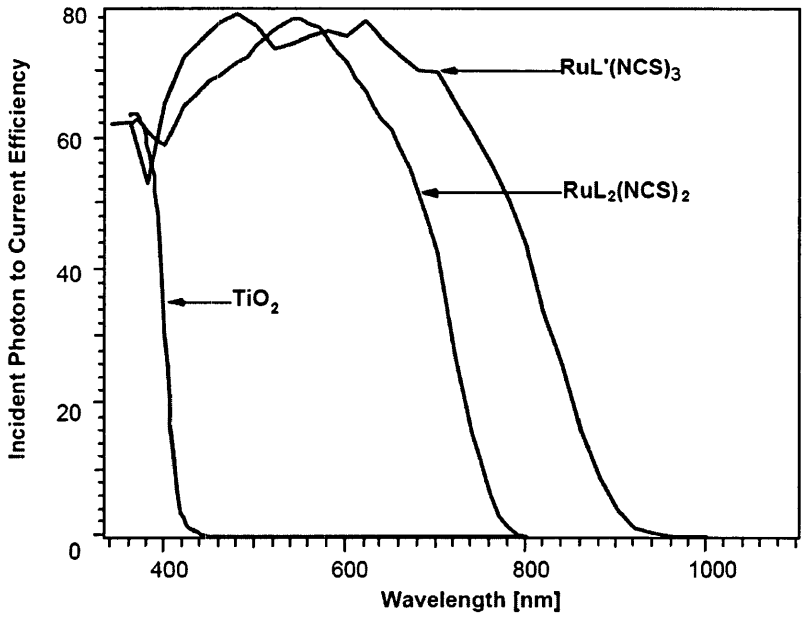

Figure 3.4. Typical IPCE curves of two dyes and plain TiO_2 film; L= 4, 4'-COOH-2,2'-bipyridine and L'= 4,4',4" -COOH-2,2':6',2"-terpyridine (Gratzel, 2003).

To draw the related graph, the *IPCE* percentage at each specific wavelength is calculated through equation 3.4 (Luque, 2003):

$$IPCE = \frac{1240 \times Jsc}{\lambda \times \Phi} \times 100\% \qquad \text{Eq. 3.4}$$

where λ is wavelength (nm) of the illuminated light and ϕ is the monochromatic light intensity. The latter is measured at each wavelength using a calibrated power meter. Note that J_{sc} in this equation refers to the J_{sc} measured at that specific wavelength.

IPCE values are dependent on three main processes that affect photon absorption, electron injection and electron collection on the substrate (TiO_2) nanocrystalline films. These parameters are formulated in Eq. 3.5:

$$IPCE(\lambda) = LHE(\lambda)\, \phi_{inj}\, \eta_c \qquad \text{Eq. 3.5}$$

where LHE(λ) is the light harvesting efficiency at the desired wavelength, ϕ_{inj} is electron injection efficiency and η_c is charge collection efficiency (Nazeeruddin, 1993).

Light harvesting efficiency (LHE) for a surface sensitized with some adsorbed species is described in Eq. 3.6:

$$LHE(\lambda) = 1 - 10^{-\Gamma\sigma(\lambda)} \qquad \text{Eq. 3.6}$$

where Γ is the number of moles of sensitizer per square centimeter of projected surface area of the film and σ is the absorption cross section in units of $cm^2\ mol^{-1}$.

For surfaces where the sensitizers are not molecules that are adsorbed to the surface but are nanocrystals, this formula can be written as:

$$LHE(\lambda) = 1 - 10^{-A(\lambda)} \qquad \text{Eq. 3.7}$$

where $A(\lambda)$ is the absorbance of the sensitizer at specific wavelengths. From the absorption spectrum of a sensitizer, one may evaluate the capture of the photons by the sensitizer.

OCVD is a technique developed to study recombination processes on solar cells based on the sensitization concept (Zaban, 2003). According to Zaban et al., in this technique electron lifetime can be defined by the reciprocal of the first derivative of the photovoltage decay curve normalized by the thermal energy (Eq. 3.8):

$$\tau_n = (- k_B T/e) \times (dV_{oc}/dt)^{-1} \qquad \text{Eq. 3.8}$$

where τ_n is the electron lifetime, $k_B T$ is the thermal energy with k_B as the Boltzman constant and T as temperature, e is the positive elementary charge, V_{oc} is open circuit photovoltage and t is time.

Bisquert et al (Bisquert, 2004b) have shown that a graph of logarithm of τ_n versus V_{oc} is very informative and describes the order of the recombination reactions and discriminate between different available recombination processes. Typical OCVD curves are shown in Figure 3.5.

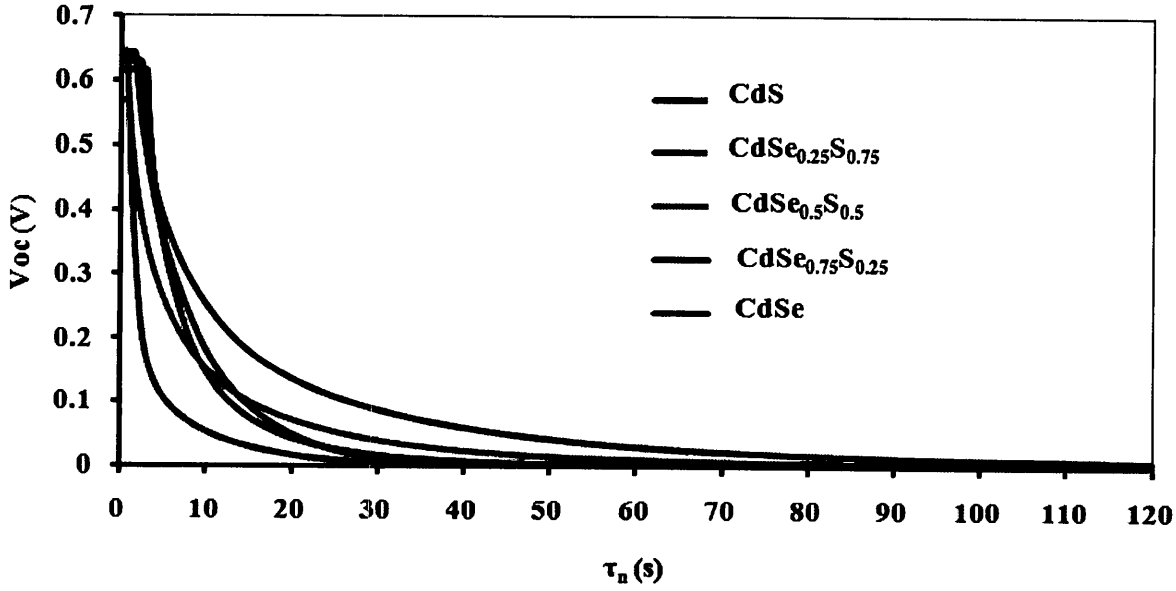

Figure 3.5. Typical OCVD curve (V_{oc} vs. τ_n) where one can see how fast electron are depleted from the CB of TiO_2 due to recombination and other electron capturing processes.

3.5 Scanning Electron Microscopy (SEM) and Energy Dispersive X-ray Analysis (EDX)

SEM analysis of the sensitized TiO_2 electrodes (either plain or sensitized with dyes or NBGS) is performed using Hitachi S4500 FESEM and elemental analysis of the electrodes is performed by 10 kV energy-dispersive beam (EDX) of the same instrument. For this purpose, all of the samples were covered with a thin layer of sputter-coated layer of conducting material (carbon or Au/Pd).

3.6 Powder X-ray Analysis

Powder X-ray diffraction (PXRD) measurements of the nanocrystals were performed by preparing the crystals in the bath of each composition where no TiO_2 substrate was inserted so that the effect of TiO_2 scattering will not block the signals from the $CdSe_xS_{(1-x)}$ crystals. After the formation of the crystals on the walls of the chemical bath, the crystals were scraped off and washed with copious deionized water, then with dry ethanol and finally with acetone where they were sonicated for 10 min. The powder was then left in ambient conditions for one hour to dry out and was subsequently kept under inert atmosphere in the dark to be analyzed with a Siemens D5000 theta/2theta diffractometer.

3.7 Atomic Absorption Spectroscopy (AAS)

To measure the amount of the sensitizing semiconductors on TiO_2, $CdSe_xS_{(1-x)}$ crystals were dissolved in 4% H_2O_2 (diluted from a 30% commercial solution, Merck) solution containing 3% of HNO_3 (diluted from a 65% commercial solution, p.a., Merck) at 65°C for 4 hours. An atomic absorption spectrometer (Perkin-Elmer 3110) was used to determine the amount of Cd in each of the resulting solutions.

The spectrometer was calibrated before each measurement, using six standard solutions of $Cd(NO_3)_2$.

3.8 Electrochemical Experiments

An Autolab electrochemical Analyzer (PGSTAT30, Eco Chemie BV, Netherlands) was used to record electrochemical measurements in a homemade three-electrode cell. Pt mesh acted as the working electrode whenever the dyes were dissolved in the solution. However if the electrochemical experiment was performed on the sensitized TiO_2 film, the working electrodes (dye-treated or bare TiO_2 films) were mounted in the cell by pressing them against an opening at the bottom of the cell using an O-ring seal (ca. 1 cm^2 area). In all measurements (in the solution or on the surface) the counter electrode was a large-surface-area Pt coil. The quasi-reference electrode was a Ag/AgCl wire (-0.045 V vs. SCE), and 0.1 M TBAP (tetrabutylammonium perchlorate) in dried acetonitrile was used as the electrolyte solution. The Ag/AgCl electrode was prepared by applying a 0.5mA cm^{-2} current to a 0.5 mm-diameter silver wire immersed in 1 M HCl until a brownish AgCl coating appeared. It was aged for a few days in distilled water before use and kept in water (Shoemaker, 1981). All potentials were converted to that of the normal hydrogen electrode (NHE), for clarity. Ferrocene was added to the solutions after each set of experiments to act as an internal standard for adjusting the potentials with the standard potentials found in the literature. Prior to all electrochemical measurements, the cells and electrolyte solutions were purged with a stream of ultra-high purity $N_2(g)$ for at least 30 min.

3.9 Thin Layer Chromatography (TLC) Experiment of the HTM materials

In order to ensure that the performance of our HTMs was not related to the presence of some hydrolysis products, and also to evaluate the significance of the presence of OTIPS groups for the function of the HTM molecules, we hydrolysed compound **1** and **2**. By hydrolysis, the OTIPS and O-methyl groups will be removed and there is –OH group left. The hydrolysis product was used to prepare an HTM solution and it was used to fabricate DSSCs. The effect of hydrolysis was monitored as follows: a 0.26 M solution of **1** or **2** was prepared in dichloromethane (DCM). A volume of 0.50 mL of this solution was transferred into a glass vial and 2.00 mL of 0.1 M HCl was added. The mixture was shaken for ca. 15 minutes and the aqueous layer was then decanted. A fresh portion of the HCl solution was then added to the vial and again shaken for ca. 15 minutes. After the aqueous solution was decanted, the HTM solution was kept in a sealed glass vial for subsequent use. In order to compare the TLC of the resulting solution to that of the non-hydrolyzed compounds, TLC were performed with a solvent mixture of chloroform and ethylacetate (9:2 v:v). Evidence of hydrolysis was detected from TLC after the first cycle of exposure to HCl.

3.10 Density Functional Theory (DFT) Calculations

DFT calculations were performed at Prof. Bender's lab at University of Toronto by using SP06 for Windows. Geometry optimizations were carried out using the Becke-Lee-Yang-Parr exchange correlation function (S11) with a 6-31G(D) basis set.

Chapter 4: Dye-Sensitized Solar Cells; Effect of Dye Structure and Functionality on the Cell's Performance

In this chapter, the effect of the structure of the sensitizing terpyridine and dipyrazinylpyridine dyes on the performance of the cells is discussed. As mentioned previously these compounds were synthesized in Prof. Potvin's lab at York University, Toronto, and were fully characterized in that lab (Stublla, 2010). In this study, eight dyes were studied for their photoelectrochemical characteristics. The structures of the tpy and dpp Ru(II) complexes applied to sensitize TiO_2 films are shown in Figure 4.1. The tpy-containing dyes are denoted according to the type of anchoring group (R in Figure 4.1). Those with phenylene spacers are denoted H**1** and Et**1** (with carboxylic acid group and with ethyl ester anchoring groups, respectively), while those lacking a phenylene spacer are analogously denoted H**2** and Et**2**, respectively. In the same manner, the dpp dyes are denoted H**3** and Et**3** with a spacer, and H**4** and Et**4** without a spacer. The following sections present physical characterization data, specifically their UV-visible and infrared spectra, as well as measurements of surface coverage and of their electrochemical, photoluminescence and photoelectrochemical properties. Both dye coverage and photoluminescence measurements were performed for selected dyes in solution as outlined in the chapter 3.

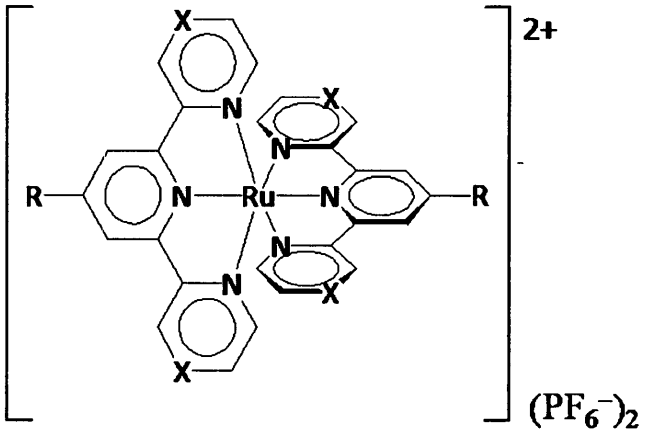

H1 X = CH, R = C_6H_4-4-COOH
H2 X = CH, R = COOH
H3 X = N, R = C_6H_4-4-COOH
H4 X = N, R = COOH
Et1 X = CH, R = C_6H_4-4-COOEt
Et2 X = CH, R = COOEt

Figure 4.1. Structures of the dye molecules.

4.1 UV-visible absorption, infrared spectroscopy, luminescence and lifetime measurements

All eight dyes displayed good light absorption behaviours both in solution and when adsorbed on TiO_2 (Figure 4.2a and 4.2b) (Stublla, 2010). Upon adsorption, there was very little change in the UV-visible absorption maxima (peaks at 480 nm were observed for the dpp dyes Et4 and H4, while the other dyes absorbed at 490 nm) corresponding to negligible red shifts (ca. 4 nm) compared to those measured in solution – too small to be ascribed to dye aggregation on the surface. A small amount of peak broadening was observed, but this can be expected from the electronic effects induced by neighboring molecules on the surface. The extinction coefficients obtained

with the tpy ligands were systematically higher than those with the dpp ligands (see Table 4.1). The absorption bands near 490 nm had been assigned to MLCT transitions from Ru(4d) orbitals to ligand-centered π* orbitals.

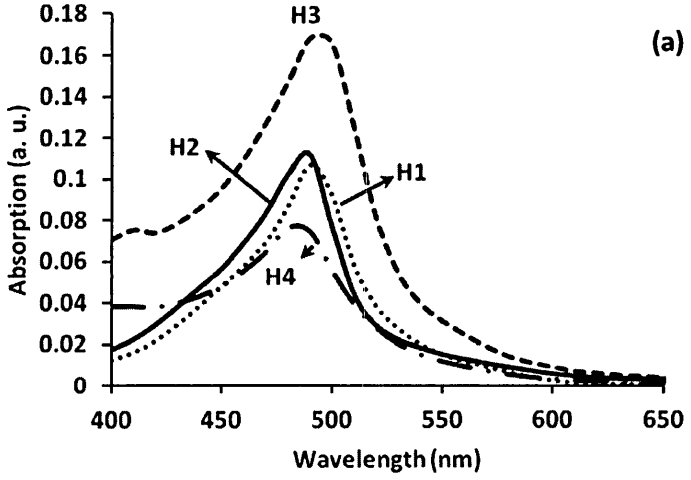

(a)

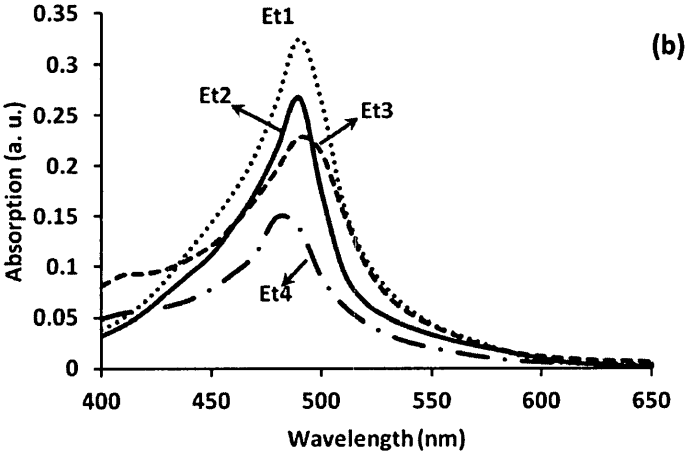

(b)

Figure 4.2. UV-visible spectra of **a)** carboxylic acid-functionalized and **b)** ester-functionalized dyes on TiO_2.

According to DFT computations these ligand-based π* orbitals are mainly located on the central pyridine rings in the tpy cases, as they are the least electron-rich owing to the flanking pyridine rings and these electron-withdrawing anchoring groups (Stublla, 2010). However, there is significant delocalization over the pyrazine rings in the dpp

cases, owing to the additional nitrogen atoms. The location of the π* orbital is one of the dominant factors affecting the efficiency of photosensitization, since it can affect the electron transfer efficiencies to the Ti(3d) orbitals. Effective overlap of the Ti(3d) and dye (π*) orbitals and the respective energy levels of the two is of significant importance. This will be discussed further in later sections.

Table 4.1 Dyes absorption, emission characteristics and surface concentrations on TiO_2

Samples	Absorption λ_{max}/nm ($\varepsilon_{max}/10^4\ M^{-1}\ cm^{-1}$)	Emission λ_{max} (nm)	Normalized[a] Emission Intensities	Surface Concentration[b] (nmol cm^{-2})
Et**1**	490 (2.60)	664	0.312	8.7 (11.0)[b]
H**1**	490 (2.76)	671	0.257	39.4
Et**2**	490 (2.26)	662	0.462	12.5 (22.4)[b]
H**2**	490(2.00)	654	0.347	49.3
Et**3**	490(2.00)	665	0.134	9.4 (13.9)[b]
H**3**	490 (1.43)	652	0.167	19.6
Et**4**	480 (1.25)	644	0.262	12.3 (20.0)[b]
H**4**	480 (1.612)	635	0.268	35.7
N3	540 (1.42)[c]	755[c]		89.5

[a] Normalized with respect to the concentration of H**1**.
[b] Surface concentrations of dyes after sensitization at room temperature and, in parentheses, in warm dye solutions.
[c]These values are obtained from Nazeeruddin (1993).

The luminescence spectra of the dyes were measured in solution (Figures 4.3a and 4.3b) and the emission maxima are reported in Table 4.1, as well as the normalized emission intensities. The emission intensities are normalized with respect to the concentration of H**1** solution used in the measurements. The maximum emissions for all

dyes lay between 635 and 671 nm. These will be used to calculate the energy gaps of the dyes in the following section.

The extent of dye attachment to the TiO_2 surface was also monitored using UV-visible spectroscopy by desorbing the dyes from the TiO_2 surfaces and evaluating the dye concentrations in the desorption solutions (see material and methods Section). Table 4.1 also reports the dye surface concentrations. It is clear from these measurements that the dyes bearing carboxyl groups (H**1**, H**2**, H**3** and H**4**) were the most extensively attached, with surface concentrations varying from 19.6 to 49.3 nmol cm^{-2}, as calculated from the geometric areas of the sample.

When deposited under the same conditions, the dyes bearing ester anchoring groups (Et**1**, Et**2**, Et**3** and Et**4**) gave significantly lower surface concentrations (8.70-12.5 nmol cm^{-2}) but these values nearly doubled when the TiO_2 films were sensitized in warm solutions of the dyes (see Table 4.1). The adsorption mechanism and the heat effect will be discussed in following sections.

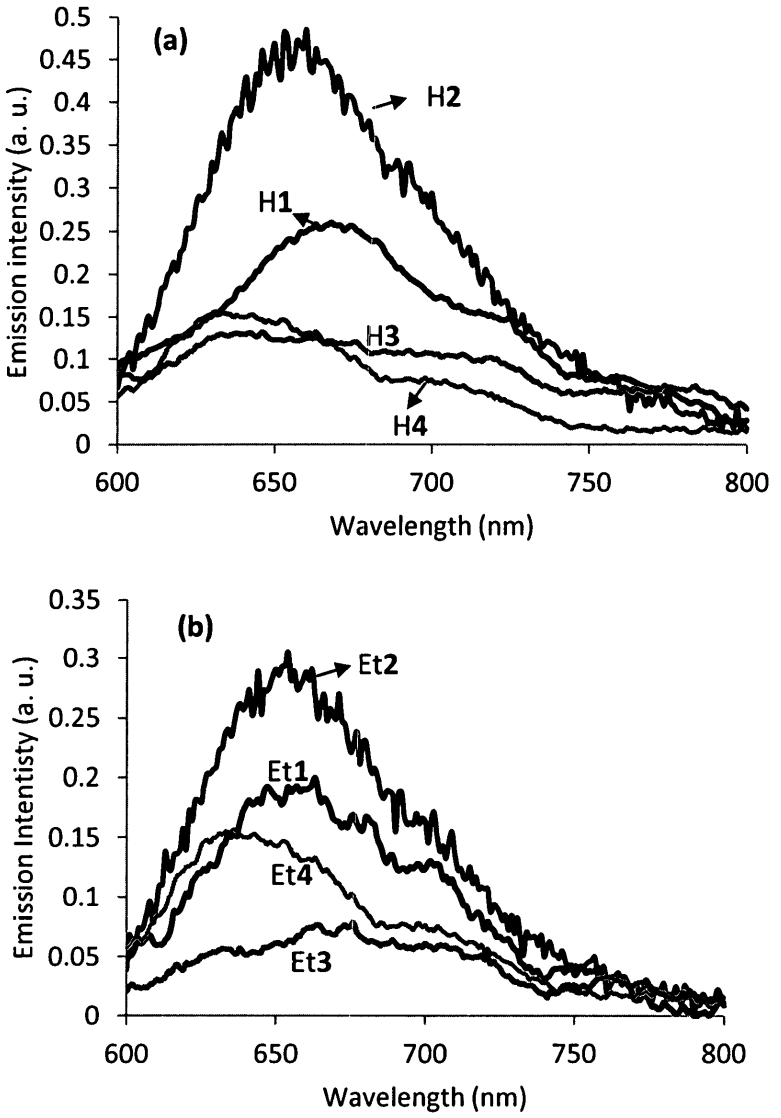

Figure 4.3. Emission intensity spectra normalized of **a)** carboxylic acid-functionalized dyes normalized with respect to the concentration of H**1** **b)** ester-functionalized dyes normalized with respect to the concentration of Et**1**. The maximum excitation wavelengths are given in Table 4.1.

FTIR measurements give information on the mode of attachment of the dyes at the surface. It was expected for both carboxylic acid and ester anchoring groups that

mainly one side of the complex will chemically react with oxygen vacancies or via ligand exchange at the TiO_2 surface. The FTIR spectra are shown in Figures 4.4a and 4.4b for carboxylic acid and ester anchoring groups, respectively. The pure compounds with carboxylic acid groups displayed characteristic bands at ca. 1690 cm^{-1}, due to the conjugated C=O stretch in the carboxylic acid groups, as well as bands at ca. 1600 cm^{-1} and 1400 cm^{-1} due to asymmetric and symmetric COO^- stretches, respectively, owing to spontaneous deprotonation in solution (Vougioukalakis, 2010). Upon reaction with a TiO_2 surface, the acid C=O stretch was expected to decrease in intensity in favour of stronger COO^- stretches, due to the formation of coordinated anchoring groups at the surface. However, the relative intensities of these bands varied greatly, indicating different levels of surface coordination for each compound. Dyes H**2**, H**3** and H**4** displayed high levels of coordination (very large COO^-/COOH band intensity ratios). In contrast, dye H**1** showed a larger quantity of free carboxylic acid in the film as evidenced by the large COOH stretch in relation to the peak at 1610 cm^{-1}. Little change was observed in the symmetric and asymmetric carbonyl stretches between the spectra of pure dye and adsorbed dye. This could indicate that the anchoring group engages in bridging coordination with TiO_2, but could also indicate that this particular dye has a tendency to form aggregates at the surface (with poor anchoring) since this dye also showed high surface coverage (see Table 4.1) (Nazeeruddin, 2004; Cahen, 2000; Zhu, 2007).

The complexes with ester anchoring groups in pure state showed bands at ca. 1280 and 1720 cm^{-1} assigned to the C–O and C=O stretches, respectively (Vougioukalakis, 2010). Typically, the adsorption of ester-functionalized dyes onto TiO_2 at room temperature generated two new bands, at ca. 1700 and ca. 1630 cm^{-1}, which can be assigned to conjugated C=O in carboxylic salt, ester group or coordinated ester group to TiO_2 via the formation of Ti-O-C bonds. Upon exposing TiO_2 to a warm solution of ester-functionalized dyes, the band at ca. 1630 cm^{-1} was blue-shifted to ca. 1670 cm^{-1}. This could be assigned to a change in the coordination of the ester group to the TiO_2 during the heat treatment as a result of transesterification and also to changes in the symmetry of the molecules upon adsorption.

One important change is the large decrease in intensity of the C–O stretch at ca. 1280 cm^{-1} in spectra from the esterified dyes, which is consistent with transesterification. Overall, our results are in agreement with previous investigations of reactivity of ester binding groups to TiO_2 upon heating (Murakoshi, 1995).

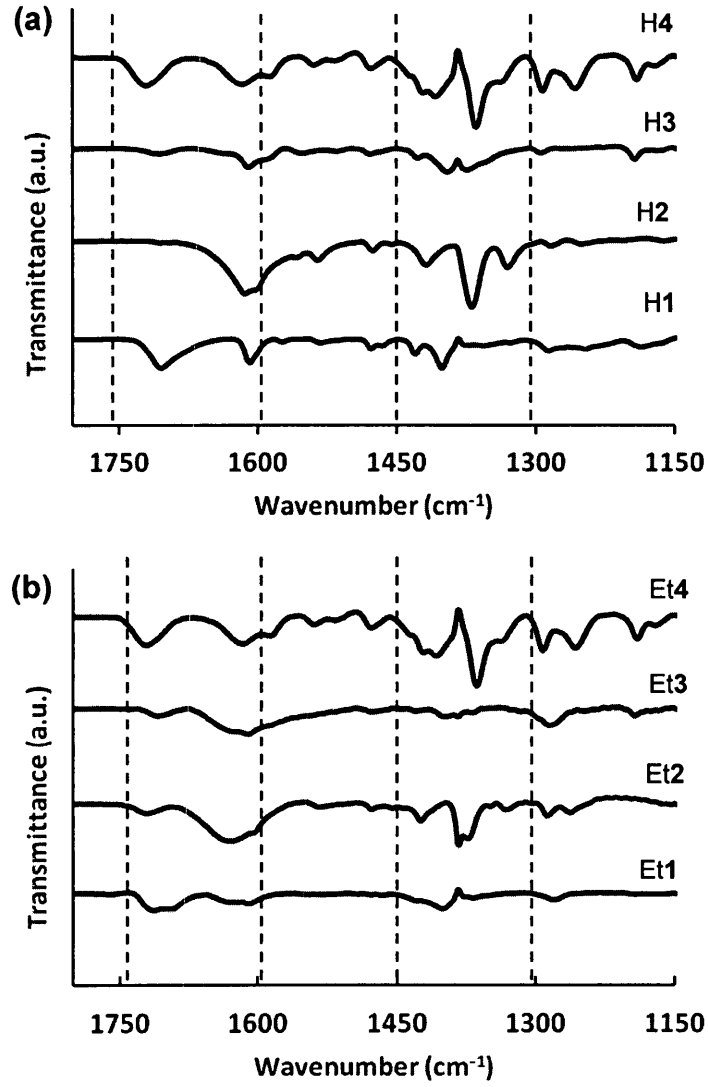

Figure 4.4. FTIR spectra of **a)** carboxylic acid-functionalized and **b)** ester-functionalized dyes on TiO_2.

The measured and fitted emission decay profiles for the representative Et**2** and H**3** dyes in acetonitrile solutions were measured at 670 and 645 nm, respectively, and are presented in Figure 4.5. The fitted excited state lifetimes τ were found to be similar (19.0 ± 1.5 ns with H**3** and 19.8 ± 1.5 ns with Et**2**). This is somewhat surprising, given that the homoleptic p-tolyl-substituted dpp complex analogous to H**3** (τ = 18 ns) showed

a significantly larger value than the p-tolyl-tpy analogue of Et**2** did (τ = 0.95 ns) in the same solvent. As has been noted with 'black dye', the tpy analogue of N3 (τ = 18 ns in fully protonated form), excited state lifetimes (and emission wavelengths) are sensitive to protonation states and subject to proton-induced quenching (Vougioukalakis, 2010; Barigelletti, 1993; Nazeeruddin, 2001). Given that surface OH groups may thus interfere, the τ values measured in solution are not directly indicative of the behavior of surface-bound states relaxation, and given that electron injection is far faster (fs timescale) than excited state decay (Anderson, 2004), the relationship between solution-state τ values and photovoltaic performance is not a simple one. While black dye has a shorter-lived excited state than does N3 (τ = 60 ns in fully protonated form) it is a better sensitizer (Gratzel, 2003). Nevertheless, these measurements demonstrate no significant difference in τ values between our dyes and black dye.

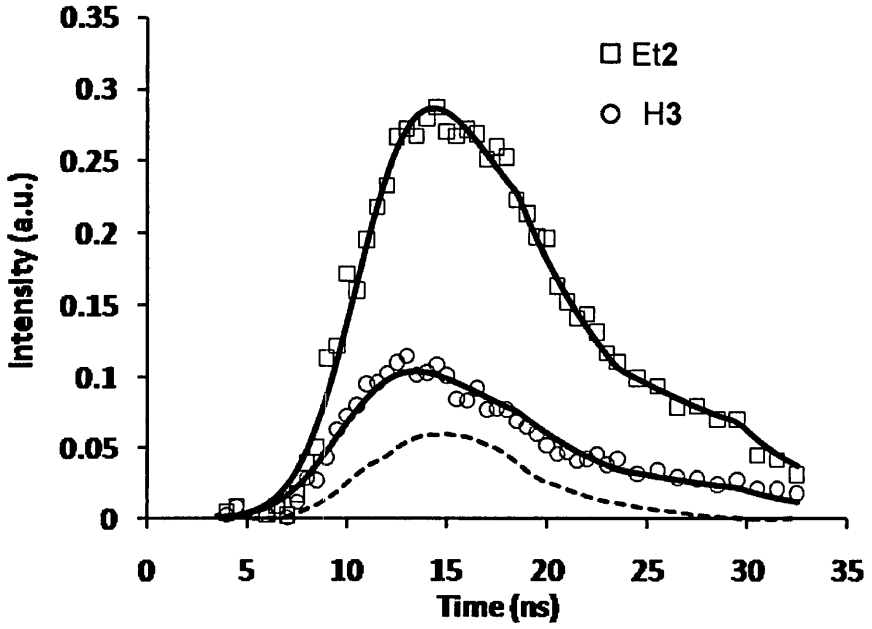

Figure 4.5. Emission decay curves for Et**2** (squares) and H**3** (circles), and the instrument response function for normalization (dashed line).

While all dyes studied have similar absorption spectra in the visible region, they behave quite differently in their capacity to attach to the TiO_2 surface. H**2**, which has two carboxylic acid anchoring groups, achieved the highest surface concentration. This can be explained by a faster adsorption kinetics and high equilibrium binding constant (ca. 1 x 10^5 M^{-1}) with the TiO_2 surface (Galoppini, 2004 and references therein). Only a marginal decrease was observed with a phenylene spacer present (in H**1**), but a larger decrease was observed when the ligand core was changed from tpy (in H**2**) to dpp (in H**4**), and a more significant decrease was caused by the presence of both a dpp core and a phenylene spacer (in H**3**). These results were completely reproducible. Based on the fact that the two classes of dyes have very similar size and charge, these factors cannot

be invoked to explain this behavior. However, both molecules generally differ in solubility, possibly owing to π-π interactions that may cause aggregation in solution and poor attachment to the surface and difficult pore penetration. Replacing carboxyl anchoring groups with ester groups resulted in poorer dye attachment at room temperature. However, this was improved after warming the dye solutions. Although higher temperatures lead to faster mass transport and adsorption kinetics, the FTIR data suggested that heat promoted transesterification reactions with surface OH groups, which would indeed result in higher loadings. These results are in agreement with studies of other dyes bearing ester anchoring groups (Murakoshi, 1995).

In this study, TiO_2 was also sensitized with N3, a highly performing dye, and its properties are included in Table 4.1 for comparison. Although our dyes show comparable or higher extinction coefficients than that of N3 or black dye, the N3 and black dye absorption envelopes are much broader and have red-shifted maxima (Gratzel, 2005; Nazeeruddin, 2001). The surface concentration for our best-performing dye, H**2**, is roughly half the value obtained with N3, indicating that having more anchoring groups (four in N3 versus two in H**2**) makes a large difference in the surface-binding ability and, no doubt, on stability. In addition, a higher surface concentration of the dye results in a greater suppression of the recombination routes at the electrolyte/anode interface and thereby allowing for a more efficient injection process to compete with the decay/quenching routes (Nazeeruddin, 1993; Hodes, 2008;

Marinado, 2010). This is in addition to the blocking role of *tert*-butyl pyridine (TBP) added in the electrolyte solution.

4.2 Electrochemical measurements of dyes on TiO_2

Using electrochemical data such as the oxidation potential and the onset of photoluminescence, one can evaluate the position of the HOMO and the lowest excited state energy of the dyes. Representative cyclic voltammograms for the adsorbed dyes on TiO_2 are given in Figure 4.6a and 4.6b and their oxidation potentials are listed in Table 4.2. Dyes H**3**, H**4** and Et**4** (Figure 4.6) display irreversible redox behavior at potentials greater than ca. 1.7 V versus NHE while, for the others, quasi-reversible behavior is observed, i.e. the difference between anodic and cathodic peaks ($Ru^{II} \leftrightarrow Ru^{III}$) were ca. 50 to 200 mV. Similar behavior was observed in solution (Stublla, 2010). The oxidation potentials of tpy complexes of Ru are always less positive than those of dpp analogues, owing to the electron-withdrawing effect of the pyrazine rings (Liegghio, 2001; Al-mutlaq, 2007). However, comparison of these dyes with unsubstituted complexes reveals oxidation potentials shifted positive due to the presence of electron-withdrawing carboxylic acid and ester groups (Maestri, 1995). The $Ru^{III/II}$ oxidation potentials on TiO_2 films, the energy levels of the HOMO and lowest excited state (LUMO), derived from the oxidation potentials and luminescence data, are reported in Table 4.2 in comparison with corresponding values with N3. The HOMO of the dyes is calculated according to the redox potentials of the molecules and the LUMO is

calculated by considering the energy gap (Gap in the table 4.2) between HOMO and LUMO as the energy equivalent to the maximum emission.

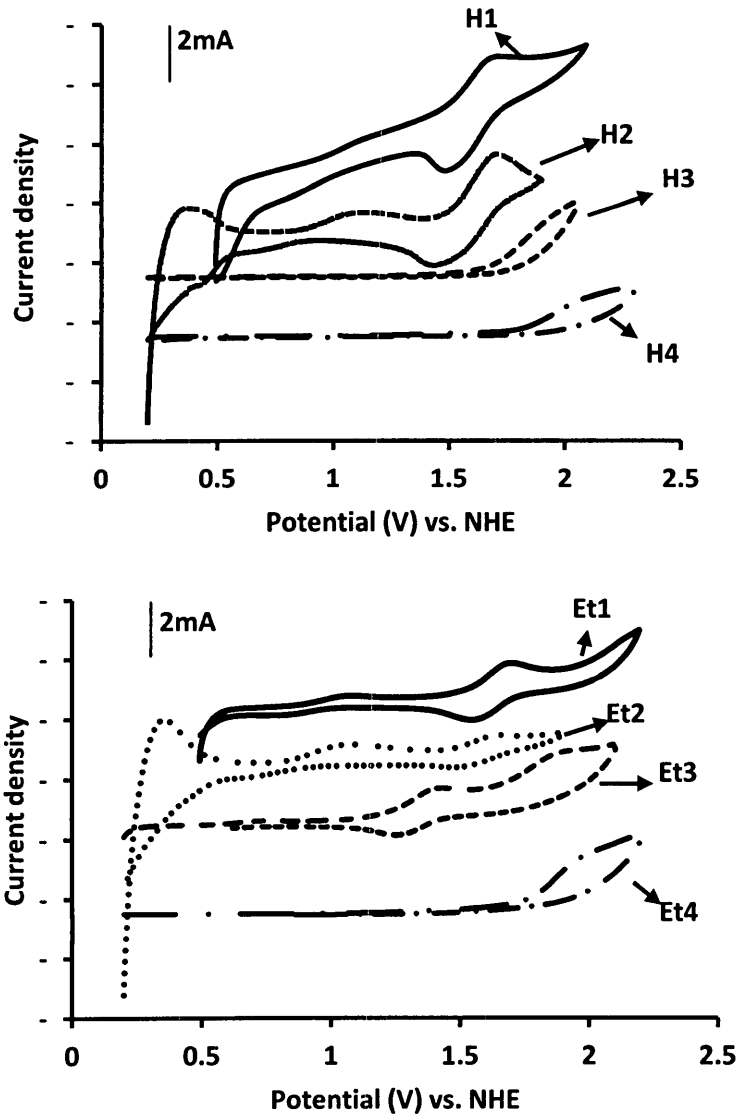

Figure 4.6. Cyclic voltamograms of **a)** ester- and **b)** carboxylic acid-functionalized dyes on TiO_2.

An energy level diagram was constructed from these data (Figure 4.7), and included for comparison are the energy levels of the I^-/I_3^- redox couple and of the TiO_2 valence and conduction bands (CB). The energy difference between the photoexcited states and CB levels can be considered as the driving force for electron injection from an excited dye to TiO_2. So the higher the difference, the bigger the driving force would be, which consequently results in higher electron-injection efficiency. The excited state levels of the tpy dyes (e.g. -0.15 eV vs. NHE for Et**2**) are more negative than those of the dpp dyes (e.g. 0.12 eV vs. NHE for Et**3**), but all are significantly more positive than the value for N3 (-0.58 eV vs. NHE). Consequently, even though our dyes have higher molar absorption coefficients than N3, their conversion efficiencies are expected to be lower than that achieved by N3 (Figure 4.7).

Table 4.2. HOMO and LUMO levels for the dyes.

Dye	E_{ox}(V) vs. NHE (HOMO levels)	Gap (eV)	LUMO (V) level vs. NHE
Et1	1.54	1.87	-0.33
H1	1.51	1.85	-0.34
Et2	1.72	1.87	-0.15
H2	1.82	1.90	-0.07
Et3	1.98	1.86	0.12
H3	2.00	1.90	0.10
Et4	2.12	1.93	0.19
H4	2.15	1.95	0.20
N3	1.10[a]	1.68[a]	-0.58[a]
TiO_2	3.00(Valence Band)a	3.2[a]	-0.2(conduction band)a

[a]The values needed for the gap and LUMO calculations were obtained from Nazeeruddin (1993).

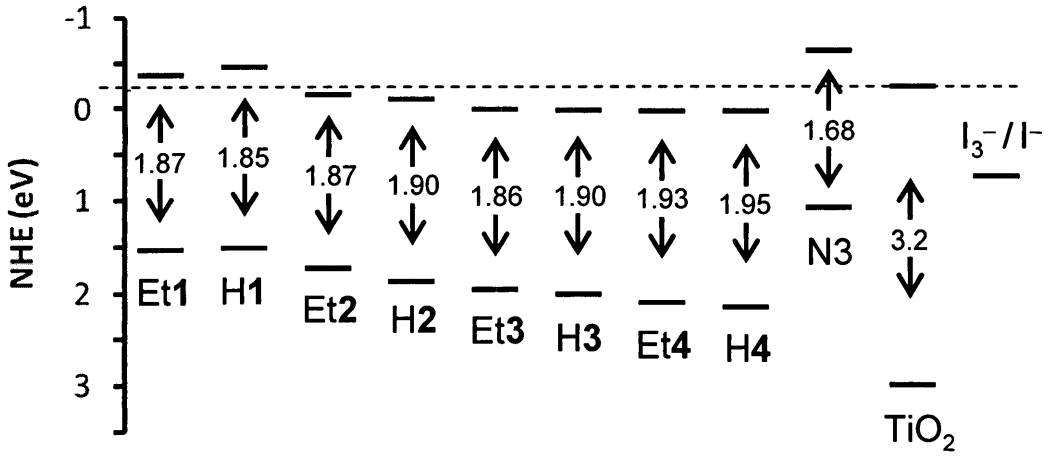

Figure 4.7. Energy diagram relating the HOMO and LUMO levels of the dyes and TiO_2, the HOMO-LUMO gaps and the triiodide/iodide redox couple.

4.3 Photoelectrochemical performances of DSSCs

The DSSC photovoltaic performance of our dyes ws measured and the resulting current-voltage curves are presented in Figure 4.8. Table 4.3 presents the relevant photoelectrochemical parameters. Several electrolyte compositions were tested in order to optimize the cell performance. The best electrolyte was then chosen for further characterizations; electrolyte **A** for cells prepared with H and Et dyes and electrolyte **B** for cells prepared with N3 (see chapter 3 for more detail).

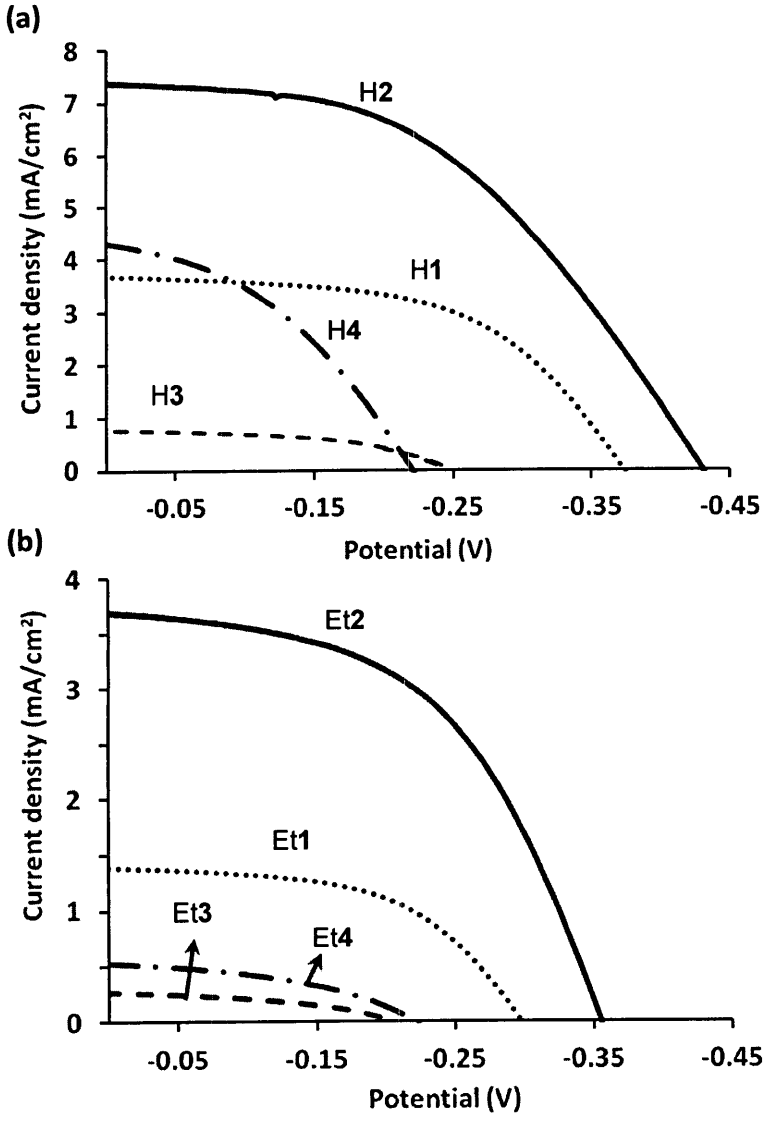

Figure 4.8. Photoelectrochemical i-V curves of **a)** carboxylic acid-functionalized and **b)** ester-functionalized dyes.

It is clear from the data that **H2** is the most efficient sensitizer of the two series. Indeed, the efficiencies of the DSSCs prepared with tpy dyes are significantly (i.e. 4 times) higher than those of the dpp dyes. In addition, the carboxylic acid dyes were more efficient than the ester analogues. While warming the ester-functionalized dye solutions can improve their adsorption on TiO_2 surfaces (Table 4.1) and consequently improve the photo-current, their overall efficiency remains lower (Table 4.3). Thirdly, the presence of a spacer between the anchoring group and the ligand core was uniformly deleterious, in part because of the lower surface concentrations (Table 4.1).

IPCE curves were also recorded for each dye (Figure 4.9). These data parallel our observations of dye performance: For instance, the IPCE of dye **H2** is 2.5-fold higher than that of dye **H1**. This cannot be solely due to a higher surface concentration of **H2** since the energy of the excited level of dye **H2** is slightly lower than the CB level of TiO_2 while the corresponding level of dye **H1** lies higher. Also **H1** has stronger absorption coefficients which in turn increases its light-absorbing compared to **H2** (Table 4.1).

Table 4.3. Summary of the performance of TiO_2 DSSCs using tpy and dpp dyes and electrolyte **A**. The values belong to the cells with the best efficiencies.

Dye	V_{OC} (mV)	J_{SC} (mA cm^{-2})	*ff*	η (%)	IPCE (%)
Et**1**	298	1.39	0.56	0.23	12.81
H**1**	766	3.68	0.56	0.77	13.84
Et**2**	355	3.69	0.53	0.70	15.94
H**2**	429	7.43	0.49	1.56	34.71
H**2**[a]	461	1.18	0.55	0.3	5.25
Et**3**	201	0.27	0.42	0.02	4.89
H**3**	246	0.79	0.49	0.10	4.89
Et**4**	214	0.53	0.43	0.05	7.97
H**4**	222	4.32	0.40	0.38	15.02
N3[a]	729	17.89	0.51	6.12	50.10

[a]For these samples, the cells were prepared with electrolyte **B**.

We may conclude that the higher IPCE value of H**2** is due to a more efficient electron transfer from the excited state of the dye to the CB of TiO_2 and that the phenylene spacer of H**1** is hindering this electron transfer step. Indeed, DFT and crystallography have shown that phenylene spacers are twisted out of coplanarity with the central pyridine rings, thus interrupting the π-conjugation and communication between anchoring group and chromophore (Stublla, 2010).

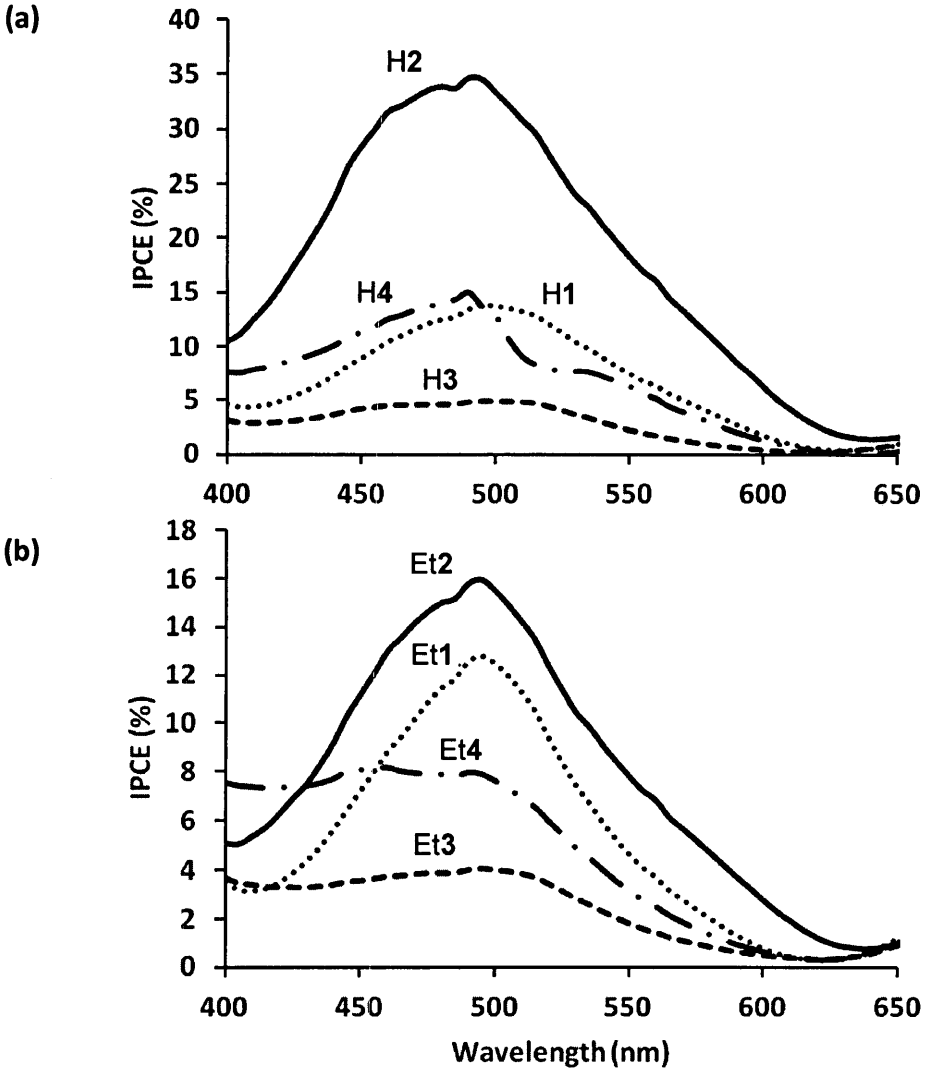

Figure 4.9. IPCE curves of dyes with **a)** carboxylic acid and **b)** ester anchoring groups. Wavelength sweep rate: 5nm s^{-1}.

4.4 Effect of the Electrolyte Solution

It should be noted here that our DSSC performed much better in I^-/I_3^- electrolyte lacking TBP (electrolyte **A**), whereas the opposite was true with N3, i.e. its cell performance increases in the presence of TBP (electrolyte **B**). The latter is in accord with

previously published work (Haque, 2005). For all our dyes, we have observed a several-fold increase in efficiency when electrolyte **A** was used instead of **B**. For example, the efficiency (η) of a TiO_2/H**2** photoanode was increased 9-fold. To understand the influence of TBP on our dyes' performance, dark currents for bare and H**2**-sensitized TiO_2 films were measured using different electrolyte solutions. Figure 4.10 shows a plot of the dark current as a function of potential for a bare TiO_2 film. The dark current is observed to decrease in the presence of TBP, indicating that TBP decreases the electron recombination rate.

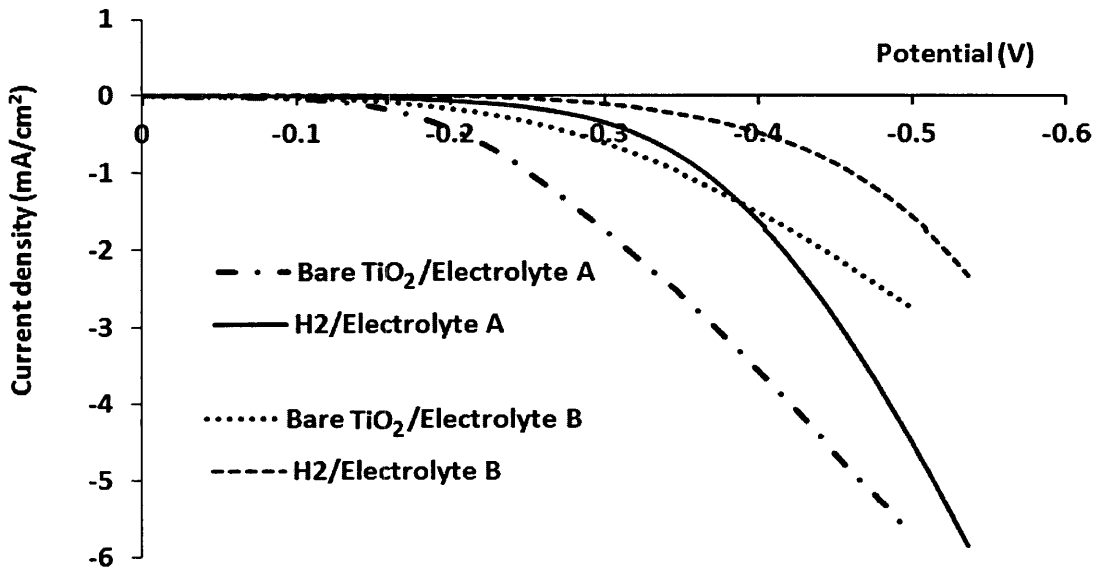

Figure 4.10. Dark current as a function of potential for bare and H**2**-sensitized TiO_2 films.

The same effect was found with TiO_2 films sensitized with H**2** (Figure 4.10). One can conclude that TBP is deleterious to η despite a useful suppression of dark currents. The influence of electrolyte composition on the conduction band of the semiconductor has been investigated by different groups (Haque, 2005; Hara, 2005; Yin, 2007). The accepted explanation for this is that components of the electrolyte shift the conduction band/trap states in the nanocrystalline TiO_2 films, where the lithium ions (Li^+ from lithium iodide added in the electrolyte solutions) cause a shift to more positive potentials whereas TBP shifts them to more negative potentials (Haque, 2005; Hara, 2005; Yin, 2007). As stated earlier, our dyes' LUMO levels lie close to or below the CB level, such that a negative shift of the CB level will retard electron injection from the excited dyes. On the other hand, Li^+ will be beneficial to electron injection, and there will be a lower energy loss during this process. As a result (Figure 4.8), the photocurrent was 12-fold higher in the electrolyte lacking TBP. Higher electron-injection efficiencies were also confirmed by IPCE measurements in the absence of TBP (Figure 4.9 and Table 4.2).

The quantitative contribution of TBP to V_{oc} values is reported to be a function of the degree to which the TBP dipole moment causes a change in the CB level. Ruhle and co-workers (Ruhle, 2005) have reported that the V_{oc} values of TiO_2 DSSCs varies linearly with the dipole moment of co-adsorbed molecules by 6-9 mV D^{-1} (D is the dipole moment of the molecule), and Kusama and co-workers (Kusama, 2008) reported that nitrogen-containing heterocycles like TBP shifted the CB by 10 mV D^{-1}. Since the dipole

moment of TBP is 2.95 D, one can calculate a ΔV_{oc} due to TBP of approximately 30 mV, in good agreement with our experimental value of 31 mV, obtained from the V_{oc} values measured in the presence (461 mV) and absence of TBP (429 mV) for a TiO_2 film sensitized with dye H**2** (Kusama, 2008).

4.5 Conclusion

In summary, newly designed and synthesized homoleptic Ru(II) complexes containing terpyridine (tpy) and dipyrazinylpyridine (dpp) ligands were used to sensitize TiO_2 in DSSCs and to investigate the effect of structural parameters on the photoelectrochemical properties of the dyes. The excited state lifetimes for both types of complexes were found to be similar. Due to electron-withdrawing effects, the $Ru^{III/II}$ oxidation potentials of all the dyes studied in this work lie positive relative to N3. Photovoltaic measurements showed that the tpy dyes functionalized with carboxylic acid groups have higher total solar conversion efficiencies than those of the dpp dyes or those with ester groups. The presence of a phenylene spacer between the chromophore and the anchoring group did not improve the efficiency, presumably because of poorer π communication between the central pyridine rings and the anchoring group. The role of TBP in the electrolyte solution has been quantitatively assessed. Under the best conditions, the total solar conversion efficiency of TiO_2 films sensitized with dye H**2** can reach 1.56%.

Hence, lower LUMO levels, higher symmetry and lower surface coverage all contributed to the performance of these dyes. Currently, we are examining asymmetric Ru(II) dyes containing only one tpy ligand and have no phenylene spacer for which we can expect higher total solar conversion efficiencies.

Chapter 5: Hole-Transport Materials: Silicon-Based Triarylamines as Redox Mediators in Dye-Sensitized Solar Cells

In this chapter of my thesis, I will demonstrate our work on employing a new class of triarylamine compound functionalized with bulky triisopropylsilyl ether (OTIPS) groups as a hole transport material (HTM) in dye-sensitized solar cells (Figure 2.7). An O-methyl (-O-CH_3) derivative of these compounds is also used as HTM to evaluate the structural impact of the HTM on the performance of the cells. The results were compared to the cells prepared by using the conventional I^-/I_3^- redox couple. We obtained high values of open circuit potential (> 0.8V) and efficiencies of up to 1.24% when using the silyl ether substituted compound in DSSCs, while cells without the OTIPS functionalization performed very poorly, pointing to the importance of OTIPS in the performance of this material.

As it was mentioned before the HTM compounds (*N*, *N*, *N'*, *N'*-tetra(4-triisopropylsilyl ether)phenyl)1,4-phenylenediamine (compound **1** also abbreviated as 1,4PDATIPS) and *N*, *N*, *N'*, *N'*-tetra(4-methoxy)phenyl)1,4-phenylenediamine (compound **2** also abbreviated as 1,4PDA)) are prepared in Prof. Bender's lab at University of Toronto, Department of Chemical Engineering and Applied Science (Figure 2.7) and fully characterized (Kamino, 2011).

The HTM solutions are used as electrolytes in nanoporous TiO_2 N3- or Z907-sensitized solar cells. The detail cell fabrication can be found in chapter 3. It is noteworthy that due to the general properties of HTM materials and their usually larger recombination rates, thinner TiO_2 films (2μm) are used for these experiments.

Dye Z907 (Figure 3.1) was chosen due to its long alkyl chain attached to one of the dipyridine groups, which makes it more hydrophobic compared to N3. This property may have an effect on how the dye molecule interacts with HTM when charge carriers are being transferred, impacting the performance of the DSSC. In addition, it has previously been shown that the presence of an alkyl chains can supress recombination between sensitizer and redox couple by altering the kinetics of charge separation (Burschka, 2012).

5.1 Photoelectrochemical Results

Tablet 5.1 shows the PEC results of the best performing cells prepared by using compound **1** as the redox mediator. Cells fabricated with I^-/I_3^- are also tested with TiO_2 films prepared under the same conditions for comparison.

Table 5.1. DSSC composition, current-voltage characteristics under illumination and performance for our best cells.

Cell Composition: dye/electrolyte	V_{oc} ± 0.1 mV	J_{sc} ± 0.04 mA cm^{-2}	*ff* ± 0.1%	Efficiency ± 0.1%	Thickness ± 0.05 μm	[Dye] on TiO_2[a] × 10^{-8} mol cm^{-2}	IPCE[b] %
N3/**1, 4PDATIPS**	-899	3.46	59.7	1.9	1.47	6.1 ± 0.4	21 ± 1
Z907/**1, 4PDATIPS**	-857	2.72	66.2	1.5	1.91	7.5 ± 0.3	18 ± 1
N3/ I_3^-,I^-	-786	5.95	61.3	2.9	1.65	6.8 ± 0.2	20 ± 1
Z907/ I_3^-,I^-	-778	8.33	41.6	2.7	1.42	5.8 ± 0.2	19 ± 2

[a]Dye concentration values are the average of values obtained from three samples.
[b]IPCE values are the average of a minimum the IPCE of three different cells.

Cell fabricated with **1** using N3 on nanoporous TiO_2 exhibited very high values of photovoltage (V_{oc}), i.e., more than ca. -900 mV on average (Figure 5.1 shows the i-V curves for the data given in Table 5.1 additional data such as i-V curves for all samples are also given in Figure 5.2). For some cells with the same configuration, V_{oc} values of more than 1 V were achieved (Figure 5.2 and Table 5.2). This large increase over cells constructed with I^-/I_3^- is mostly attributed to the higher redox potential of **1** (E_{redox} = 0.621 V vs. NHE) compared to that of I^-/I_3^- (E_{redox} = 0.480 V vs NHE) (Kamino, 2011; Oskam, 2001). Because Voc is partially determined by the potential difference between the Fermi level of TiO_2 and redox potential of the electrolyte, we find that **1** is able to generate superior photovoltages (Lambert, 1999; Cahen, 2000).

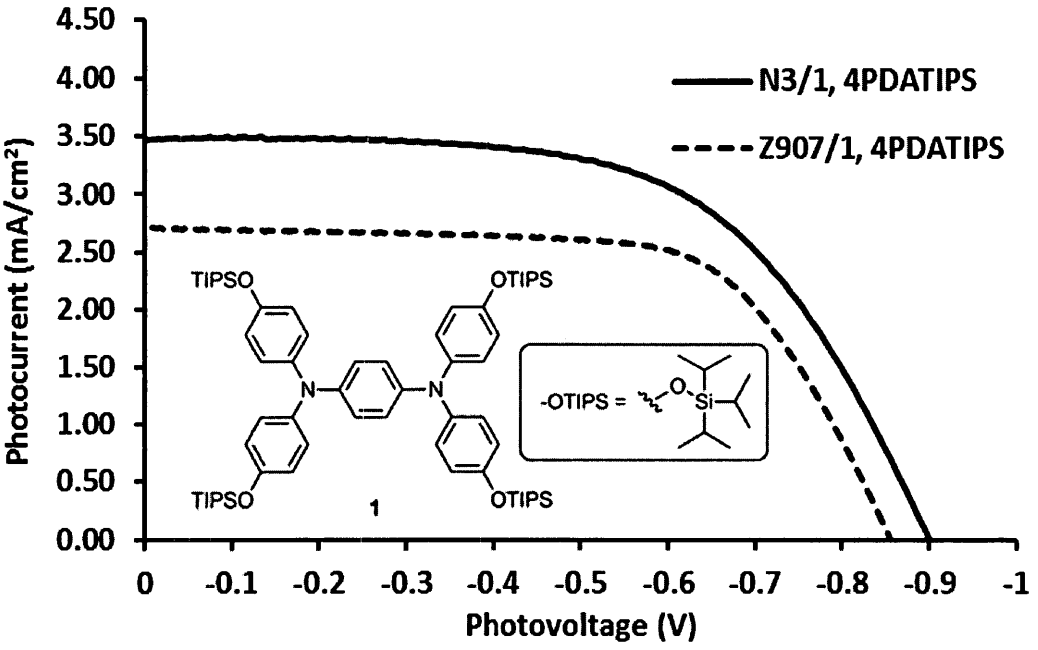

Figure 5.1. Photoelectrochemical i-V curves for our best cells prepared with N3 (solid line) and Z907 (dashed line) sensitized TiO_2 film and a solution of **1** as HTM. Insert: structure of compound **1** (see also Table 5.1).

a)

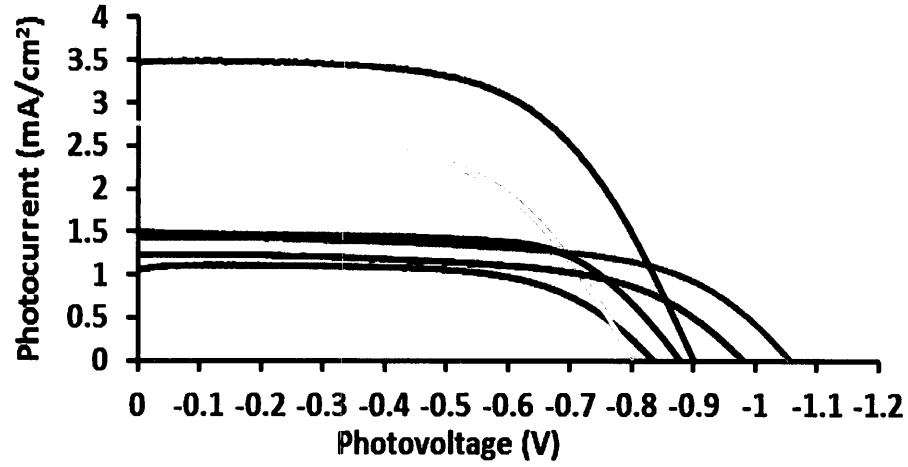

b)

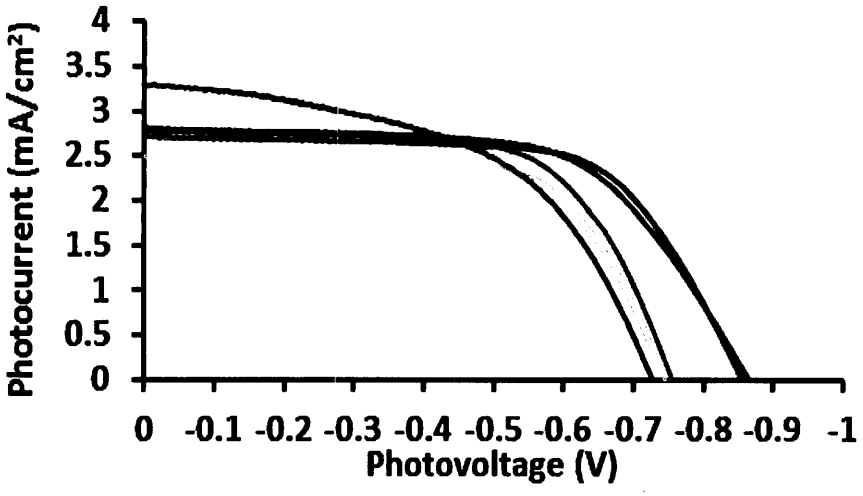

Figure 5.2. Photoelectrochemical i-V curves for all **a)** N3 and **b)** Z907 sensitized solar cells fabricated with thin TiO_2 film and using a solution of **1** HTM as redox mediator. The experimental condition is the same for all the samples. All the measurements are shown in order to show the large V_{oc} values obtained in all measurements.

Comparing the effect of the sensitizer on the performance of **1**, we find that there is little effect of the nature of the sensitizer on the cell efficiencies. On average efficiencies of ca. 1.23% are obtained when N3 or Z907 are used (Table 5.2). A closer

inspection of the average data indicates that the J_{sc} value for Z907/**1** is higher than that of N3/**1** (Table 5.2). This is mainly explained due to the slightly thicker TiO_2 film used in Z907 cell, which consequently had more adsorbed dye on the surface and hence higher photocurrent density (J_{sc}) (average thicknesses are shown in Table 5.1). The significantly high V_{oc} value in N3 DSSCs (ca. -900 mV) is balanced out by the higher J_{sc} of Z907 DSSCs and improved the overall efficiency of the latter cells. These PEC results confirm that **1** can successfully regenerate both N3 and Z907, indicating that **1** functions as a successful redox couple with both dyes.

Table 5.2. DSSC composition, characteristics and performances (average values) for cells prepared with compound **1**; actual i-V plots are given in Figure 5.2.

Cell Composition: dye/electrolyte	V_{oc} (mV)	Jsc (mA cm^{-2})	*ff* (%)	Efficiency (%)	Thickness[a] ± 0.05 μm	(Dye) on TiO_2[a] $\times 10^{-8}$ mol cm^{-2}
N3/**1**, **4PDATIPS**	-910 ± 74	1.9 ± 0.8	61 ± 3	1.0 ± 0.3	1.47	6.1 ± 0.4
Z907/**1**, **4PDATIPS**	-789 ± 55	2.8 ± 0.2	55 ± 14	1.4 ± 0.1	1.91	7.5 ± 0.3
N3/ I^-,I_3^-	-773 ± 9	5.4 ± 0.4	62.1 ± 0.5	2.6 ± 0.2	1.65	6.8 ± 0.2
Z907/ I^-,I_3^-	-729 ± 33	6.0 ± 1.6	56 ± 10	2.3 ± 0.3	1.42	5.8 ± 0.2

5.2 IPCE and Recombination Studies of HTMs

In order to better understand the parameters that affect fill factor, the UV-Vis spectra of N3 and Z907 dyes are compared with their IPCE spectra (Figure 5.3a) when

HTMs are used. It is evident that photon absorption of the dye takes place over a wide range of visible wavelengths. However, electron injection does not properly occur on the entire photon absorption range (Figure 5.2a). UV-Vis absorption spectra of the dyes (N3 and Z907) and electrolyte **1** are also shown in Figure 5.3b. As shown this electrolyte has relatively weak absorption that overlaps only partially with Z907 absorption spectrum and therefore, cannot be the reason for lower IPCE values. As shown in Figure 5.3c, the light harvesting efficiency (LHE) of the films is high, implying that photon absorption is not the hindering factor.

The low IPCE values obtained for the cells with **1** can be due to inefficient electron injection or charge collection (Hagfeldt, 2010). These losses were evaluated using open-circuit photovoltage decay (OCVD, Figure 5.4).

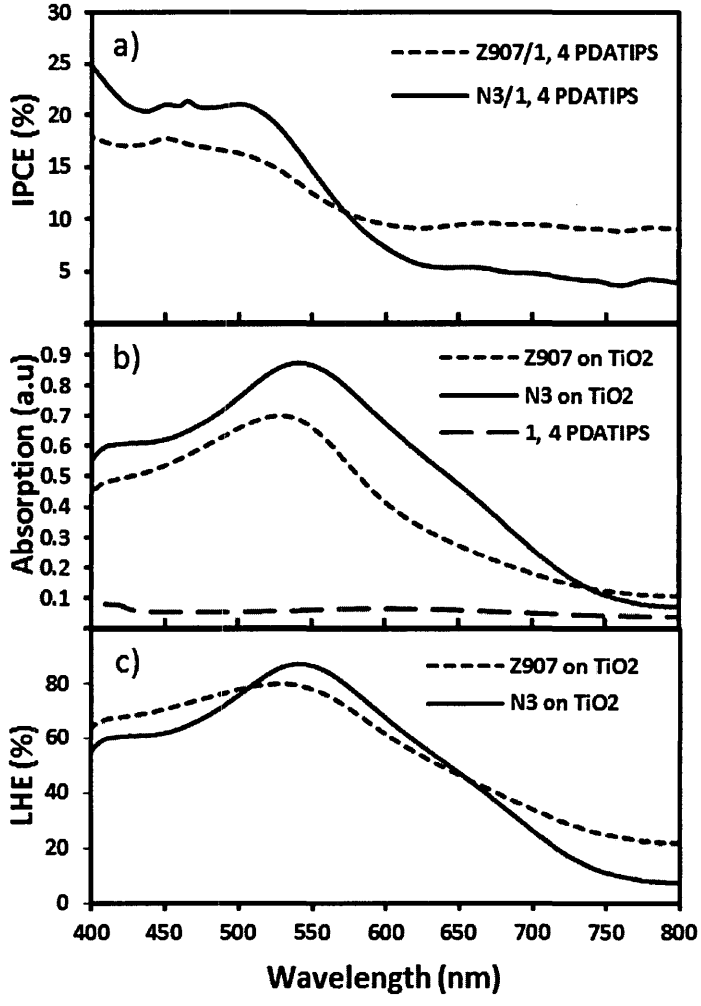

Figure 5.3. Comparison of **a)** IPCE of solar cells fabricated with N3 and Z907 sensitized TiO_2 films using 1 as HTM; **b)** UV-Vis spectra of N3 and Z907 dyes sensitized TiO_2 and solution of **1**; and **c)** LHE for the cells characterized in a).

The electron lifetime in the TiO_2 conduction band (τ_n) versus V_{oc} were calculated from these measurements for N3 and Z907 sensitized solar cells (Figure 5.5 and Figure 5.6, respectively), and suggests much faster recombination from the CB of TiO_2 back to the redox mediator when compound **1** is used versus I^-/I_3^-, regardless of the dye used (Figure 5.5) (Bisquert, 2004). Therefore, the recombination of electrons from the CB of TiO_2 back to the redox mediator is faster with our HTM than with the ordinary I^-/I_3^- electrolyte (Zaban, 2003; Bisquert, 2004).

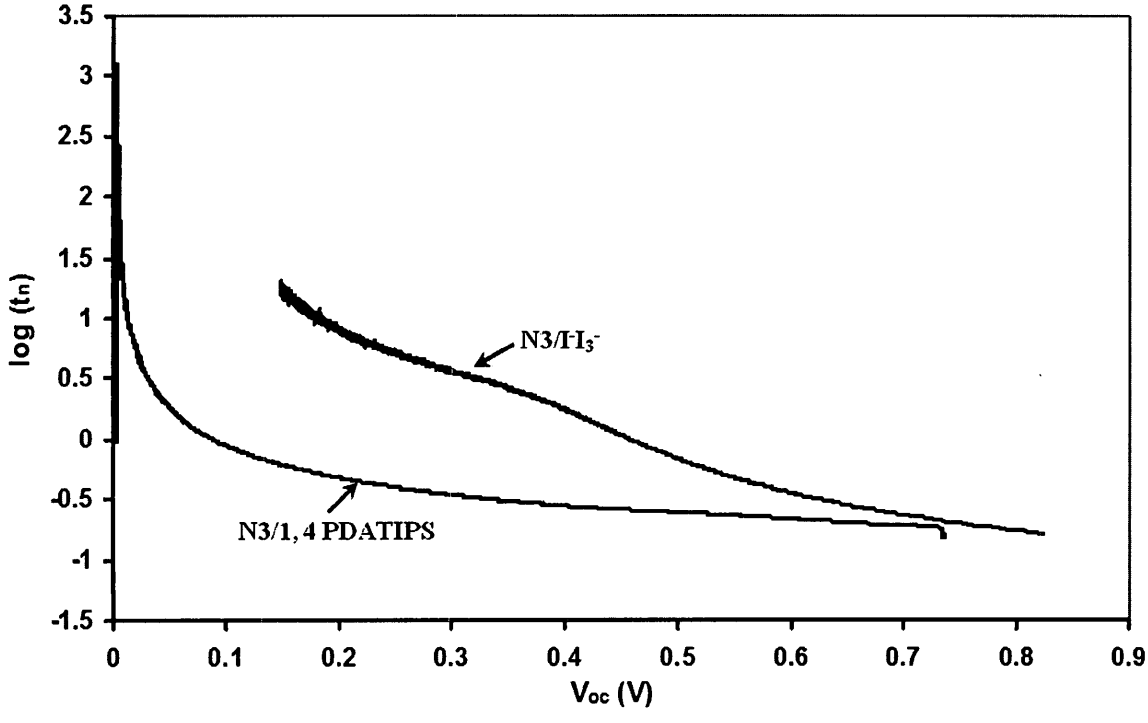

Figure 5.4. CB electron Lifetime (τ_n) versus V_{oc} plots derived from corresponding open circuit voltage potential decays for N3 sensitized TiO_2 in contact with compound **1** and I^-/I_3^- as redox mediators (see Figure 5.5a for OCVD data). Similar data were also obtained when Z907 was used as the sensitizer (Figures 5.5b and 5.6).

a)

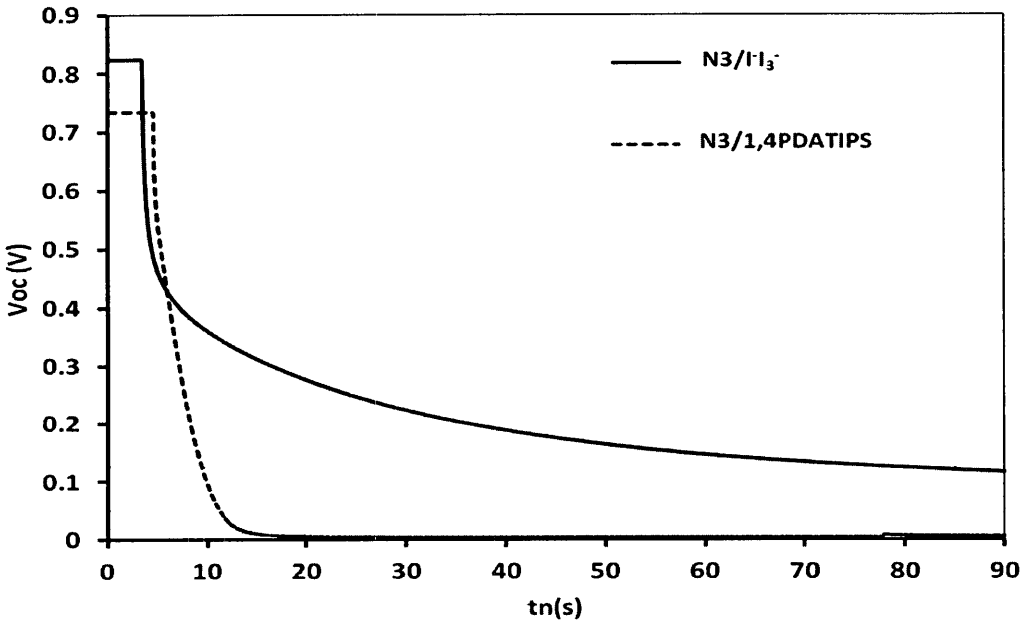

b)

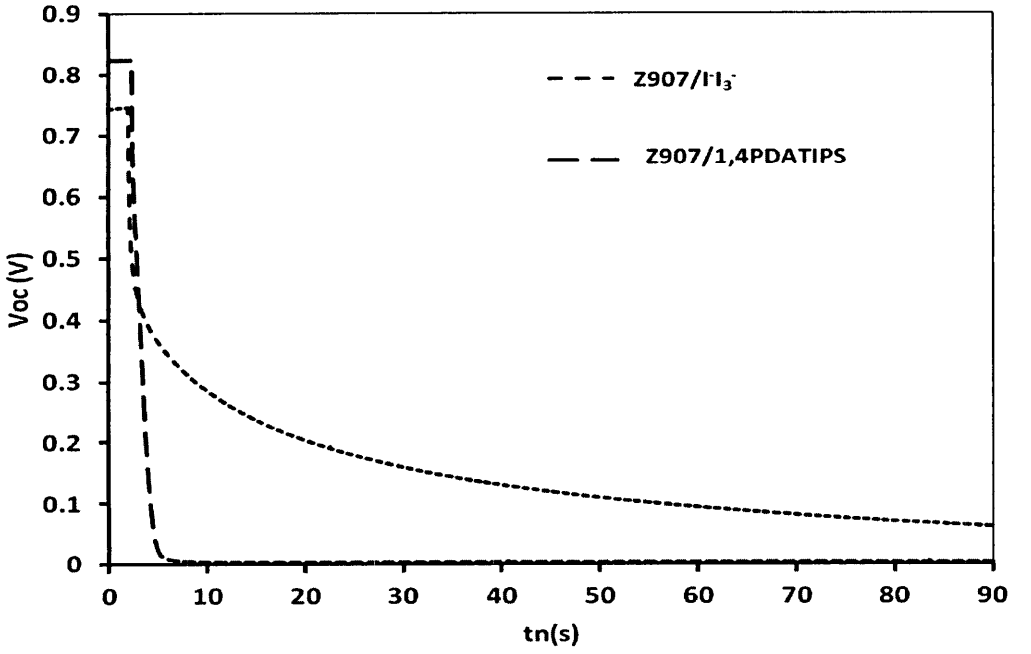

Figure 5.5. Comparison of the OCVD of **a)** N3- and **b)** Z907-sensitized solar cells prepared using **1** and I^-/I_3^- as HTMs.

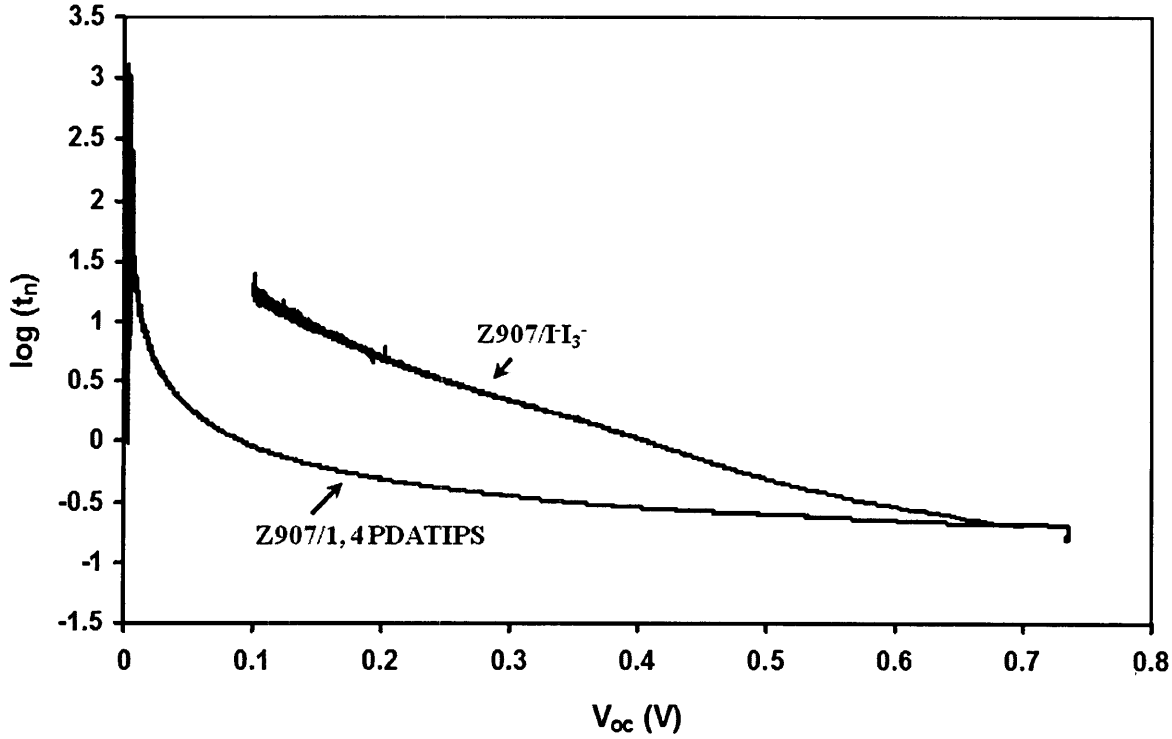

Figure 5.6. Lifetime (τ_n) versus Voc plots derived from corresponding open circuit voltage potential decays (see Figure 5.5 OCVD data) for Z907 sensitized TiO_2 in contact with compound **1** and I^-/I_3^- as redox mediators.

The cells fabricated with **1** have a very fast V_{oc} decay upon cutting off the illumination, in comparison to the cells prepared with I^-/I_3^-. This suggests slower recombination for the I^-/I_3^- electrolyte. Therefore, the recombination of electrons from the CB of TiO_2 back to the redox mediator, is faster with our HTM than the ordinary I^-/I_3^- electrolyte. This result is in agreement with a "shorter diffusion length" of the electrons in **1** (Lambert, 1999; Cahen, 2000).

Initially, we found these promising results somewhat surprising, given the large percentage of molecular mass taken up by non-conjugated triisopropylsilyl ether groups on each molecule. It was initially assumed that these electronically inert groups would slow down electron-transfer and limit performance. In order to investigate how these bulky groups impact the performance of the redox mediator, the analogous triarylamine without silyl ether groups (**2**) was used in a DSSC (see Figure 2.7). Surprisingly, in spite of **1** and **2** having identical redox potentials, when **2** was used as a redox mediator in similar cells, no significant photoconversion is observed (Figure 5.7).

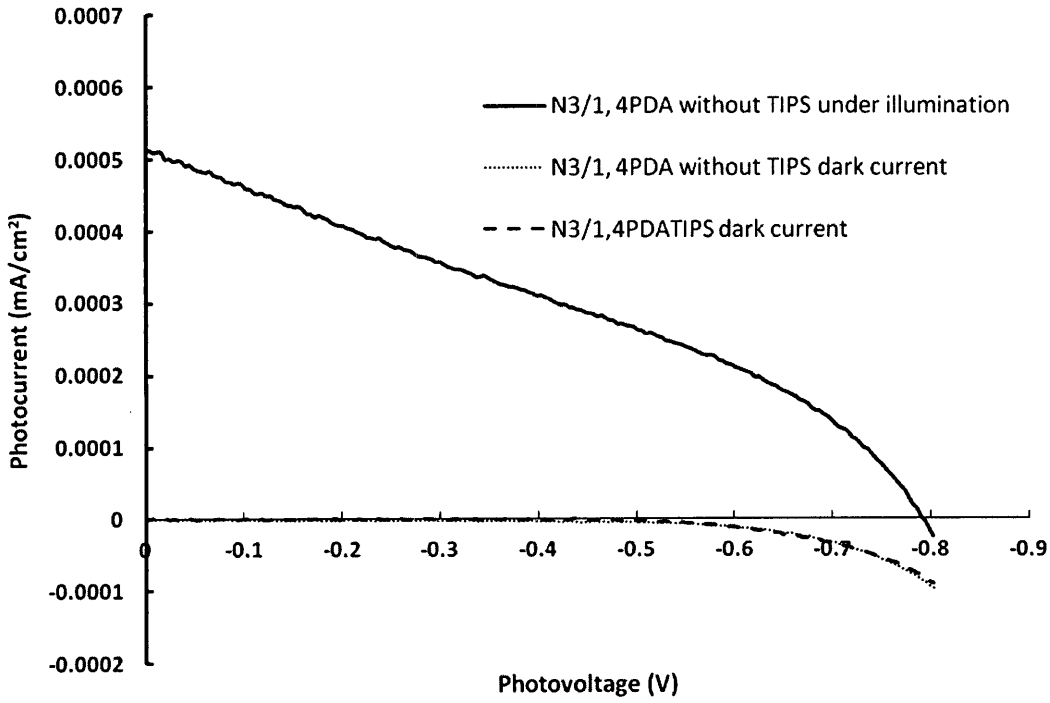

Figure 5.7. Photoelectrochemical i-V curve for N3 sensitized solar cells fabricated with thin TiO_2 film and using a solution of **2** HTM (solid line). Also shown in this graph is the dark current for two N3-sensitized TiO_2 cells using solutions of **1** (dash line) and **2** (dotted line) as the HTM. The dark currents for both HTMs are identical.

This seems to indicate that the recombination rate is not the factor responsible for the inactivity of the non silyl-ether derivative. The role of OTIPS was also investigated using DFT calculations. The calculations reveals that both molecules have almost identical HOMO and LUMO energies (Table 5.3) and that there is an absence of charge density at the terminal groups beyond the oxygen at the frontier energies (Sepehrifard, 2012).

Table 5.3. Calculated HOMO and LUMO energy levels for compounds **1** and **2**.

Compound	Calculated HOMO (eV)	Calculated LUMO (eV)
1	-4.32	-0.39
2	-4.24	-0.32

The similarities between the HOMO and LUMO energies are paralleled by similarities in the redox potentials of both molecules (Lambert, 1999; Kamino, 2011). While good orbital overlap can play an important role in the dye restoration, it is not obvious how this is favoring **1** over **2**. One then needs to turn to arguments based on physical properties rather than energy levels of the HTM. It could be argued that the presence of OTIPS may afford appropriate spacing between the sensitized surface and the HTM to promote good regeneration while slowing down recombination.

The hydrophobicity of the OTIPS has little effect since the performances are roughly the same with N3 and Z907, where the latter dye has two carbon chains of CH_2 on the dipyridine ligand. Although unlikely, the hydrolysis of OTIPS was investigated as a

possible modification of **1** during processing. This possibility was ruled out since hydrolysis had a negative effect on the cell performance (Figure 5.8).

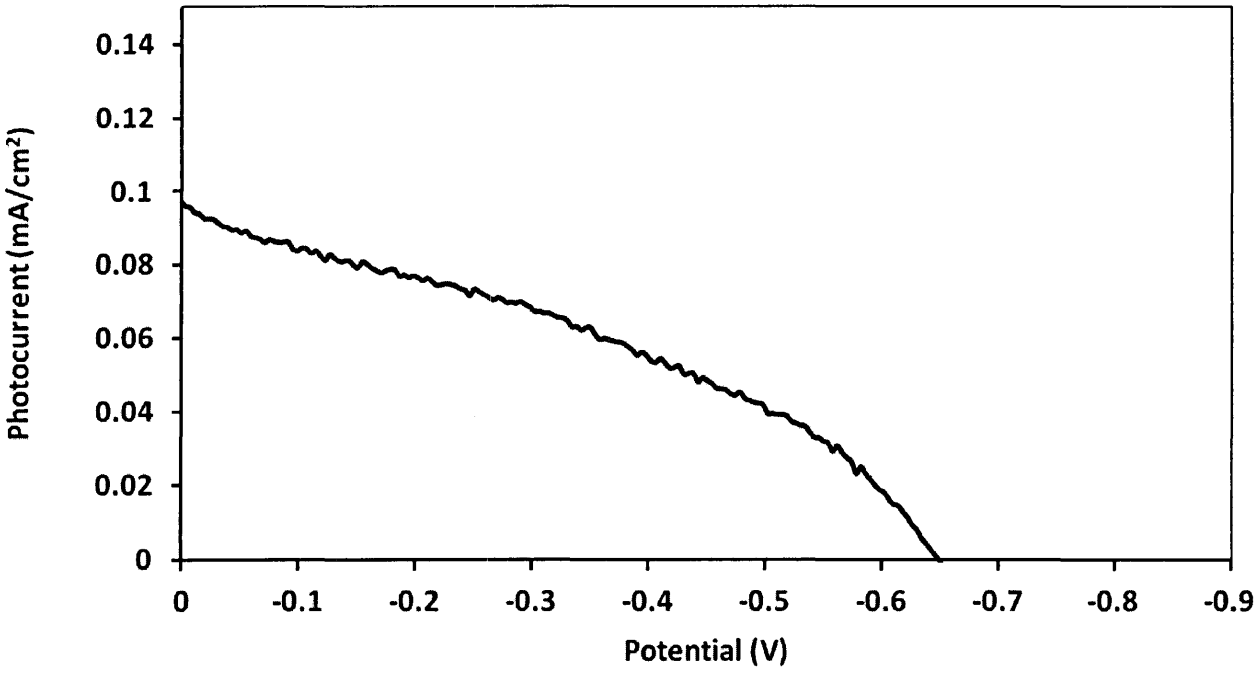

Figure 5.8. Photoelectrochemical i-V curves for N3 sensitized solar cells fabricated with thin TiO_2 film and using a solution of **1** after hydrolysis (see chapter 3 for experimental conditions).

DSSCs was studied. The photoelectrochemical, optical and electrochemical properties of this material show that it has high capability for being used in solar cells based on sensitization of wide band gap semiconductors. Cells using **1** as a redox mediator show very high V_{oc} values (ca. -900 mV) and promising overall efficiencies of up to 1.9% with N3 (a value of 2.9% was obtained using I^-/I_3^- for the same TiO_2 thickness). When the

analogous triarylamine without silyl-ether functionality is used (**2**), no photo conversion is observed. This suggests that the addition of bulky, electronically inert groups is critical to the performance of the redox mediator in this example. It remains that recombination still limits this material's performance. Further investigations will focus on the effect of other bulky silyl-ether groups in improving the performance over non-functionalized hole-transport materials.

Chapter 6: Semiconductor-Sensitized Solar Cells; Cadmium Selenosulfide Sensitizers and the Effect of Preparation Methodology on Cell Performance

Chemical bath deposition (CBD) has always been considered as the first choice for depositing ternary alloys of cadmium selenosulfide ($CdSe_xS_{(1-x)}$), mainly due to the simplicity of the preparative apparatus and chemicals needed (Hodes, 2003). It was also shown that solar cells sensitized with CdS and CdSe, prepared by CBD, are more efficient compared to alternative methods (Mora-Sero, 2008).

Many research groups have studied deposition of ternary alloys of Cd, Se and S with CBD methods (Corer, 1994; Kainthla, 1982; Shahane, 1997a; 1997b, 2001; Chaudhari, 2008). There are only a few reports where ternary alloys of $CdSe_xS_{(1-x)}$ are used to sensitize mesoporous substrates for solar cell applications (Biancardo, 2006; 2007). In these publications many of the aspects of TiO_2 sensitization with $CdSe_xS_{(1-x)}$ were not studied in depth. These effects vary by the change of the bath composition and impact the physical and chemical properties of the sensitizers, which consequently affects the performance of the sensitizers used in solar cells.

In this study, I explored the effect of the preparation conditions in the chemical bath on the properties of the deposited $CdSe_xS_{(1-x)}$ crystals and their effect on the performance of SSSCs once used in sensitizing the TiO_2 substrates. Detailed preparation methodologies and procedures can be found in chapter 3.

6.1 Structural and Optical Characterization of $CdSe_xS_{(1-x)}$ crystals

On Figure 6.1 the UV-Vis spectra of TiO_2 films sensitized with different $CdSe_xS_{(1-x)}$ compositions of NH_3 and NTA CBHs are shown. Films prepared in NH_3 CBHs show a gradual increase in the absorption range by increasing the percentage of Se content where the absorption intensity decreases, most likely due to decrease in the load of the deposited sensitizer. The gradual increase in the absorption is indicative of a solid solution structure of the sensitizers in NH_3 CBHs where CdSe and CdS form on single matrix made of $CdSe_xS_{(1-x)}$ (Mane, 1997; Kainthla, 1982; Shahane 1997a; 1997b; 2001). In contrast, films prepared in NTA CBHs show immediate increase in the absorption range when selenide has been introduced in the CBHs (the absorption increase starts right on $CdSe_{0.25}S_{0.75}$ and only increases slightly when the selenium content of the CBH is increased for other compositions). $CdSe_{0.75}S_{0.25}$ from NTA CBH has the strongest absorption where CdSe has the weakest, when compared on the same wavelength.

According to Table 6.1, $CdSe_{0.50}S_{0.50}$ and $CdSe_{0.75}S_{0.25}$ from NH_3 and NTA CBHs have the highest load of sensitizers deposited on them. This explains higher absorption of these films seen in Figure 6.1 and also low absorption of CdS and CdSe films prepared from NH_3 and NTA CBHs, respectively.

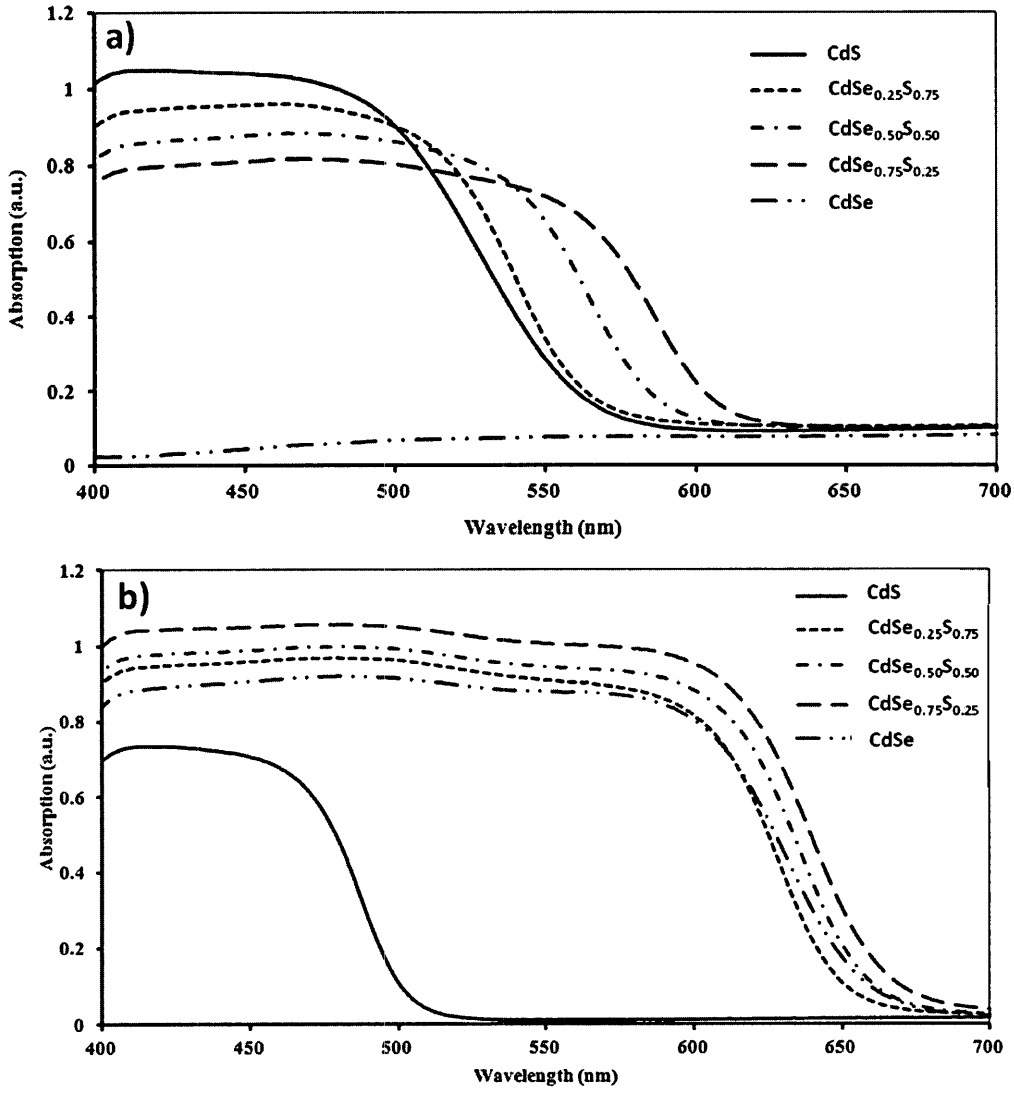

Figure 6.1. UV-Vis spectra of $CdSe_xS_{(1-x)}$ sensitizers deposited on TiO_2 from **a)** NH_3 CB and **b)** NTA CB.

Table 6.1. Cadmium detected on TiO_2 surface through AAS analysis of samples prepared from NH_3 and NTA CBHs.

Sensitizer	Cadmium (mol cm^{-2}) ($\times 10^{-6}$)
CdS	3.19±0.16 (1.06±0.10)*
$CdSe_{0.25}S_{0.75}$	1.78±0.12 (2.10±0.11)
$CdSe_{0.5}S_{0.5}$	1.16±0.10 (2.74±0.13)
$CdSe_{0.75}S_{0.25}$	0.92±0.11 (2.38±0.14)
CdSe	0.37±0.08 (2.11±0.15)

*The values in outside of parenthesis belong to Cd detected on NH_3-CBH samples and the numbers in parenthesis belong to NTA-CBH samples.

During chemical bath deposition, not only chalcogenides of cadmium deposit, but due to the basic nature of the baths, $Cd(OH)_2$ co-deposits. Tables 6.2 and 6.3 show the EDX analysis of the films prepared from both CBHs. When films are post-treated with sulfide-rich solutions (all the films composition in parenthesis in tables 6.2 and 6.3) a decrease in Cd/(S+Se) ratios occurs, which is indicative of the initial presence of $Cd(OH)_2$ and the subsequent OH^- replacement with S^{2-} upon sulfide treatment. This ratio shows dependence on the pH of the CBs. In CBs with higher content of Se where the initial pH of the CBH is less basic, the Cd/(S+Se) ratio is smaller. All of this indicates that there are $Cd(OH)_2$ crystals left in the matrix of the sensitizer. However quantitative measurement of the absolute amount of $Cd(OH)_2$ is not possible.

Based on the ratios of Cd, Se and S obtained from EDX analysis, the composition ratio of the CdSeS crystals is calculated and tabulated in Tables 6.2 and 6.3 and also

shown in Figure 6.2. According to these, for films prepared from NH_3 CBH there is more control on the ratio of CdSe and CdS. For the NTA films, right after introducing the precursor of Se into the bath, there is more deposition of CdSe than of CdS. For simplicity along this report, films are referred to, based on their proposed composition in the baths. EDX spectra can be found in the appendix A (Figures A1 to A18).

Table 6.2. Atomic percentages obtained from EDX analysis for the films prepared in NH_3 CBs. The real compositions are calculated based on the atomic percentages as well.

Atomic Percentages				
Element	CdS	$CdSe_{0.25}S_{0.75}$	$CdSe_{0.5}S_{0.5}$	$CdSe_{0.75}S_{0.25}$
S	38.96 (40.90)*	29.25 (35.06)	21.52 (30.97)	14.47 (29.77)
Se	0.00 (0.00)	7.52 (7.82)	13.09 (9.97)	19.40 (12.24)
Cd	61.04 (59.10)	63.23 (57.12)	65.39 (59.06)	66.13 (57.98)
Total	100.00 (100.00)	100.00 (100.00)	100.00 (100.00)	100.00 (99.99)
Cd/(Se+S)	1.57 (1.44)	1.72 (1.33)	1.89 (1.44)	1.95 (1.38)
Real Composition	CdS	$CdSe_{0.20}S_{0.80}$ ($CdSe_{0.18}S_{0.82}$)	$CdSe_{0.38}S_{0.62}$ ($CdSe_{0.24}S_{0.76}$)	$CdSe_{0.57}S_{0.43}$ ($CdSe_{0.29}S_{0.71}$)

*The numbers in parenthesis represent the values for the films after being in contact with polysulfide solution.

Table 6.3. Atomic percentages obtained from EDX analysis for the films prepared in NTA

Atomic Percentages					
Element	CdS	$CdSe_{0.25}S_{0.75}$	$CdSe_{0.5}S_{0.5}$	$CdSe_{0.75}S_{0.25}$	CdSe
S	36.10 (42.07)*	8.00 (21.17)	5.94 (21.54)	5.83 (15.18)	2.02 (18.78)
Se	0.00 (0.00)	32.64 (21.51)	36.07 (23.05)	37.20 (27.12)	35.66 (20.99)
Cd	63.90 (57.93)	59.35 (57.32)	58.00 (55.41)	56.98 (57.70)	62.32 (60.23)
Total	100.00 (100.00)	99.99 (100.00)	100.01 (100.00)	100.01 (100.00)	100.00 (100.00)
Cd/(Se+S)	1.77 (1.38)	1.46 (1.34)	1.38 (1.24)	1.32 (1.36)	1.65 (1.51)
Real Composition	CdS	$CdSe_{0.80}S_{0.20}$ ($CdSe_{0.50}S_{0.50}$)	$CdSe_{0.86}S_{0.14}$ ($CdSe_{0.52}S_{0.48}$)	$CdSe_{0.86}S_{0.14}$ ($CdSe_{0.64}S_{0.36}$)	$CdSe_{0.95}S_{0.05}$ ($CdSe_{0.53}S_{0.47}$)

CBs. The real compositions are calculated based on the atomic percentages as well.
*The numbers in parenthesis represent the values for the films after being in contact with polysulfide solution.

PXRD of the films from NTA CBs shows that there are discrete nanocrystals of CdSe and CdS forming on the surface with mainly cubic and zinc blend structures, respectively (Figures B3 and B4 in the appendix). Films from NH_3 CBHs form crystals of CdSeS and separate crystals are not distinguishable based of PXRD results (Figures B1 to B4). According to SEM images (Figure 6.3), films prepared from both NH_3 and NTA CBHs show the same morphology and within the resolution provided by SEM, the variation in morphology cannot be discriminated and all films have similar appearance. UV-Vis spectra (Figure 6.1a) and XRD results show that films from NH_3 CBHs are solid solution crystals as was mentioned before.

As one can see, the composition of the films prepared from the NTA bath is very different from their counterparts prepared in the NH_3 bath. Hence a comparison only based on chemical composition of the deposited films will not be a thorough comparison and results obtained from other techniques are employed below to elaborate on the parameters affected by the deposition method and impacting the performance of the cells.

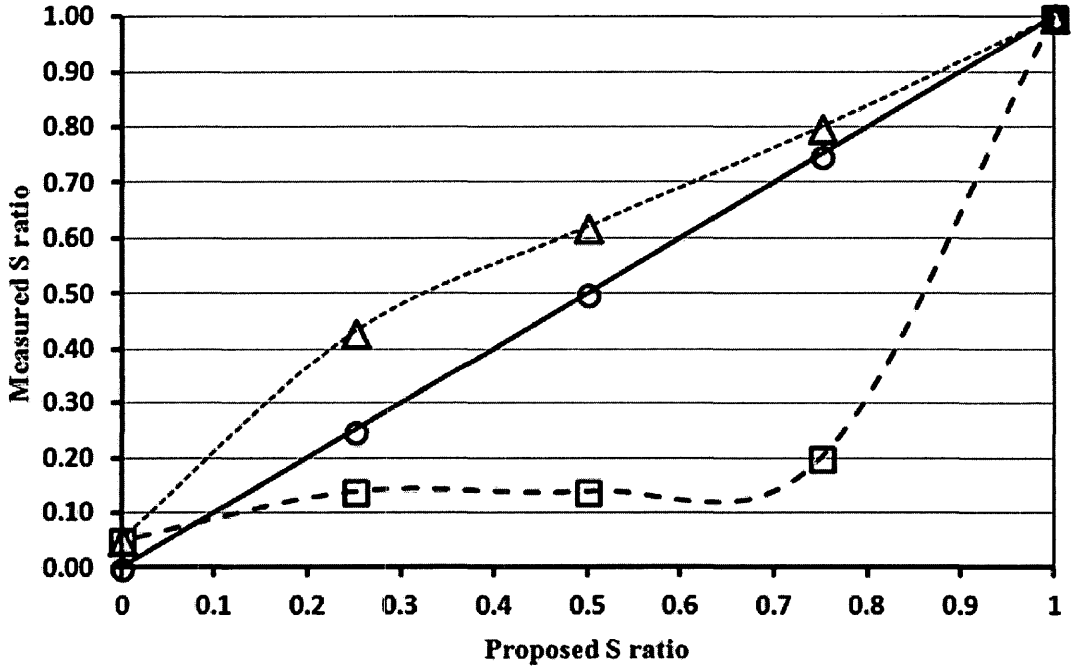

Figure 6.2. Comparison between the proposed sulphur ratio (amount of sulfide added in the CBH) and the real deposited amount for NH_3 CBH (triangles) and NTA CBH (squares). The circles represent and ideal condition at which both solution and surface ratios of sulphur mach. The atomic percentages are derived from EDX results in tables 6.2 and 6.3.

SEM images of both NH_3 and NTA CBHs films (Figure 6.3) with different compositions show that upon deposition of sensitizer nanocrystals, the nanoporous structure of the films do not change significantly when compared to plain TiO_2 film (Figure 6.3a). SEM images of the cross section of the sensitized films do not show distinguishable borders between TiO_2 and the sensitizer layer.

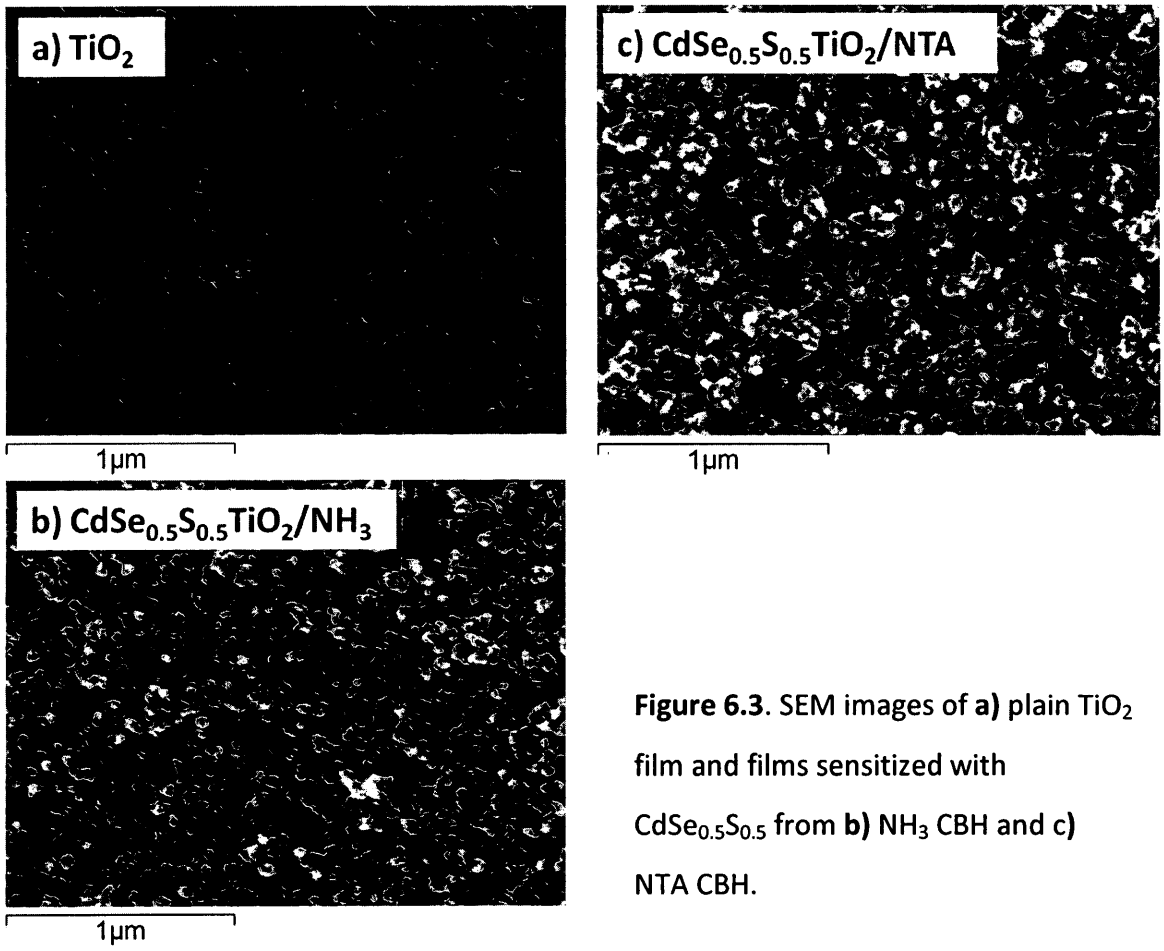

Figure 6.3. SEM images of **a)** plain TiO_2 film and films sensitized with $CdSe_{0.5}S_{0.5}$ from **b)** NH_3 CBH and **c)** NTA CBH.

6.2 Photoelectrochemistry (PEC) and its Correlation to the Chemical Bath Composition

Table 6.4 shows the PEC results of films from both NH_3 and NTA CBHs. PEC efficiency of NTA films are higher than the corresponding NH_3 films with the same chemical structure. Films from NH_3 CBHs have relatively higher photocurrent (J_{sc}) and photovoltage (V_{oc}) values but poor fill factor (*ff*) is the main reason for lower efficiency (η) of these films when compared to their NTA alternatives. Lower *ff* values may be related to recombination abundance, which will be discussed in following sections. For

both NH_3 and NTA films, V_{oc} and J_{sc} values increase and reach a maximum for compositions $CdSe_{0.25}S_{0.75}$ and $CdSe_{0.50}S_{0.50}$.

Table 6.4 PEC of TiO_2 films sensitized with different $CdSe_xS_{(1-x)}$ compositions. The films are sensitized in a chemical bath based on NTA and NH_3.

Bath Composition	V_{oc} (mV)	J_{sc} (mA cm^{-2})	*ff* (%)	η (%)	IPCE(%)
CdS	-330 (-325)*	5.41 (1.32)	18.5 (33.4)	0.33 (0.14)	26.0 (27.8)
$CdSe_{0.25}S_{0.75}$	-465 (-518)	10.9 (9.06)	24.8 (32.8)	1.25 (1.54)	48.8 (38.6)
$CdSe_{0.50}S_{0.50}$	-527 (-535)	10.2 (9.97)	24.3 (31.8)	1.31 (1.70)	33.1 (26.2)
$CdSe_{0.75}S_{0.25}$	-531 (-502)	6.21 (9.47)	24.3 (31.7)	0.80 (1.51)	29.6 (24.0)
$CdSe_{0.95}S_{0.05}$	-547 (-477)	5.31 (4.98)	24.5 (36.1)	0.71 (0.86)	23.7 (21.9)
CdSe	-551 (-453)	4.84 (3.79)	24.0 (44.8)	0.64 (0.77)	15.0 (24.8)

*The numbers in parenthesis belong to the films from NTA CBHs.

PEC graphs can be seen in Figure 6.4a and b. When comparing the stability of the performance of the films, TiO_2 films sensitized in NTA CBHs, can be illuminated for extended durations (4-5 hours) whereas NH_3 films do not show a stable performance and photocurrent decreases by increasing the illumination time (0.21 mA min^{-1}). This is mainly attributed to the presence of $Cd(OH)_2$ in the structure of the films (Tachibana, 2009). For the films with higher content of $Cd(OH)_2$ (normally films prepared in NH_3 CBHs and also films with higher initial pH from both NH_3 and NTA CBHs), the rate of change in performance upon longer illumination duration is faster (ca. 0.20 mA min^{-1}). It

is also evident that films with higher content of $Cd(OH)_2$ (films prepared from NH_3 CBH) have inferior performance and lower efficiency compared to the films with lower $Cd(OH)_2$ content (Figure 6.4).

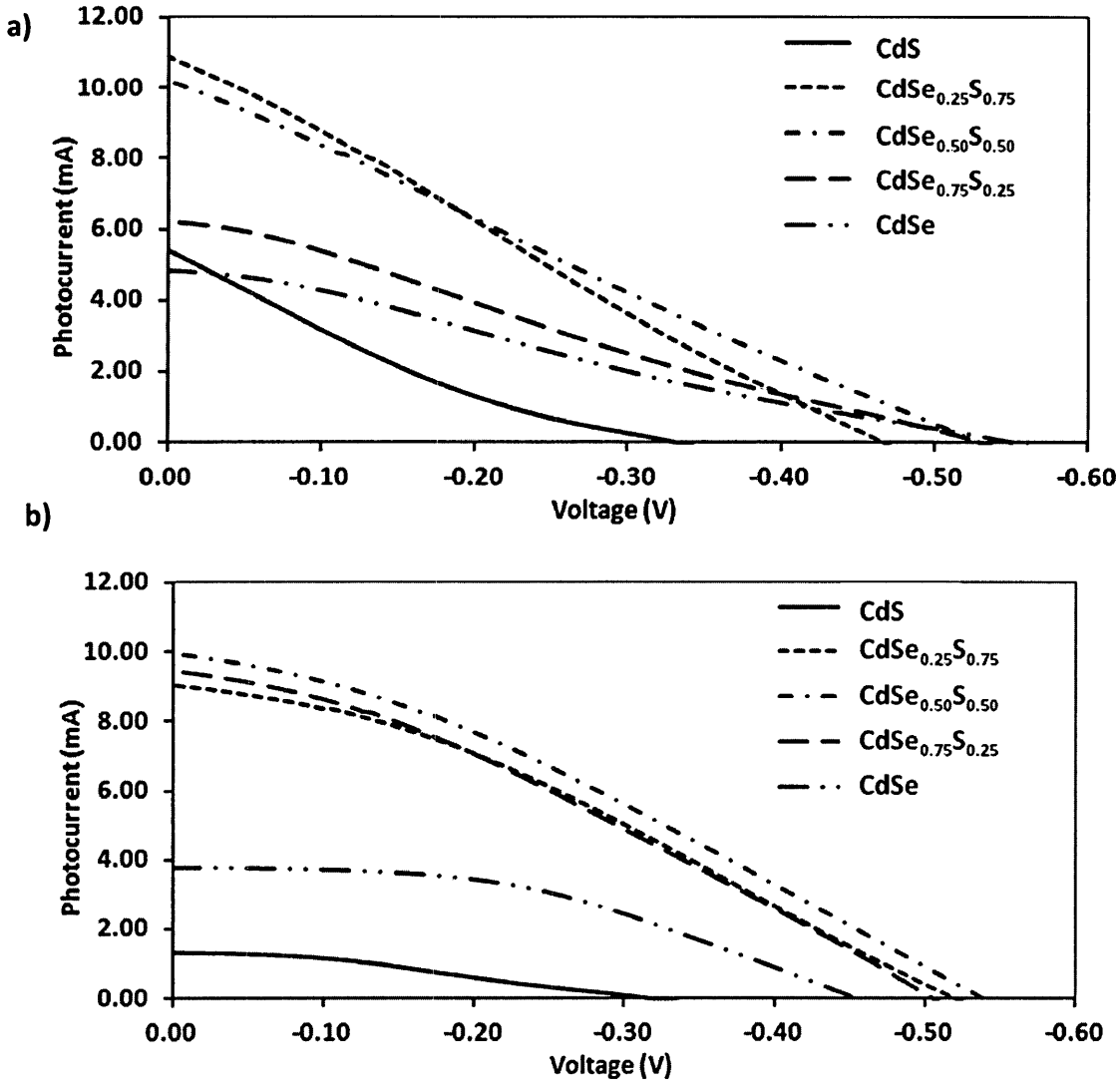

Figure 6.4. PEC graphs of TiO_2 films sensitized with different compositions of $CdSe_xS_{(1-x)}$ prepared from **a)** NH_3 CBH and **b)** NTA CBH. All experiments are performed at 1.5AM light intensity and with polysulfide (3 M S, 2 M Na_2S) as electrolyte with Pt-coated FTO as counter electrode. The scan rate was 50 mV s^{-1}.

We performed PEC for the films with all bath composition and from both NH_3 and NTA baths with and without being post-treated with S^{2-}-rich solutions. The results (Figures C1-C8 in the appendix) show that after treating the films with sulfide solutions, the efficiency of the films does not increase significantly. However there are valuable conclusions that can be drawn from these results. For the films prepared from NH_3 CBH, there is improvement observed in fill factor values. Also, the post-treated cells show improved stability when used in experiments with longer illumination time. This can be mainly correlated to the exchange of the loosely attached $Cd(OH)_2$ particle with CdSe and CdS crystals whereas the resulting $CdSe_xS_{(1-x)}$ crystals are not strongly attached to the surface of TiO_2 and cannot contribute to proper electron injection to TiO_2 CB (Niitsoo, 2006). In addition, films prepared from NTA films generally show an increase in J_{sc}, which can be attributed to an increase on the CdS content of the films after post-treatment and replacement of the $Cd(OH)_2$ crystals that do not absorbs the photons of visible light. The mechanism of sensitizers and $Cd(OH)_2$ deposition will be discussed in the following paragraphs. This help better understand the post-treatment effect and how the $Cd(OH)_2$ crystals deposit on the surface of TiO_2. In addition to surface analysis techniques, as a rule of thumb, the presence of $Cd(OH)_2$ on the surface can be tested by immersing a film in any bath without precursors of Se^{2-} and S^{2-} and only with Cd^{2+} and then taking the film out and washing it and immersing it in a S^{2-} solution. Observing yellow color confirms the presence of $Cd(OH)_2$ on the surface (Niesen, 2002).

The depth of exchange of OH^- with S^{2-} and Se^{2-} on the crystals matrix may not be long enough to convert all OH^- ions to S^{2-} and Se^{2-} (Mueller, 1981). In this case, there would be a thin layer of $Cd(OH)_2$ remaining at the borderline of sensitizer and TiO_2 particles. This thin layer of $Cd(OH)_2$ may act as an insulator between the sensitizer and the TiO_2 particle as the CB of $Cd(OH)_2$ is located higher than that of $CdSe_xS_{(1-x)}$ sensitizers (Licht, 1985).

6.3 Recombination Analysis based on Open-Circuit Photovoltage Decay

In order to better understand the electron injection processes in our cells, IPCE and OCVD experiments were necessary. The Maximum IPCE values (Table 6.4) show that films from NTA CBHs have superior IPCE when compared to NH_3 alternatives. IPCE graphs (Figure 6.5) confirm that NTA films have better performance over a wider range of wavelengths, which was expected from UV-Vis spectra as well. This can be related to better light harvesting, more efficient electron injection or better charge collection on TiO_2 film, all affecting the IPCE according to Eq. 3.4.

According to Figure 6.6, light-harvesting efficiency (LHE) of films from NTA and NH_3 are more than 90% without correcting light scattering and reflection on the films. So photon absorption on crystals prepared in both NTA and NH_3 CBHs is very strong. Also, NBGS are well-known for absorption coefficients higher than organometallic dyes (Schaller, 2004; Ellingson, 2005; Lee, 2008; Protasenko, 2006; Yu, 2003). In almost all of

the NH_3 films, LHE decreases around 100 nm earlier than NTA films. This will, to some extent, explain the lower values of IPCE obtained with NH_3 films

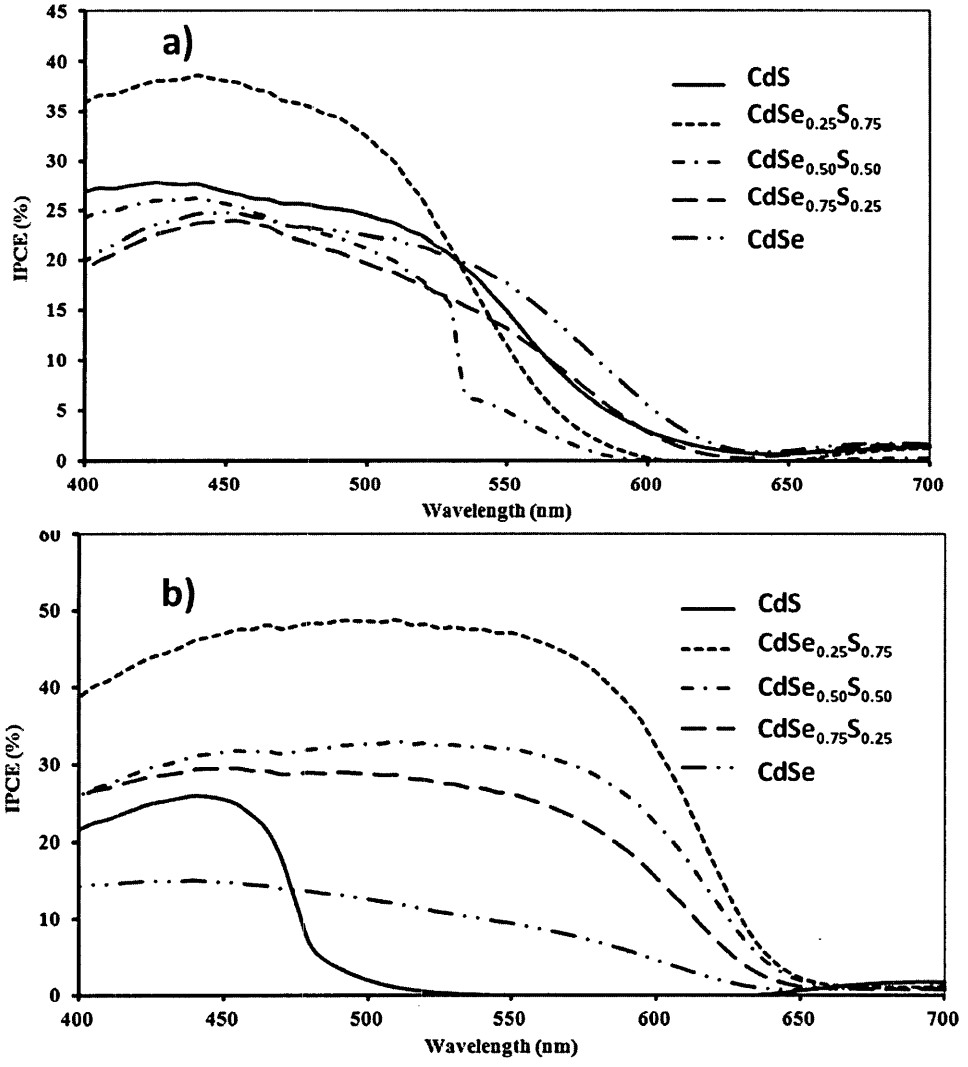

Figure 6.5. IPCE graphs of TiO_2 films sensitized with different compositions of $CdSe_xS_{(1-x)}$ prepared from **a)** NH_3 CBH and **b)** NTA CBH. All experiments are performed with polysulfide (3 M S, 2 M Na_2S) as electrolyte with Pt-coated FTO as counter electrode. The wavelength scan rate was 5 nm s^{-1}.

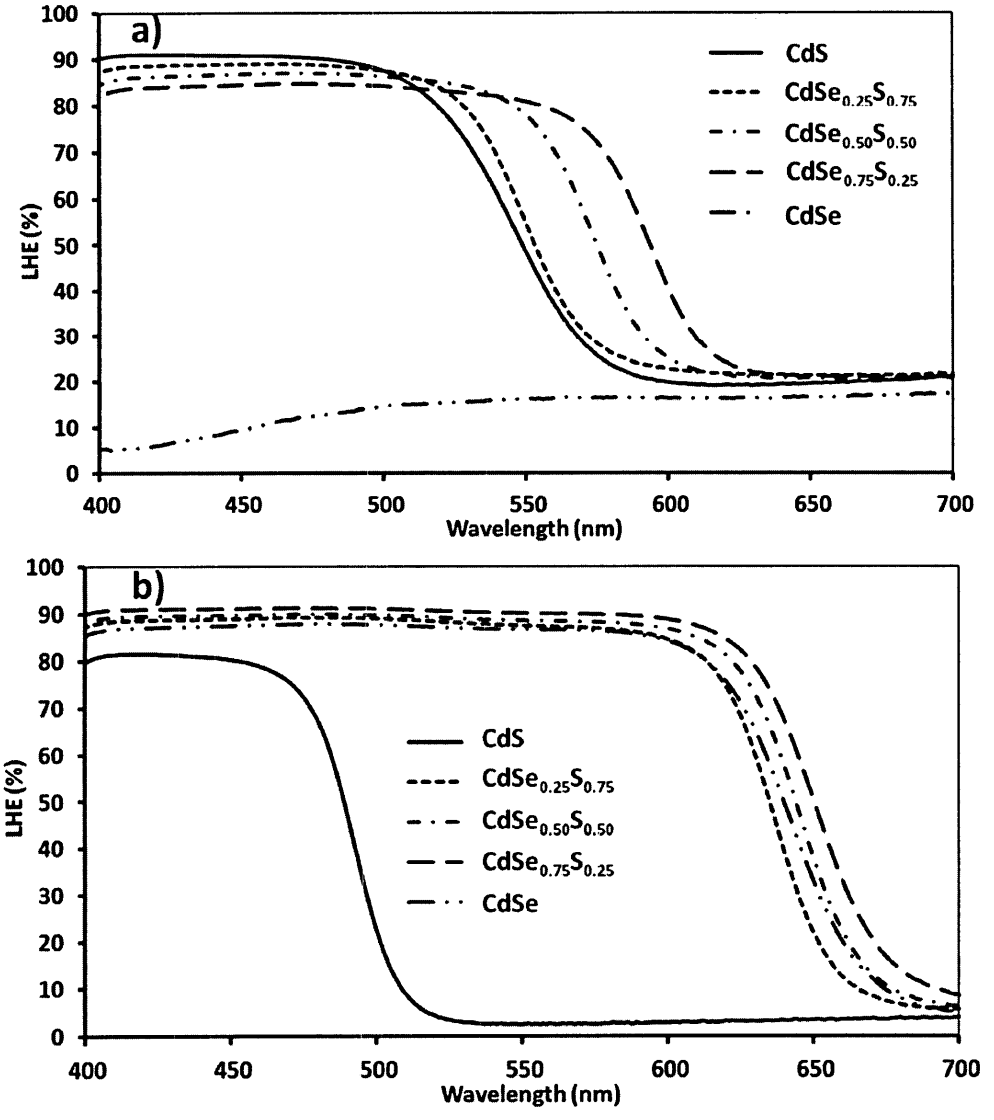

Figure 6.6. LHE graphs of TiO_2 films sensitized with different compositions of $CdSe_xS_{(1-x)}$ prepared from **a)** NH_3 CBH and **b)** NTA CBH.

Charge collection efficiency on TiO_2 films (at least collection and diffusion of the electrons in TiO_2 matrix) must not be the hindering factor in cells sensitized with semiconductors, as these structures have proper charge collection when sensitized with

dye molecules (Diamant, 2004). PEC and IPCE (Table 4.3 and Figure 4.9) of the films sensitized with N3 dye and fabricated with the I^-/I_3^- electrolyte show that charge collection efficiency on our TiO_2 films is not a major issue in reducing the efficiency of cells sensitized with semiconductors. However, recombination, being considered as one of the elements of charge collection loss, can be an important factor in determining the performance of the cells. As has been emphasized by Haque et al. (Haque, 2005), it is the ratio between forward (injection) and backward (recombination) electron transfer processes that is important in deciding the performance of a cell and not the absolute values of each process. Consequently, although the conduction band of sensitizing semiconductors is located above the conduction band of TiO_2, which provides enough driving force for electron injection, better understanding of recombination processes and their abundance can guide us in understanding the performance of the cells prepared in different CBHs.

Open circuit photovoltage decay (OCVD) technique has been originally developed for dye-sensitized solar cells (DSSCs) but using it in a comparative study of cells sensitized with semiconductors can be informative on recombination processes (Chi, 2011). Figure 6.7 shows the OCVD results obtained with films sensitized in NH_3 and NTA CBHs. It is clear that films sensitized in NTA CBHs have slower decay compared to their NH_3 alternatives. So NTA films have less recombination of electrons from the CB of TiO_2, back to the electrolyte solution and sensitizing semiconductor. It is also noteworthy that

when compared to DSSCs, cells sensitized with semiconductors, regardless of the preparation technique, have much faster V_{oc} decay (Bisquert, 2004b).

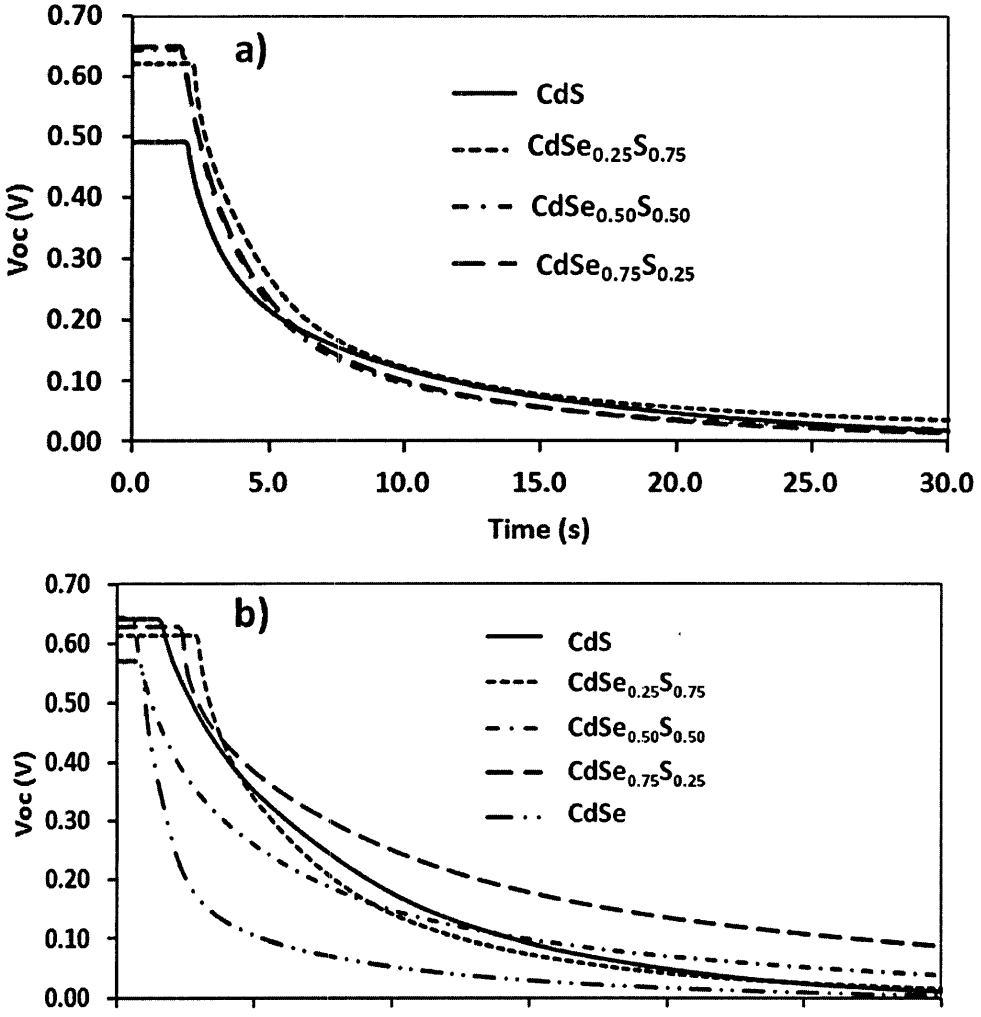

Figure 6.7. OCVD graphs of TiO_2 films sensitized with different compositions of $CdSe_xS_{(1-x)}$ prepared from **a)** NH_3 CBH and **b)** NTA CBH.

Shorter lifetime of CB electrons is due to faster kinetics of electron recombination in SSSCs (Gomez-Jahn, 1992). Our experimental results show that the presence of $Cd(OH)_2$ on the surface of SSSCs can increase the recombination abundance in such cells. Treatment of sensitized films with sulfide-rich solution improves the performance of the cells (Niitsoo, 2006). This treatment also improves the stability of the cells illustrated after the cells were illuminated for a long period of time, as was discussed above. OCVD results of the treated films also show improvement in the stability of the cells upon being exposed to sulfide-rich solutions (Figure 6.8).

6.4 Deposition Mechanism and Change of Chemical Bath Composition to Alter the Mechanism

In NH_3 chemical baths, deposition of $CdSe_xS_{(1-x)}$ occurs via a cluster mechanism where first nanocrystals of $Cd(OH)_2$ form (Eq. 6.1) (Corer, 1994). After the release of Se^{2-} and S^{2-} from their precursors and when their concentrations reach the needed level (this is called induction period) determined by their product solubility constant (K_{sb}), Se^{2-} and S^{2-} can replace the OH^- ions on $Cd(OH)_2$ and form CdSe and CdS crystals (Eq. 6.2).

$$[CdL_n]^{2+}_{(aq)} + 2OH^-_{(aq)} \longrightarrow Cd(OH)_{2\,(s)} + nL_{(aq)} \qquad \text{Eq. 6.1}$$

$$Cd(OH)_{2\,(s)} + Se(S)^{2-}_{(aq)} \longrightarrow CdSeS_{\,(s)} + 2OH^-_{(aq)} \qquad \text{Eq. 6.2}$$

On the other hand the solutions prepared from NTA, depending on the pH of the solution, have two different deposition mechanisms i.e. a cluster mechanism and an ion-

by-ion mechanism (Yochelis, 2004). In ion-by-ion mechanism, the formation of the CdSe and CdS crystals commences immediately after the concentration of the Se^{2-} and S^{2-} reached the needed level for precipitation and the ions react directly. The needed concentration is determined by the K_{sb} value of CdSe and CdS.

$$[CdL_n]^{2+}_{(aq)} + Se(S)^{2-}_{(aq)} \longrightarrow CdSeS_{(s)} + nL_{(aq)} \qquad \text{Eq. 6.3}$$

The dominance of each of the mechanisms is dependent on Cd/NTA ratio and initial pH of the solutions (Hodes, 2007). In this work we have set Cd/NTA ratio on 1.88 so that both of the mechanisms are equally operative. We, therefore expect to have less amount of un-reacted $Cd(OH)_2$ on NTA films than the NH_3 films as in NH_3-based solutions, for which the only available mechanism is cluster mechanism. Hence, faster V_{oc} decay and shorter electron lifetime in NH_3 films are main reasons for the inferior performances of NH_3 cells.

Table 6.1 shows that films from NH_3 CBHs, in which there is maximum amount of NH_3 added, have more content of Cd. This extra amount of Cd has contributed to higher photocurrent in NH_3 cells with CdS, $CdSe_{0.25}S_{0.75}$ and also $CdSe_{0.5}S_{0.5}$ compositions. Despite higher photocurrent obtained for short time illumination of these cells, the photocurrent is not stable for these cells and decreases very rapidly upon long-time illumination of the cells. Furthermore, the fill factor deteriorates drastically when the NH_3 cells are illuminated for longer periods. We propose that this is mainly due to replacement of OH^- ions with S^{2-} in polysulfide electrolyte, which eventually creates

"looser" crystals on the surface compared to the crystals formed by ion-by-ion mechanism (Niitsoo, 2006). The ion exchange of $Cd(OH)_2$ crystals with polysulfide solution is light-catalyzed, which in turn increases the photocurrent obtained with films of high $Cd(OH)_2$ content (Tenne, 1980; Licht, 1986). Once the OH^- are replaced, the photocurrent will only depend on the available sensitizers deposited on the surface and are strongly bound to the surface.

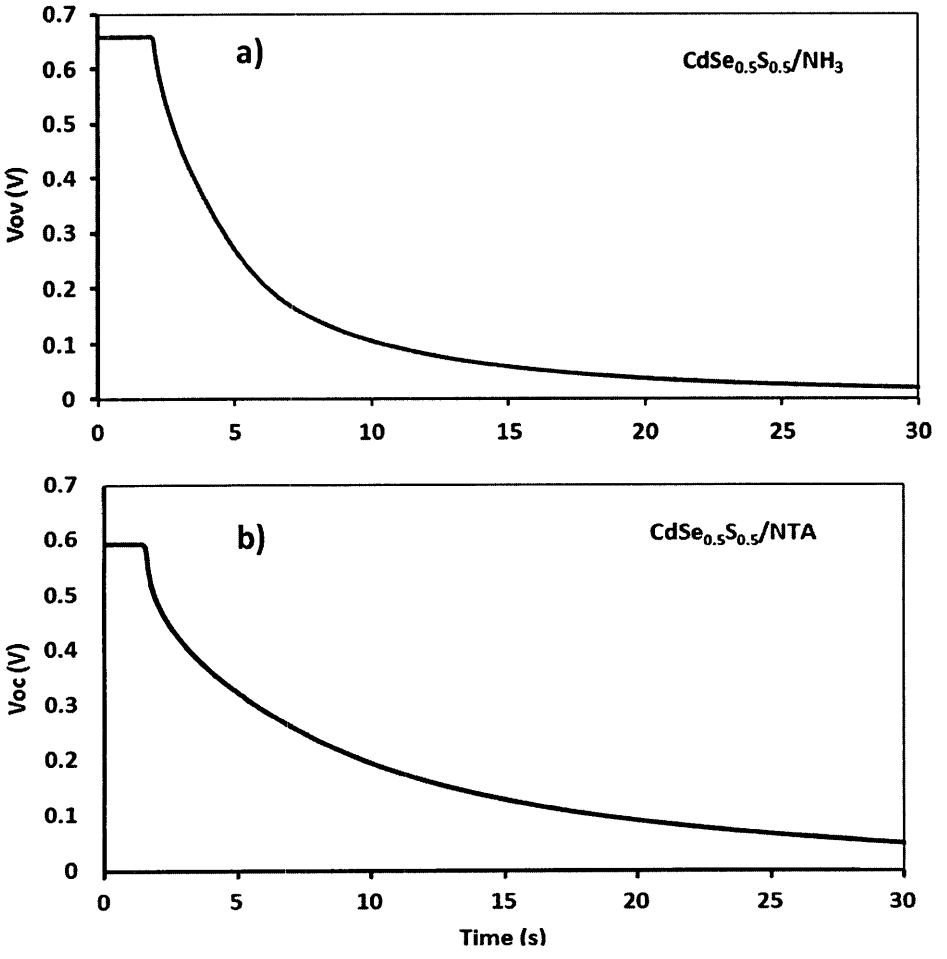

Figure 6.8. OCVD graphs of TiO_2 films sensitized with $CdSe_{0.5}S_{0.5}$ prepared from **a)** NH_3 CBH and **b)** NTA CBH and post-treated with sulfide-rich solutions before being used in a cell.

As previously mentioned, EDX analysis (Tables 6.2 and 6.3) shows that when films are exposed to sulfide-rich solutions, the ratio of Cd/(Se+S) decreases. This directly indicates that, in addition to the sensitizing CdS and CdSe crystals, there is another cadmium-containing crystal deposited on the TiO_2 substrate. X-ray photoelectron spectroscopy (XPS) results demonstrate that these unknown crystals have Cd-O bonds (Figures D1 to D10 in the appendix). So, with regard to the chemical bath preparation conditions, the only possible species of cadmium that contains oxygen can be $Cd(OH)_2$.

$Cd(OH)_2$ crystals are amorphous as they are deposited from gross precipitation in CBHs (Ristic, 2004; Licht, 1984). Amorphous nanocrystals are very prone to possess defects on the surface so that replacement of Se^{2-} and S^{2-} in their structures does not seem to be improving the surface structure and morphology (Licht, 1985b; Ellis, 1977). These defects can translate into potential recombination pathways after the $Cd(OH)_2$ crystals have transformed to $CdSe_xS_{(1-x)}$ crystals. Loef et al (Loef, 2009) have shown that the presence of shallow energy level at the space charge of CdSe is responsible for recombination. This abundance of these acceptor energy levels (acceptor density) decreases strongly with increasing quantum dot size. The presence of these defect states may give rise to Auger recombination in small quantum dots and therewith decrease the efficiency of quantum-dot sensitized solar cells. Accordingly, in NH_3 CBH, where the most dominant deposition mechanism is cluster mechanism and the size of the final sensitizer crystals is decided by the size of the initial $Cd(OH)_2$ crystals, such

recombination pathways are even more abundant, explaining to great extent the lower performance of the films prepared from NH_3 CBH.

In cells prepared from NTA CBHs, as there is ca. 50% less probability of cluster mechanism responsible for the deposition of the sensitizers, there is less chance of $Cd(OH)_2$ remaining on the surface so that V_{oc} is more stable in such cells. NTA films also have more content of Cd-containing crystals (Table 6.1) and the Cd/(Se+S) ratio does not change as significant as it happens in NH_3 films after bringing the films in contact with sulfide-rich solutions (Table 6.2 and 6.3).

Reduction of the pH of the chemical baths does not improve the performance of the cells to an indefinite level because for two main reasons. Firstly, cluster mechanism in NH_3 and NTA CBHs and the presence of nano-crystals of $Cd(OH)_2$ are essential for increasing the load of the of the deposited sensitizer. Secondly, basicity of the baths is crucial for the release of selenide and sulfide from their precursors and if the pH is adjusted too low, there would be no deposition of $CdSe_xS_{(1-x)}$ crystal happening on the surface. Also if pH is adjusted such that the release of sulfide and selenide occurs it may be yet not sufficient for the precipitation of enough of sensitizer on the surface. Table provided on Figure 6.9 shows the results of an experiment where for NTA $CdSe_{0.5}S_{0.5}$ cell, pH was initially adjusted at 10.11, and despite the deposition of the sensitizer, the PEC performance is not as strong as the same films prepared at pH 10.35 (Table 3.1). Based on this, a change in the initial pH will affect various parameters different ways,

convoluting the analysis and making a straightforward comparison unachievable. However, based on the information we have obtained up to now, one can optimize the conditions of the deposition for best cell performance such that the proper solution composition can be foreseen.

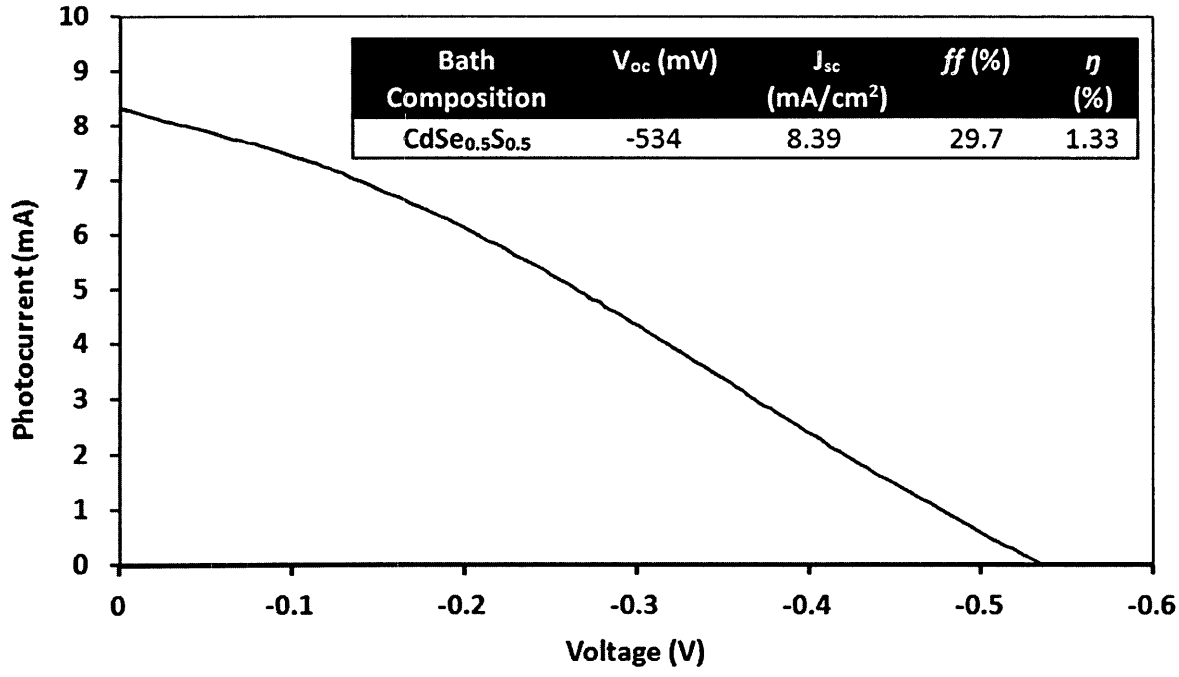

Figure 6.9. PCE graph of TiO_2 films sensitized with $CdSe_{0.5}S_{0.5}$ prepared from NTA CBH at initial pH of 10.11. The performance is inferior to the same films prepared at pH of 10.35 (see Table 6.4).

Increasing the metal (Cd) to ligand (NTA) ratio may also reduce the formation of $Cd(OH)_2$ crystals because it will basically shift the deposition mechanism toward ion-by-ion mechanism. As control experiments, we sensitized TiO_2 films with $CdSe_{0.5}S_{0.5}$ in NTA-based CBHs with a Cd/NTA ratio of 2.2 for nanocrystals to form exclusively through the

ion-by-ion mechanism (Corer, 1994). Such films do not show noticeable change in Cd/(Se+S) ratio after being in contact with sulfide-rich solutions (Figure 6.10 and the table therein). Also when used in a SSSC, the photocurrent and performance of the cells, over a long period illumination, is stable (Figure 6.11 and Table therein). However, the efficiency of such cells is inferior to the films prepared from NTA CBHs with Cd/NTA=1.88 simply because the process of crystals deposition is slower in such baths and there will be less sensitizer deposited on the TiO_2 films (Table 6.4) (Corer, 1994). Leaving the films for longer in this chemical bath does not increase the deposition of the sensitizers most likely due to the high Cd/NTA ratio and that Na_2SeSO_3 as the precursor of Se^{2-} deteriorates over longer storage and heating periods (Hodes, 2003).

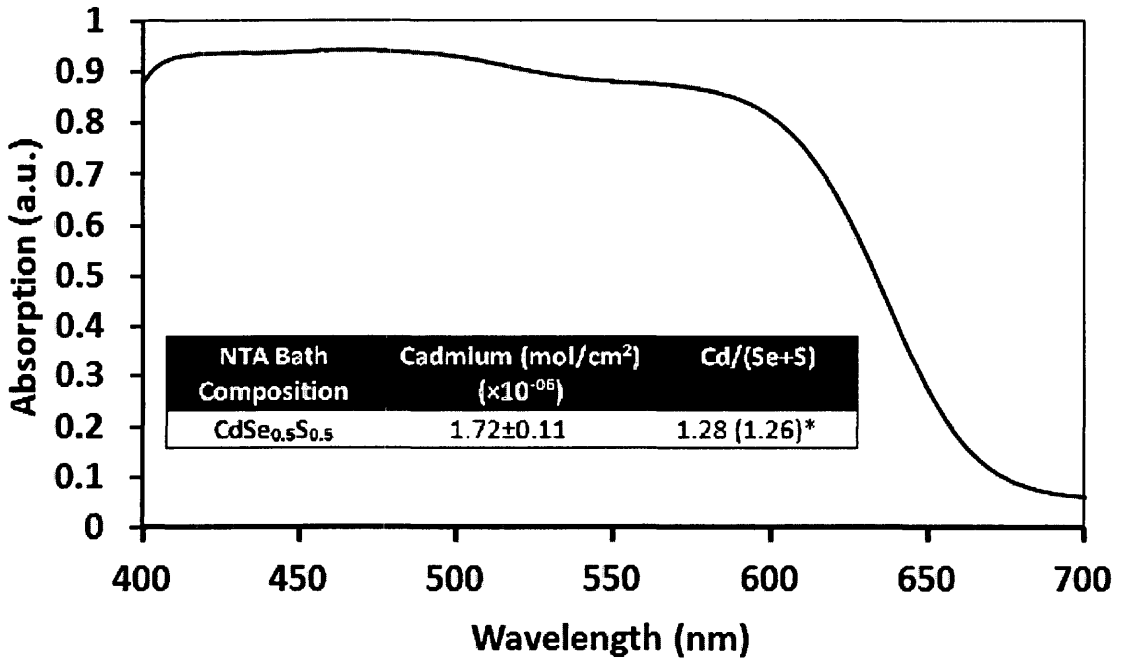

Figure 6.10. UV-Vis graph of TiO_2 films sensitized with $CdSe_{0.5}S_{0.5}$ prepared from NTA CBH with NTA/Cd molar ratio adjusted at 2.12. The cadmium salts loaded on TiO_2 was measured with AAS and reported in the included table. Also the Cd to (Se+S) ratio before and after post-treatment is shown in the table.

When the films that were prepared in CBHs with cluster mechanism were left in sulfide-rich solutions before being fabricated into a cell, the performance did not improve to the extent one might expect (Figure 6.11). The deposited $Cd(OH)_2$ crystals are considered as "loosely" attached on TiO_2 surface (Niitsoo, 2006). These crystals do not have strong interaction with the substrate underneath and after ionic exchange with sulfide-rich solutions, will not result in strongly-bound sensitizer crystals (Corer, 1994). The attachment of the crystals has strong impact on electron injection processes so

loose attachment of the sensitizers to the surface can reduce electron injection efficiency.

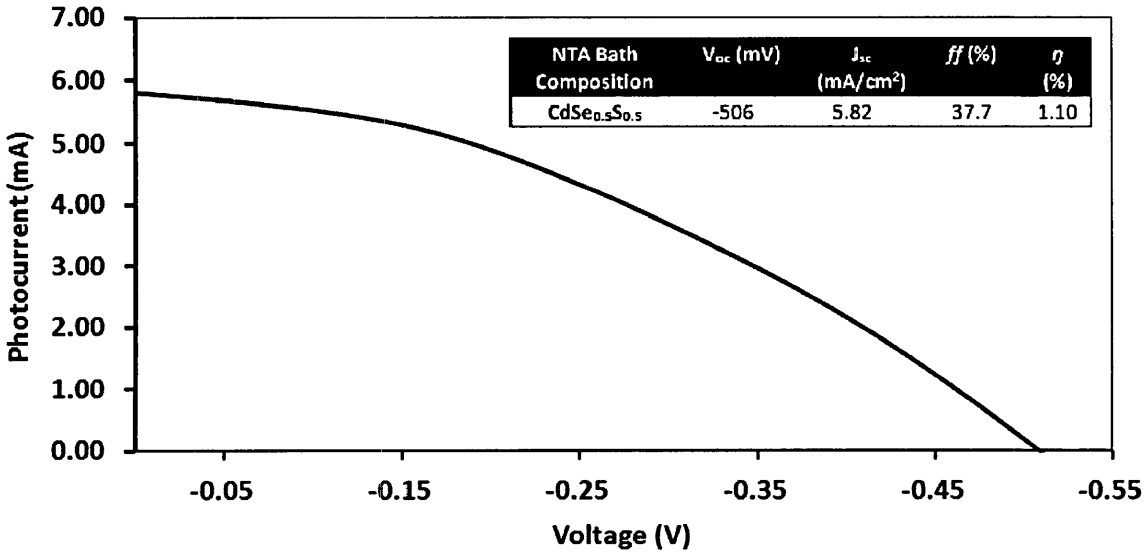

Figure 6.11. PCE graph of TiO_2 films sensitized with $CdSe_{0.5}S_{0.5}$ prepared from NTA CBH with NTA/Cd molar ratio adjusted at 2.12. All other experimental conditions are kept the same as the cells presented in Table 6.4.

6.5 Conclusion

In conclusion, sensitization of TiO_2 nano-porous films with cadmium selenium sulfide ternaries, prepared from two different chemical baths with NTA and NH_3 as deposition-rate controlling compounds, has been studied. We have shown that the structure of the sensitizers, their attachment to the surface, and load of deposition and co-deposition of other possible species are directly related to the composition of the

chemical bath. All these parameters were shown to directly impact the performance of the cells through electrochemical, chemical and physical properties of the sensitizers.

It was shown that the presence of co-deposited $Cd(OH)_2$ on the TiO_2 surface introduces some other routes for electron injection and charge transport in the sensitizer/TiO_2 interface that are not completely beneficial to the performance of the cells. It was also shown that the basicity of the chemical bath cannot be reduced to avoid the deposition of $Cd(OH)_2$ on the surface as it will simply reduce the load of the sensitizer on the surface and may leave some parts of the TiO_2 uncovered.

I believe that the nature of the attachment of the $CdSe_xS_{(1-x)}$ sensitizers on TiO_2 must be studied in depth in order to develop better strategies for sensitizing the TiO_2 film and improving electron injection, charge collection and impeding recombination through unwanted but necessary co-deposits such as $Cd(OH)_2$.

Chapter 7: Concluding Remarks and Contributions to the Original Research

Photoelectrochemical solar cells based on sensitization concept were the core of this research. Effect of the structure of the sensitizing terpyridine and dipyrazinil pyridine dyes on performance of the cells was studied in order to obtain insight about these dyes and their applications in dye-sensitized solar cells.

In addition, the effect of siliconized triarylamines and of the peripheral functional groups as HTM in DSSCs on cell performance was studied.

Cadmium chalcogenides as a promising sensitizing semiconductor was also studied and the preparation conditions were correlated to the performance of the cells. This part of my research was performed in order to study chemical bath deposition parameters and their influence on the structure and composition of deposited CdSeS.

According to the results presented in this thesis, the contributions to the original objectives of my research can be summarized as follows:

a) **Dye-Sensitized Solar Cells; Effects of dye structure and functionality on the Cells Performance**

A comprehensive study and comparison between terpyridine and dipyrazinil pyridine ruthenium sensitizers was performed. We demonstrated that:

i) Among these dyes, the terpyridine family are more efficient sensitizer for various reasons: (a) they have longer excited-state lifetime, which increases the electron injection efficiency of the dyes; (b) they have higher-located LUMO; and (c) they have stronger affinity for adsorption on the TiO_2 surface, which increases the load of the dyes on the surface and as a result, more photons are absorbed under illumination.

ii) The existence of aromatic rings between the aromatic rings of the terpyridine/dipyrazinil pyridine and the anchoring groups impedes the orbital overlap, decreases the electron injection and reduces the performance of the cells.

iii) The nature of the anchoring group, carboxylic acid or ester, has direct impact on the adsorption kinetics of the sensitizers, which then affects the light harvesting and electron injection based on the number of the attached dye on the surface. It was demonstrated that carboxylic acid-functionalized sensitizer have larger load of the adsorbed molecules on the TiO_2 surface and hence, higher photocurrent and efficiency. It was also shown that heating the solution of ester dye during the dye adsorption increases the rate of adsorption of these dyes and improves the cells performance with comparison to the films prepared from the same dye solution at room temperature.

iv) The performance of these sensitizers strongly depends on the composition of the electrolyte solution and how the additives in the electrolyte solution alter the energy levels of the TiO_2 particles. It was shown that the presence of the pyridine moieties and also solvents such as NMO, which are capable of raising the position of the TiO_2 conduction band, directly affects the performance of the cells by reducing the electron injection from the excited dye and hence reducing the photocurrent. Accordingly, the choice of the electrolyte solution is important when making cells with terpyridine and dipyrazinil pyridine ruthenium sensitizers.

b) Hole-Transport Materials: Silicon-Based Triarylamines as Redox Mediator in Dye-Sensitized Solar Cells

Siliconized triarylamines were used as hole-transport material in dye-sensitized solar cells and high photovoltages were obtained under standard measurement conditions. It was shown that:

i) Siliconized triarylamines can achieve unprecedented photovoltages of more than 1 V with simple manufacturing and measurement techniques.

ii) The presence of OTIPS is essential for the redox role of such HTMs and it was shown that the removal of such group nullifies the redox activity of the HTM in the cells.

iii) Recombination rates in cells fabricated with such triarylamines is faster than ordinary iodie/triiodie electrolytes and it was related to the recombination of electrons from the TiO_2 conduction band to the oxidized form of the HTM and also the pore-filling of the HTM in the matrix of TiO_2 which is less that I^-/I_3^-.

c) Semiconductor-Sensitized Solar Cells; Cadmium Selenosulfides as Sensitizers and Preparation Effect on Cells Performance

Cadmium selenosulfides with different compositions and prepared from two most common chemical baths, NH_3 and NTA, were used as sensitizers and the performance of the cells was related to the preparative procedures , the resulting film structure, the energy levels and the composition of the sensitizers. To the best of our knowledge, there has been no such thorough study published with respect to $CdSe_xS_{(1-x)}$ sensitizers. We demonstrated that

i) The sensitizers prepared from NTA chemical baths are more efficient in light harvesting, electron injecting and have less recombination compared to the sensitizers deposited through NH_3 based chemical baths. It was

shown that film from NTA chemical baths have higher load of sensitizer deposited on the surface. However, in NTA chemical baths, the rate of selenide deposition is faster than that of NH_3 baths which will increase the load of the CdSe and hence widens the light absorption of the sensitizer. In addition to the higher load of sensitizer deposited from NTA increases the light harvesting of the films and electron injection.

ii) The presence of the co-deposited $Cd(OH)_2$ on the TiO_2 surface has direct effect on the recombination processes on the surface. The deposition of $Cd(OH)_2$ is shown to be dependent on the composition of the chemical bath used in sensitization and the relative Cd/complexing agent ratio and on the pH of the bath. Changing these parameters affected the deposition mechanism of the sensitizers, which determines the load of the $Cd(OH)_2$ on the surface. Removal of the $Cd(OH)_2$ through exchange of OH^- with S^{2-}, reduces the recombination and also increases the light absorption of the sensitizers. The films from NTA bath had less $Cd(OH)_2$ content and hence showed better performance as sensitizers.

iii) Films prepared from NTA chemical baths with $CdSe_{0.5}S_{0.5}$ structure are the most efficient cells among all the other structures prepared from the two different baths. Films prepared from NTA chemical baths with Cd/NTA and pH adjusted such that both cluster and ion-by-ion mechanism are present have better performances compared to the other ratios where only one

mechanism is present. This is explained by considering that a cluster mechanism could be dominant under the conditions used where initial deposition of $Cd(OH)_2$ is necessary for increasing the amount of the deposited sensitizer on the surface and the concurrent presence of ion-by-ion mechanism improves the quality of the deposited sensitizers by reducing the amount of $Cd(OH)_2$.

References

A

-Adams, W. G.; Day, R. E. Proc. R. Soc. Lond. A **1877,** *25,* 113-117.

- Al-mutlaq, F.A.; Potvin, P.G.; Philippopoulos, A.I.; Falaras, P. Europ. J. Inorg. Chem. **2007,** 2121-2128.

- An, J. M.; Franceschetti; A.; Dudiy, S. V.; Zunger, A. Nano Letters **2006,** *6,* 2728-2735.

- Anandan, S.; Latha, S.; Maruthamuthu, P. J. Photochem. Photobiol. A: Chem. **2002,** *150,* 167-175.

- Anderson, N. A.; Lian, T. Coord. Chem. Rev. **2004,** *248,* 1231-1246.

- Anikeeva, P. O.; Halpert, J. E.; Bawendi, M. G.; Bulovic, V. Nano Letters **2009,** *9,* 2532-2536.

-Archer, M. D.; Nozik, A. J. Nanostructured and photoelectrochemical systems for solar photon conversion, Imperial College Press: London, 2008.

-Ardo, S.; Meyer, G. J. Chem. Soc. Rev. **2009,** *38,* 115-164.

B

-Balzani, V.; Juris, A. Coord. Chem. Rev. **2001,** *211,* 97-115.

-Barbé, C. J.; Arendse, F.; Comte, P.; Jirousek, M.; Lenzmann, F.; Shklover, V.; Gratzel, M. J. Am. Ceram. Soc **1997,** *80,* 3157-3171.

- Barigelletti, F.; Flamigni, L.; Balzani, V.; Collin, J. P.; Sauvage, J. P.; Sour, A.; Constable, E. C.; Cargill-Thompson, A. M. W. J. Chem. Soc. Chem. Commun. **1993,** *11,* 942-944.

- Beard, M. C.; Midgett, A. G.; Law, M.; Semonin, O. E.; Ellingson, R. J.; Nozik, A. J. Nano Letters **2009,** *9,* 836-845.

-Becquerel ,A. E., Comtes Rendus de l'Academie des Sciences, **1839,** *9,* 31-33.

-Becquerel, A. E. C. R. C. R. Acad. Sci. Paris, **1872,** *75,* 296-303.

- Bender, T. P.; Graham, J. F.; Duff, J. M. Chem. Mater. **2001,** *13,* 4105-4511.

- Benko, G.; Kallioinen, J.; Korppi-Tommola, J. E. I.; Yartsev, Villy, A. P. S. J. Am. Chem. Soc. **2002,** *124,* 489-493.

- Benkstein, K.D.; Kopidakis, N.; van de Lagemaat, J.; Frank, A.J. J. Phys. Chem. B **2003,** *107,* 7759-7767.

-Biancardo, M.; West, K.; Krebs, F. C. J. Photochem. Photobiol. A: Chem. **2007,** *187,* 395-401.

-Biancardo M.; West K.; Krebs F.C.; Sol. Energy Mater. Sol. Cells **2006,** *90,* 2575-2588.

-Bimberg, D., Semiconductor Nanostructures, Springer: Berlin, 2008.

-Bisquert, J.; Cahen, D.; Hodes, G.; Ruhle, S.; Zaban, A. J. Phys. Chem. B **2004a,** *108,* 8106-8118.

-Bisquert, J.; Zaban, A.; Greenshtein, M.; Mora-Sero, I. J. Am. Chem. Soc. **2004b,** *126,* 13550-13559

-Blackburn, J. L.; Selmarten, D. C.; Nozik, A. J. J. Phys. Chem. B **2003,** *107,* 14154-14157.

-Burfeindt, B.; Hannappel, T.; Storck, W.; Willig, F. J. Phys. Chem. **1996,** *100,* 16463-16465.

-Burschka,J.; Brault, V.; Ahmad, S.; Breau, L.; Nazeeruddin, M. K.; Marsan, B.; Zakeeruddin, S. M.; Gratzel, M. Energy Environ. Sci. **2012,** *5,* 6089-6097.

-Burschka, J.; Dualeh, A.; Kessler, F.; Baranoff, E.; Cevey-Ha, N-L.; Yi, C.; Nazeeruddin, M. K. J. Am. Chem. Soc. **2011,** *133,* 18042-18045.

C

-Cahen, D., Hodes, G.; Gratzel, M.; Guillemoles, J. F.; Riess, I. J. Phys. Chem. B **2000,** *104,* 2053-2059.

-Cameron, P. J.; Peter, L. M.; Hore, S. J. Phys. Chem. B **2005,** *109,* 930-936.

-Cameron, P. J.; Peter, L. M.; Zakeeruddin, S. M.; Gratzel, M. Coord. Chem. Rev. **2004,** *248,* 1447-1453.

-Campbell W. M., Burrell, A. K.; Office, D. L.; Jolley, K. W. Coord. Chem. Rev. **2004,** *248,* 1363-1379.

-Cao, F.; Oskam, G.; Meyer, G. J.; Searson, P. C. J. Phys. Chem. B **1996**, *100,* 17021-17027.

-Chaudhari, J.B.; Deshpande, N.G.; Gudage, Y.G.; Ghosh, A.; Huse, V.B.; Sharma R. Appl. Surf. Sci. **2008,** *254,* 6810-6816.

-Chi, C.; Cho, H.; Teng, H.; Chuang, C.; Chang, Y.; Hsu, Y.; Lee, Y. Appl. Phys. Lett. **2011,** *98,* 012101.

-Choi, J. J.; Lim, Y.-F.; Santiago-Berrios, M. E. B.; Oh, M.; Hyun, B.-R.; Sun, L.; Bartnik, A. C.; Goedhart, A.; Malliaras, G. G.; Abruna, H. D.; Wise, F. W.; Hanrath, T. Nano Lett. **2009,** *9,* 3749 -3755.

-Corer, S.; Hodes, G. J. of Phys. Chem. 1994, 98, 5338-5346.

-Crutchley, R. J.; Lever, A.B.P. Inorg. Chem. **1982,** *21,* 2276-2282.

-Czochralski, J. Z. Phys. Chem. **1918,** *92,* 219-221.

D

-Dare-Edwards, M. P.; Goodenough, J. B.; Hamnet, A.; Seddon, K. R.; Wright, R. D. Photochemistry, Faraday Disc. Chem. Soc. **1980,** *70,* 285-290.

-Desilvestro, J.; Gratzel, M.; Kavan, L.; Moser, J.; Augustynski, J. J. Am. Chem. Soc. **1985,** *107,* 2988-2990.

-Diamant, Y.; Chappel, S.; Chen, S.G.; Melamed, O.; Zaban, A. Coord. Chem. Rev. **2004,** *248,* 1271-1276.

-Diguna, L. J.; Shen, Q.; Kobayashi, J.; Toyada, T. Appl. Phys. Lett. **2007,** *91,* 023116.

-Durrant, J. R., Haque, S. A.; Palomares, E. Coord. Chem. Rev. **2004,** *248,* 1247-1257.

E

-Einstein, A. Ann. Phys. **1905,** *17,* 132-148.

-Ellingson, R. J.; Beard, M. C.; Johnson, J. C.; Yu, P.; Micic, O. I.; Nozik, A. J.; Shabaev, A.; Efros, A. L. Nano Lett. **2005,** *5,* 865-871.

-Ellis A. B.; Kaiser, S. W.; Bolts, J. M.; Wrighton, M. S. J. Am. Chem. Soc. **1977,** *99,* 2839-2848.

F

-Fritts, C. E., A. J. Sci. **1883,** *26,* 465-472.

-Fujishima, A.; Honda, K. Nature, **1972,** *238,* 37-38.

-Finnie, K. S.; Bartlett, J. R.; Woolfrey, L. Langmuir **1998,** *14,* 2744-2749.

-Ferber, J.; Luther, J. J. Phys. Chem. B 2**001**, *105,* 4895-4903.

-Fallahpour, R-A. Synthesis, **2003,** *2,* 155-184.

-Fitzmaurice, D. J.; Eschle, M.; Frei, H; Moser, J. J. Phys. Chem. **1993,** *97,* 3806-3812.

-Feldt, S. M.; Gibson, E. A.; Gabrielsson, E.; Sun, L.; Boschloo, G.; Hagfeldt, A. J. Am. Chem. Soc. **2010,** *132,* 16714-16724.

-Friedman, D.J. Curr. Op. Sol. Stat. Mat. Sci. **2010,** *14,* 131-138.

G

-Galoppini, E. Coord. Chem. Rev. **2004,** *248,* 1283-1297.

-Garcia, C.G.; Iha, M.; Argazzi, R.; Bignozzi, C. A. J. Braz. Chem. Soc. **1998,** *9,* 13-15.

-Garcia, C.G.; Iha, M. Int. J. Photoenergy **2001,** *3,* 131-135.

-Garcia, C.G.; Nakano, A. K.; Kleverlaan, C. J.; Iha, M. J. Photochem. Photobiol. A: Chem. **2002,** *151,* 165-171.

-Gerischer, H.; Tributsch, H. Ber. Bunsenges. Phys. Chem. **1968,** *72,* 437-445.

-Ginger, D. S.; Greenham, N. C. Phys. Rev. B **1999,** *59,* 10622-10629.

-Gomez-Jahn, L. A.; Miller, R. J. D. J. Chem. Phys. **1992**, *96,* 3981-3995.

-Gorer, S.; Hodes, G. J. Phys. Chem. **1994,** *98,* 5338 -5346.

-Gorer, S.; Albu-Yaron, A.; Hodes, G. J. Phys. Chem. **1995,** *99,* 16442-16448.

-Gratzel, M. Energy Resources through Photochemistry and Catalysis, New York: Academic Press, 1983.

-Gratzel, M. Nature **2001,** *414,* 338-344.

-Gratzel, M. Inorg. Chem. **2005,** *44,* 6841-6851.

-Gratzel, M. J. Photochem. Photobiol. C: Photochem. Rev. **2003,** *4,* 145-153.

-Gratzel, M.; Moser, J. E. Balzani, V. In Electron Transfer in Chemistry, Wiley-VCH: Weinheim, 2001.

-Green, M. A.; Emery, K.; Hishikawa, Y.; Warta, W.; Dunlop, E. D. Prog. Photovolt: Res. Appl. **2013,** *21,* 1–11.

-Greenham, N. C.; Peng, X.; Alivisatos, A. P. Phys. Rev. B **1996,** *54,* 17628-17637.

-Gregg B. A. Coord. Chem. Rev. **2004,** *248,* 1215-1224.

-Gregg B. A. J. Phys. Chem. B **2003,** *107,* 4688-4698.

-Gregg, B.A.; Pichot, F; Ferrere, S.; Fields, C.L. J. Phys Chem. B, **2001,** 105, 1422-1429.

H

-Hagfeldt, A.; Gratzel, M. Chem. Rev. **1995,** *95,* 49-68.

-Hagfeldt, A.; Gratzel, M. Acc. Chem. Res. **2000,** *33,* 269-277.

-Hetsch, F.; Xu, X.;, Wang, H.; Kershaw, S. V.; Rogach, A. L. J. Phys. Chem. Lett. **2011,** *2,* 1879-1887.

-Hodes, G. J. Phys. Chem. C **2008,** *112,* 17778-17787.

-Hodes, G. Adv. Mater. **2007,** *19,* 639-655.

-Hagfeldt, A.; Boschloo, G.; Lindstrom, H.; Figgemeier, E.; Holmberg, A.; Aranyos, V.; Magnusson, E.; Malmqvist, L. Coord. Chem. Rev. 2004, 248, 1501.

-Hagfeldt A., Boschloo, G.; Sun, L.; Kloo, L.; Pettersson, H. Chem. Rev. **2010,** *110,* 6595-6663.

-Hodes, G.; Manassen, J.; Cahen, D. J. Appl. Electrochem. **1977a,** *7,* 182-182.

-Hodes, G.; Manassen, J.; Cahen, D. J. Electrochem. Soc. **1977b,** *127,* 544-549.

-Haque, S. A.; Tachibana, Y.; Klug, D. R.; Durrant, J. R. J. Phys. Chem. B **1998,** *102,* 1745-1749.

-Haque, S. A.; Palomares, E.; Cho, B. M.; Green, A. N. M.; Hirata, N.; Klug, D. R.; Durrant, J. R. J. Am. Chem. Soc. **2005,** *127,* 3456-3462.

-Haque, S. A.; Tachibana, Y.; Willis, R. L.; Moser, J. E.; Gratzel, M.; Klug, D. R.; Durrant, J. R. J. Phys. Chem. B **2000,** *104,* 538-547.

-Hara K., Sugihara, H.; Singh, L.P.; Islam, A.; Katoh, R.; Yanagida, M.; Sayama, K.; Murata, S.; Arakawa, H. J. Photochem. Photobiol. A: Chem. **2001a,** *145,* 117-122.

-Hara, K.; Nishikawa, T. Kurashige, M.; Kawauchi, T.; Kashima, T.; Sayama, K.; Aika, K.; Arakawa, H. Sol. Energ. Mat. Sol. Cell **2005,** *85,* 21-30.

-Hara K., Sugihara, H.; Tachibana, Y.; Islam, A.; Yanagida, M.; Sayama, K.; Arakawa, H.; Fujihashi, G.; Horiguchi, T.; Kinoshita, T. Langmuir **2001b,** *17,* 5992-5999.

-Hodes, G. Phys. Chem. Chem. Phys. **2007,** *9,* 2181-2196

-Hodes, G. Chemical Solution Deposition of Semiconductor Films, Marcel Dekker Inc: New York, NY, 2003.

-Huang, S.Y.; Schlichthörl, G.; Nozik, A. J.; Gratzel, M.; Frank, A. J. J. Phys. Chem. B **1997,** *101,* 2576-2582.

-Haga, M-A.; Dodsworth, E. S.; Eryavec, G.; Seymour, P.; Lever, A.B.P. Inorg. Chem. **1985,** *24,* 1901-1906.

-Hodes, G.; Albu-Yaron, A.; Decker, F.; Motisuke, P. Phys. Rev. B **1987,** *36,* 4215-4221.

-Huynh, W. U.; Dittmer, J. J.; Alivisatos, A. P. Science **2002,** *295,* 2425-2427.

-Hillhouse, H. W.; Beard, M. C. Curr. Opin. Colloid Interface Sci. **2009,** *14,* 245-259.

-Hendrickx, E.; Guenther, B. D.; Zhang, Y.; Wang, J. F.; Staub, K.; Zhang, Q.; Marder, S. R.; Kippelen, B.l.; Peyghambarian, N. Chem. Phys. **1999,** *245,* 407-415.

-Hamann, T. W., Ondersma, J. W. Energy Environ. Sci. **2011,** *4,* 370-381.

I

-Islam A., Sugihara, H.; Hara, K.; Singh, L.P.; Katoh, R.; Yanagida, M.; Takahashi, Y.; Murata, S.; Arakawa, H. J. Photochem. Photobiol. A: Chem. **2001,** *145,* 135-145.

-Isborn, C. M.; Kilina, S. V.; Li, X.; Prezhdo, O. V. J. Phys. Chem. C **2008,** *112,* 18291-18294.

J

-Juris, A.; Bariagelleti, F.; Campagna, S.; Balzani, V.; Belser, P.; von Zelewsky, A. Coord. Chem. Rev. **2001,** *84,* 85-277.

-Jdira, L.; Liljeroth, P.; Stoffels, E.; Vanmaekelbergh, D.; Speller, S. Phys. Rev. B **2006,** *73,* 115305.

K

-Kainthla, R. C.; Payanda, D. K.; Chopra, K. L. J. Electrochem. Soci. **1982,** *129,* 99-102.

-Kalyanasundaram K., Graatzel M.; Photosensitization and photocatalysis using inorganic and organometallic compounds, Dordrecht; Kluwer Academic Publishers: Boston, 1993.

-Kalyanasundaram, K. Dye-sensitized solar cells, CRC Press: Boca Raton, Fla, 2010.

-Kalyanasundaram, K.; Gratzel, M. Coord. Chem. Rev. **1998,** *177,* 347-414.

-Kamino, B. A.; Castrucci, J.; Bender, T. P. Silicon **2011,** *3,* 125-137.

-Kamat, P., V. Chem. Rev. **1993,** *93,* 207-300.

-Kamat, P.V.; Gevaert, M.; Vinodgopal, K. J. Phys. Chem. B **1997,** *101,* 4422-4427.

-Kamat, P. V. J. Phys. Chem. C **2008,** *112,* 18737-18753.

-Kan, S.; Mokari, T.; Rothenberg, E.; Banin, U. Nat. Mater. **2003,** *2,* 155-158.

-Katoh R.; Furube A.; Barzykin A. V.; Arakawa H.; Tachiya M. Coord. Chem. Rev. **2004,** *248,* 1195-1213

-Kato, F.; Hayashi, N.; Murakami, T.; Okumura, C.; Oyaizu, K.; Nishide, H. Chem. Lett. **2010,** *39,* 464-465.

-Kazmerski, L. L. NREL/CP-520-28407, **2000,** 1-7. http://www.nrel.gov/docs/fy00osti/28407.pdf (Accessed on May 01, 2013)

-Kietzmann, R.; Willig, F.; Weller, H.; Vogel, R.; Nath, D. N.; Eichberger, R.; Liska, P.; Lehnert, J. Mol. Cryst. Liq. Cryst. **1991,** *194,* 169-180.

-Kiwi, J.; Kalyanasundaram, K.; Gratzel, M. Struct. Bonding **1982,** *49,* 37-125.

-Kopidakis, N.; Schiff, E.A.; Park, N.-G.; van de Lagemaat J.; Frank, A. J. J. Phys. Chem. B **2000,** *104,* 3930-3936.

-Kocha, S.W.; Meier, T.; Hoyera, W.; Kira, M. Physica E **2002,** *14,* 45-52.

-Kron, G.; Egerter, T.; Werner, J. H.; Rau, U.; J. Phys. Chem. B **2003,** *107,* 3556-3564.

-Kumar S.; Scholes G. D. Microchim. Acta, **2008,** *160,* 315-325.

-Kusama, H.; Orita, H.; Sugihara, H. Langmuir **2008,** *24,* 4411-4419.

L

-Lambert, C.; Noll, G. J. Am. Chem. Soc. **1999,** *121,* 8434-8442.

-Lee, H. J.; Yum, J-H.; Leventis, H C.; Zakeeruddin, S. M.; Haque, S. A.; Chen, P.; Seok, S.; Gratzel, M.; Nazeeruddin, M. K. J. Phys. Chem. C **2008,** *112,* 11600-11608.

-Lees, A.C.; B. Evrard, T.E. Keyes, J.G. Vos, C.J. Kleverlaan, M. Alebbi, C.A. Bignozzi, Eur. J. Inorg. Chem. **1999,** 2309-2317.

-Leschkies, K. S.; Beatty, T. J.; Kang, M. S.; Norris, D. J.; Aydil, E. S. ACS Nano **2009,** *3,* 3638-3648.

-Lewis, N. S. Annu. ReV. Phys. Chem. **1991,** *42,* 543-580.

-Li, Y.X.; J. Hagen, W. Schaffrath, P. Otschik, D. Haarer, Sol. Energy Mater. Sol. Cells **1999,** *56,* 167-178.

-Licht, S.; Tenne, R.; Dagan, G.; Hodes, G.; Manassen, J.; Cahen, D.; Appl. Phys. Lett., **1985a,** *46,* 608-610.

-Licht, S.; Manassen, J.; J. Electrochem. Soc.: Electrochem. Sci. Tech. **1985b,** *132,* 1076-1081.

-Licht, S.; Tenne, R.; Flaisher, H.; Manassen, J.; J. Electrochem. Soc. **1986,** *133,* 52-59.

-Licht, S.; Manassen, J.; J. Electrochem. Soc. **1984,** *132,* 1076-1081.

-Liegghio, R.; Potvin, P.G.; Lever, A.B.P. Inorg. Chem. **2001,** *40,* 5485-5486.

-Lifshitz, E.; Dag, I.; Litvin, I.; Hodes, G.; Gorer, S;, Reisfeld, R.; Zelner, M.; Minti, H. Chem. Phys. Lett. **1998,** *288,* 188-196.

-Liy, Y. J., J.R.; Oarameswaran, M.; Wang, Q. Energy Environ. Sci. **2011,** *4,* 564-571.

-Loef, R.; Houtepen, A. J.; Talgorn, E.; Schoonman, J.; Goossens, A. Nano Letters **2009,** *9,* 856-859.

-Luque A.; Hegedus S. Handbook of photovoltaic science and engineering, Hoboken, Wiley: NJ, 2003.

M

-Maestri, M.; Armaroli, N.; Balzani, V.; Constable, E.C.; Cargill Thompson, A. M. W. Inorg. Chem. **1995,** *34,* 2759-2767.

-Mane, R. S.; Lokhande, C. D.; Thin Solid Films **1997,** 304, 56-60.

-Mane, R. S.; Lokhande, C. D.; Mate. Chem. Phys. **2000,** *65,* 1-31.

-Marinado, T.; Nonomura, K.; Nissfolk, J.; Karlsson, M. K.; Hagberg, D. P.; Sun, L.; Mori, S.; Hagfeldt, A. Langmuir **2010,** *26,* 2592-2598.

-Markvart, T.; Castanner, L. Practical Handbook of Photovoltaics : Fundamentals and Applications, Elsevier: Oxford, New York, 2003.

-Meissner, D.; Lauermann, I.; Memming, R.; Kastening, B. J. Phys. Chem. **1988,** *92,* 3484-3488.

-Memming, R.; Semiconductor Electrochemistry, WILEY-VCH Verlag GmbH: Weinheim, Germany, 2001.

-Mora-Sero, I.; Gimenez, S.; Moehl, T.; Fabregat-Santiago, F.; Lana-Villareal, T.; Gomez, R.; Bisquert, J. Nanotechnology, **2008,** *19,* 424007.

-Mosurkal, R.; S. Roy, J. Kumar, L.A. Samuelson, S.K. Tripathy, J. Macromol. Sci. Pure **2002,** *A39,* 1195-1206.

-Mueller, N.; Tenne, R.; Cahen, D. J. Electroanal. Chem. **1981,** *130,* 373-379.

-Murakoshi, K.; Kano, G.; Wada, Y.; Yanagida, S.; Miyazaki, H.; Matsumoto, M.; Murasawa, S. J. Electroanal. Chem. **1995,** *396,* 27-34.

N

-Nakade, S.; Makimoto. Y.; Kubo, W.; Kitamura, T.; Wada, Y.; Yanagida, S. J. Phys. Chem. B, **2005,** *109,* 3488-3493.

-Namba, S.; Hishiki, Y. J. Phys. Chem. **1965,** *69,* 774-779.

-Nazeeruddin, M. K.; Kay, A.; Rodicio, R.; Humpbry-Baker, R.; Miiller, E.; Liska, P.; Vlachopoulos, N.; Gratzel, M. J. Am. Chem. Soc. **1993,** *115,* 6382-6390.

-Nazeeruddin, M., K.; Müller, Humphry-Baker, E., R.; Vlachopoulos, N.; Gratzel, M. J. Chem. Soc. Dalton Trans. **1997,** 4571.

-Nazeeruddin, M. K.; Pechy, P.; Renouard. T.; Zakeeruddin, S. M.; Humphry-Baker, R.; Comte, P.; Liska, P.; Cevey, L.; Costa, E.; Shklover, V.; Spiccia, L.; Deacon, G. B.; Bignozzi, C. A.; Gratzel, M. J. Am. Chem. Soc. **2001,** *123,* 1613-1624.

-Nazeeruddin Md. K., Zakeeruddin, S. M.; Lagref, J.-J.; Liska, P.; Comte, P.; Barolo, C.; Viscardi, G.; Schenk, K.; Gratzel, M. Coord. Chem. Rev. **2004,** *248,* 1317-1328.

-Nazeeruddin Md. K., Klein, C.; Liska, P.; Gratzel, M. Coord. Chem. Rev. **2005,** *249,* 1460-1467.

-Nelson, J. The Physics of Solar Cells, Imperial College Press: London, 2003.

-Niesen, T. P.; De Guire, M. R. Solid State Ionics **2002,** *151,* 61-68.

-Niitsoo, O.; Sarkar, S. K.; Pejoux, C; Ruhle, S.; Cahen, D.; Hodes, G. J. Photochem. Photobiol. A. **2006,** *181,* 306-313.

-Nozik, A. J. Physica E **2002,** *14,* 115-120.

O

-Ohl, R., Light Sensitive Electric Device, US patent 2402662, 1946.

-O'Regan, B.; Gratzel, M. Nature **1991,** *353,* 737-740.

-O'Regan, B. C.; Durrant, J. Acc. Chem. Res. **2009,** *42,* 1799-1808.

-Oskam, G.; Bergeron, B.V.; Meyer, G.J.; Searson, P.C. J. Phys. Chem. B **2001,** *105,* 6867-6873.

-Onsager, L.; R.M. Fuoss, J. Phys. Chem. **1932,** *36,* 2689-2778.

P

-Patthey, L.; Rensmo, H.; Persson, P.; Westermark, K.; Vayssieres, L.; Stathans, A.; Petersson, A.; Brühwiler, P. A.; Siegbahn, H.; Lunell, S.; Martensson, N. J. Chem. Phys.**1999,** *110,* 5913-5918.

-Perlin J. From Space to Earth : the story of solar electricity, Ann Arbor, Aatec Publications: Mich, 1999.

-Peter, L. M. J. Phys. Chem. C **2007a,** *111,* 6601-6612.

-Peter, L. M. Phys. Chem. Chem. Phys. **2007b,** *9,* 2630-2642.

-Pichot, F.; Gregg, B. A. J. Phys. Chem. B 2000, 104, 6-10.

-Polo A. S.; Itokazu, M. K.; Iha, N. Y. M. Coord. Chem. Rev. **2004,** *248,* 1343-1361.

-Protasenko, V.; Bacinello, D.; Kuno, M. J. Phys. Chem. B, **2006,** *110,* 25322-25331.

R

-Rajeshwar, K., Encyclopedia of Electrochemistry: Fundamentals of Semiconductor Electrochemistry and Photoelectrochemistry; Edited By Bard, A. J.; Stratmann, M.; Pages 1-52, Wiley-VCH, 2006.

-Ramamurthy, V.; Schanze K. S. Semiconductor photochemistry and photophysics, New York: Marcel Dekker, 2003.

-Remacle, F.; Collier, C. P.; Markovich, G.; Heath, J. R.; Banin, U.; Levine, R. D.; J. Phys. Chem. B **1998,** *102,* 7727-7734.

-Ribierre, J. C.; Aoyama, T.; Muto, T.; Imase, Y.; Wada, T. Org. Electron. **2008,** *9,* 396-400.

-Rinke, T. J.; Bergmann, R. B.; Werner, J. H. Appl. Phys. A **1999,** *68,* 705-707.

-Ristic, M.; Popovic, S.; Music, S. Mat. Lett. **2004,** *58,* 2494-2499.

-Ribierre, J.; Aoyama, T.; Kobayashi, T.; Sassa, T.; Muto, T.; Wada, T. J. Appl. Phys. **2007,** *102,* 033106.

-Robel, I.; Subramanian, V.; Kuno, M.; Kamat, P. V. J. Am. Chem. Soc. **2006,** *128,* 2385-2393.

-Robel, I.; Kuno, M.; Kamat, P.V. J. Am. Chem. Soc. **2007,** *129,* 4136-4137.

-Robertson N.; Angew. Chem. Int. Ed. **2006,** *45,* 2338-2345.

-Rogach, A. L.; Katsikas, L.; Kornowski, A.; Su, D.; Eychmller, A.; Weller ,H. Ber. Bunsen Phys. Chem. **1996,** *100,* 1772-1778.

-Rogach, A. L.; Franzl, T.; Klar, T. A.; Feldmann, J.; Gaponik, N.; Lesnyak, V.; Shavel, A.; Eychmller, A.; Rakovich, Y. P.; Donegan, J. F. J. Phys. Chem. C **2007,** *111,* 14628-14637.

-Rosenheim, G.; Stadler, W.; Mayer, V. J. Zeitschrift für anorganische und allgemeine Chemie **1906a,** *49,* 1-444.

-Roy P.; Berger S.; Schmuki P. Angew. Chem. Int. Ed. **2011,** *50,* 2904-2939.

-Ruhle, S.; Greenwald, S.; Koren, E.; Zaban, A. Opt. Express **2008,** *16,* 21801-21806.

-Ruhle S.; Shalom M.; Zaban A. ChemPhysChem **2010,** *11,* 2290-2304.

S

-Santiago, F.F.; Belmonte, G.G.; Bisquert, J.; Zaban, A.; Salvador, P. J. Phys. Chem. B **2002,** *106,* 334-339.

-Sapp, S. A., C. Elliott, M.; Contado, C.; Caramori, S.; Bignozzi, C. A. J. Am. Chem. Soc. **2002,** *124,* 11215-11222.

-Sauvage, J-P.; Collin, J-P.; Chambron, J-C.; Gullerez, S.; Coudret, C.; Balzani, V.; Barigelletti, F.; Cola, L.; Flamingi, L. Chem. Rev. **1994,** *94,* 993-1019.

-Sayama, K.; Suguhara, H.; Arakawa, H. Chem. Mater. **1998,** *10,* 3825-3832.

-Schwarzburg, K.; Willig, F. J. Phys. Chem. B **1999,** *103,* 5743-5746.

-Schwarz, O.; van Loyen, D.; Jockusch, S.; Turro, N. J.; Dürr, H.; J. Photochem. Photobiol. A: Chem. **2000,** *132,* 91-246.

-Schlichthörl, G.; Huang, S.Y.; Sprague, J.; Frank, A. J. J. Phys. Chem. B **1997,** *101,* 8141-8155.

-Schiff, E.A. Sol. Energy Mater. Sol. Cells **2003,** *78,* 567-595.

-Schlichthörl, G.; Park, N.-G.; Frank, A. J. J. Phys. Chem. B **1999,** *103,* 782-791.

-Schaller, R. D.; Klimov, V. I. Phys. Rev. Lett. **2004,** *92,* 186601.

-Schwanitz, K.; Weiler, U.; Hunger, R.; Mayer, T.; Jaegermann, W J. Phys. Chem. C **2007,** *111,* 849-854.

-Sepehrifard, A.; Stublla, A.; Haftchenary, S.; Chen, S.G.; Potvin, P. G.; Morin, S. J. New Mat. Electrochem. Sys. **2008,** *11,* 281-285.

-Sepehrifard, A.; Kamino, B. A.; Bender, T. P.; Morin, S. ACS Appl. Mater. Interfaces **2012,** *4,* 6211-6215.

-Shah, A.; Meier, J.; Buechel, A.; Kroll, U.; Steinhauser, J.; Meillaud, F.; Schade, H.; Dominé, D. Thin Solid Films **2006,** *502,* 292-299.

-Shen, Q.; Katayama, K.; Yamaguchi, M.; Sawada, T.; Toyada, T. Thin Solid Films **2005,** *486,* 15-19.

-Shahane, G. S.; More, B. M.; Rotti, C. B.; Deshmukh, L. P. Mater. Chem. Phys. **1997a,** *47,* 263-265.

-Shahane, G. S.; Garadkar, K. M.; Deshmukh, L. P. Mater. Chem. Phys. **1997b,** *51,* 246-251

-Shahane, G. S.; Deshmukh, L. P. Mater. Chem. Phys, **2001,** *70,* 112.

-Shevchenko, E. V.; Ringler, M.; Schwemer, A.; Talapin, D. V.; T. Klar, A.; Rogach, A. L.; Feldmann, J.; Alivisatos, A. P. J. Am. Chem. Soc. **2008,** *130,* 3274-3275.

-Shirota, Y.; Kageyama, H. Chem. Rev. **2007,** *107,* 953-1010.

-Shoemaker, D.P.; Garland, C. W.; Steinfeld, J. I.; Nibler, J. W.; Experiments in Physical Chemistry, 4th edition, Mcgraw-Hill, New York, 1981.

-Smestad, G. P. Optoelectronics of Solar Cells, SPIE PRESS, Bellingham, Washinton, 2002.

-Smith, W. J. Soc. Telegraph Engineers, **1873,** *1,* 711-714.

-Snaith, H. J.; Zakeeruddin, S. M.; Wang, Q.; Peechy, P.; Gratzel, M. Nano Lett. **2006,** *6,* 2000-2003.

-Sodergren, S.; Hagfeldt, A.; Olsson, J.; Lindquist, S. E. J. Phys. Chem. **1994,** *98,* 5552-5556.

-Soloviev, N. V.; Eichhofer, A.; Fenske, D.; Banin, U. J. Am. Chem. Soc. **2001,** *123,* 2354-2364.

-Spokoyny, A. M.; Li, T. C.; Farha, O. K.; Machan, C. W.; She, C. X.; Stern, C. L.; Marks, T. J.; Hupp, J. T.; Mirkin, C. A. Angew. Chem., Int. Ed. **2010,** *49,* 5339-5343.

-Sugihara H., Singh, L.P.; Sayama, K.; Arakawa, H.; Nazeeruddin, M.K.; Gratzel, M. Chem. Lett. **1998,** *10,* 1005-1006.

-Stublla, A.; Potvin, P.G. Eur. J. Chem. **2010,** 3040-3050.

T

-Tachan, Z.; Ruhle, S.; Zaban, A. Sol. Energy Mater. Sol. Cells **2010,** *94,* 317-322.

-Tachibana, Y.; Umekita, K.; Otsuka, Y.; Kuwabata, S. J. Phys. Chem. C, **2009,** *113,* 6852-6858.

-Takagahara, T.; Takeda, K. Phys. Rev. B **1992,** *46,* 15578-15581.

-Takahashi, Y.; H. Arakawa, H. Sugihara, K. Hara, A. Islam, R. Katoh, Y. Tachibana, M. Yanagida, Inorg. Chim. Acta **2000,** *310,* 169-174.

-Tennakone, K.; Kumara, G. R. R. A.; Kottegoda, I. R. M.; Perera, V. P. S. Chem. Comm. **1999,** *15,* 15-16.

-Tenne, S.; Hodes, G. Appl. Phys. Lett. **1980,** *37,* 428-431.

-Tessler, N.; Medvedev, V.; Kazes, M.; Kan, S. H.; Banin, U. Science **2002,** *295,* 1506-1508.

-Tian, H. N.; Jiang, X. A.; Yu, Z.; Kloo, L.; Hagfeldt, A.; Sun, L. C. Angew. Chem., Int. Ed. **2010,** *49,* 7328–7331.

-Tributsch, H. Coord. Chem. Rev. **2004,** *248,* 1511-1530.

-Toivola, M.; Ferenets, M.; Lund, P.; Harlin, A.; Thin Solid Films **2009,** *517,* 2799-2802.

-Travino, M. R. Dye-Sensitized Solar Cells and Solar Cell Performance, Nova Science Pub Incorporated: Hauppauge, NY, 2011.

-Tsubomura, H.; Matsumura, M.; Noyamaura, Y.; Amamyiya, T. Nature **1976,** *261,* 402-403.

U

-US Department of Energy, The History of Solar, http://www1.eere.energy.gov/solar/pdfs/solar_timeline.pdf (Accessed on Nov 12, 2012)

V

-Van de Krol R.; Graatzel M.; Photoelectrochemical hydrogen production, Springer: New York, 2012.

-Van de Lagemaat , J.; Park, N.-G.; Frank, A. J.; J. Phys. Chem. B **2000,** *104,* 2044-2052.

-Van de Lagemaat, J.; Frank, A.J. J. Phys. Chem. B **2001,** *105,* 11194.

-Vanmaekelbergh, D.; de Jongh, P.E.; J. Phys. Chem. B **1999,** *103,* 747-450.

-Vogel, R.; Pohl, K.; Weller, H.; Chem. Phys. Lett. **1990,** *174,* 241-246.

-Vogel, R.; Hoyer, P.; Weller, H. J. Phys. Chem. **1994,** *98,* 3183-3188.

-Vougioukalakis, G. C.; Stergiopoulos, T.; Kantonis, G.; Kontos, A. G.; Papadopoulos, K.; Stublla, A.; Potvin, P. G.; Falaras, P. J. Photochem. Photobiol A: Chemistry **2010,** *214,* 22-32.

W

-Wang[a], H. X.; Nicholson, P. G.; Peter, L.; Zakeeruddin, S. M.; Gratzel, M. J. Phys. Chem. C **2010,** *114,* 14300-14306.

-Wang[b], M. K.; Chamberland, N.; Breau, L.; Moser, J. E.; Humphry-Baker, R.; Marsan, B.; Zakeeruddin, S. M.; Gratzel, M. Nat. Chem. **2010,** *2,* 385-389.

-Wang[c], A.; Zhao, J.; Wenham, S. R.; Green, M. A. Prog. Photovolt.: Res. & Appl. **1996,** *4,* 55-58.

-Weintraub, B.; Wei, Y.; Wang, Z. L. Angew. Chem. **2009a,** *121,* 9143-9147

-Weintraub, B.; Wei, Y.; Wang, Z. L. Angew. Chem. Int. Ed. **2009b,** *48,* 8981-8985.

-Wuister, S. F.; Houselt, A.; Mello Doneg, C.; Vanmaekelbergh, D.; Meijerink, A. Angew. Chem. (Inter. Ed.) **2004a,** *116,* 3091-3095.

-Wuister, S. F.; Houselt, A.; Mello Doneg, C.; Vanmaekelbergh, D.; Meijerink, A. Angew. Chem. Int. Ed. **2004b,** *43,* 3029-3033.

-Wurfel, P. Physica E **2002,** *14,* 18-26.

X

-Xie, P.-H.; Hou, Y.-J.; Wei, T.-X.; Zhang, B.-W.; Cao, Y.; Huang, C.-H. Inorg. Chim. Acta **2000,** *308,* 73-79.

-Xu[a],Y.; Schoonen, M. A. A. American Mineralogist **2000,** *85,* 543-556.

-Xu[b], D.; Adachi, C. Appl. Phys. Lett. **2009,** *95,* 053304.

Y

-Yanagida M.; Singh, L. P.; Sayama, K.; Hara, K.; Katoh, R.; Islam, A.; Sugihara, H.; Arakawa, H.; Nazeeruddin, M. K.; Gratzel, M. J. Chem. Soc., Dalton Trans. **2000,** 2817-2822.

-Yanagida, M.; Islam, A.; Tachibana, Y.; Fujihashi, G.; Katoh, R.; Sugihara, H.; Arakawa, H.; New J. Chem. **2002,** *8,* 963-265.

-Yin, X.; Zhao, H.; Chen, L.; Tan, W.; Zhang, J.; Weng, Y.; Shuai, Z.; Xiao, X.; Zhou, X.; Li, X.; Lin, Y. Surface and Interface Analysis **2007,** *39,* 809-816.

-Yochelis, S.; Hodes, G. Chem. Mater. **2004,** *16,* 2740-2744.

-Yu, W. W.; Qu, L.; Guo, W.; Peng, X. Chem. Mater. **2003,** *15,* 2854-2860.

Z

-Zaban, A.; Micic, O. I.; Gregg, B. A.; Nozik, A. J. Langmuir **1998,** *14,* 3153-3156.

-Zaban, A.; Greenshtein, M.; Bisquert, J. CHEMPHYSCHEM **2003,** *4,* 859-864.

-Zhu, K.; Neale, N.R.; Miedaner, A.; Frank, A. Nano Letters **2007,** *7,* 69-74.

Appendices

Appendix A: EDX Spectra of the $CdSe_xS_{(1-x)}$ Films Prepared from NH_3 and NTA Baths.

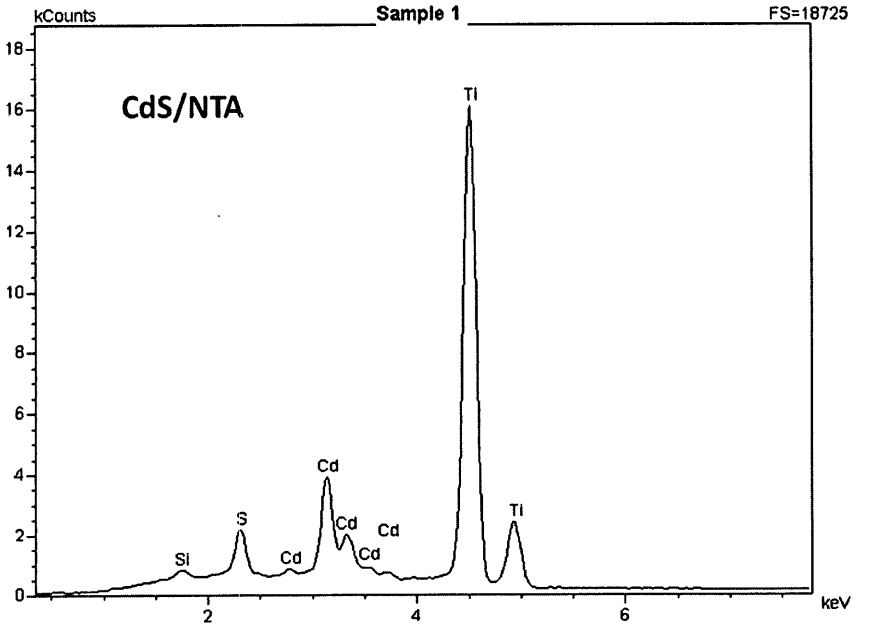

Figure A.1 EDX spectrum of TiO_2 film sensitized with CdS in NTA bath.

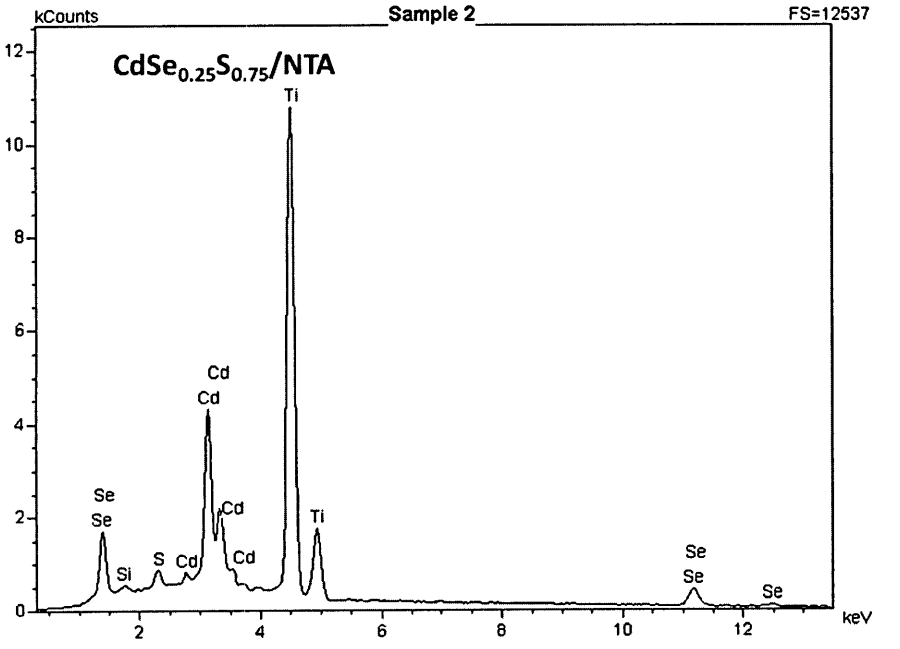

Figure A.2 EDX spectrum of TiO_2 film sensitized with $CdSe_{0.25}S_{0.75}$ in NTA bath.

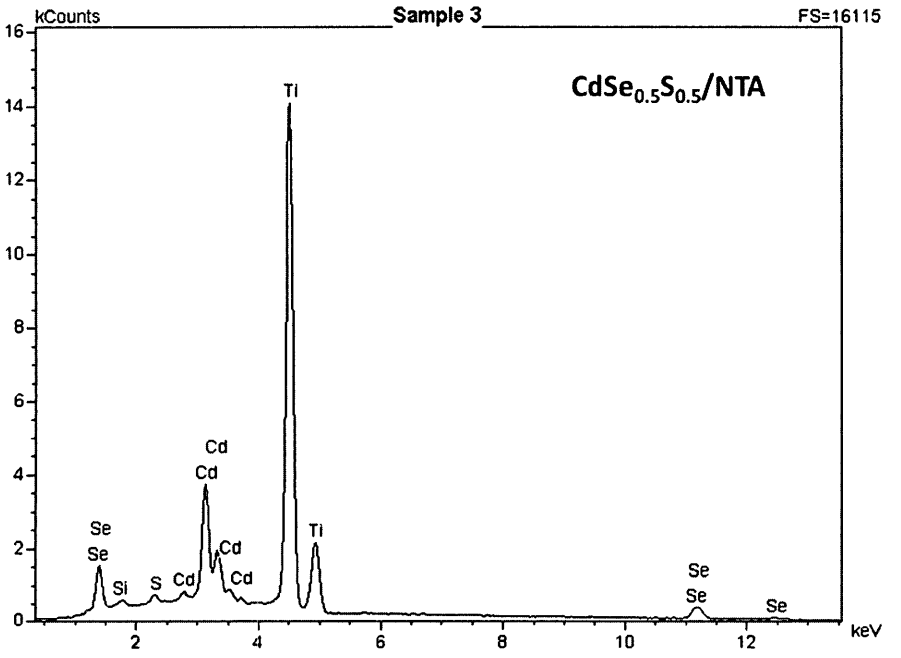

Figure A.3 EDX spectrum of TiO_2 film sensitized with $CdSe_{0.5}S_{0.5}$ in NTA bath.

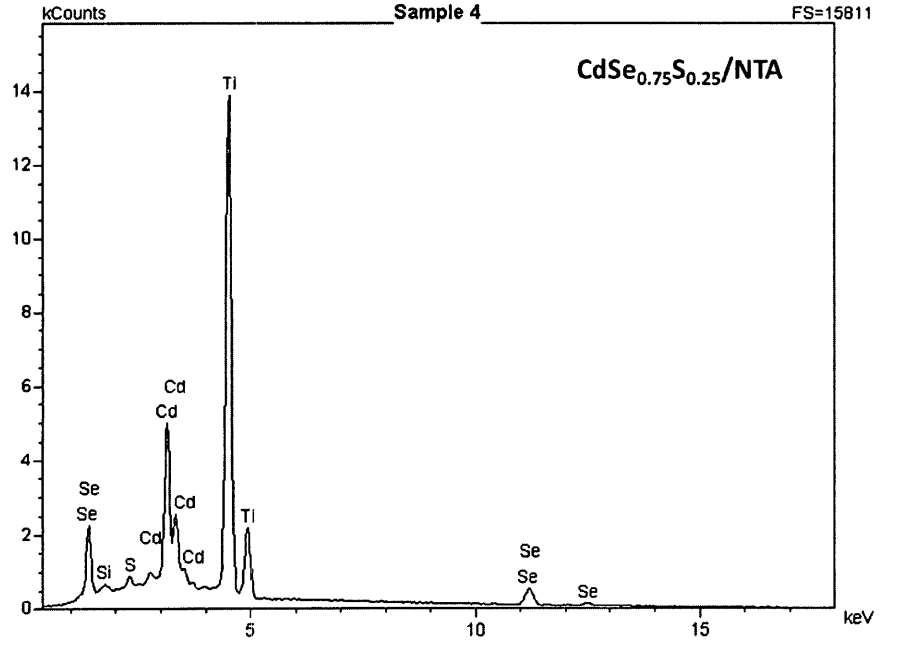

Figure A.4 EDX spectrum of TiO_2 film sensitized with $CdSe_{0.75}S_{0.25}$ in NTA bath.

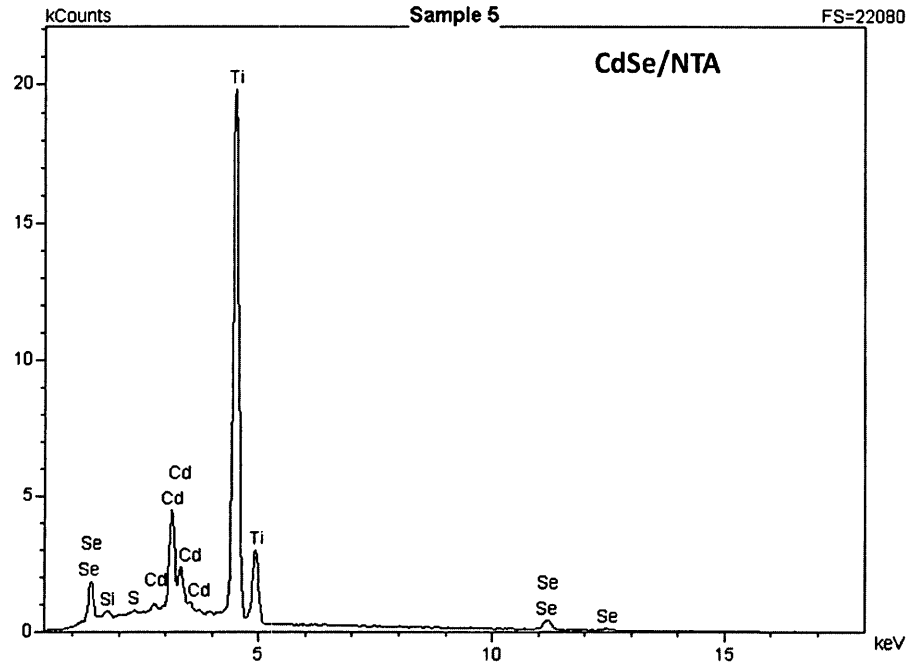

Figure A.5 EDX spectrum of TiO_2 film sensitized with CdSe in NTA bath.

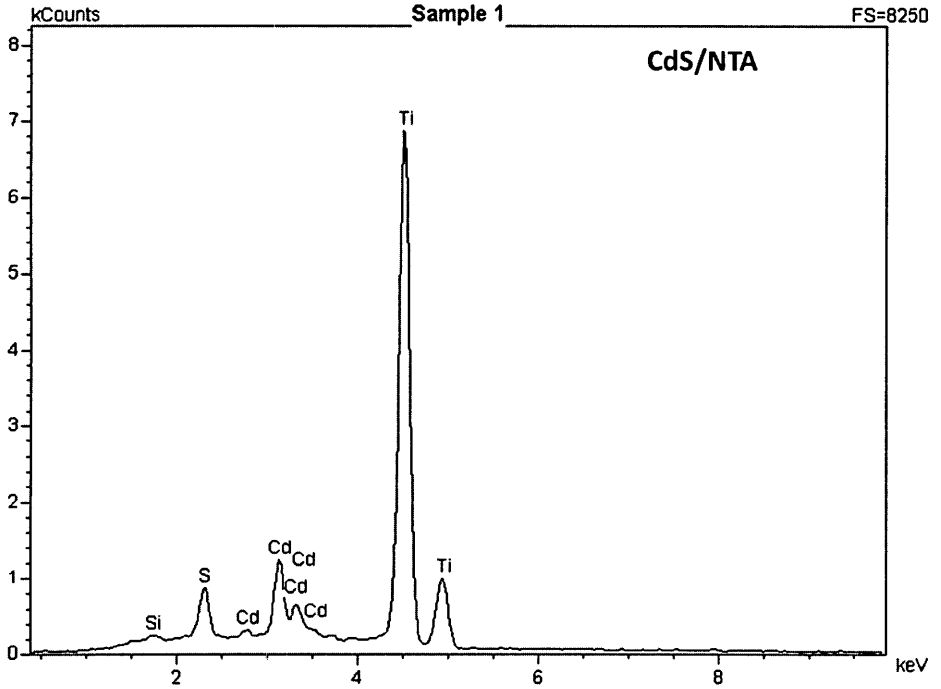

Figure A.6 EDX spectrum of TiO_2 film sensitized with CdS in NTA bath and post-treated with S^{2-}-rich solution.

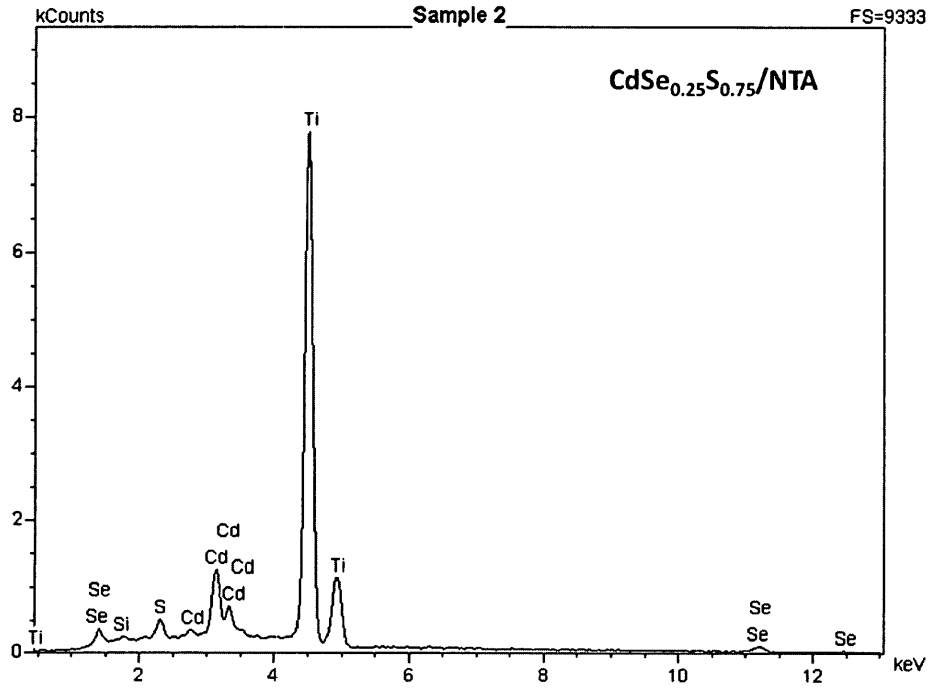

Figure A.7 EDX spectrum of TiO_2 film sensitized with $CdSe_{0.25}S_{0.75}$ in NTA bath and post-treated with S^{2-}-rich solution.

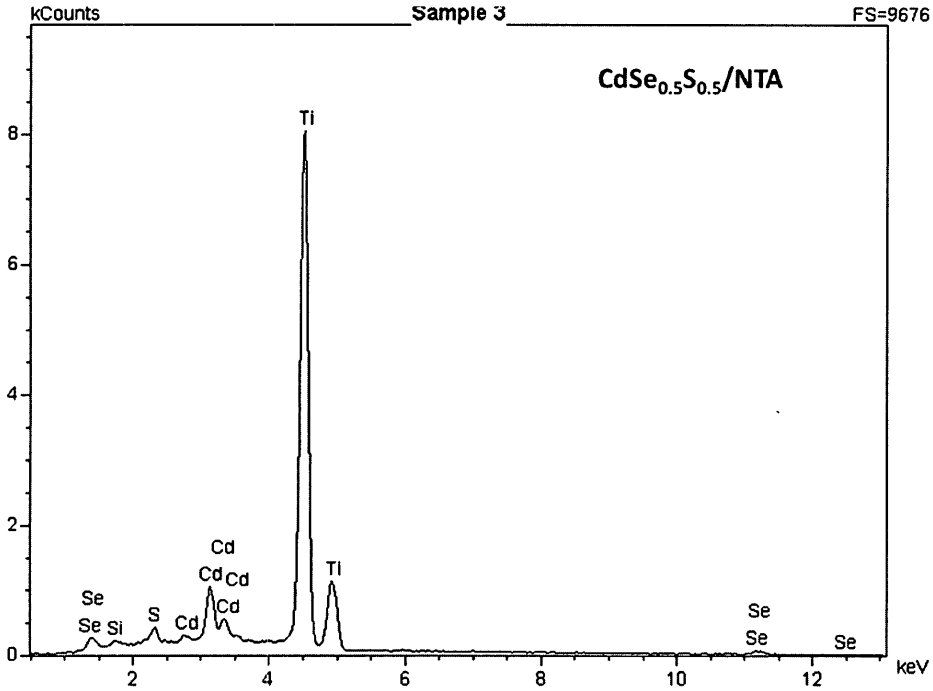

Figure A.8 EDX spectrum of TiO_2 film sensitized with $CdSe_{0.5}S_{0.5}$ in NTA bath and post-treated with S^{2-}-rich solution.

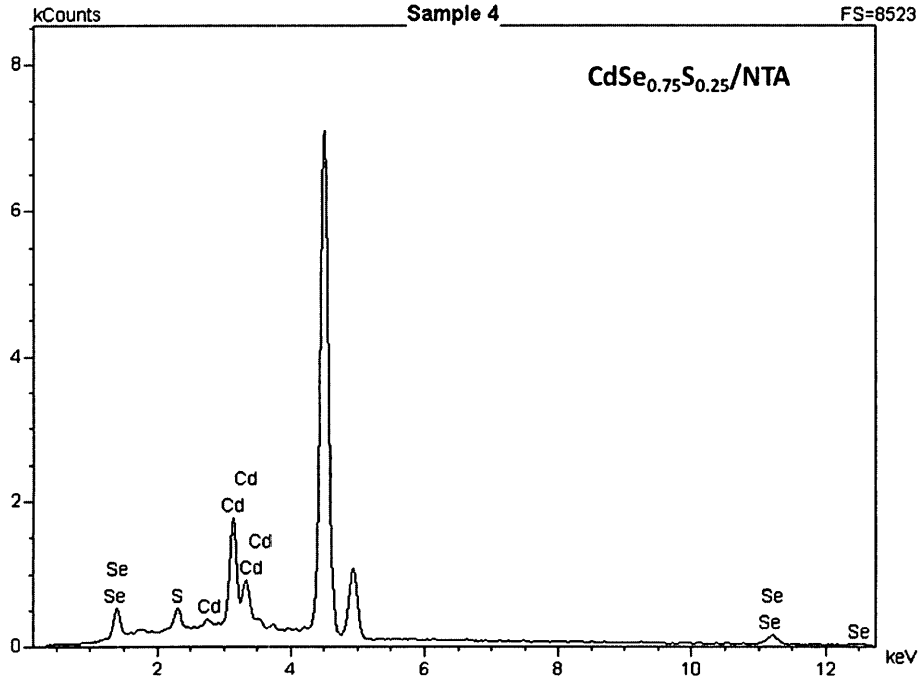

Figure A.9 EDX spectrum of TiO_2 film sensitized with $CdSe_{0.75}S_{0.25}$ in NTA bath and post-treated with S^{2-}-rich solution.

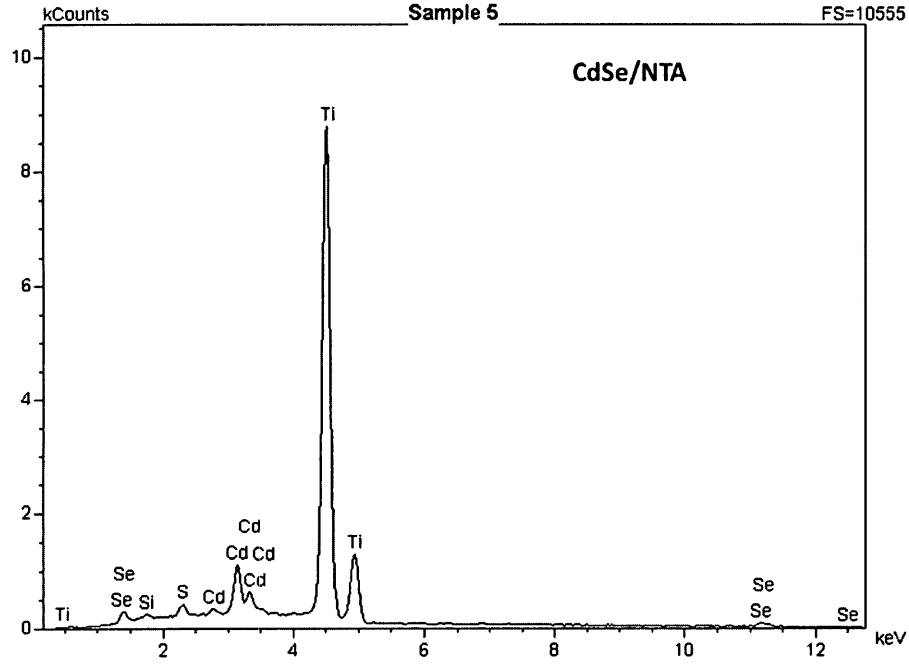

Figure A.10 EDX spectrum of TiO_2 film sensitized with CdSe in NTA bath and post-treated with S^{2-}-rich solution.

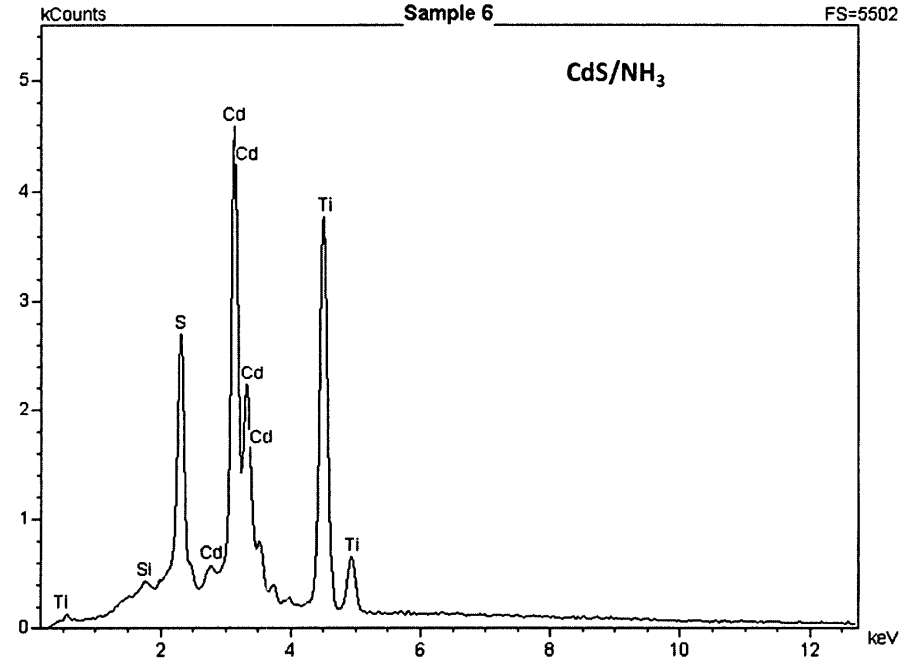

Figure A.11 EDX spectrum of TiO_2 film sensitized with CdS in NH_3 bath.

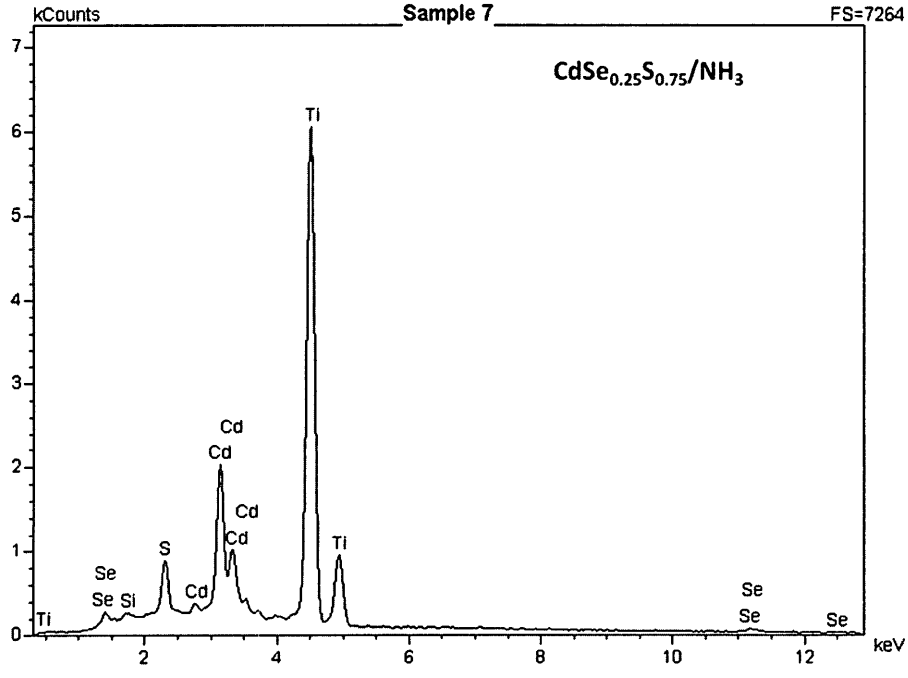

Figure A.12 EDX spectrum of TiO_2 film sensitized with $CdSe_{0.25}S_{0.75}$ in NH_3 bath.

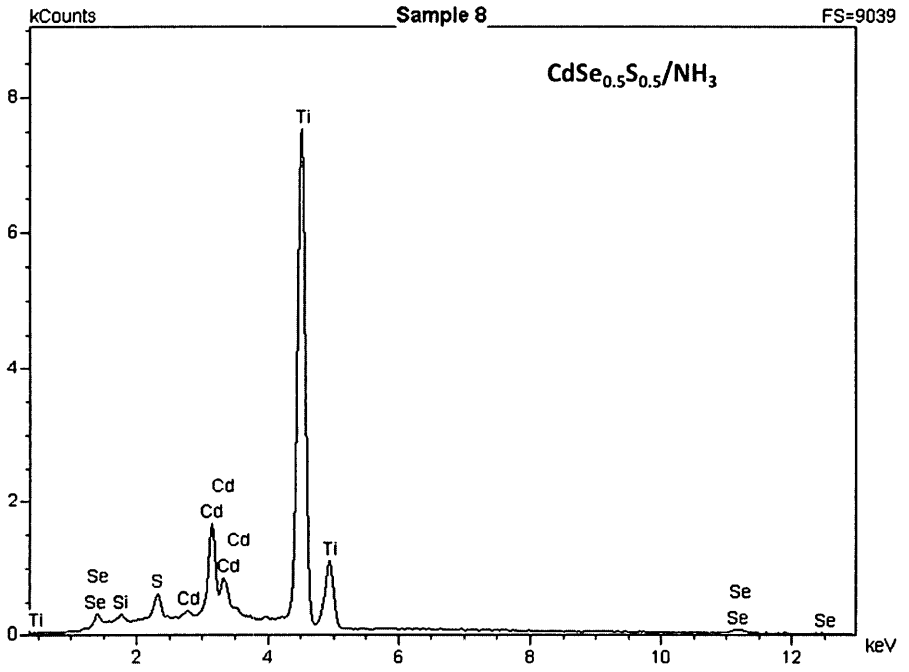

Figure A.13 EDX spectrum of TiO_2 film sensitized with $CdSe_{0.5}S_{0.5}$ in NH_3 bath.

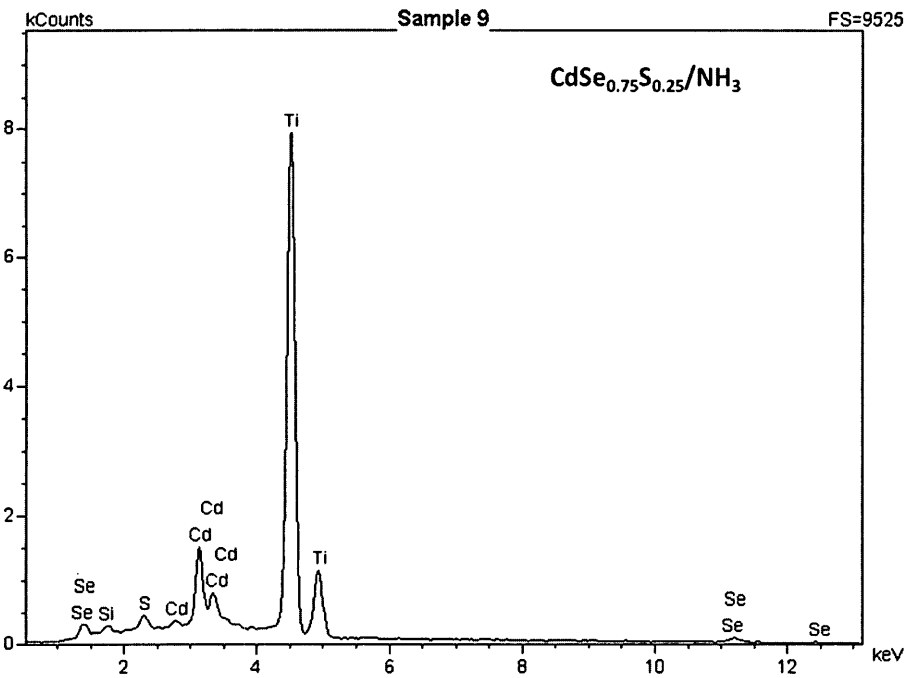

Figure A.14 EDX spectrum of TiO_2 film sensitized with $CdSe_{0.75}S_{0.25}$ in NH_3 bath.

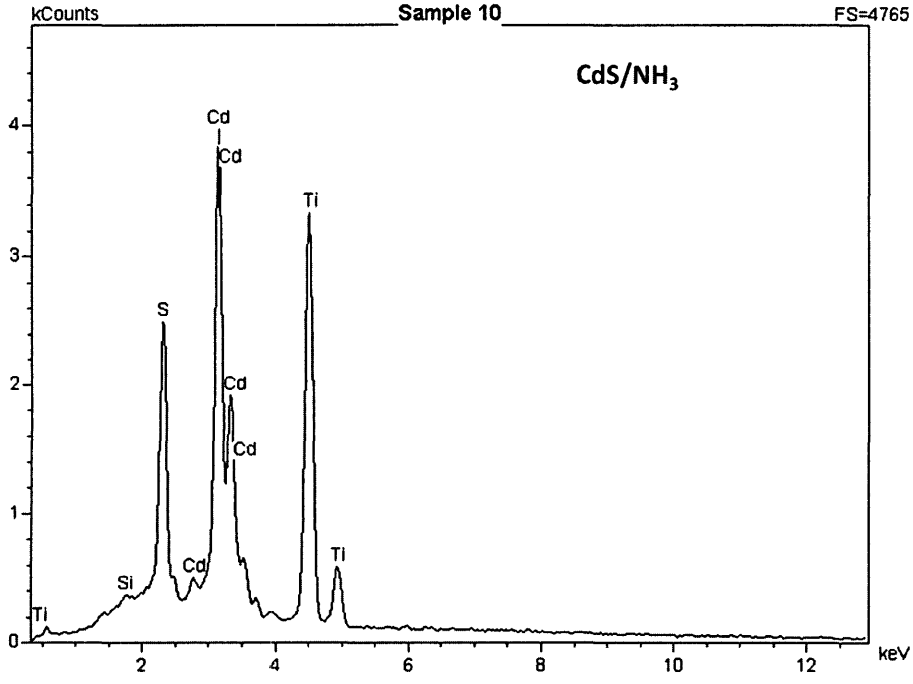

Figure A.15 EDX spectrum of TiO_2 film sensitized with CdS in NH_3 bath and post-treated with S^{2-}-rich solution.

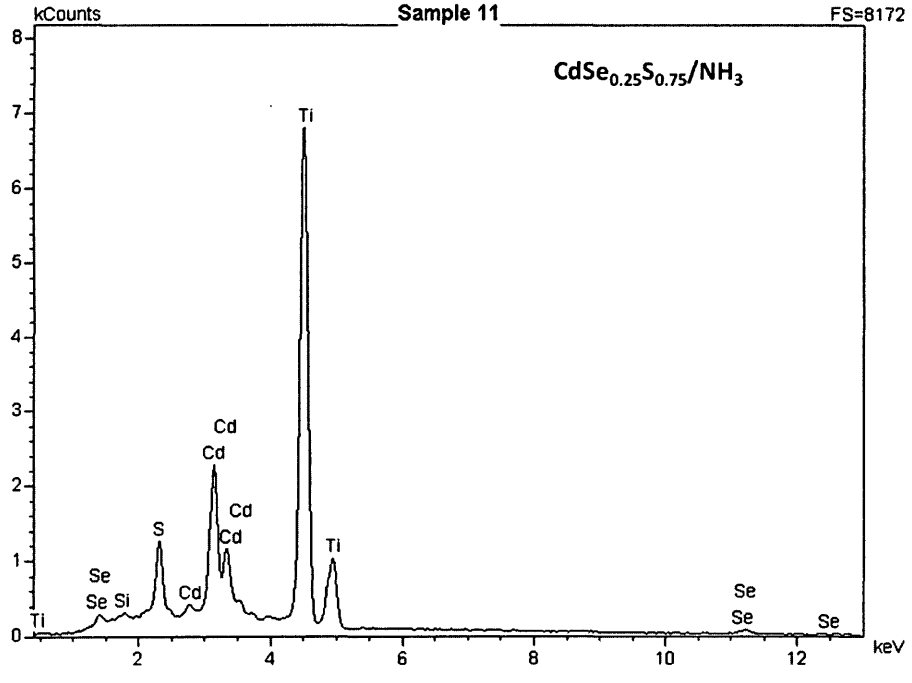

Figure A.16 EDX spectrum of TiO_2 film sensitized with $CdSe_{0.25}S_{0.75}$ in NH_3 bath and post-treated with S^{2-}-rich solution.

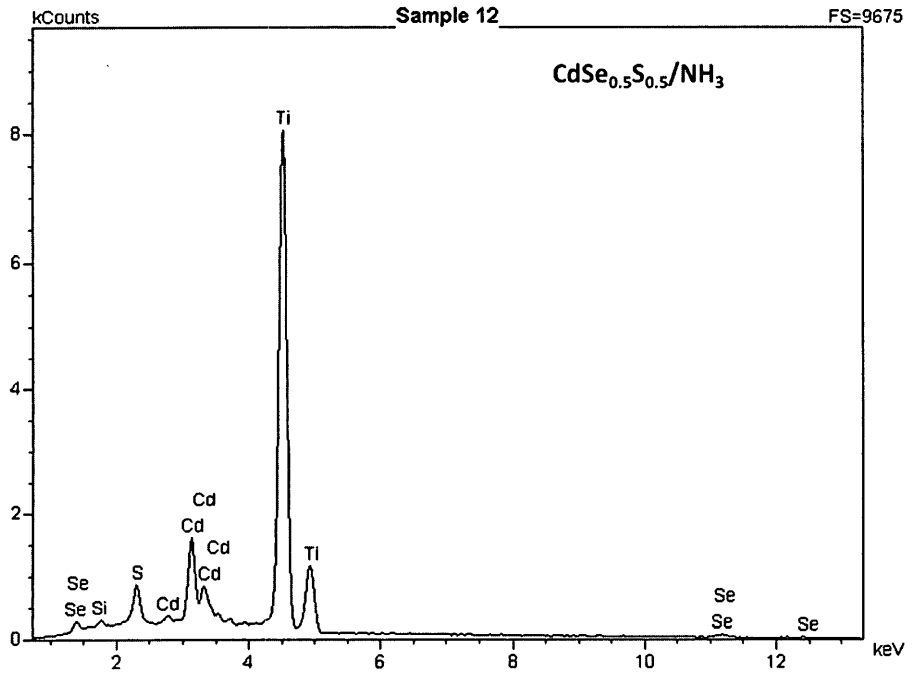

Figure A.17 EDX spectrum of TiO_2 film sensitized with $CdSe_{0.5}S_{0.5}$ in NH_3 bath and post-treated with S^{2-}-rich solution.

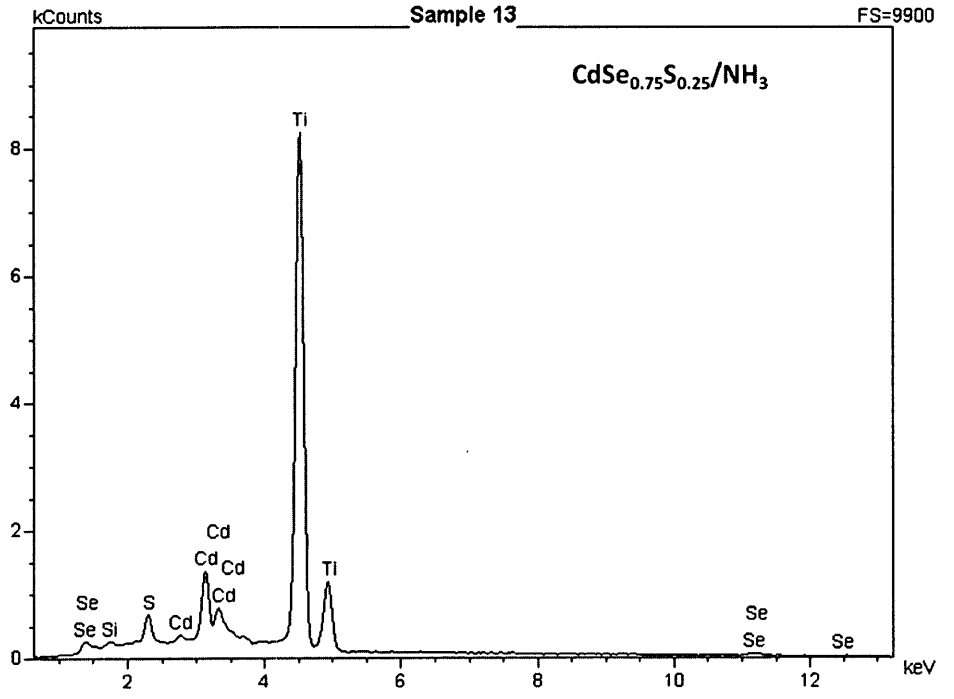

Figure A.18 EDX spectrum of TiO_2 film sensitized with $CdSe_{0.75}S_{0.25}$ in NH_3 bath and post-treated with S^{2-}-rich solution.

Appendix B: PXRD Spectra and Analysis of powder $CdSe_xS_{(1-x)}$ prepared from NTA solutions.

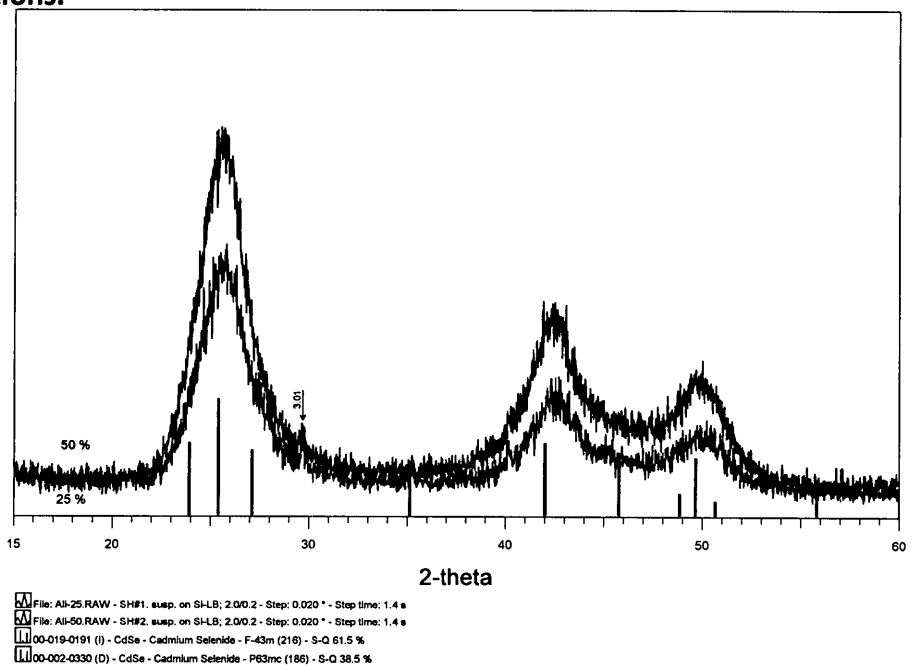

Figure B.1 PXRD patterns of powdered samples $CdSe_{0.25}S_{0.75}$ (black colored) and $CdSe_{0.5}S_{0.5}$ (red colored) compred with the reference patterns of CdSe polymorphs.

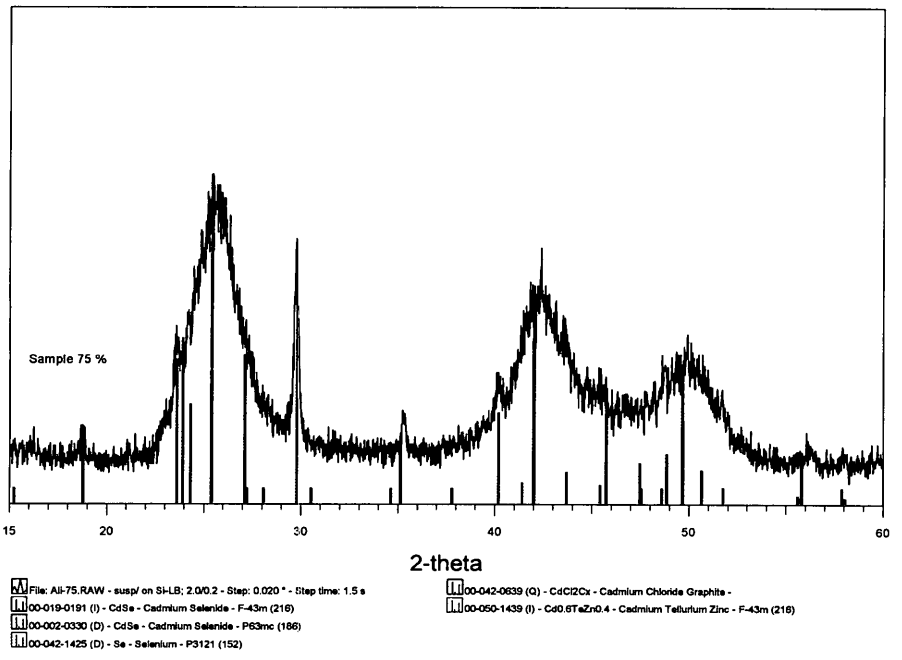

Figure B.2 PXRD patterns of powdered samples $CdSe_{0.75}S_{0.25}$ prepared from NTA chemical bath.

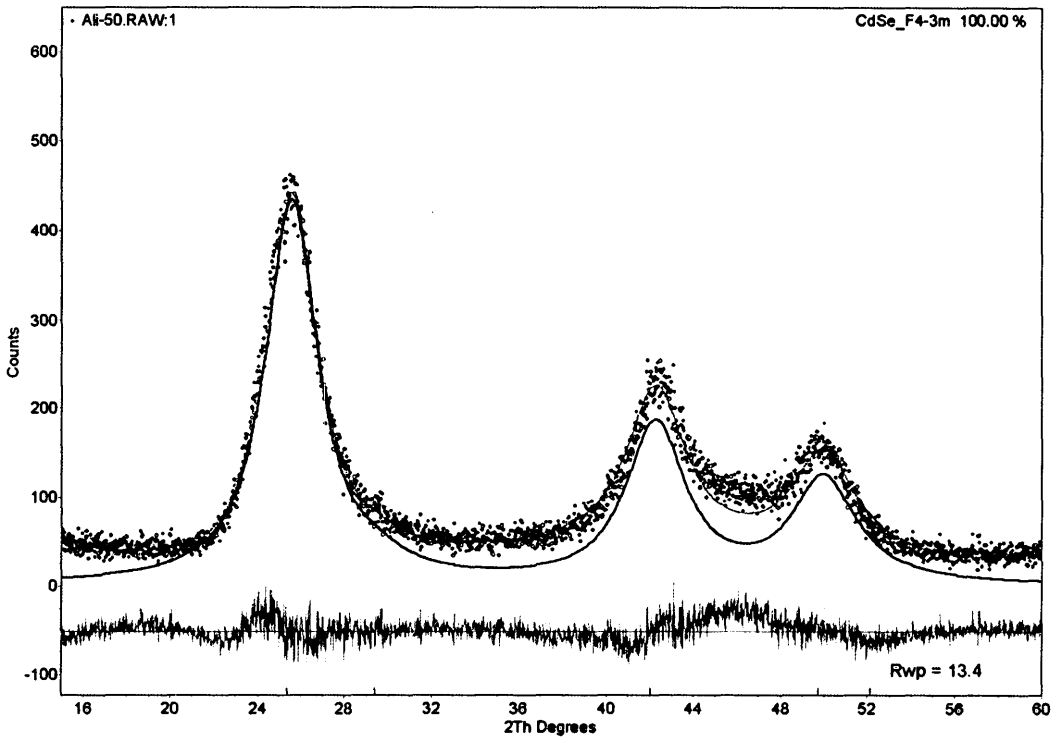

Figure B.3 Rietveld deconvolusion of the PXRD patterns of powdered samples $CdSe_{0.5}S_{0.5}$ prepared from NTA chemical bath. One phase was characterized.

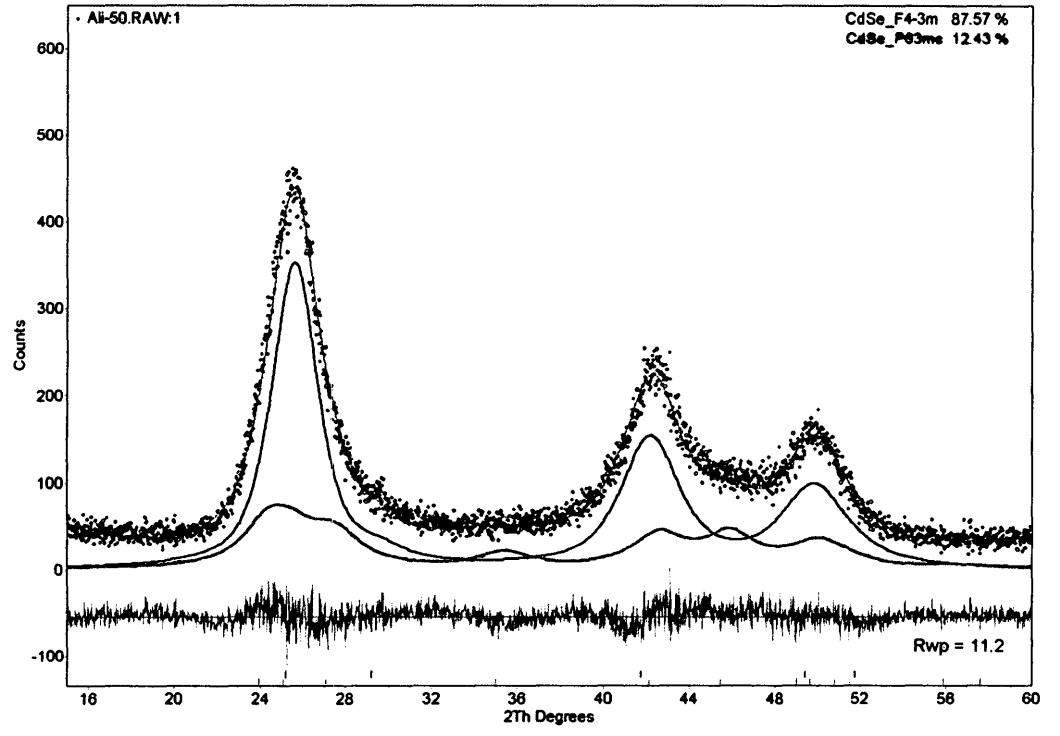

Figure B.4 Rietveld deconvolusion of the PXRD patterns of powdered samples $CdSe_{0.5}S_{0.5}$ prepared from NTA chemical bath. Two phases were characterized.

Appendix C: PEC Graphs of $CdSe_xS_{(1-x)}$ Films Post-Treated with S^{2-}-Rich Solution

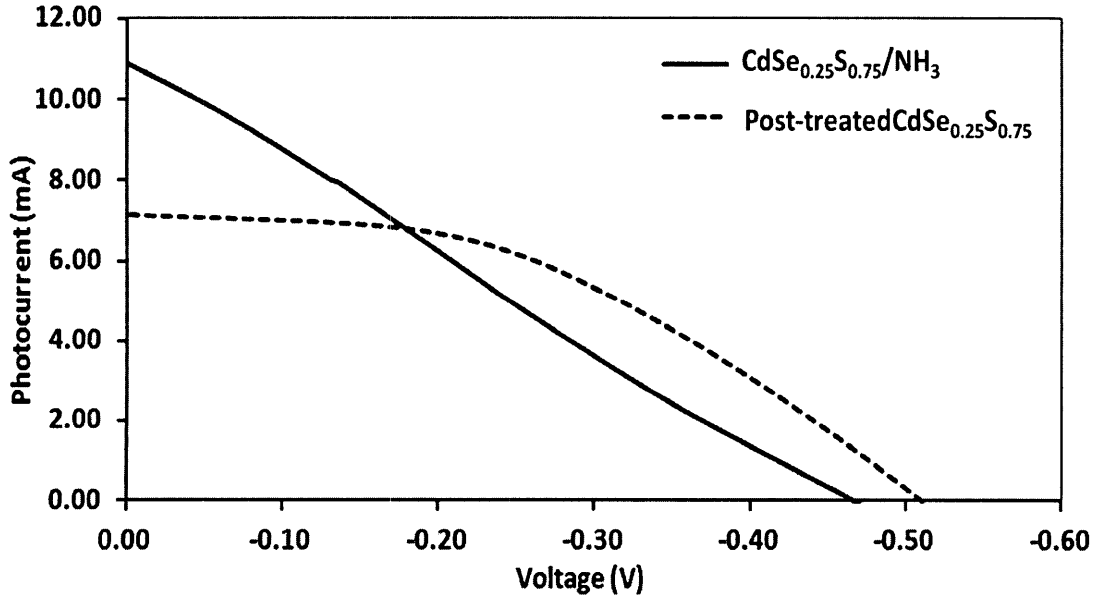

Figure C.1 i-V graph of $CdSe_{0.25}S_{0.75}$ films prepared from NH_3 bath; solid line is non-treated; dashed line is post-treated with S^{2-}-rich solution.

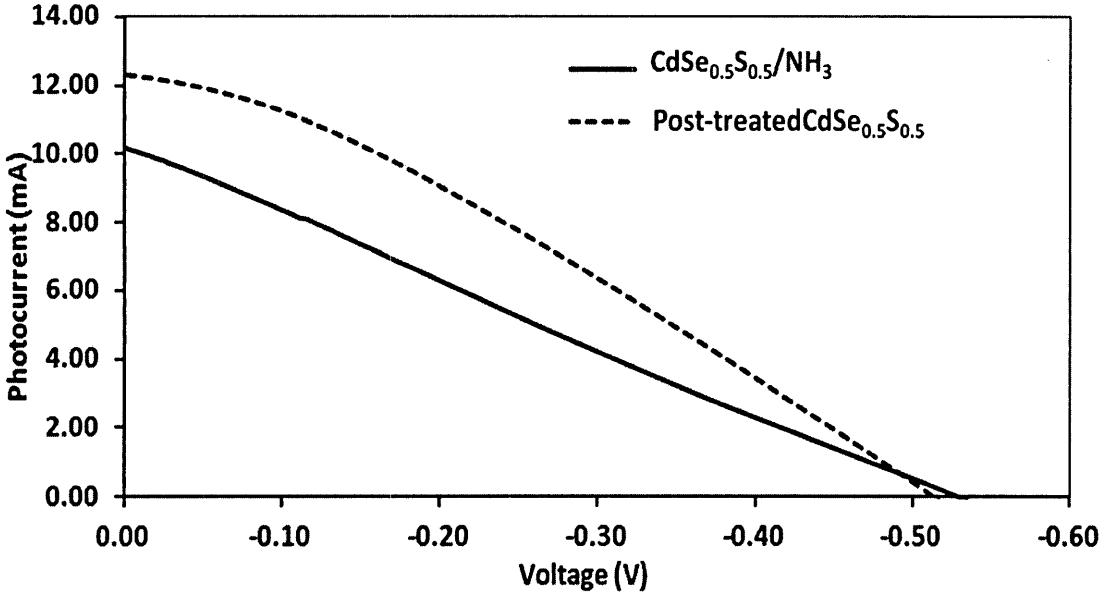

Figure C.2 i-V graph of $CdSe_{0.5}S_{0.5}$ films prepared from NH_3 bath; solid line is non-treated; dashed line is post-treated with S^{2-}-rich solution.

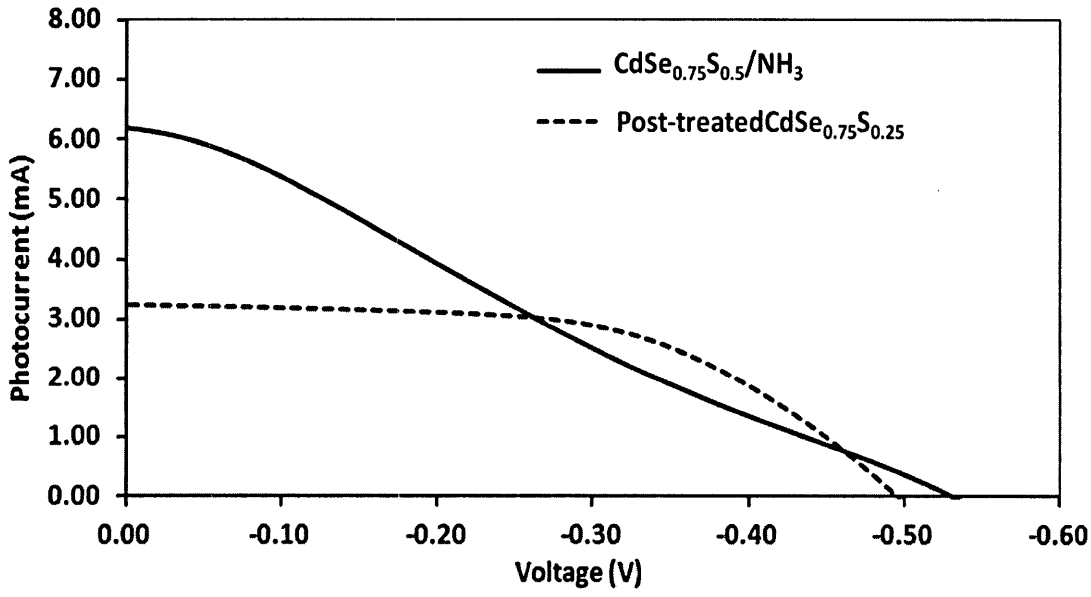

Figure C.3 i-V graph of $CdSe_{0.75}S_{0.25}$ films prepared from NH_3 bath; solid line is non-treated; dashed line is post-treated with S^{2-}-rich solution.

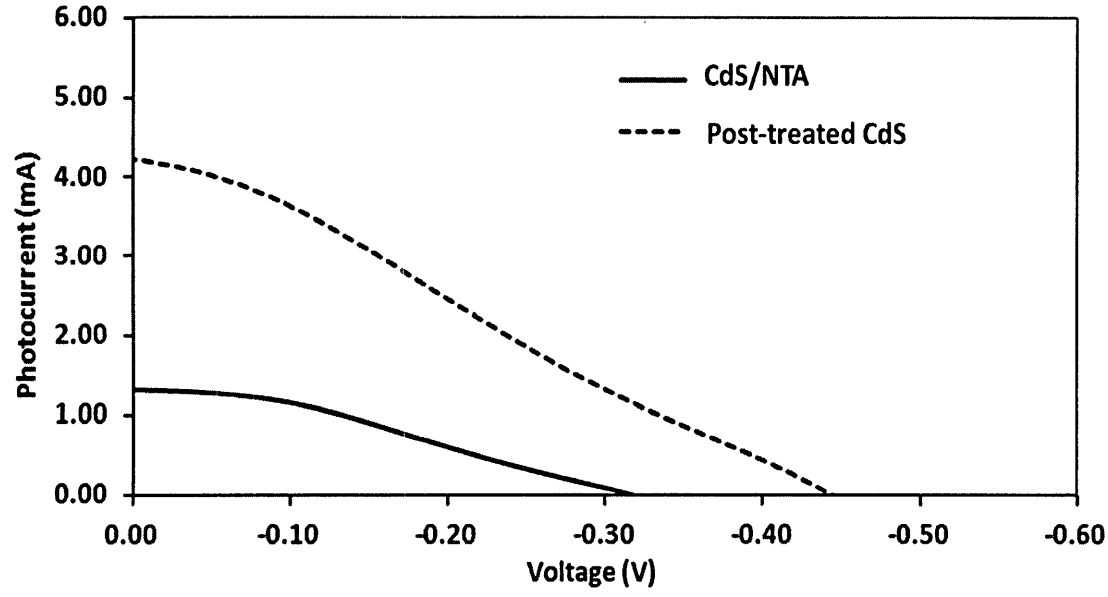

Figure C.4 i-V graph of CdS films prepared from NTA bath; solid line is non-treated; dashed line is post-treated with S^{2-}-rich solution.

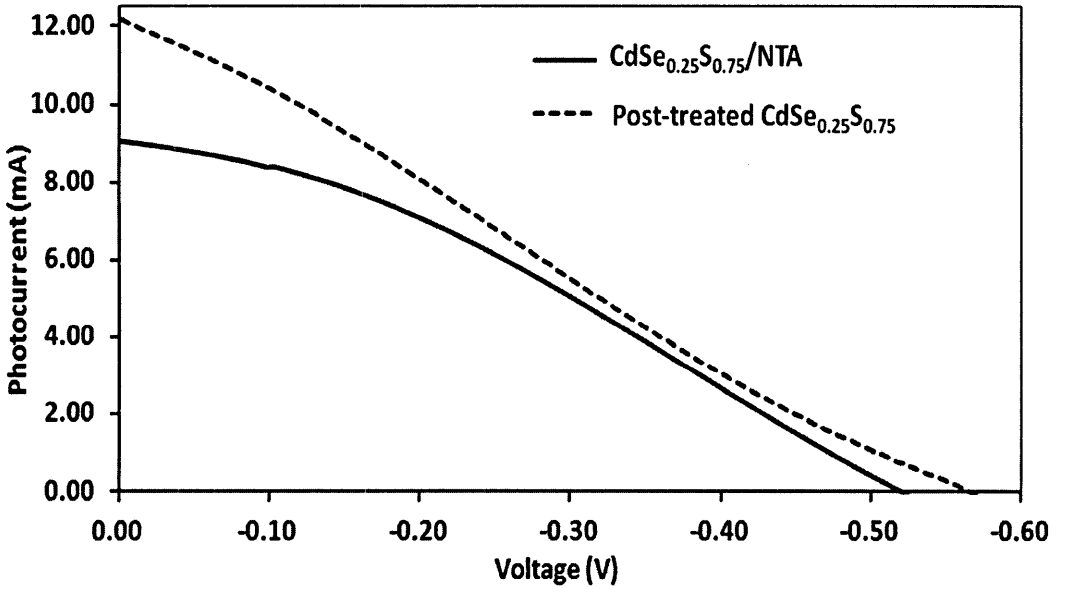

Figure C.5 i-V graph of $CdSe_{0.25}S_{0.75}$ films prepared from NTA bath; solid line is non-treated; dashed line is post-treated with S^{2-}-rich solution.

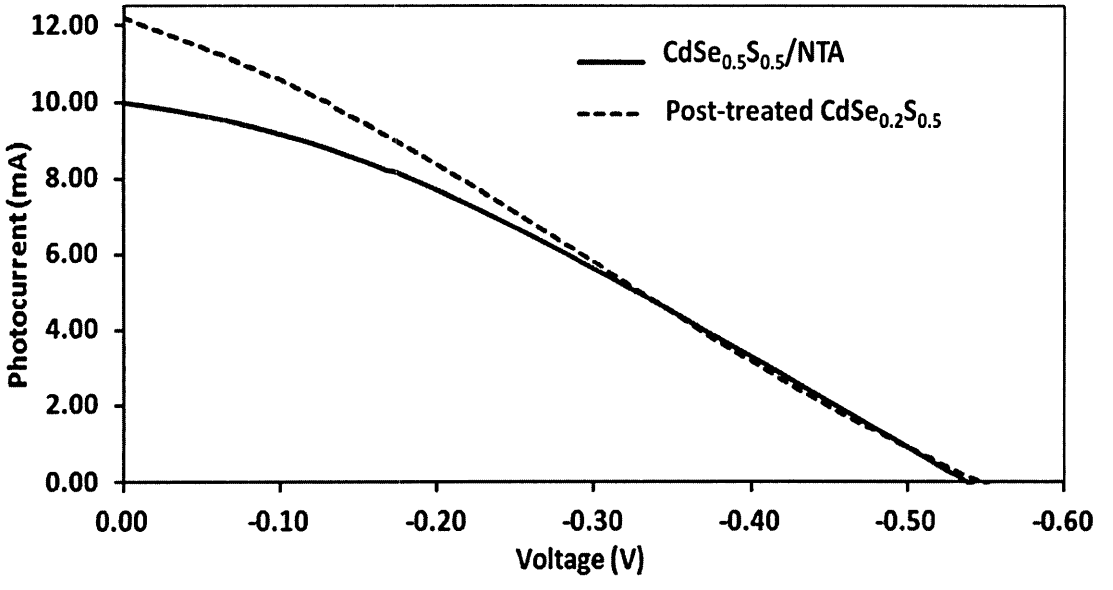

Figure C.6 i-V graph of $CdSe_{0.5}S_{0.5}$ films prepared from NTA bath; solid line is non-treated; dashed line is post-treated with S^{2-}-rich solution.

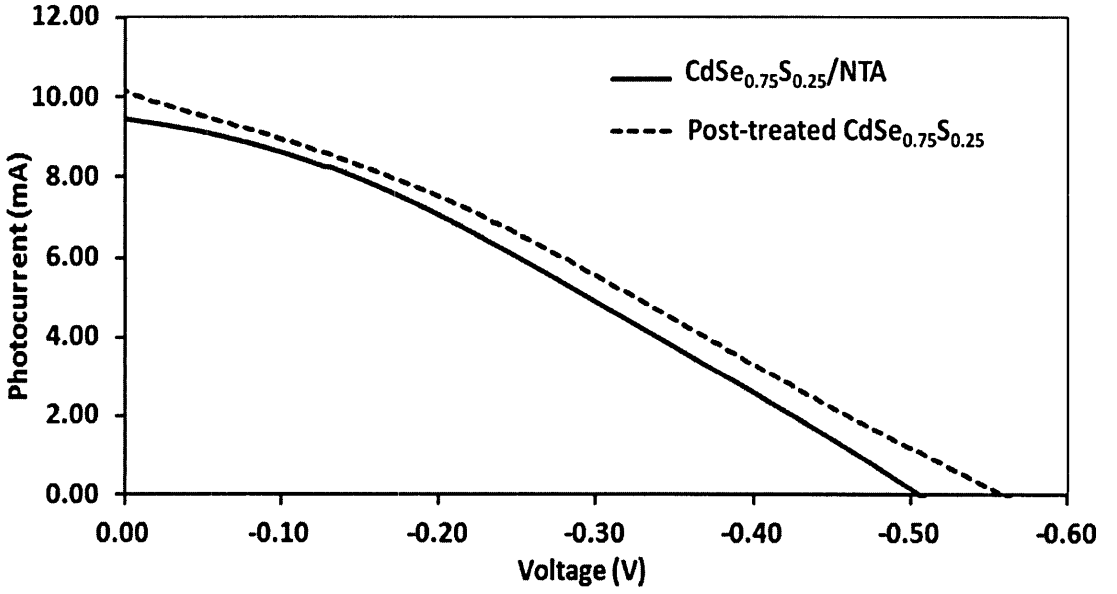

Figure C.7 i-V graph of $CdSe_{0.75}S_{0.25}$ films prepared from NTA bath; solid line is non-treated; dashed line is post-treated with S^{2-}-rich solution.

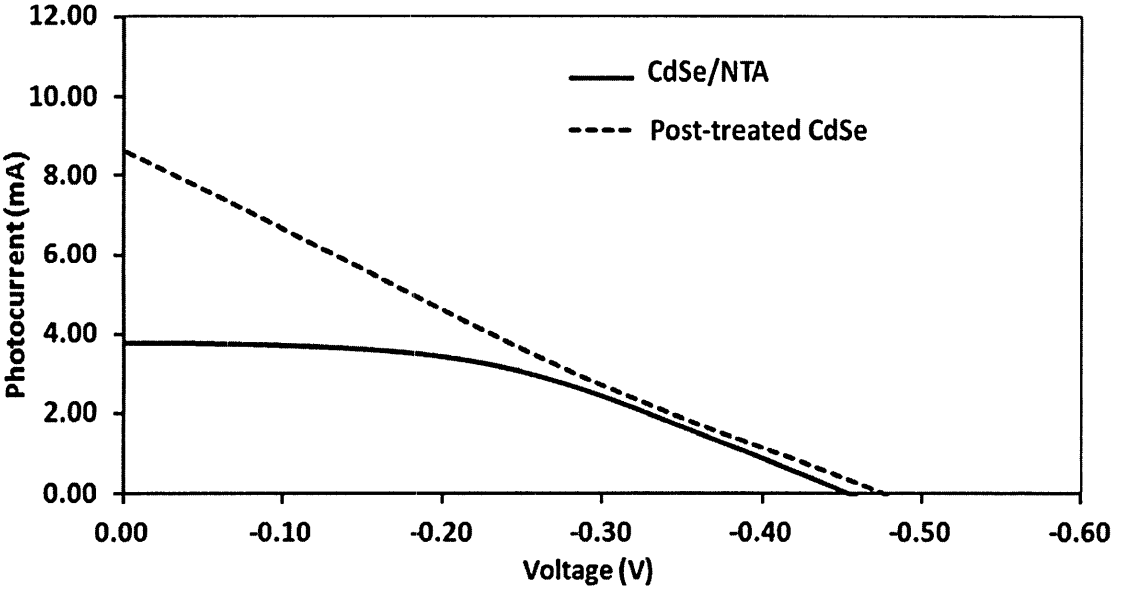

Figure C.8 i-V graph of CdSe films prepared from NTA bath; solid line is non-treated; dashed line is post-treated with S^{2-}-rich solution.

Appendix D: High-Resolution XPS Spectra of films prepared by NH_3 Chemical Baths

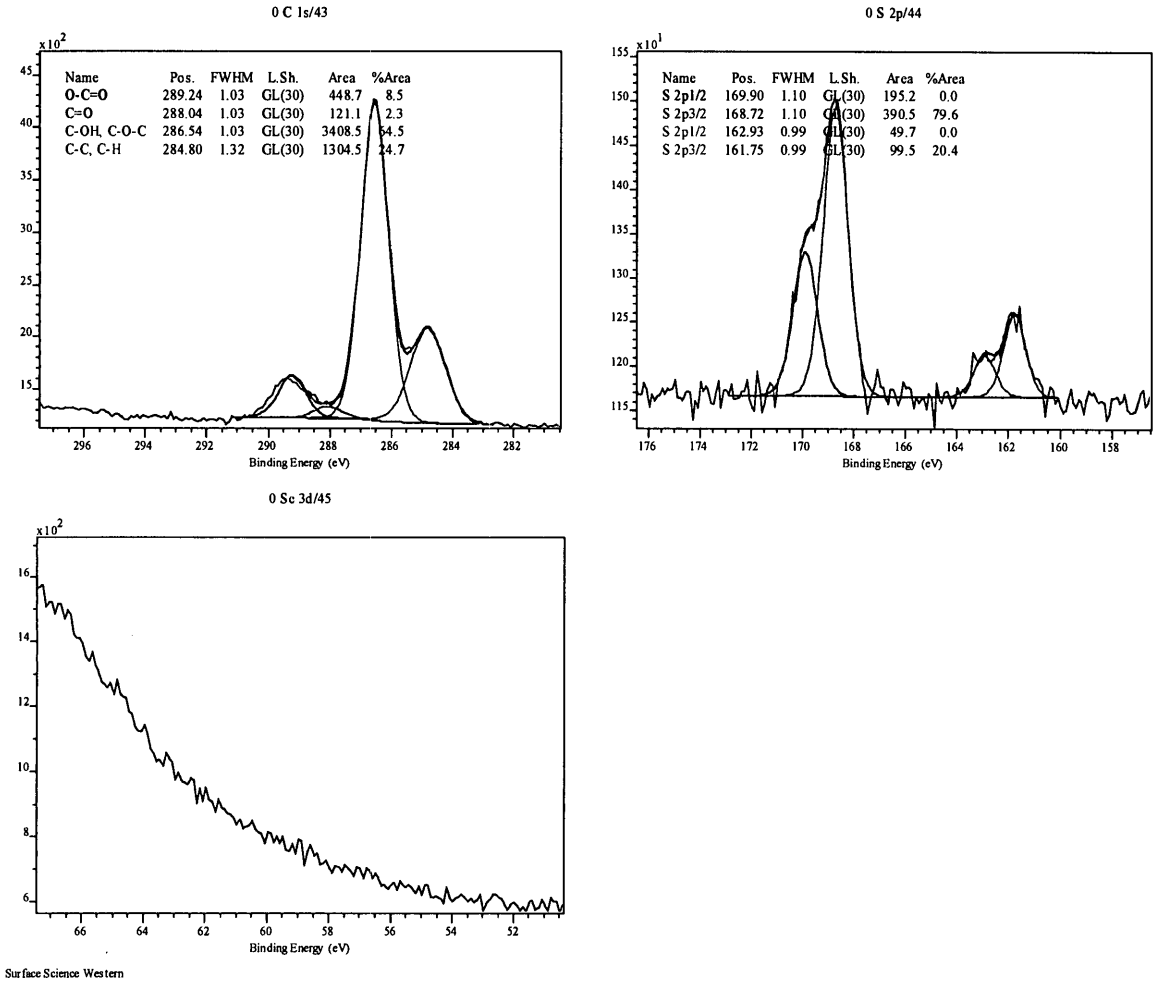

Figure D.1 High-resolution XPS spectra of CdS prepared in NH_3 chemical bath. Energy Zone 1.

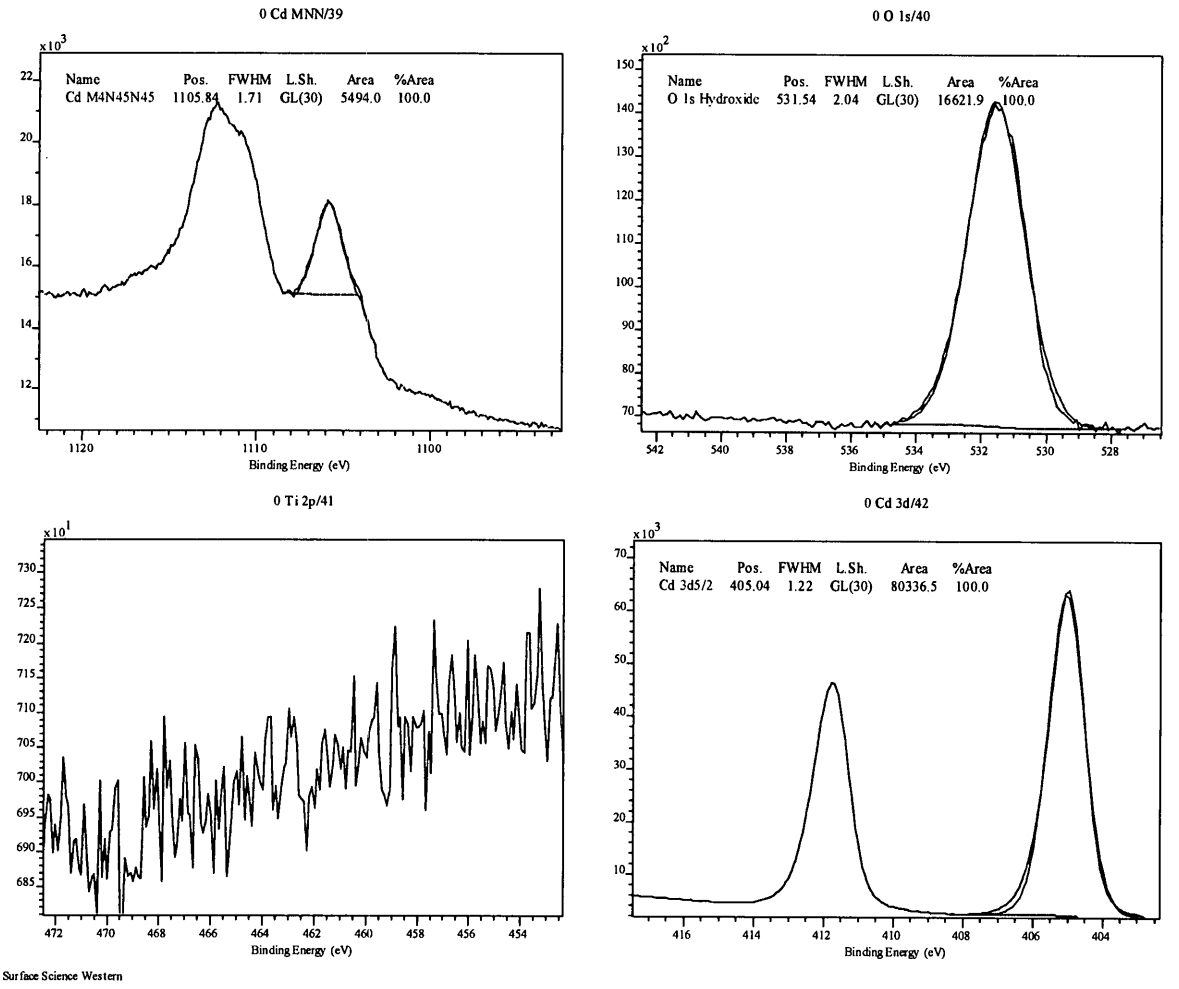

Figure D.2 High-resolution XPS spectra of CdS prepared in NH_3 chemical bath. Energy Zone 2.

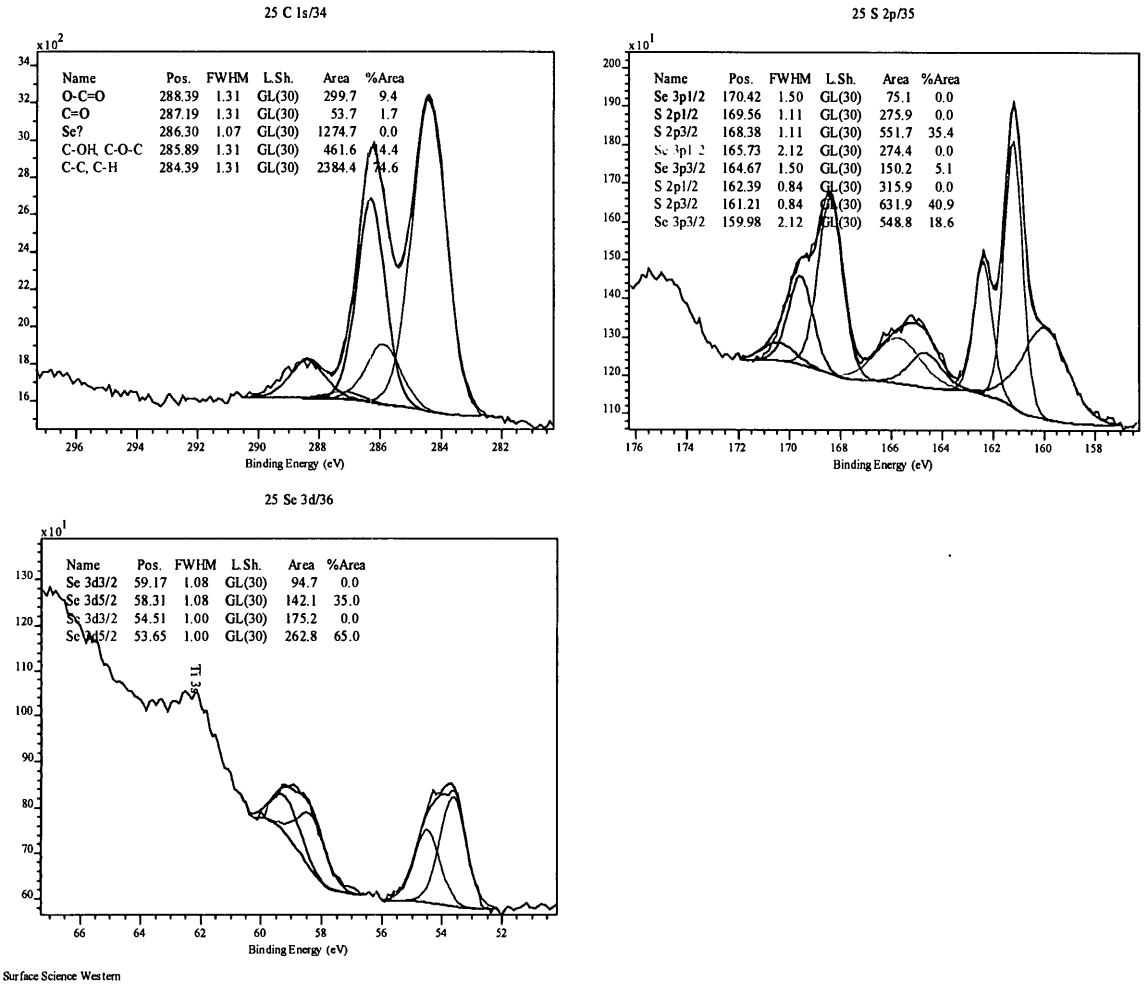

Figure D.3 High-resolution XPS spectra of $CdSe_{0.25}S_{0.75}$ prepared in NH_3 chemical bath. Energy Zone 1.

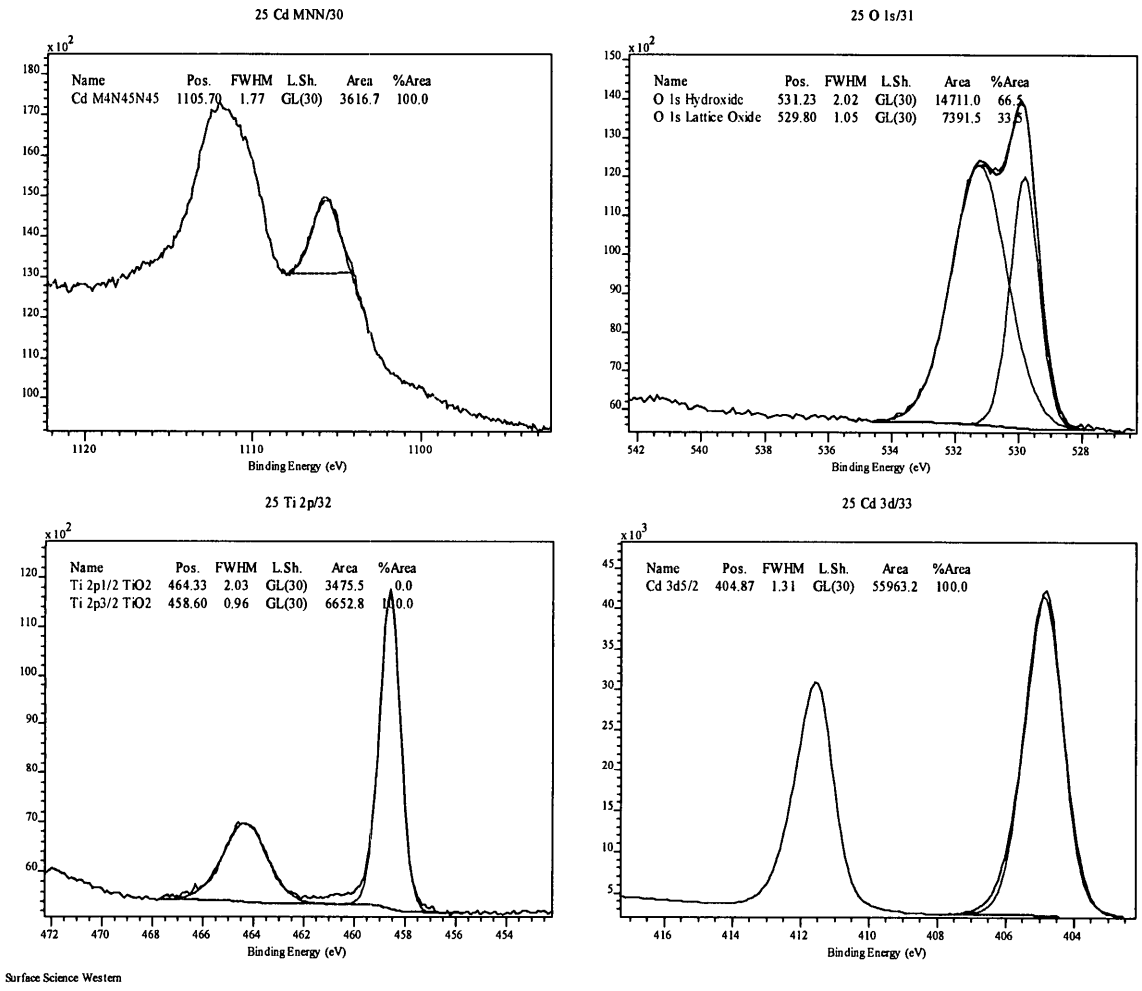

Figure D.4 High-resolution XPS spectra of $CdSe_{0.25}S_{0.75}$ prepared in NH_3 chemical bath. Energy Zone 2.

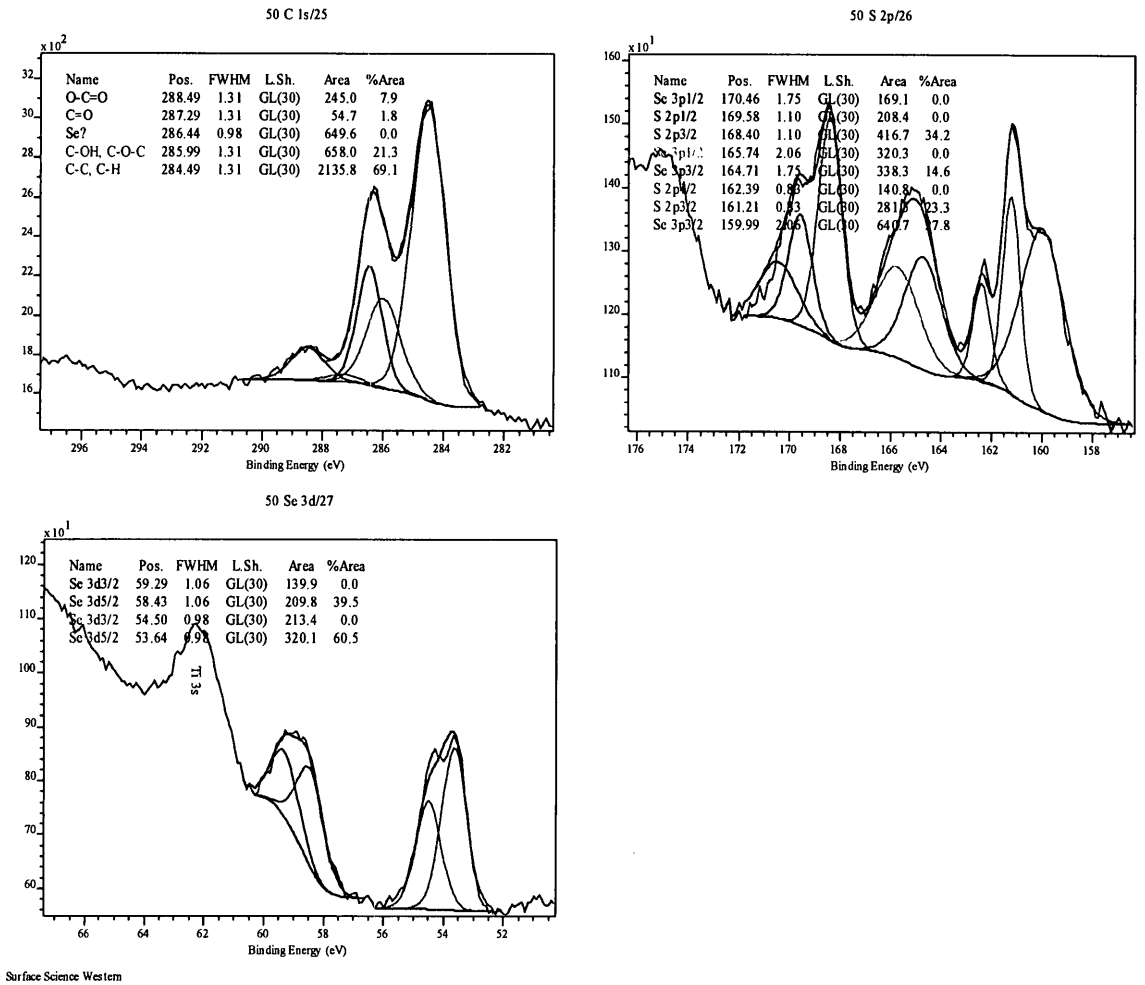

Figure D.5 High-resolution XPS spectra of $CdSe_{0.5}S_{0.5}$ prepared in NH_3 chemical bath. Energy Zone 1.

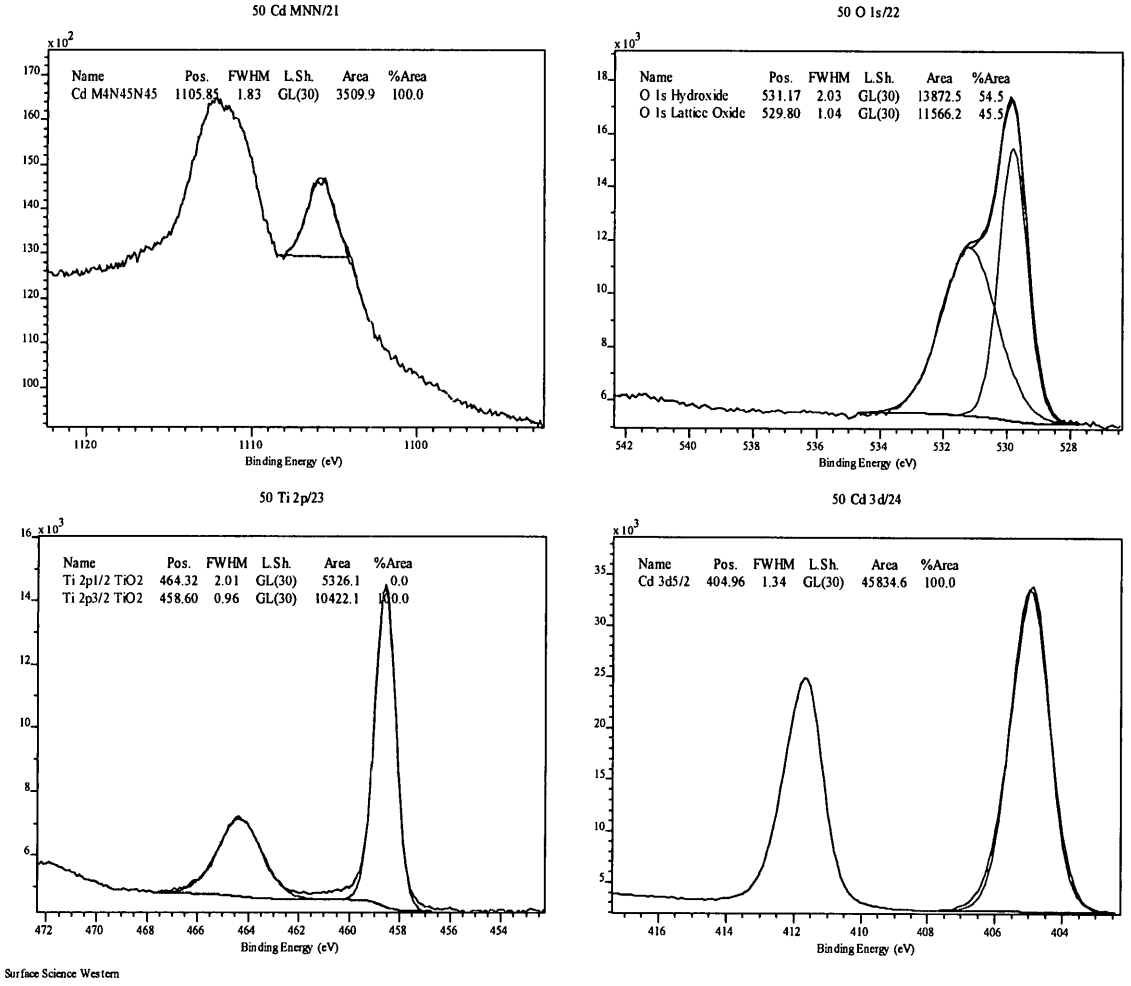

Figure D.6 High-resolution XPS spectra of $CdSe_{0.5}S_{0.5}$ prepared in NH_3 chemical bath. Energy Zone 2.

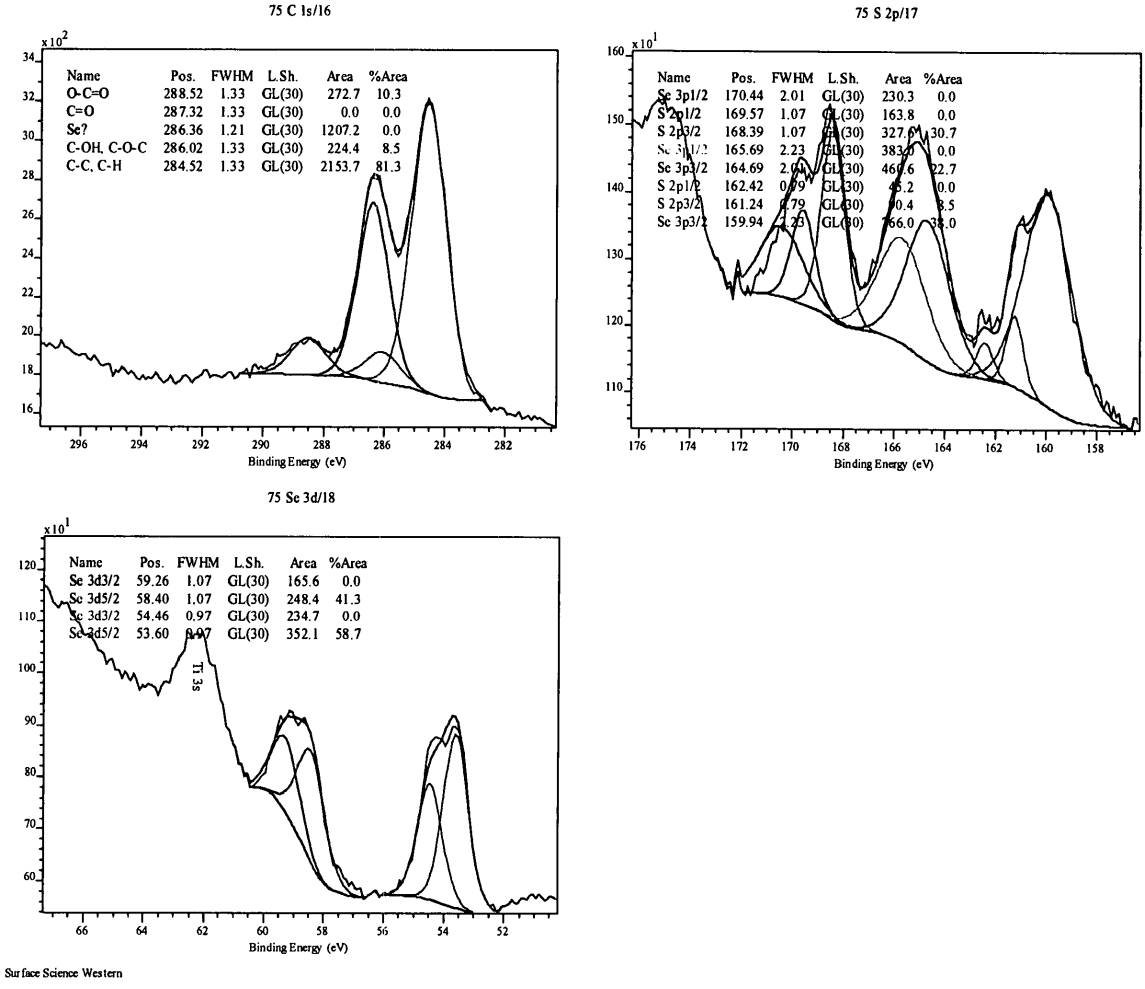

Figure D.7 High-resolution XPS spectra of $CdSe_{0.75}S_{0.25}$ prepared in NH_3 chemical bath. Energy Zone 1.

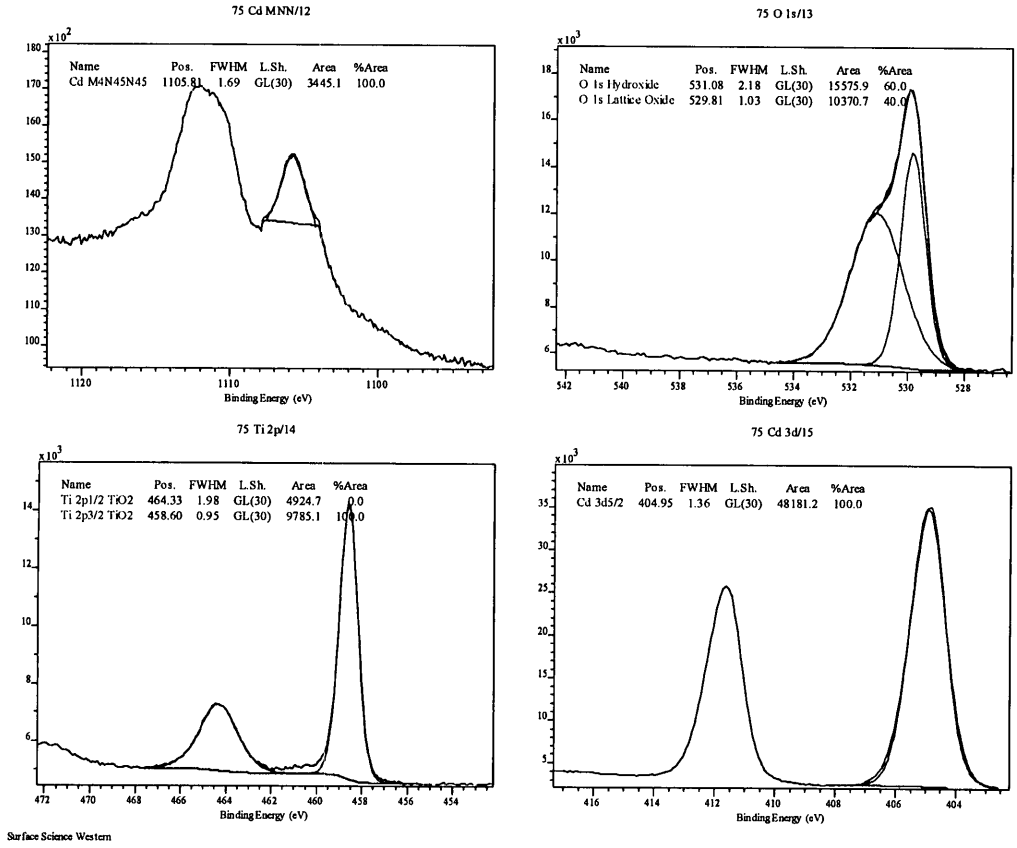

Figure D.8 High-resolution XPS spectra of $CdSe_{0.75}S_{0.25}$ prepared in NH_3 chemical bath. Energy Zone 2.

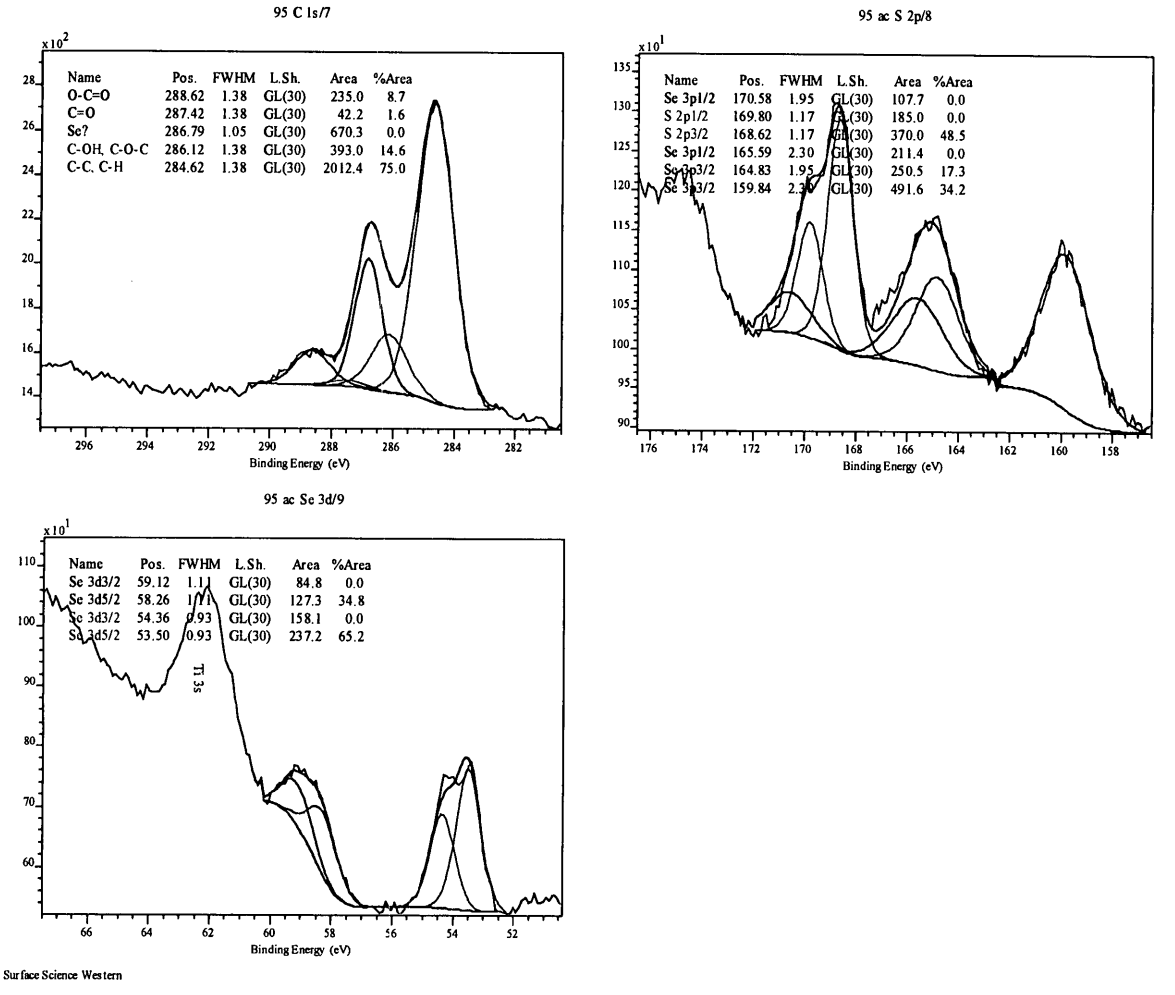

Figure D.9 High-resolution XPS spectra of CdSe prepared in NH_3 chemical bath. Energy Zone 1.

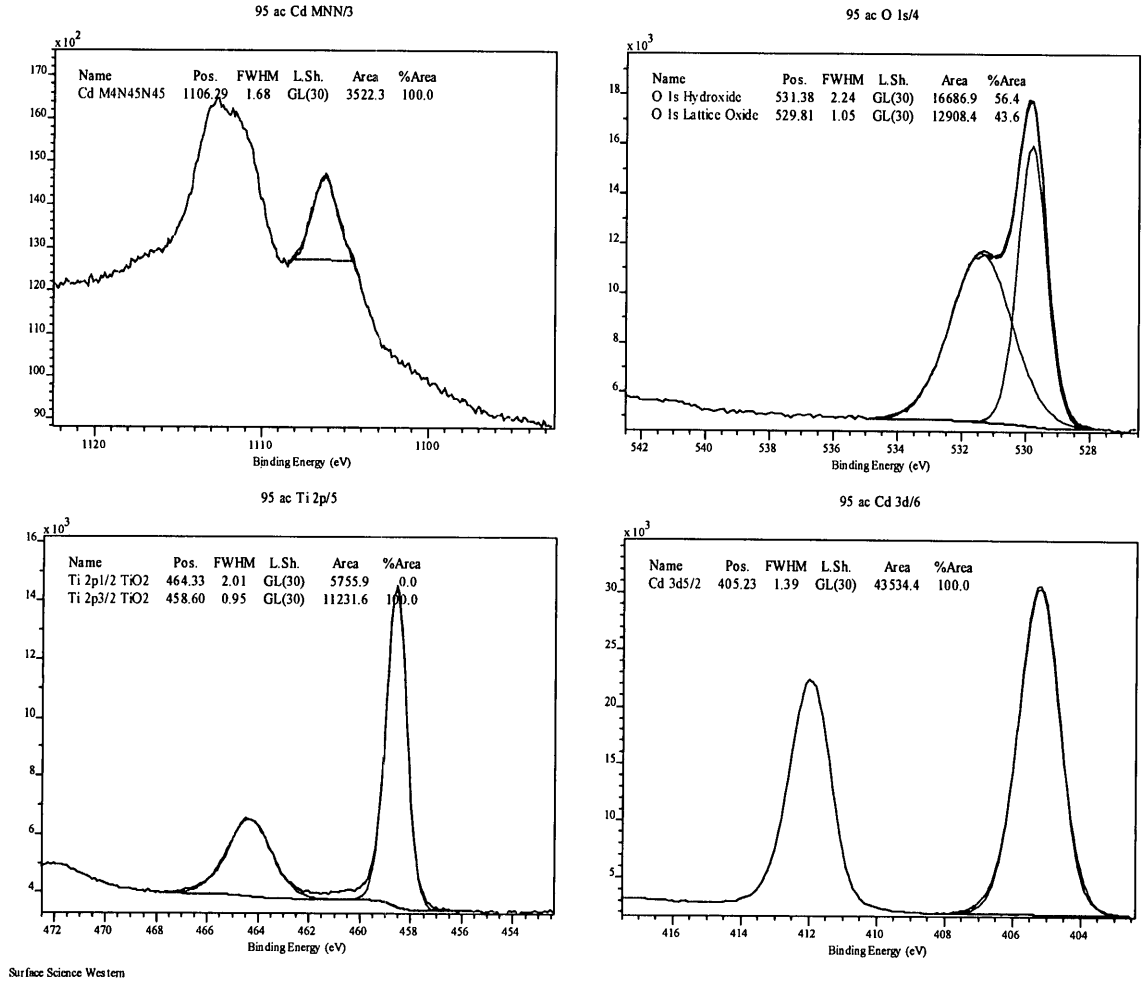

Figure D.10 High-resolution XPS spectra of CdSe prepared in NH_3 chemical bath. Energy Zone 2.